Nonlinear seismic response of the soil-structure system : experimental analyses

Johanes Chandra

UNIVERSITÉ DE GRENOBLE

THÈSE

Pour obtenir le grade de

DOCTEUR DE L'UNIVERSITÉ DE GRENOBLE

Spécialité : **Sciences de la Terre, l'Univers et l'Environnement**

Arrêté ministériel : 7 août 2006

Présentée par

Johanes CHANDRA

Thèse dirigée par **Philippe GUEGUEN**

préparée au sein de l'**Institut des Sciences de la Terre**
dans **l'École Doctorale Terre, Univers, Environnement**

Analyses expérimentales de la réponse sismique non-linéaire du système sol-structure

Thèse soutenue publiquement le **28 Octobre 2014,**
Devant le jury composé de :

Pr. Arezou MODARESSI
Ecole Centrale Paris, Rapporteur
Pr. Roberto PAOLUCCI
Politecnico di Milano, Rapporteur
Pr. Alain PECKER
Ecole des Ponts ParisTech, Examinateur
Pr. Olivier COUTANT
ISTerre, Univ. Joseph Fourier, Grenoble, Président
Dr. Philippe GUEGUEN
ISTerre, Univ. Joseph Fourier, Grenoble, Directeur de thèse

Dr. Luis Fabian BONILLA (invité)
Université Paris Est, IFSTTAR, Paris

Université Joseph Fourier / Université Pierre Mendès France /
Université Stendhal / Université de Savoie / Grenoble INP

Foreword

I never forget the joy when I read Philippe's letter as the beginning of my PhD journey. I keep that joy as my motivation that drove me through all the up and down moments during these three years. I am grateful to have Philippe Guéguen as my mentor who has been patiently guiding me through the entire process. I really could not ask for a better supervisor! I would like to thank as well, Fabian Bonilla, for his enlightening collaboration, and Jamie Steidl which gave me a glimpse of the fieldwork reality.

I would like to thank Pierre-Yves Bard, Jean-François Semblat, Fernando Lopez Caballero, Céline Gélis, Emmanuel Chaljub and other heaps of names that I cannot all list here for all the fruitful discussions that we had. I would also like to thank Roberto Paolucci and Arezou Modaressi for their time reading and commenting this manuscript. I thank the aforementioned juries as well as Alain Pecker and Olivier Coutant for assisting and being part of the defense process.

I would like to express my gratitude to these following names for supporting me, becoming my family, and sharing this process: Afifa Imtiaz, Ismaël Riedel, Olga Ktenidou, Hilal Tasan, Claudia Aristizabal, Zahra Mousavi, Anne Obermann, Amir Asnaashari, Haskell Sie, Maria E. Suryatriyastuti, Jessica Sjah, PPI Grenoble, all ISTerre; To them who proofread my manuscript without burning them: Haskell Sie, Eleanor Bakker, Paul Wellington, and Olga Ktenidou; and of course all the names that again I could not list here without making this acknowledgement thicker than the manuscript itself. To Philippe Perrin who bore all the craziness at the end of the journey without losing his sanity!

I do not forget my family who is always in my heart despite this 11,361 km distance, for all their prayers and supports: Siauw Jonny Sarsono, Khoe Chun Lan, Christian Chandra, and Michael Chandra.

I have been blessed!

Johanes

This page intentionally left blank

Table of Contents

This page intentionally left blank

General Introduction

The earth consists of several moving tectonic plates. While moving, these plates store strain energy, and as the shear stress on these fault planes passes the shear strength of the rock along the fault, this strain energy is released as what we known as earthquake. These earthquakes are one of the most detrimental natural disasters that mankind face. Depending on its level, the energy release can generate death and destruction. For example, during the period between 2000 and 2010, earthquakes have contributed to the death of approximately 699,000 people (Holzer and Savage, 2013). Some recent noteworthy earthquakes include the 2004 Sumatra-Andaman earthquake (Mw = 9.1) that killed more than 220,000 people; the 2010 Haiti earthquake (Mw = 7.0) with around 316,000 deaths; and the 2011 Tohoku earthquake (Mw = 9.0) that killed more than 22,000 people.

When discussing global risk management, it is important to understand the definition of risk itself. Risk is not only related to hazard, but is also the product of vulnerability and exposure.

RISK = HAZARD x VULNERABILITY x EXPOSURE

In short, hazard can be defined as the physical impact of disturbance. As such seismic hazard refer to the ground motion itself. This depends on the characterization of ground motion parameters. The seismic hazard analysis consists of quantifying the ground-shaking hazards at a particular site (Kramer, 1996). The most common ways to "measure" earthquake are either by its intensity, magnitude or energy. Intensity is more qualitative measure, while magnitude (and energy) is more directly applicable to hazard quantification. Probabilistic Seismic Hazard Analysis (PSHA) is the current approach to attempt to estimate hazard and to predict ground motion responses. This analysis can be performed either at one site or in terms of a global hazard map through the Ground Motion Prediction Equations (GMPEs). The ground motion responses, however, differ from one earthquake event to another, depending on the source, path, and local geology condition. These numerous and complex parameters have not

been fully integrated into the prediction equation, and as a result, large uncertainties remain either from the aleatory variability (natural randomness), or the epistemic uncertainty (Cotton et al., 2006; Al Atik et al., 2010).

Vulnerability can be generally defined as the loss susceptibility (0% to 100%) resulting from a phenomenon that engenders victims and causes material damages. When talking about seismic vulnerability analysis (earthquake loss susceptibility) of a particular event, the complexity varies depending on the scale of study (building, city, country, or global). The concept of vulnerability also differs depending on its epistemological orientations (e.g. society, structure, economic vulnerability). The tools to assess seismic vulnerability of an area have been developed over the past 40 years, including empirical, analytical, and hybrid methods (Calvi et al., 2006). Empirical methods that are based on remote sensing information and data-mining methods are being developed to assess large scale vulnerability in low to moderate seismic prone regions (Riedel et al., 2014).

Exposure relates closely to vulnerability, which is why most of the literatures associate these two terminologies as one concept. While it is not untrue, it is, however, not complete, and it is important to distinguish between exposure, which is the elements affected by hazard, e.g. population, important facilities, and number of buildings.

Although numerous researches have lead us to a better understanding on natural disasters in general and earthquakes in particular, it is statistically shown that losses (both human and economic) have dramatically increased over the years due to population growth (Bankoff, 2011; Coburn and Spence, 2002; Oliveira et al., 2006). These facts lead to a pronouncement that our society has become more vulnerable. United States Geological Survey (http://www.usgs.gov/) reported that annually, earthquakes occur on average 1,469 times and 1,443,000 times, for magnitude higher and lower than 5 respectively. This highlights that earthquakes have always been (and will still be) a daily menace and that the increase of the risk is directly related to the increase of the population in urban environments. Since our abilities in earthquake prediction are no perfect, the need for understanding and quantifying earthquake risk is still as pertinent as it has ever been.

World population has increased exponentially such as shown in Fig. I.1, and in the same time similar trend is happening for the size and number of cities. Figure I.1 shows also the individual earthquakes with more than 50,000 fatalities according to USGS catalog.

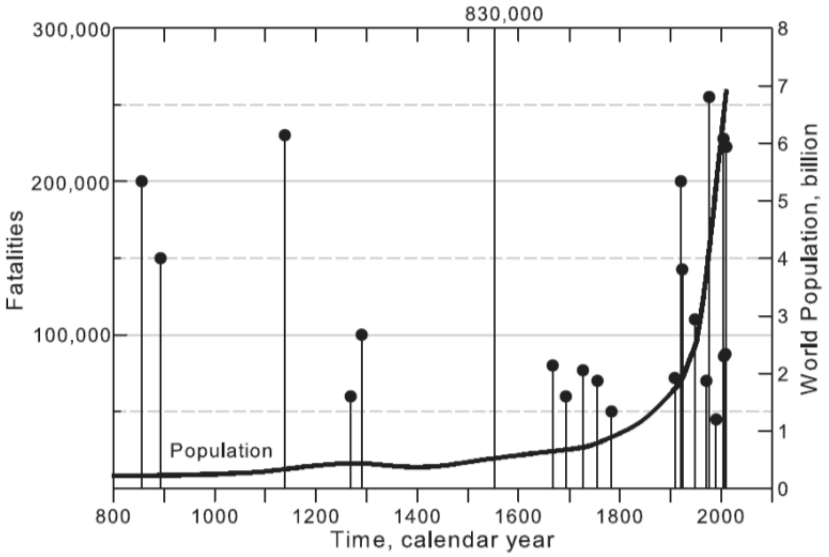

Figure I.1. Individual earthquakes from 800 to 2011 with more than 50,000 fatalities from USGS catalog (after Holzer and Savage, 2013).

Global seismic hazard and mega-cities population can be summarized by Fig I.2 which shows that we are actually living earthquake. Most earthquakes occur in urban areas, for example: California, Mexico, Japan, Chile, Indonesia, New Zealand, and China. This trend will persist and even increase where population is concentrated in urban areas. Cohen (2006) reported that around 3 billion people (half of the world's total population) live in urban areas, and over the next 30 years, it is expected that all of the world's population will be concentrated in these urban settlements. As urbanization increases, rural areas are developed into cities, and cities are developed into mega cities. This concentration of world population means that global seismic exposure is increased in high hazard regions which results in the growth of seismic risk.

Studies from Coburn and Spence (2002), Bilham [2004, 2009], and Holzer and Savage (2013) show that the rate of seismic vulnerability reduction cannot keep up with the increase and concentration of world population in seismic prone regions. While reducing the fatality rates percentage, the absolute number of fatalities increases. Bilham (2009) projected that the population explosion will be followed by the construction boom at least up to the next three

decades. Although seismic building codes already exist, insufficient awareness may hinder adequate construction plans in seismically vulnerable cities.

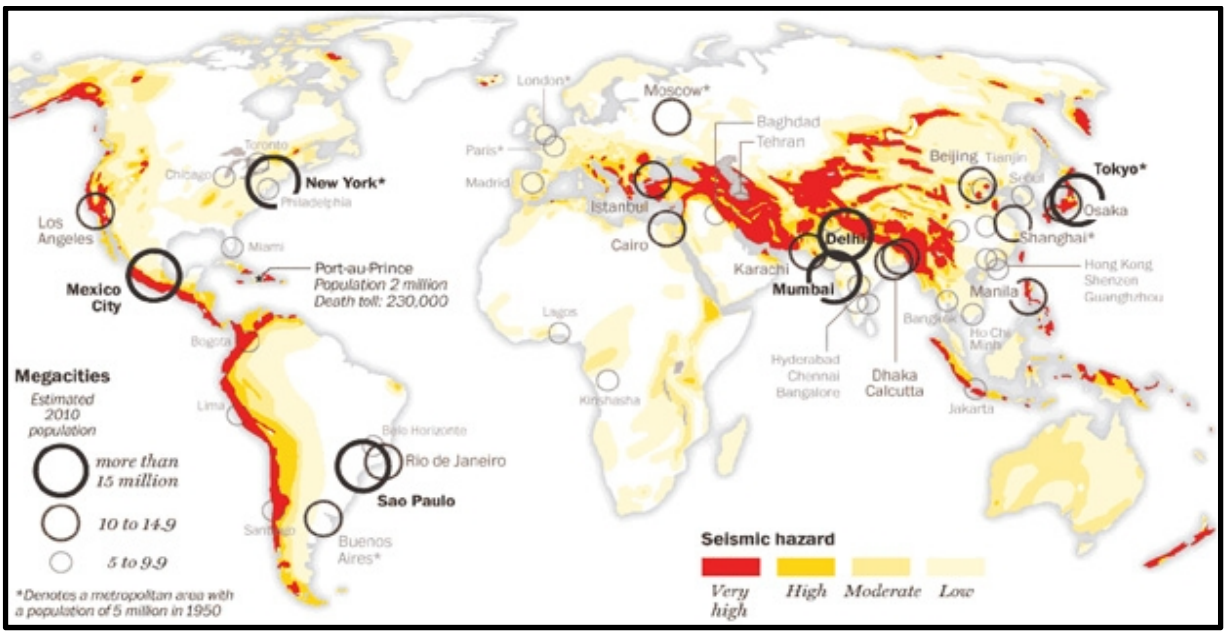

Figure I.2. Map of global seismic hazard and world population (after Karklis, 2010).

The urbanization trend related to increased exposure is hard to avoid since population has been concentrated in the lowlands and close to fresh water resources (Jackson, 2006). Most of these lowlands have been covered by sediments that were shed from the erosion or transported from the higher places. Sediment layers greatly enhance the seismic hazard through alteration of the ground motion response, due to what is known as site effects. One hand, sediments tend to amplify the ground motion (direct site effects) and on the other hand, the earthquake induces material deformation/modification (soil nonlinearity) which can cause liquefaction and slope instabilities.

An example is the famous case of the 1985 Mexico City earthquake (Mw = 8.0) where the ground motion recorded on the sediment area was almost 5 times larger than the one recorded on bedrock area. The amplification of ground motion is caused by the impedance between bedrock and sediments. The same 1985 Mexico City earthquake, together with the 1989 Loma Prieta earthquake are also important of adding empirical data and changing the nonlinear threshold from previously 0.13g (Seed et al., 1976; Fig I.3a) to around 0.4g (Idriss, 1990; Fig I.3b). Such as shown in Fig.I.3, the soil nonlinearity tends to deamplify the ground motion responses on soil sites compared to the rock sites. The importance of site effects have

been as well observed throughout several other earthquakes, such as the 1994 Northridge earthquake, the 1995 Kobe earthquake, and the 2003 Bam earthquake, where the ground motion recorded in sediments were modified compared to the one in bedrock.

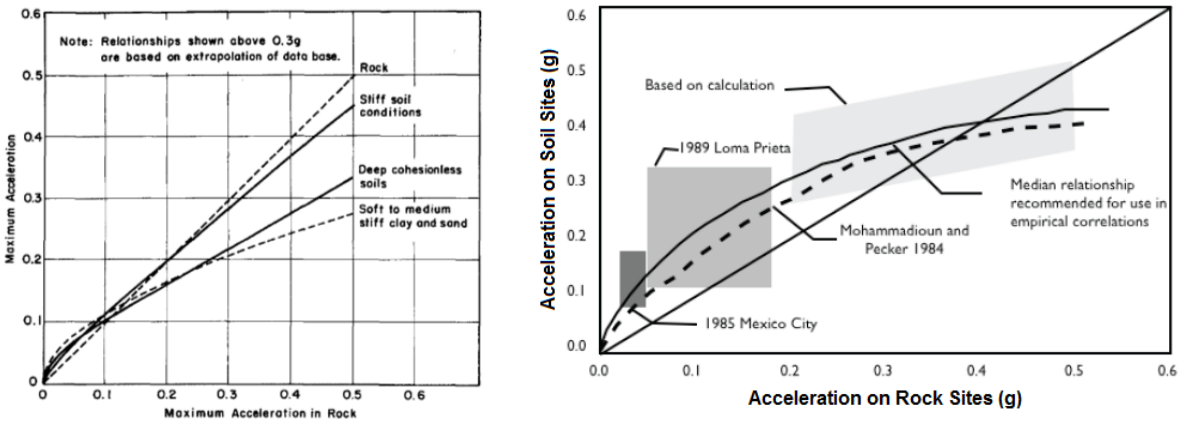

Figure I.3. Comparison between acceleration on soil sites and rock sites. (a). Before (taken from Seed et al., 1976), and (b).After the 1985 Mexico City earthquake (taken from Guéguen, 2009, after Idriss, 1990).

The direct site effects, as well source and path properties have been taken into account in the classic criterion for selecting ground motion models for PSHA, as discussed by Cotton et al. (2006). This criterion, however, only incorporates the linear site properties depending on the value of average shear wave velocity up to 30m depth (Vs_{30}). It is just only recently that the importance of soil nonlinearity is considered in the construction of GMPEs (Al Atik and Abrahamson, 2010). In addition to the previous GMPEs criterion selection, Bommer et al. (2010) added the importance of non-linear magnitude-dependence and soil nonlinearity, as well as site effects models without considering the Vs_{30}. The exclusion of Vs_{30} is important since different sites with the same Vs_{30} may have completely different frequency and energy content. Nonetheless, Vs_{30} may be the simplest engineering parameter that can be used for practical purposes. In this paper they show that very few (only 8 from 150) ground motion models incorporate all the criterion proposed, including for example Abrahamson and Silva (2008), Akkar and Bommer (2010), and Campbell and Bozorgnia (2008). Nevertheless, several nonlinear site amplification models, for example Walling et al. (2008) which based on numerical modeling, and Sandikkaya et al. (2013) based on empirical approach, are still using site specific Vs_{30} as their main parameters.

Furthermore, population explosion and concentration is always followed by the growth of infrastructure and building constructions, such as previously projected by Bilham (2009). The common perception of the society is that buildings have always been subjected to earthquakes. This concept is not complete, because when ground motion travels through the soil to the structure, the ground motion will travel through and shake the buildings (giving damage to buildings) and then going back to the soil until its energy is totally absorbed by material damping (Housner, 1957; Jennings and Bielak, 1973). This means that the presence of the structures also modifies ground motion; hence, as construction rate increases, the modification of ground motion becomes more complicated. This coupling between soil and structure, known as Soil-Structure Interaction (SSI), has been studied extensively these past years. In addition to aforementioned works from Housner, and Jennings and Bielak; some other examples include Wong and Trifunac (1975), Şafak (1998a), and Guéguen and Bard (2005).

Coburn and Spence (2002) reported that approximately 75% of casualties related by earthquakes are caused by the buildings collapse. This high contribution makes SSI, which controls the structure and ground motion responses in urban area, an essential issue to better determine those responses. A precise definition of SSI is difficult to provide (Kausel, 2010), because whenever coupling between soil and structure modifies the wave propagation, the SSI exists. It means that SSI covers a broad range of problem covering the wave modification from soil to foundation, from foundation to structure, from structure back to the ground (Soil-Structure-Soil Interaction/ SStSI), as well as multi-soil-structure interactions (or Soil-City Interaction/SCI) a concept proposed by Guéguen (2000). Despite all the studies that have been done on this matter, we are still not able to take into account all the complexity, especially in urban area where SCI occurs, it is still a debate on if these effects are detrimental or beneficial.

Guéguen and Bard (2005) did a thorough study on SSI and SStSI using passive experiments at the Volvi test site (Greece), and reported that the latter is significant, thus cannot be neglected. However, in previously mentioned ground motion models, for example, the site effects has not incorporated the important modification from radiated back wave came from the SStSI. Wirgin and Bard (1996) examined the SCI using a simple numerical model from the 1985 Mexico City earthquake case and show the importance of these buildings effects.

Most of the researches on this matter have been done using numerical approaches and active experiments. Despite all these studies, the importance of SCI has rarely been taken into account in the site effects study, considering the difficulty to choose the governing parameters. Furthermore, nonlinearity has been a complicating factor that is recently incorporated on the SSI study (Pecker and Chatzigogos, 2010; Pecker et al., 2014). This nonlinear dissipating energy is a non-negligible element that often abandoned in the previous studies.

To sum up, the recent global urbanization trends towards concentrated seismic prone cities will have impacts on the increase of seismic risks, firstly through the increase of seismic exposure and vulnerability due to population and building concentrations, and secondly the modification of seismic risks through presence of sediments and dense structures in the urban environment. Therefore, seismic risk analysis is important to understand and predict ground motion responses, estimate damages, and to be able to reduce and minimize losses through urban design strategies and policies. A comprehensive seismic risk assessment needs to integrate a thorough seismic hazard assessment, and complete seismic vulnerability and exposure assessments.

Objectives of the Study

The final goal of seismic risk study was and will always be the reduction of loss. This loss reduction can be achieved by reducing seismic risks. One key element of this reduction is a better understanding and/or prediction of ground motion (hazard). By predicting the ground motion responses, we would be able to design more resistance structures, hence, reducing damage during earthquakes. Contemplating the vast and complex issues of the seismic hazard analysis, this study will focus only on two urban related seismic hazard problems, which are the soil nonlinearity and the soil-structure interaction. Consequently, this study will not cover the vulnerability and exposure parts, although the intersection with these two elements cannot be avoided.

In addition to the direct site effects, the problem of soil nonlinearity and SSI are the key elements of ground motion characteristics on urban area. These ground motion responses are

important related to the deformation of the near-surface sediments (where most of sub-surface structures are located) and the surface structure. These problems are interesting as they require the combination of seismology, earthquake engineering, geotechnical (soil dynamics), and structural dynamics understanding.

This dissertation is presented in 5 chapters in addition to the general introduction and conclusion. In Chapter 1, the state of the art approaches used for understanding soil nonlinearity (and site effects in general) and soil-structure interaction (as well as the derivative soil-structure-soil and site-city interaction) will be presented. The context and the importance of the effects, the theoretical background, some definitions, as well as some previous studies on these matters will be detailed to give the necessary foundation to comprehend the perspective of the following chapters. This chapter also gives the notion of the 1D wave propagation as well as the deconvolution method that will be used throughout this study.

In chapter 2 and 3, we focus on the soil nonlinearity problem. Although this problem has been observed by the geotechnical engineering community for decade, it has only been recognized recently by the seismology community after the 1989 Loma Prieta earthquake (Chin and Aki, 1991). Most of the studies on this matter were conducted by laboratory experimentation using disturbed sample and/or by numerical modeling. These approaches do not represent what is actually happening in real *in-situ* conditions, resulting in discrepancies from these results to *in-situ* measurements. The best approach by far to study this matter is by using the downhole vertical array. There are, however, very few sites that allow the observation of soil nonlinearity, hence, data is limited. To overcome this difficulty, we use two experimental approaches: the dynamic centrifuge test and *in-situ* observation.

In chapter 2 we use the dynamic centrifuge test to constrain the nonlinear soil problem. The centrifuge test has interested many researchers for it gives a close representation of the real condition. This advanced experiment is important as a benchmark, since *in-situ* recorded data related to this study is still very limited. To complete the study, Chapter 3 presents the analyses on *in-situ* recorded data from The Garner Valley Downhole Array (GVDA) and The Wildlife Liquefaction Array (WLA) data. This study is important as an actualization of what happens in real condition. From these two chapters we attempt to answers several questions

that remain on this matter, e.g. what parameters can be used as a soil nonlinearity proxy (which would be convenient to incorporate the nonlinear problem into the GMPEs for instance)? Is the dynamic centrifuge test capable of capturing the real condition responses? How are the *in-situ* responses? Are Idriss's 0.3-0.4 g limit still relevant for the nonlinear response of the soil, and whether nonlinear behavior can occur at a very small strain level? May soil nonlinearity occur only at shallow depth? Is nonlinear anisotropy can be observed in real site, changing the isotropic assumption of the site response? And does soil nonlinearity depend only to the intensity of the excitation?

The last two chapters focus on the Soil-Structure Interaction problem using the same approaches, i.e. the centrifuge test (Chapter 4) and *in-situ* recorded data (Chapter 5). As with before, interests of these approaches are to observe the real ground motion responses and to analyze the discrepancies between laboratory and *in-situ* measurement. Considering the lack of well instrumented SSI test sites, the observation of *in-situ* data allows us to analyze what happened in the real site. The complexity of the SSI problem is to separate the different mechanisms related to the soil, soil-structure coupling, and the structure, which are normally mixed as the system response. Although it has been discussed by Todorovska [2009a, 2009b] in an instrumented building, the complexity of the urban environment might add certain confusion and might not reveal the true response of a soil-structure system. Using nonparametric system identification procedures, we try to untangle these different mechanisms to be able to analyze the importance of each element, including their nonlinear behavior.

In Chapter 4, using centrifuge testing, the importance of SSI from only two excitations levels on different type of building (rigid and flexible) is discussed. The SSI behavior of different type of structures is discussed. The system identification procedures are applied to separate different contributing elements of SSI. The nonlinear SSI is discussed by monitoring changes in the modal parameters. In addition, the presence of more than one structure that "represents" the Site-City Interaction (SCI) problem will also be discussed. How is the modification due to these structure-soil-structure interactions (StSStI)? And what are the observed phenomena when two structures are presented? Furthermore, this chapter will also discuss the free-field contamination problem from the derived Soil-Structure-Soil Interaction (SStSI) problem. We aim to analyze the governed parameters of this free-field contamination, and how much does

this contamination take effects from the radiated building. Using the same procedure, Chapter 5 analyzes the importance of SSI from multiple earthquake recordings using the *in-situ* measurement in one site. The identification of each contribution elements are extracted using the same procedures as in Chapter 4. In both chapters, the importance of nonlinearity on SSI is discussed. How far does nonlinearity change the soil-structure system response? And where does this nonlinearity come from? Moreover which elements are influencing these different nonlinearities?

Chapter 1

From Near Surface Effects to Soil-Structure Interactions: a 1D Wave Propagation Approach

Variability of ground motion depends on the source (location, focal mechanism, rupture mechanism, and in certain case the directivity effects which are direction dependence), the crustal propagation (waves scattering and attenuation), and the site effects. While the first two effects are mostly of interest to the seismology community, the site effects are of interest to both seismology and engineering communities.

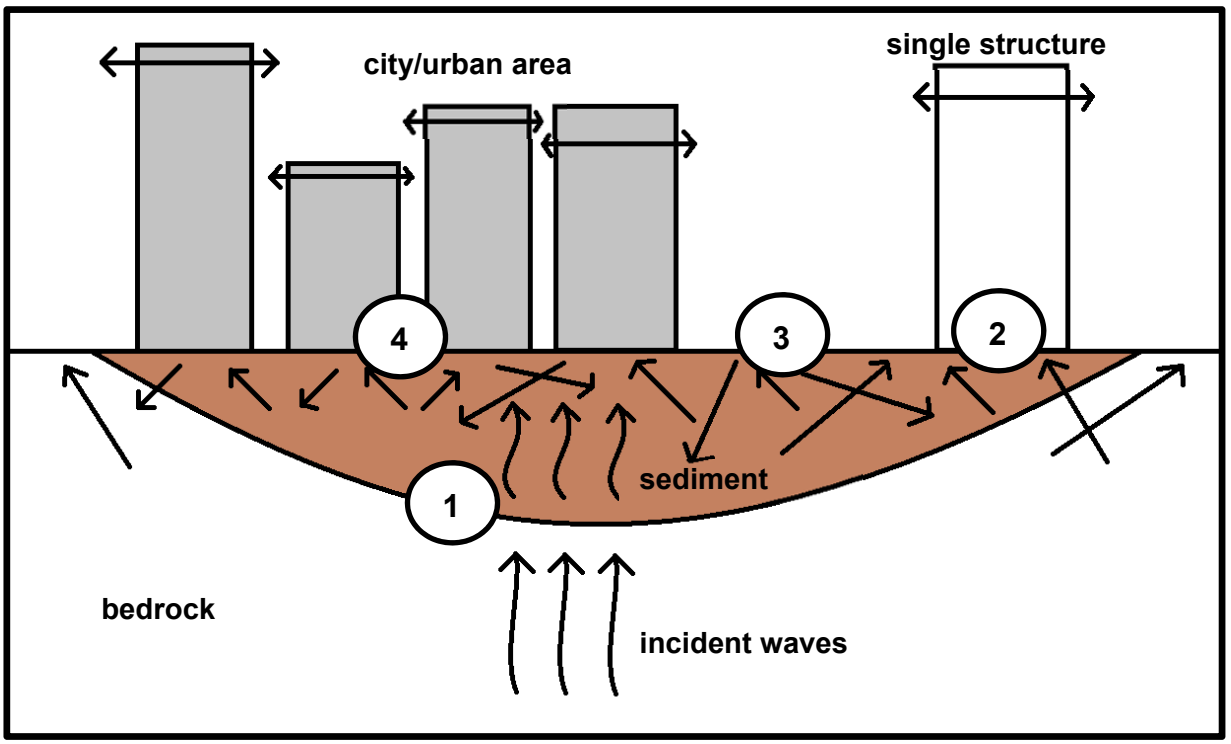

Figure 1.1. Ground motion modification at near surface of an urban area

Figure 1.1 describes what happens at near surface of an urban area during an earthquake. The waves propagate from the source through a medium. Ground motion characteristics are modified due to the intrinsic properties of the path. Upon its arrival at the bedrock-sediment boundary, the site effects first take place and modify the ground motion. Then, when the waves arrive at the soil-structure interface, the soil-structure coupling effects take place and again modify the waves. Referring to the numbers in Figure 1.1, and after Guéguen (2000) these effects consist of Site Effects (No.1), Soil-Structure Interaction/SSI (No.2) that modifies the response of the structure due to the coupling between soil and structure, Soil-Structure-Soil Interaction/SStSI (No.3) that corresponds to the inertial damping due to the energy of vibration radiated back into the soil through surface seismic waves, and Site-City Interaction/SCI (No. 4) when the urban medium is composed by several buildings. When there are only 2 buildings, the effects are called Structure-Soil-Structure Interaction/StSStI.

This means that the seismic responses of soil-structure system in the urban area are primarily governed by two effects: site effects and soil-structure interaction. It is therefore essential to study and characterize these phenomena to be able to incorporate them into the seismic risk analysis, to further be applied in building codes, urban planning, insurance calculations, as well as emergency and/or mitigation planning.

Site effects and soil-structure interaction effects have been studied and discussed as the fundamental elements of seismic risk management. In most of the literature, the discussions of these effects are inseparable, for example in Kramer (1996), Oliveira et al. (2006), and Schanz and Iankov (2009). Site effects or near surface effects are the effects caused by a local geology configuration (also known as local geology effects). These site effects can be distinguished as direct site effects, induced site effects, and geometry effects. Although there exists other site effects such as the topography effects (when the waves propagate into a convex area, e.g. mountain summit) and surface ruptures effects, they appears locally and will not be discussed further.

Direct site/sediment effects (classic site effects) happen due to the impedance between bedrock (stiff soil) and sediment (soft soil). These effects are manifested through ground motion amplification. Direct sediment effects have been studied comprehensively especially after the 1985 Mexico earthquake (Campillo et al., 1989; Chavez-Garcia and Bard, 1994).

These effects, however, will not be of interest in this study. Induced site effects are in most cases demonstrated as soil nonlinearity. Soil nonlinearity is an intrinsic problem of the soil, i.e., how soil is deformed when subjected to different levels of earthquake stress. These effects are manifested through a ground motion deamplification and a shear wave velocity reduction. Depending on different parameters, these effects can be followed by either the liquefaction phenomenon, cyclic mobility phenomenon, or the slope instabilities. The detail of this effect is discussed in Chapter 1.1.

Geometry effects, also known as basin effects, are those induced by the geometry or the presence of the sedimentary basin. These effects consist of the trapping and the resonance of the waves inside the basin, considered 2D and 3D. Some studies have incorporated the basin effects, such as Frankel et al. (2002) in the Seattle basin using seismic recordings from the M 6.8 Nisqually earthquake, Cornou et al. (2004) in Grenoble basin where the noise energy bursts and trapping of harmonic waves were observed, Sleep (2010) who indicated a reverberation of surface waves within sedimentary basins, and Gélis and Bonilla (2012) where the 2D basin effects were taken into account in numerical modeling. These effects, however, will not be of interest in this study.

The first two aforementioned effects (direct effects and soil nonlinearity) are those that occur most frequently in an urban area due to soft sediment deposits. These near surface effects are complicated due to their contradictory effects of amplification and deamplification of the ground motion. Since both effects appear normally during strong earthquake excitation, these effects are mixed and their separation is rarely examined.

In the presence of a stand-alone structure, there is a coupling between the soil and structure when seismic waves travel from sediment to the structure that modifies the ground motion characteristics. These interactions, known as SSI, consist of the kinematic interactions and inertia interactions. Kinematic interactions include the scattering phenomenon due to the dynamic impedance between soil and structure, where structure is normally represented by the foundation. Inertia interactions come from the vibration of the structure system that depends on the dynamic properties of the structure. The kinematic effects are present at lower level of ground shaking by the long period and radiation damping. At stronger ground motion level, the inertial interactions become more dominant, shown by displacements and bending

strains concentrated near the ground surface. The detail of this effect is discussed in Chapter 1.2.

After this modification, the structure vibrates and radiates back-waves to the free-field. These back-waves join the incident free-field waves and hence modify their properties. This free-field modification is known as the Soil-Structure-Soil Interaction (SStSI). In a city or an urban area where more than one structures are present, the waves propagate and are modified from one structure to another depending on the modification of their properties. These interactions are very complex depending, for example, on the structure or the density of the city (Guéguen et al., 2002).

1.1. Soil Nonlinearity

1.1.1. Rheological Notions

Unlike the direct site effects that are engendered by the impedance of the materials, soil nonlinearity effects are generated by intrinsic properties of the material, in this case the sediment/soil. These intrinsic properties control the responses of the soil when subjected to dynamic loading. Before moving further, it is important to review the rheological problem of the soils during cyclic loading (earthquake).

Like other materials, soil responses depend on its stress-strain evolution. The stress states at different points in a soil mass are characterized by the normal (σ) and shear (τ) stresses. Equation 1.1 shows the stress description in a matrix form, where x, y, and z indicate the directions, so that σ_{xx}, σ_{yy}, and τ_{xy} are the normal stresses and the shear stress that are working on the xy-plane.

$$\underline{\underline{\sigma}} = \begin{bmatrix} \sigma_{xx} & \tau_{xy} & \tau_{xz} \\ \tau_{yx} & \sigma_{yy} & \tau_{yz} \\ \tau_{zx} & \tau_{zy} & \sigma_{zz} \end{bmatrix} \tag{1.1}$$

Since soils do not resist tensile, the stress terms are associated to normal compressive stress and shear stress that are present during seismic loading. The stress state of any points in a soil mass can be represented by a Mohr circle representation as shown in Figure. 1.2.

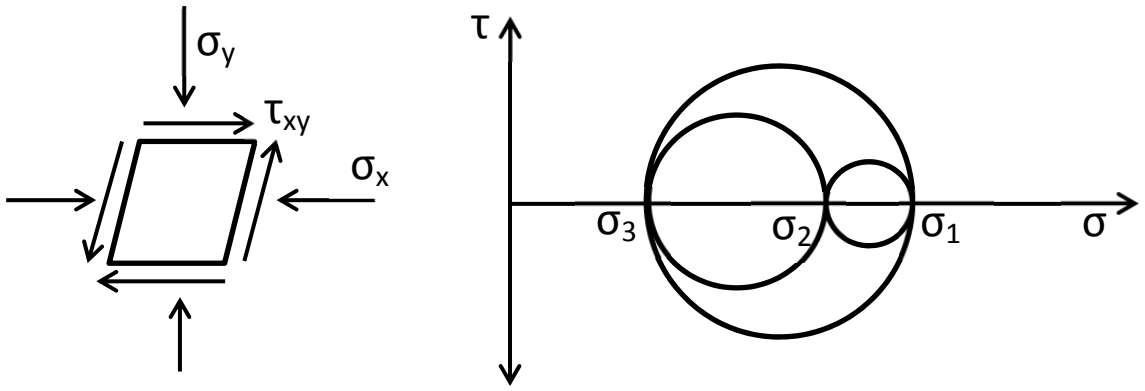

Figure 1.2. Stress state and its Mohr circle representation at any points in a soil mass under earthquake excitation

σ_1 is the largest principal stress, called major principal stress, σ_3 is the smallest principal stress, called minor principal stress, and σ_2 is the intermediate principal stress. On the *xy*-plane (Figure. 1.2 left), σ_{yy} is the major principal stress, and σ_{xx} is the minor principal stress.

Rheological problem of soils have been based mainly on laboratory experiment, especially from triaxial compression tests. Based on these observed experiments, different constitutive models were determined to explain behavior of soils for different stress conditions. Fundamental definitions of some soil conditions under cyclic loading are discussed below.

- Linear x Nonlinear

At small strain, soil behavior follows the Hooke's law where force (stress) is proportional to deformation (strain).

$$\sigma = E \cdot \varepsilon \tag{1.2}$$

$$\tau = G \cdot \gamma \tag{1.3}$$

In Equations (1.2) and (1.3), E is the Young's modulus, ε is the normal strain, G is the shear modulus, and γ is the shear strain. In tensorial, Equation 1.2 can be written as:

$$\underline{\underline{\dot{\sigma}}} = \underline{\underline{\underline{\underline{C^e}}}} : \underline{\underline{\dot{\varepsilon}^e}} \tag{1.4}$$

where C is the stiffness in 4th order tensor, and e indicates the elastic state. The stiffness tensor, C, depends on the Lame coefficients λ and μ:

$$C = \lambda \mathrm{I} \otimes \mathrm{I} + 2\mu| \tag{1.5}$$

where I is the second-rank identity tensor and | is the symmetric part of the fourth-rank identity tensor. The Lame coefficients depend on Young's modulus, E, and a poisson coefficient, v.

$$\lambda = \frac{vE}{(1+v)(1-2v)} \tag{1.6}$$

$$\mu = \frac{E}{2(1+v)} \tag{1.7}$$

As we can see in Figure 1.3, linear behavior always occurs in the elastic region (Line A-B). Nonlinear behavior on the other hand, occurs when the stress and strain value no longer follows a proportional (linear) relationship. Nonlinear behavior can occur in the elastic region (Line B-C) as well as in the plastic region (Line C-D).

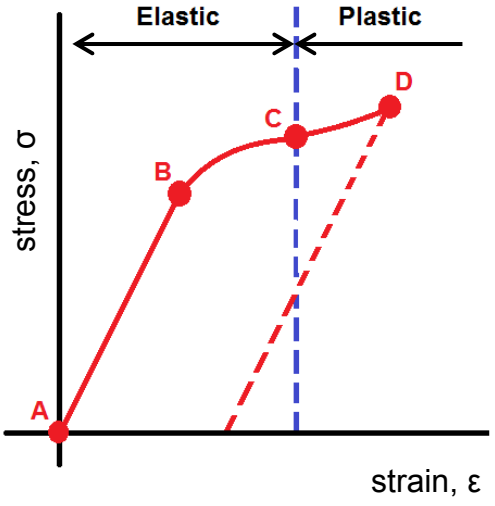

Figure 1.3. Stress-strain relationship model in materials.

- Elastic x Plastic

Soils are said to be in an elastic state if after being deformed, they return to their original state. On the other hand, soils are said to be in a plastic/inelastic state if after having been deformed they end up having some permanent deformations (Figure 1.3).

- Isotropic x Anisotropic

Soils are said to be isotropic if they have uniformity in all directions. However, in most cases, soils are anisotropic, thus they do not deform uniformly in all directions. Nonetheless, in most simplified models, the isotropic model is used and its elastic relation can be described as:

$$\begin{bmatrix} \dot{\sigma_{xx}} \\ \dot{\sigma_{yy}} \\ \dot{\sigma_{zz}} \\ \dot{\sigma_{yz}} \\ \dot{\sigma_{xz}} \\ \dot{\sigma_{xy}} \end{bmatrix} = \frac{E}{(1+\nu)(1-2\nu)} \begin{bmatrix} 1-\nu & \nu & \nu & 0 & 0 & 0 \\ \nu & 1-\nu & \nu & 0 & 0 & 0 \\ \nu & \nu & 1-\nu & 0 & 0 & 0 \\ 0 & 0 & 0 & 1-2\nu/2 & 0 & 0 \\ 0 & 0 & 0 & 0 & 1-2\nu/2 & 0 \\ 0 & 0 & 0 & 0 & 0 & 1-2\nu/2 \end{bmatrix} \begin{bmatrix} \dot{\varepsilon_{xx}} \\ \dot{\varepsilon_{yy}} \\ \dot{\varepsilon_{zz}} \\ \dot{\varepsilon_{yz}} \\ \dot{\varepsilon_{xz}} \\ \dot{\varepsilon_{xy}} \end{bmatrix} \quad \dots (1.8)$$

These rheological notions are important because variations of ground motion are controlled by the nonlinear responses of the soil. These soil dynamic behaviors depend on the characteristics of the soils and the incident waves which control the frequency-dependent soil dynamic parameters, i.e., the shear modulus (since earthquake controls the shear properties of the soil) and the damping (ξ). Under a strong level of shaking, the induced deformation will exceed the linear limit. In addition, when strain increases, the shear modulus decreases as the material damping increases. An increase of material damping results in a deamplification of ground motion acceleration, and since shear wave velocity (*Vs*) is related to *G* and mass density (ρ) as according to

$$Vs = \sqrt{G/\rho} \quad (1.9)$$

, the shear wave velocity decreases when strain increases.

1.1.2. Existing Methods and Studies

Several approaches exist to study the dynamic responses (shear modulus, shear wave velocity, and material damping) of soils under cyclic loading. These approaches are based on theoretical, numerical, or experimental approaches. Experimental approaches can be categorized into two categories: laboratory experimentations and field tests.

Due to the use of a discrete sample, laboratory tests do not represent real soil conditions. Nevertheless, their preliminary results are important as a benchmark or reference for further studies. Most laboratory experiments are conducted to determine the behavior of soils and are done on cohesionless soils that lack cohesion. There are two reasons to this: first, because the evolution from linear to nonlinear behavior was observed to occur more in this type of soils, and second, because most laboratory experiments are more adapted to this type of soils. Some early studies are presented by Seed and Idriss [1969, 1970], and Hardin and Drnevich (1970) where the governing parameters for G and ξ are the shear strain (γ), effective mean principal stress (σ'_m), void ratio (e), loading cycles (N), and degree of saturation (S). Seed et al. (1984) discussed the moduli and damping factors for dynamic analyses of cohesionless soils using the cyclic undrained triaxial tests. Vucetic and Dobry (1991) studied the effect of plasticity index (PI) during cyclic response on laboratory testing using different over consolidated ratio (OCR). As laboratory equipments advance, new techniques are developed. Some existing laboratory measurements include the cyclic triaxial test (e.g. Boulanger et al., 1998), resonant column test, bender element test (e.g. Atkinson, 2000), direct simple shear test, and cyclic torsional shear test (e.g. Georgiannou et al., 2008).

Based on these dynamic properties measurements, some thresholds of cohesionless soil nonlinearity were established. These thresholds are related to linear-equivalent analyses because linear-equivalent models are still the most preferred approach to analyze the nonlinear problem. Figure 1.4 shows the popular shear degradation modulus and an increase in the damping curve as a function of shear strain.

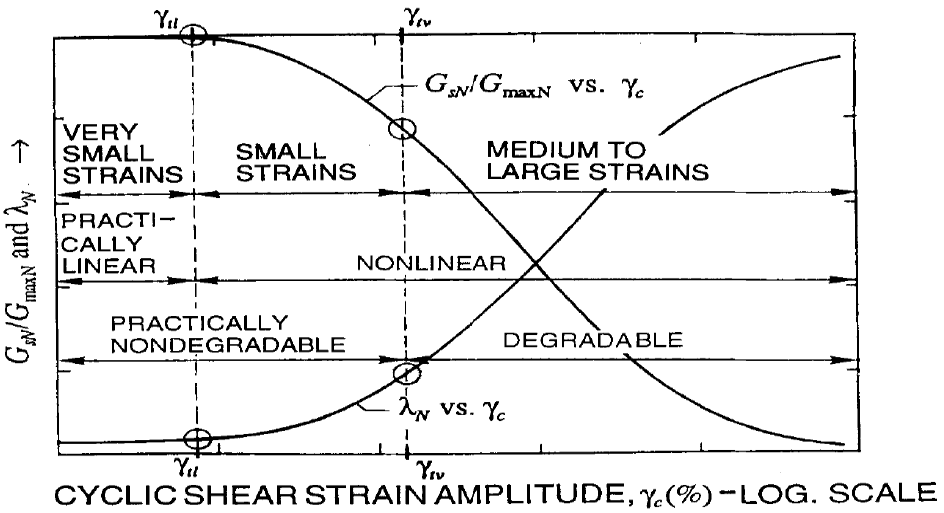

Figure 1.4. Typical shear degradation modulus and damping curves in function of shear strain (after Vucetic, 1994).

In this figure, Vucetic (1994) separated two different thresholds for nonlinear analyses, i.e.

1. γ_{tl} which is the linear cyclic threshold shear strain, and
2. γ_{tv} which is the volumetric cyclic threshold shear strain.

From these two limits we can characterize the behavior of the soils. Therefore:

1. when $\gamma < \gamma_{tl}$, the soils exhibit a linear-elastic behavior.
2. when $\gamma_{tl} < \gamma < \gamma_{tv}$, the soils are in nonlinear-elastic zone. This means that nonlinear behavior already occurs, but they remain elastic with negligible or no permanent deformation.
3. when $\gamma > \gamma_{tv}$, the soils are in a nonlinear-plastic zone, where soils behave nonlinearly and permanent deformations can no longer be neglected.

Hardin and Black (1968), Drnevich and Richart (1970), and Anderson and Richart (1976) set the volumetric threshold, γ_{tv} to 10^{-4}. Other laboratory experiments were done in a drained condition, where water can flow freely. Vucetic (1994), and Youd (1972) found the $\gamma_{tv}(Dr)$ at a strain value of $2x10^{-4}$. In an undrained condition, where there is no volumetric change, Dobry and Ladd (1980) set the volumetric limit γ_{tv} to 10^{-4}, and Johnson and Jia (2005) saw that nonlinear elastic started to occur at a strain value of 10^{-7}.

In addition to these tests, there exist some laboratory scaled model techniques, such as shaking tables and centrifuge tests that have been used to extract the dynamic properties of

soils. Some examples can be found in Brennan et al. (2005) and Li et al. (2013) where shear stresses and shear strains are calculated indirectly using the accelerometers measurements, following Equations (1.10)-(1.11).

$$\tau(z) = \int_0^z \rho \ddot{u}\, dz \tag{1.10}$$

$$\gamma_{1-2} = \frac{(u_2 - u_1)}{(z_2 - z_1)} \tag{1.11}$$

Here, z is the depth, $\ddot{u}$ is the acceleration, and u is the displacement.

Measurement of dynamic soil properties can also be done using field experiments as characterization tests. This can be divided to invasive and non-invasive methods. Standard tests based on non-invasive field measurements include the seismic refraction test, seismic reflection test, and spectral analysis of surface waves test (SASW). The invasive methods include the seismic cross-hole test, seismic downhole test, standard penetration test (SPT), and cone penetration test (CPT). Most of these tools are active measurements, which means that the measurements are done by introducing an active source. In geotechnical measurements such as SPT and CPT, empirical equations exist between the geotechnical results and shear wave velocity values such as described in Wair et al. (2012). Further details for both laboratory and field experiments can be found in any geotechnical reference textbooks, e.g. Kramer (1996).

Numerical approaches have been developed to characterize the cyclic soil behavior. The simplest numerical approach that has been used widely is the linear equivalent model. This approach uses an idealization of nonlinear problem by treating them as an equivalent-linear model, and finding the generalized evolution of shear modulus and damping. Although simple, this approach is less realistic compare to other numerical methods. More accurate approaches can be found for example by the cyclic nonlinear models where the actual stress-stain paths are observed during a cyclic loading. This loading and unloading are characterized using some additional constraints, for example the extended Masing rules. However, these models are not able to take into account the shear-induced volumetric strain. The most complex and realistic numerical approaches are the theoretical constitutive models. These

models describe the evolution from linear elastic to soil plastic condition up to rupture. We can refer to the fundamental Mohr-Coulomb model which takes into account the elastic-perfectly plastic model for isotropic material. We can also refer to Drucker-Prager model, Tresca, Von-Mises, and Hill, which can be applied for both isotropic and anisotropic materials. Most of these constitutive models take into account only a compression limit state and can be coupled with any tensile criterion for complete assessments, although it may or may not be necessary considering that soils do not resist tensile. We do not discuss the details of these models, and the readers can be referred to any rheological textbooks (e.g. Yamamuro and Kaliakin, 2005). These models are elastic-perfectly plastic models, and so can be completed by integrating the strain hardening properties of the soils to models such as the Cam-Clay or Modified Cam-Clay models that were developed at Cambridge University (Roscoe and Burland, 1968; Roscoe, 1970), and the Hujeux model developed at Ecole Centrale Paris (Hujeux, 1985). The latter are the most used constitutive models at the present time.

Although the problem of soil nonlinearity had been recognized by the earthquake engineering community, it was not after the 1989 Loma Prieta earthquake that seismologists acknowledged this problem (Chin and Aki, 1991; Aki, 1993). At the beginning of the observations, the nonlinear footprints can be identified by a deamplification of ground motion, a shear wave velocity reduction, and a shift in energy towards a lower frequency (as shown by the linear-equivalent modeling). Yu et al. (1992) analyzed the nonlinear response of several strong motion recordings using numerical codes. They concluded that during nonlinear responses, there is a frequency dependency of the shifting of Fourier spectral ratios, which are unaffected at low frequency, decreasing at moderate frequency and increasing at high frequency. These results showed that nonlinear behavior of the soils is governed not only by the amplitude of ground motion but also its frequency content. Beresnev and Wen (1996) wrote a short review on soil nonlinearity from a seismologist point of view. Şafak (2001), and Trifunac (2009) examined the local site effects by taking into account both amplification due to different impedance and nonlinear site responses. An empirical nonlinear curve was established by Idriss (1990) adding the data observations from the Mexico City and Loma Prieta earthquake (Figure I.3) where the nonlinear behavior, marked with the deamplification of ground motion, starts at around 0.3 to 0.4 g (of ground motion recorded at rock sites).

Following the Loma Prieta earthquake, multiple site nonlinearity observations have been studied for different earthquake events. Due to its simplicity, most processing are done using linear-equivalent models such as shown in the following examples, unless otherwise stated. These observations of site nonlinearity can be done using borehole or surface recordings depending on the availability of the seismic array at site. Some observations based on borehole observations were done by Satoh et al. (1995) who examined the recordings at the Ashigara Valley from four earthquake recordings during the period of 1990 and 1991. Using the inversion technique, the nonlinear actions were observed by a 10% *Vs* reduction and a 50% increased damping. Sato et al. (1996), Aguirre and Irikura (1997), and Satoh et al. (2001) used the recordings at different areas that were struck by the 1995 Kobe earthquake. Applying spectral analysis and inversion techniques, *Vs* reductions were observed and strain-dependent nonlinear characteristics were formed. Pavlenko and Irikura [2002, 2003] also used the recordings and analyzed the time-dependent model for nonlinear behaviors at these sites, following the changes of stress-strain curve in the time domain. Nonlinearity evidences were also present at the 1994 Northridge earthquake. Bonilla et al. [2003, 2005] worked with borehole data in Japan and California and modelled the shear modulus degradation due to nonlinearity; Assimaki et al. (2008a) showed the nonlinear effects during the 2003 Miyagi-Oki earthquake using different techniques of surface-to-downhole spectral ratios (SSR), cross-spectral ratios, and horizontal-to-vertical (H/V site) responses. Although these observations are mostly found at sediment sites, Régnier et al. (2013) recently showed some nonlinear behavior in relatively stiff soil during moderate earthquakes from the Japanese KiK-net strong motion data using the SSR techniques.

When borehole data recordings do not exist, nonlinear observations are obtained from the available surface recordings, mostly by comparing the rock and soil sites that are situated in the vicinity. As discussed in Steidl et al. (1996), however, the difficulty of choosing the reference rock sites may results in a misleading conclusion. Field et al. (1997) compiled multiple surface recordings at sediments and hard rock from the 1994 Northridge earthquake, and showed a ground motion deamplification during strong motion at sediments. Hartzell (1998), and Beresnev et al. (1998) did a similar analysis by comparing the weak and strong ground motion and they found a deamplification due to strong ground motion around the San Fransisco and Los Angeles basin. Dimitriu et al. (2001) investigated the dependence of high frequency spectral-decay parameter, κ, and showed κ_0 as a tool to measure sediment

nonlinearity using accelerograms from Lefkas, western Greece. Frankel et al. (2002) observed a shift of resonance frequency towards lower frequency and studied the basin effects in Seattle for the 2001 Nisqually earthquake. Moreover, Rubenstein and Beroza [2004, 2005] and Rubenstein et al. (2007) showed evidences of nonlinearity from different earthquakes, i.e., the 1989 Loma Prieta earthquake, the 2003 Tokachi-Oki earthquake, and the 2004 Parkfield earthquake. Using a waveform cross correlation, they identified velocity reduction in shallow sediments, but not significant at greater depth.

In addition to these observations, some numerical studies were conducted in order to be able to "predict" the nonlinear soil effects. This kind of prediction is normally done by developing mathematical models for specific soil types, sites, and earthquakes, and then comparing the results with responses from seismic recordings. Hartzell et al. (2004) used different approaches ranging from equivalent-linear to nonlinear models and gave recommendations for formulations of the nonlinearity. They showed that their model is comparable to the 2001 Nisqually earthquake for class D and E sites. Pavlenko (2001) used a nonlinear system identification method to study the evolutions of the nonlinear effects in frequency domain. Bernardie et al. (2006) implemented CyberQuake constitutive models that were derived from the Hujeux's model to simulate the nonlinear site response during the 1999 Chi-Chi earthquake.

In spite of all these extensive researches, the review from Field et al. (1998) summed up the remaining challenges from a nonlinearity study that share the same perspectives in the context of this study. First, even though laboratory studies do not reflect the *in-situ* behavior of soils, they are important to have as a reference. These studies however have to be completed with *in-situ* data. The best approach by far to study this matter is by using the downhole vertical array. Unfortunately, this downhole array data are very limited. In terms of processing approaches, while equivalent-linear model is very limited to explain the nonlinear behavior (compare to complex constitutive models, for instance), its simplicity regarding to the extensive results that can be provided will still be the first choice for researchers to conduct nonlinear studies. In addition, we notice that most early studies based on laboratory experiments captured only the nonlinear-plastic limit (since plastic deformation starts to occur after passing this threshold), ignoring the nonlinear elastic response that occurs at very small strain value.

1.2. Soil-Structure Interaction (SSI)

Soil-Structure Interaction has received increased attention, even more than Soil Nonlinearity. While the fundamental tools to treat this problem have been extensively discussed, some crucial problems related to SSI remain unsolved. Kausel (2010) conducted a complete and thorough investigation of the early history of soil-structure interaction. The author agrees on Kausel's "definition" on soil-structure interaction: "it is eminently clear that the concept of soil-structure interaction refers to static and dynamic phenomena mediated by a compliant soil and a stiffer super-structure, but the discipline encompasses so many different, sometimes tenuously connected aspects that is difficult indeed to enounce a cogent definition in just a few words." In his paper, Kausel mentioned that the study of SSI began in the nineteenth century with the development of some solid mechanics' fundamental solutions, for example by Lamé and Clapeyron with the development of half-space problems. Another milestone came from Stokes' solutions which later became the fundamental of Boundary Element Method (BEM), geophysics, acoustics, and other branches of science. In addition, Boussinesq developed solutions for more complicated problems, especially in static SSI problems. However, it was not until 1936 that Reissner started the study on the dynamic SSI where time-harmonic vertical loads were applied to circular disks on elastic half-spaces.

1.2.1. Dynamic Equilibrium of the Structures

The problems of structural dynamics have been of interest not only to the civil engineering community, but also the seismologist community. These problems have been discussed in details in many structural dynamics textbooks, such as in Chopra (2007). A fixed-base structure is characterized by its degrees of freedom (DOF) which are the number of relative displaced positions of all the masses in the system. Structures in SSI system can be simplified as a single degree of freedom (SDOF) system that consists of a concentrated/ lumped mass, m, at the roof level contributing to the inertial properties of the system, the stiffness of the system, k, that is modeled by a massless frame, and a viscous damper (a dashpot), c, that dissipates vibrational energy of the system. The dynamics of this system are characterized by the following three forces that are associated to the aforementioned elements and the displacement, $u(t)$ at any DOF point, respectively: the inertial forces acting on the mass at one

instant time ($f_I = m.\ddot{u}$), the elastic resisting forces, associated with the rigidity of the structure ($f_S = k.u$), and the damping resisting forces due to a linear viscous damper ($f_D = c.\dot{u}$).

The equation of motion for elastic SDOF systems under an earthquake excitation can be derived by applying either the D'Alembert's principle or Newton's second law of motion to the equations, yielding:

$$m.\ddot{u}^t + c.\dot{u} + k.u = 0$$
$$m.\left(\ddot{u} + \ddot{u}_g\right) + c.\dot{u} + k.u = 0$$
$$m.\ddot{u}(t) + c.\dot{u}(t) + k.u(t) = -m.1^T.\ddot{u}_g(t) \quad (1.12)$$

where $\ddot{u}^t$ is the total acceleration and $\ddot{u}_g$ is the ground motion acceleration. The solution to Equation 1.12 can be found in many references, for example in Chopra (2007). Under earthquake excitations, the system can be modeled as in Figure 1.5.

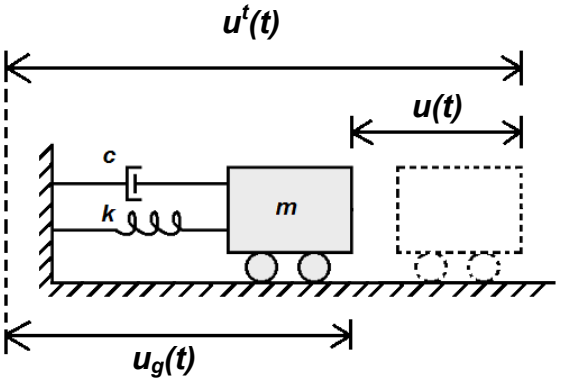

Figure 1.5. SDOF system under harmonic excitation (modified after Guéguen, 2000)

1.2.2. Kinematic and Inertial Interactions

Soil-structure interaction phenomena can be divided to two different interactions. Based on their order of appearances, these interactions are summarized as follows:

1. Kinematic Interaction

After modifications due to the site effects (including nonlinearity), seismic waves go through another modification caused by an impedance between soil and structure (represented by its foundation), which occurs at the soil-structure interface. The different impedances between the rigid foundation and soft soils cause the incident waves to be diffracted back to the ground and transmitted to the structure. Transmitted waves that are the Foundation Input Motion (FIM) are different than the incident motion. The scattering of this incident waves depends on the foundation stiffness, surface and geometry of the foundations, and the embedment type. In this study we are not interested to go into details on this kinematic interaction. More coherence studies on the impedance functions and dynamic soil-foundation interaction can be found in Gazetas (1991), Gazetas and Makris (1991), and Makris and Gazetas (1992). Lai and Martinelli (2013) noticed that in the special case of a shallow foundation struck by a vertically propagating S-wave, the kinematic interaction is not present.

2. Inertial Interaction

The inertial interaction is caused by the transmitted waves that travel and vibrate structure due to the material damping and stiffness modification. This interaction also includes the impedances between foundation and structure that have to be included in an inertial interaction through the foundation impedance matrix. In addition, similar to what happens inside the soils under a strong excitation, building must behave nonlinearly. This behavior is frequency dependent, referring to Equation 1.13, where T_n is the natural period of the structure.

$$T_n = 2\pi\sqrt{\frac{m}{k}} \tag{1.13}$$

1.2.3. Existing Methods

Similar to other researches, there exist three main axes of methods to study the problem of soil-structure interaction, i.e., the Theoretical, Numerical and Experimental methods. The theoretical methods might be the oldest approaches that have been explored by researchers. These methods attempt to provide a closed-form solution to the equation of motion of the systems. We can refer to the previously mentioned Kausel's (2010) paper that provides the

historical development of these theoretical methods. Early works that covered the whole dynamic of building-soil interaction can be found for example in Jennings and Bielak (1973) who applied the discrete foundation and half-space analyses to an idealized structure. However, in this dissertation we will not provide any further details except when it is necessary.

The numerical methods can be distinguished to two different approaches (Pecker, 2007, and Lai and Martinelli, 2013):

1. Direct/Global Method

This method consists of solving one global dynamic equation (Equation 1.12) that takes into account both the soil and structure systems using any discretization techniques, e.g. Finite Element Method (FEM), Spectral Element Method (SEM), and Finite Difference Method (FDM). Although its solution is direct and adaptable for either a linear or a nonlinear analysis, the global method is arduous and expensive in terms of computation. The results depend on the constitutive law that is adapted for the soil and structure systems, and comprehensive and thorough investigations of the geotechnical condition are necessary in order to produce relevant results. This direct method is preferred when a detailed analyses is needed, for example for historical monuments. However, for urban modeling, this method will not be efficient regarding its computational time and cost.

2. Indirect/Substructure Method

Rather than solving the SSI problem as one global system as in the direct method, the indirect/substructure method decomposes the SSI problem into sub-systems in order to separate the effects of kinematic and inertia interactions. The response of each sub-system is solved individually and step-by-step successively. Since each sub-system is solved separately, this method is less arduous than the direct method and is a preferred solution to urban assessment when a scale of a city is analyzed. The classic decomposition of the SSI system for the substructure method that has been widely used (e.g. Kausel et al., 1976; Endres et al., 1984; Guéguen, 2000; Mylonakis et al., 2006; Pecker, 2007; and Lai and Martinelli, 2013) is shown in Figure 1.6. For each sub-system, we need to formulate the equation of motion including the boundary conditions (the stress and displacement continuity) at each interface. These equations are preferred to be solved in frequency domain.

This decomposition consists on solving these following three steps:

- Determination of rigid foundation movement due to the kinematic interaction. The Foundation Input Motion (FIM) is determined at this step. The equation of motion of sol-foundation sub-system (without structure) is:

$$-\omega^2 \begin{bmatrix} \underline{\underline{m}}_{FS} & \underline{\underline{0}} \\ \underline{\underline{0}} & \underline{\underline{m}}_S \end{bmatrix} \begin{bmatrix} \underline{\tilde{u}}_F^* \\ \underline{\tilde{u}}_S^* \end{bmatrix} + \begin{bmatrix} \underline{\underline{K}}_{FF} & \underline{\underline{K}}_{FS} \\ \underline{\underline{K}}_{SF} & \underline{\underline{K}}_{SS} \end{bmatrix} \begin{bmatrix} \underline{\tilde{u}}_F^* \\ \underline{\tilde{u}}_S^* \end{bmatrix} = \begin{bmatrix} \underline{0} \\ \underline{Q}_R \end{bmatrix} \tag{1.14}$$

Here, m is the mass, K is the stiffness, F indicates foundation, S indicates soil, FS indicates a foundation-soil system, ~ indicates the frequency domain, R is the model boundary, and thus the vector Q_R does not have any zero values except at these nodes. The underline denotes a vector as two underlines denotes a matrix, u^* is the displacement of the kinematic interaction, and u^i is the displacement of the inertial interaction, where

$$\underline{u}^i = \underline{u} - \underline{u}^* \tag{1.15}$$

- Estimation of foundation impedance matrix, done by solving the equation of motion as follows:

$$-\omega^2 \begin{bmatrix} \underline{\underline{m}}_{FS} & \underline{\underline{0}} \\ \underline{\underline{0}} & \underline{\underline{m}}_S \end{bmatrix} \begin{bmatrix} \underline{\tilde{u}}_F^i \\ \underline{\tilde{u}}_S^i \end{bmatrix} + \begin{bmatrix} \underline{\underline{K}}_{FF} & \underline{\underline{K}}_{FS} \\ \underline{\underline{K}}_{SF} & \underline{\underline{K}}_{SS} \end{bmatrix} \begin{bmatrix} \underline{\tilde{u}}_F^i \\ \underline{\tilde{u}}_S^i \end{bmatrix} = \begin{bmatrix} -\underline{\tilde{P}}_F \\ \underline{0} \end{bmatrix} \tag{1.16}$$

where P_F indicates the force that is working on the foundation.

- Computation of the response of the structure related to the previously solved impedance matrix and the kinematic interaction. This is done by solving the equation of motion as follows:

$$-\omega^2 \begin{bmatrix} \underline{\underline{m}}_B & \underline{\underline{0}} \\ \underline{\underline{0}} & \underline{\underline{T}}^T \underline{\underline{m}}_{FB} \underline{\underline{T}} \end{bmatrix} \begin{bmatrix} \underline{\tilde{u}}_B \\ \underline{\tilde{u}}_0 \end{bmatrix} + \begin{bmatrix} \underline{\underline{K}}_{BB} & \underline{\underline{K}}_{BF} \underline{\underline{T}} \\ \underline{\underline{T}}^T \underline{\underline{K}}_{FB} & \underline{\underline{T}}^T \left(\underline{\underline{K}}_{FF} + \underline{\tilde{S}}_F \right) \underline{\underline{T}} \end{bmatrix} \begin{bmatrix} \underline{\tilde{u}}_B \\ \underline{\tilde{u}}_0 \end{bmatrix} = \begin{bmatrix} \underline{0} \\ \underline{\underline{T}}^T \underline{\tilde{S}}_F \underline{\tilde{u}}_F^* \end{bmatrix} \tag{1.17}$$

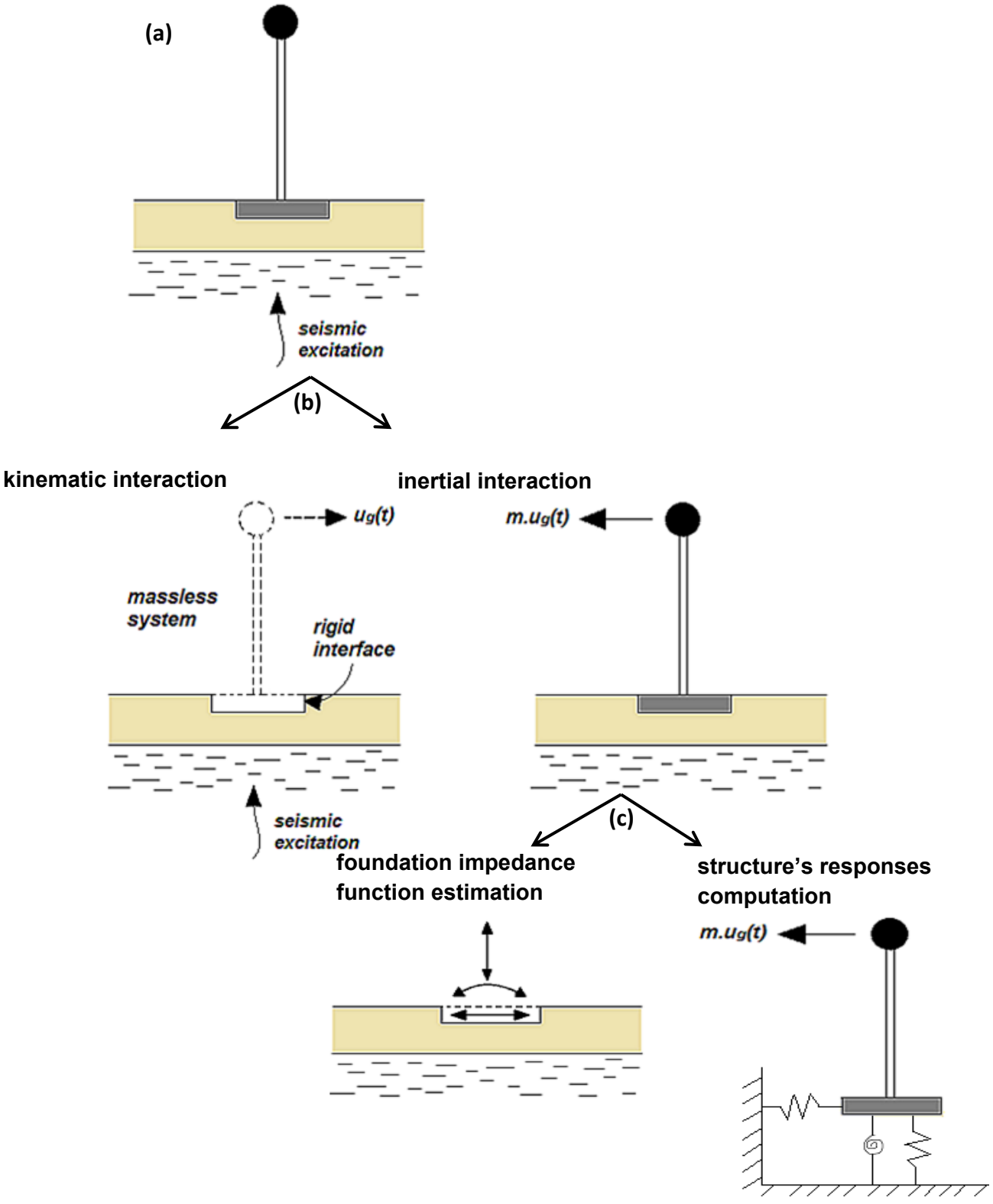

Figure 1.6. (a) The geometry of soil-structure interaction problem; (b) decomposition of ISS into kinematic and inertial interaction; (c) decomposition of inertial interaction into estimation of foundation impedance function and structure system response. (modified after Guéguen, 2000; Mylonakis et al., 2006)

Here, B indicates the building, $\underline{\underline{T}}$ is the transformation matrix, $\underline{\tilde{u}}_0$ is the displacement vector and rotation of the center of the foundation, with

$$\underline{\tilde{u}}_F = \underline{\underline{T}}\,\underline{\tilde{u}}_0 \tag{1.18}$$

and $\underline{\underline{\tilde{S}}}_F$ is the impedance matrix of the foundation.

In addition to these methods, there exists a macro-element method that is considered to be effective to treat the nonlinear problem of the whole SSI system that is not taken into account by the sub-structure method.

A simple analogic model related to separation of different motions when SSI takes place during earthquake can be seen in Figure 1.7. (Guéguen, 2000; Pecker, 2007).

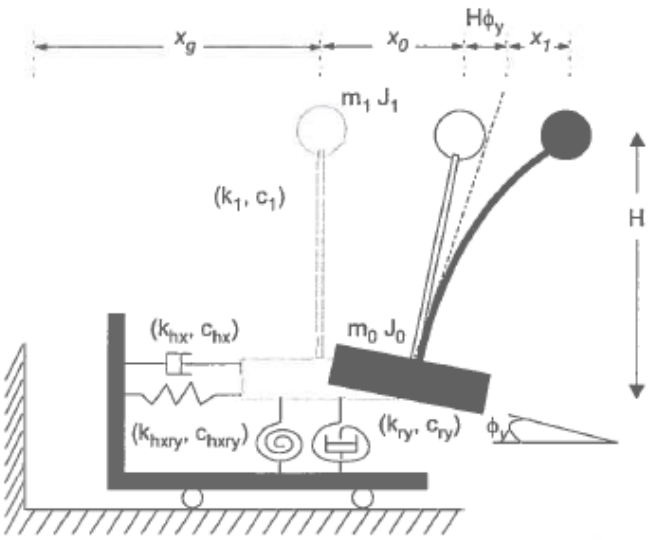

Figure 1.7. Model of the soil-foundation-structure with its related motion (taken from Guéguen, 2000)

In Figure 1.7, *h* and *r* denote horizontal and rotation, respectively, and 0 and 1 indicate the position of foundation (bottom) and top of the structure, respectively. These motions are:

1. Translation of the soil due to the ground motion, u_g,
2. Translation of the foundation relative to the soil, due to the ground motion, u_0,

3. Rotation or rocking of the structure (including the foundation), $h\phi$, and
4. Structural drift, which is the relative translation of the structure to the foundation, u_1

The total motion, u_t, is the superposition of all these motions, so that:

$$u_t = u_g + u_0 + h\phi + u_1 \tag{1.19}$$

Approximate solutions to the interaction equations have been discussed for different base fixity for example by Luco (1980) and Stewart and Fenves (1998). Both solutions use the classic normal mode approach. While Luco solved the solution in the frequency-domain transmissibility function, Stewart and Fenves used the Laplace domain transfer function. Nonetheless, both gave matching results. Luco and Lanzi (2013) gave a similar solution using a perturbation approach.

In our work, the solution of these interaction equations will be detailed following Stewart and Fenves (1998) in Laplace domain. Taking the relationship between mass, m, damping, c and stiffness, k, such as shown in Equations (1.20)-(1.21), Equation (1.12) can be expressed as in Equation (1.22).

$$\omega_0 = \sqrt{\frac{k}{m}} \tag{1.20}$$

$$\zeta = \frac{c}{2\sqrt{mk}} \tag{1.21}$$

$$\ddot{X}_j(t) + 2\zeta_j\omega_j\dot{X}_j(t) + \omega_j^2 X(t) = -\frac{L_j^*}{m_j^*}\ddot{u}_g(t) \tag{1.22}$$

where ω_0 is the undamped natural frequency, ζ is the damping ratio, j indicates the mode, X is the generalized coordinates, m^* is the generalized mass, and L^* is the generalized influence factor for vibration mode shapes, Φ. The superposition of all vibration modes gives the Laplacian solution to Equation (1.12) in acceleration as shown in Equation (1.23).

$$\ddot{u}^t(s) = \sum_{j=1}^{J} \Phi_j \ddot{X}_j(s) + 1^T \ddot{u}_g(s) \tag{1.23}$$

while

$$1^T \approx \sum_{j=1}^{J} \frac{L_j^*}{m_j^*} \Phi_j \tag{1.24}$$

we get

$$\ddot{u}^t(s) = H(s)\ddot{u}_g(s) \tag{1.25}$$

where

$$H(s) = \sum_{j=1}^{J} \frac{L_j^*}{m_j^*} \Phi_j H_j(s) \tag{1.26}$$

$$H_j(s) = \frac{2\zeta_j \omega_j s + {\omega_j}^2}{s^2 + 2\zeta_j \omega_j s + {\omega_j}^2} \tag{1.27}$$

Here, *H(s)* is the sum of contributions from *J* modes, as in Equation (1.25). It represents the transfer function between the ground (input) and degree-of-freedom *j* (output) in the structure. Using the transfer function of different input-output pairs, the solution of an SSI model can be obtained and the responses for different base conditions can be extracted.

Stewart and Fenves (1998) summarized the input and output pairs such as shown in Tab.1.1. The output pairs are the same for all base conditions, which is the total motion recorded at the sensor on the top of the structure.

Table 1.1. Input and output pairs for system identification procedures (Stewart and Fenves, 1998)

System	Input	Output
Flexible base	u_g	$u_g + u_0 + h\phi + u_1$
Pseudo-flexible base	$u_g + u_0$	$u_g + u_0 + h\phi + u_1$
Fixed base	$u_g + u_0 + h\phi$	$u_g + u_0 + h\phi + u_1$

In the flexible base case, the transfer function of the input-output pairs in Table 1.1 is given by the solution of system frequency and damping as shown in Equations (1.28)-(1.29).

$$\omega_{sys}^2 = \frac{\omega_\theta^2 \omega_H^2 \omega_1^2}{\omega_1^2 \omega_H^2 + \omega_\theta^2 \omega_H^2 + \omega_1^2 \omega_\theta^2} = \frac{1}{1/\omega_1^2 + 1/\omega_\theta^2 + 1/\omega_H^2} \tag{1.28}$$

$$\zeta_{sys} = \left(\frac{\omega_{sys}}{\omega_H}\right)^3 \zeta_H + \left(\frac{\omega_{sys}}{\omega_1}\right)^2 \zeta_1 + \left(\frac{\omega_{sys}}{\omega_\theta}\right)^2 \zeta_\theta \tag{1.29}$$

where the subscript *sys* indicates (flexible base) system, *1* indicates fixed-base, θ indicates rocking, and *H* indicates the foundation translation.

The pseudo-flexible case represents a partial rigid body condition with only base rocking. The transfer function of the input-output pairs in Table 1.1 gives the solution of system frequency and damping as shown in Equations (1.30)-(1.31). The pseudo-flexible base is often given through the apparent flexible base. Hence, its responses are denoted with subscript *app* for apparent responses.

$$\omega_{app}^2 = \frac{\omega_\theta^2 \omega_H^2 \omega_1^2}{\omega_1^2 \omega_H^2 + \omega_\theta^2 \omega_H^2} = \frac{1}{1/\omega_1^2 + 1/\omega_\theta^2} \tag{1.30}$$

$$\zeta_{app} = \left(\frac{\omega_{app}}{\omega_1}\right)^3 \zeta_1 + \left(\frac{\omega_{app}}{\omega_\theta}\right)^3 \zeta_\theta \tag{1.31}$$

Fixed base responses represent the structural responses. These responses can be extracted from the flexible as in Equations (1.28)-(1.29) or pseudo-flexible as in Equations (1.30)-

(1.31). Otherwise, these fixed base responses can also be extracted following Paolucci (1993). Incorporating the matrix with all motions considered, Equation (1.12) leads to:

$$(k_1 - \omega^2 m_1)u_1 - k_1 u_0 - k_1 h\phi = 0 \tag{1.32}$$

$$-k_1 u_1 + (k_1 + k_0 - \omega^2 m_0)u_0 + (k_1 h + k_{h\theta})\phi = -p\,\ddot{u}_g \tag{1.33}$$

$$-k_1 h.\, u_1 + (k_1 h + k_{h\theta})u_0 + (k_1 h^2 + k_\theta - \omega^2 J)\phi = -p\,\ddot{u}_g \tag{1.34}$$

where the subscript $h\theta$ indicates the coupling horizontal-rocking, and $-p\,\ddot{u}_g$ is the earthquake forces. Equation (1.32) can also be described as

$$\frac{u_1}{u_0 + h\phi} = \frac{k_1}{k_1 - \omega^2 m_1} = \frac{1}{1 - \frac{\omega^2}{\omega_1^2}} \tag{1.35}$$

This equation gives the fixed base responses because the left-hand equation will be close to infinity if the value of ω approaches ω_1.

We have so far shown the example of some theoretical and numerical studies of the SSI. Early studies of the use of earthquake recordings either by field measurement or laboratory testing was found for example by Housner (1957) that used several recordings from buildings in Southern California after the 1952 Arvin-Tehachapi earthquake and compared the soil-structure coupling between buildings with different stiffness. Bard (1988) used 7 California Strong Motion Instrumentation Program strong motion data sets to demonstrate the importance of rocking related to soil-structure interaction in building motion. Paolucci (1993) and Meli et al. (1998) studied the soil-structure interaction effects in Mexico City after the importance of these effects were found in the 1985 Mexico City earthquake. Stewart, and Fenves have studied these effects from different earthquake recordings, for example in Stewart et al. [1998, 1999a, 1999b], Stewart and Fenves (1998), and Fenves and Serino (1990). In addition to these earthquake recordings, some active tests have been conducted in order to understand these SSI effects, for example by Guéguen and Bard (2005) at the Volvi test site (Greece). Laboratory testing has also been conducted to study these SSI effects, notably by using the centrifuge test as done by Chazelas et al. (2003), Ghosh and Madabhushi (2007), and Mason et al. (2013).

Up until now, there have been many texts and papers that discussed the SSI effects. The importance of these effects is also demonstrated in numerous seminars and workshops, for example by Celebi and Okawa (1998), by Schanz and Iankov (2008) up to the recent by Kotronis et al. (2013). Numerous dissertations have been produced as well, for example from Guéguen (2000), Kham (2004), and Gu (2008). The fact that such workshops are still available shows that all these dissertations have worked on different parts of the cake and none of them is similar to one another, again showing how vast, large and complicated these problems are. The development of the study has indeed been a direct consequence to the evolution of the state of the art of this topic. The separations of different components of the interactions, i.e., the kinematic and inertial interaction, still need to be discussed, although some of the studies mentioned earlier have tried to tackle this matter. The frequency-dependent nonlinear soil-structure interactions have been the main axis of the research lately. The need for well-instrumented test sites has never been so pertinent, in addition to more extensive researches on scaled laboratory model. The development of effective and efficient numerical tools and model is essential. Finally, the incorporation of all aspects of the soil-structure interaction effects, first in ground motion prediction equation into the building codes, and then for the urban planning management standard operating procedures, would be the final goal in urban risk management.

1.3. 1D Wave Propagation System

As soil and structure can be modeled as a shear resonance system, one approach to analyze the response of a soil-structure system in a vertical array under seismic excitation is by using a 1-dimensional (1D) wave propagation method. The simplest generalization using an infinite rod in a layered body is discussed in Kramer (1996) where an incident waves (Equation 1.36) will be transmitted (Equation 1.37), and reflected (Eq. 1.38).

$$\sigma_I(x,t) = \sigma_i e^{i(\omega t - k_1 x)} \tag{1.36}$$

$$\sigma_T(x,t) = \sigma_t e^{i(\omega t - k_1 x)} \tag{1.37}$$

$$\sigma_R(x,t) = \sigma_r e^{i(\omega t - k_1 x)} \tag{1.38}$$

In this model, the soil and structure are modeled as a 1D-horizontally layered media that is subjected to anti-plane (*SH*) incident waves. In several cases, the layered media can also be represented as a 1D lumped mass system. In most of the cases, the propagation of upward and downward waves is formulated based on Thomson-Haskell matrices (Thomson, 1950; Haskell, 1953).

Several examples of the use of this approach for extracting soil responses from borehole data can be found in Satoh et al. [1995, 2001], Assimaki et al. (2006). Others used this method in their numerical simulations, such as in Phillips and Hashash (2009), and Rovithis et al. (2011). Several others used this approach to extract or identify buildings' responses, such as discussed by Şafak [1998b, 1999], Snieder and Şafak (2006), and Rahmani and Todorovska (2013). In all these examples, the soil and structure problems were separated, hence allowing the extraction of individual response (either soil or structure) to be possible. Şafak [1998a, 1998b] developed the discrete-time equations based on this wave propagation method to analyze the soil-structure systems. The soil and structure were combined as a single system with an *SH* incident wave propagating vertically inside the system (Figure 1.8).

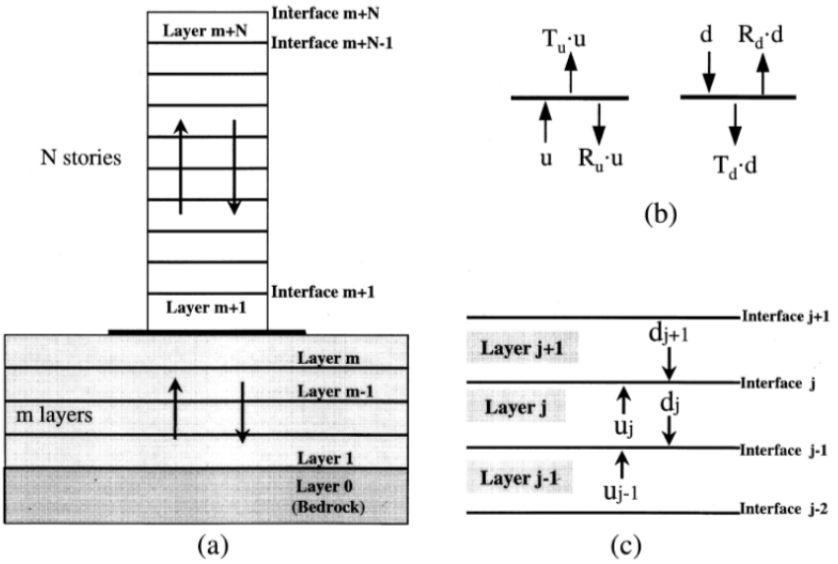

Figure 1.8. Bedrock-soil-building system: (a) layers, interfaces, and upgoing and downgoing waves; (b) reflection and transmission of upgoing and downgoing waves; (c) three consecutive layers with upgoing and downgoing waves. (taken from Şafak, 1998a).

The reflected and transmitted coefficients are derived from this multi-layered systems, and are discussed in Şafak (1999). He summarized the final expressions in Equations (1.39)-(1.40).

$$R_{u,j} = \frac{I_j - I_{j+1} - i \cdot 2\pi f \cdot m_j}{I_j - I_{j+1} + i \cdot 2\pi f \cdot m_j}, \quad T_{u,j} = 1 + R_{u,j} \tag{1.39}$$

$$R_{d,j} = \frac{I_{j+1} - I_j - i \cdot 2\pi f \cdot m_j}{I_j - I_{j+1} + i \cdot 2\pi f \cdot m_j}, \quad T_{d,j} = 1 + R_{d,j} \tag{1.40}$$

where R denotes reflected, T is transmitted, I_j is the impedance of layer j, m_j is the concentrated mass at interface j, u denotes upgoing, and d denotes downgoing waves.

In a realistic wave propagation analysis, the amplitude of the waves is attenuated due to material and radiation (geometric) damping. Material damping is the attenuation due to conversion of energy into heat associated with the intrinsic properties of the material. This damping absorbs the elastic energy and is defined in the viscous properties of the materials. In viscoelastic wave propagation, the Kelvin-Voigt solid model is often used (Figure 1.9.a).

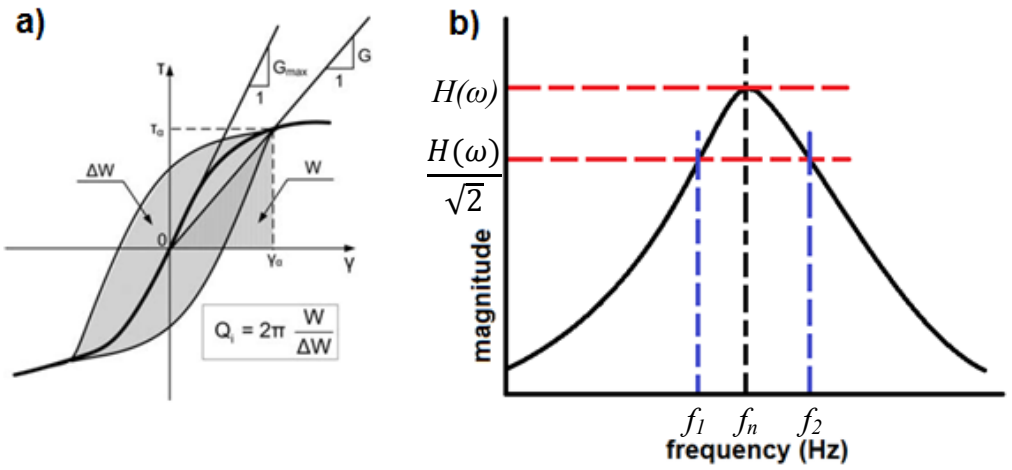

Figure 1.9. (a). Schematic representation of elastic damping in hysterical model (taken from Assimaki et al., 2008b); (b). Damping estimation using half-power bandwidth method.

In Figure 1.9.a, W is the peak energy during cycle, ΔW is the elastic energy dissipated in one cycle, Q is the amplification or quality factor related to the damping as:

$$\xi = \frac{1}{2Q} \tag{1.41}$$

The radiation damping is the attenuation of specific energy through spreading of energy over a greater volume of material. The elastic energy is conserved in radiation damping. The decay due to this radiation damping is shown to be at a rate of $1/r$ and $1/\sqrt{r}$ for body waves and surface waves, respectively. Details of the radiation damping in 1D wave propagation have been discussed by Dobry (2013). In a transfer function (Figure 1.9.b), the damping can be computed using the half-power bandwidth method, where

$$\xi = \frac{f_2 - f_1}{f_n} \tag{1.42}$$

where f_n is the resonance/peak frequency, $H(\omega)$ is the peak amplitude of transfer function, and f_1 and f_2 are the frequency where the amplitude of the transfer function is 3dB lower than $H(\omega)$ or equal to $H(\omega)/\sqrt{2}$.

1.4. Seismic Interferometry by Deconvolution

Seismic interferometry is a method to obtain the Green's function between receivers. This method simply consists of cross-correlating the seismic responses from different receivers, thus removing the propagation from the source to the first receiver and making it able to extract the seismic response from a receiver array (Wapenaar et al., 2010). The basic principle of this method for an example of reflected-wave interferometry can be seen in Figure 1.10.

Instead of using cross-correlation, the seismic interferometry method is developed using a deconvolution method to extract the impulse responses function (IRF). Clayton and Wiggins (1976) applied this deconvolution to the teleseismic bodywaves to separate the source and transmission path phenomena. They noted that the elimination of the source propagation gave an advantage of independency of the method to the source, and provided information of the causal and acausal propagation within the system. It also gave better estimation of the arrival times and amplitudes.

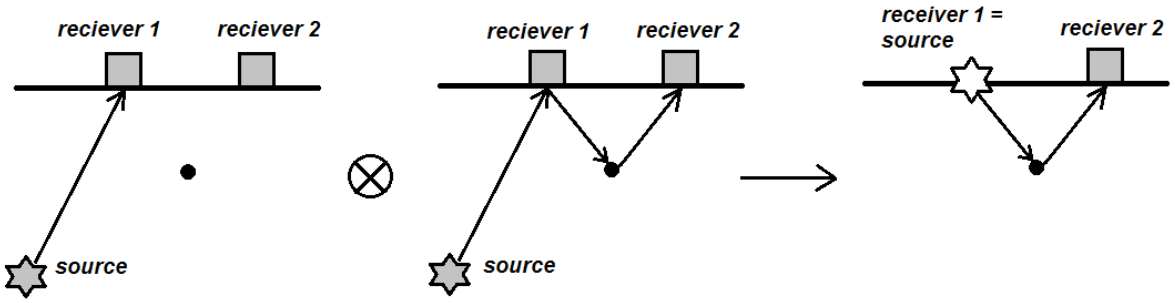

Figure 1.10. (left). Emitted wave from source to surface receiver 1. (middle). Reflected waves captured by receiver 2. (right). Cross-correlation eliminates the source to receiver 1 propagation and receiver 1 acts as the source.

By applying this to a resonance system, we can obtain the impulse responses function of the system, hence extracting the responses parameters. As a soil-structure system can be considered as a wave propagating system (Figure 1.8), this method can be applied to extract its responses.

Using an input-output pair, the estimated IRF of a resonant system can be obtained as the inverse Fourier transform of the spectrum of output (O) motion divided by the input (I) motion (Equation 1.43).

$$\tilde{H}(\omega) = \frac{O(\omega)}{I(\omega)} = \frac{I(\omega).I(\omega)^*}{\left|\tilde{I}(\omega)\right|^2} H(\omega) + \frac{\tilde{I}(\omega)^*}{\left|\tilde{I}(\omega)\right|^2} N(\omega) \tag{1.43}$$

where * denotes complex conjugates and ~ is estimated function. The value of $\left|\tilde{I}(\omega)\right|^2$ tends to have a zero value that can give a false estimation of the responses function. Hence, a minimum input amplitude, named water level, is used to limit the importance of the noise term, and is expressed as a fraction of the input. Incorporating this water level parameter k, where $0 \leq k \leq 1$, the eq. 1.43 became:

$$\tilde{H}(\omega) = \frac{I(\omega).I(\omega)^* H(\omega) + N(\omega)\tilde{I}(\omega)^*}{max\left\{\left|\tilde{I}(\omega)\right|^2, \left(k.\left|\tilde{I}(\omega)\right|_{max}\right)^2\right\}} \tag{1.44}$$

The deconvolution will be stable if the factor in Equation (1.45) remains stable as a function of frequency

$$\frac{I(\omega).I(\omega)^*}{max\left\{\left|\tilde{I}(\omega)\right|^2,\left(k.\left|\tilde{I}(\omega)\right|_{max}\right)^2\right\}} \tag{1.45}$$

1.5. Conclusion

In this chapter we presented the elements on soil nonlinearity and soil-structure interaction assessment in modifying the ground motion in urban area. The basic and fundamental concept of both effects often occurs together and is troublesome in terms of separating each effect. The existing methods for these effects are presented so readers have the fundamental knowledge on each effect. Numerous researches based on the existing methods are presented in order to display the development of each problem. Although all of these can be found in many references and books, we tried to synthesize and summarize the important elements to be used as a stepping point for the rest of this dissertation.

We showed that this cross-border research which attracts the seismologists, the geotechnical engineers, as well as the structural engineers has never been as relevant as it is now in terms of nonlinear soil and structure study. Moreover, the necessity to combine the study of soil nonlinearity and SSI effects using the appropriate and realistic approaches is indispensable to be able to understand their responses under earthquake excitation.

The 1D wave propagation method that will be useful for this lecture is also discussed. The wave propagation inside a multi-layered shear resonance system such as soil and structure is powerful to extract the information of the system's responses, and has been used widely such as described previously. The estimation of damping is also presented, as in realistic wave propagation models, attenuation due to material and radiation damping cannot be avoided. Finally, the deconvolution based on the wave propagation method is discussed in details in order to extract the impulse response function of a resonant system, i.e., soil-structure system.

Chapter 2

On the Use of *PGV/Vs* as a Proxy for Predicting Nonlinear Soil Response

Johanes CHANDRA, Philippe GUEGUEN, and Luis Fabian BONILLA

From a submitted paper to the Soil Dynamics and Earthquake Engineering (In review)

Summary

In this paper, a proxy for predicting the nonlinear response of soil is analyzed using centrifuge tests and numerical modeling, and finally applied to Japanese K-NET and KiK-net data. Weak and strong input motions are applied at the base of the soil column, and seismic ground motion is recorded at and below the surface performing vertical arrays. The seismic interferometry by deconvolution method is applied to extract the shear-wave velocity profile throughout the soil column. Herein, the ratio between particle velocity and the equivalent linear shear wave velocity computed between two successive sensors, v*/Vs*,is assumed to be a proxy of strain. The particle acceleration, a*, versus the v*/Vs* relationship is proposed as a stress-strain representation for nonlinear analysis of soil response. The interferometry by deconvolution method is first validated using simple 1D modeling (Cyclic 1D) and the Vs profile obtained is compared with the initial profile. We show that this method is a relevant and efficient solution for assessing the Vs profile applied to vertical seismic array, allowing observation of the variation of Vs as a function of deformation. Moreover, v*/Vs* is showed to be a good proxy of soil strain, and analyzing the variation of v*/Vs* as a function of a* allows the nonlinear response of the soil to be assessed in an earthquake situation. The classic two-parameter hyperbolic model to model the nonlinear stress-strain relationship is built. These proxies are then applied to the Japanese K-NET and KiK-net data, and Vs30 instead of Vs is used related to its practical use related to site classification recommendation.

2.1. Introduction

Near-surface geology effects (i.e., site effects), together with source and path effects, control seismic ground motion. They depend mainly on the mechanical properties of the uppermost soil and the input motion (Kramer, 1996). Under a 1D assumption (Chapter 1.3), the seismic response of the soil and the amplification observed during an earthquake are usually related to the shear-wave velocity *Vs*, the thickness *H* of the upper layer, and the impedance contrast between sediment and bedrock (Haskell, 1953; Dobry, 2013). The fundamental frequency, f0 of a soft layer overlaying stiff bedrock follows the relation $f_0=Vs/4H$. Depending on the level of shaking, seismic soil response is described by its stress-strain relationship, following elastic-linear or nonlinear behavior. The nonlinear response depends on the soil properties and excitation variations over time. One of the most crucial variations is cyclic loading, as observed during earthquake motion, which results in a hysteresis loop of the soil stress-strain relationship (τ-γ curve). This nonlinear behavior is characterized by the degradation of the shear modulus *G* and the increase of the damping ζ during excitation, following the types of soil. As strain increases, shear wave velocity *Vs* (related to *G* by the formula $Vs=\sqrt{(G/\rho)}$, where ρ is density) decreases and damping increases, resulting in a frequency shift of the frequency site response and attenuation of the seismic ground motion (Field et al., 1997).

After the 1989 Loma Prieta earthquake (Chin and Aki, 1991), seismologists became increasingly interested in the experimental assessment of soil nonlinearity. Since then, the nonlinearity observed in field records has been confirmed by many authors applying experimental methods (e.g. Aguirre and Irikura, 1997; Hartzell, 1998; Dimitriu et al., 2001; Frankel et al., 2002; Pavlenko and Irikura, 2002; Bonilla et al., 2003; Rubinstein and Beroza, 2004; Rubinstein and Beroza, 2005; Assimaki et al., 2008a; Bonilla et al., 2011; Régnier et al., 2013), numerical simulation (e.g. Assimaki et al., 2008b; Gélis and Bonilla, 2012), and a combination of both (e.g. Beresnev et al.,1998; Roumelioti and Beresnev, 2003; Bonilla et al., 2005). Nonlinear behavior is mostly observed in soft sediment (e.g., Field et al., 1998; Beresnev and Wen, 1996; Şafak, 2001; Bonilla et al., 2005), and is considered to be insignificant in hard rock, although recent studies tend to show some nonlinear behavior in relatively stiff soil during moderate earthquakes (Régnier et al., 2013). The nonlinear response tends to reduce site amplification related to the increase in damping and to shift the frequency response towards lower frequencies related to the decrease in shear-wave velocity

(Bonilla et al., 2005; Wu et al., 2009; Régnier et al., 2013). Nevertheless, discrepancies remain common between laboratory and field tests. These discrepancies might be due to the inability of laboratory tests to reproduce site conditions, the choice of reference site for the measurement of site-reference spectral ratios (Steidl, et al., 1996; Bonilla et al., 2002; Assimaki et al., 2008a), or the difficulty in separating nonlinear effects from site amplification effects, including 2D/3D geometrical effects (Frankel et al., 2002; Assimaki et al., 2008b; Sleep, 2010; Gélis and Bonilla, 2012).

Since the nonlinear response is directly related to the variation of the shear modulus and damping ratio with strain, one solution consists in assessing and monitoring these two parameters during periods of strong ground motion. Traditional methods using cross correlation have been applied (e.g., Rubinstein and Beroza, 2004; Rubinstein and Beroza, 2005) and a new technique based on coda or interferometry deconvolution was recently applied to borehole data (e.g., Sawazaki et al., 2009; Nakata and Snieder, 2011; Nakata and Snieder, 2012), providing *Vs* along the soil profile. Recently, Guéguen et al. (2011) applied modal analysis techniques to a vertical array to identify the depth of nonlinear behavior.

The difficulties arise from the rather limited number of vertical arrays and observations of strong motion, particularly in low-to-moderate seismic prone regions, and problems related to reproducing site stress-strain conditions of the soil column in the laboratory (Ghosh and Madabhushi, 2007), can be avoided by using centrifuge tests to analyze the nonlinear relationship between shear-wave velocity and ground motion. Nevertheless, the principal way to represent the soil nonlinear behavior is by observing its stress-strain evolution on site. The wave propagation-based ground strain has been derived using the ratio between Peak Ground Velocity *PGV* and shear wave velocity Vs (*PGV/Vs*). Idriss (2011) recently proposed the use of PGV/Vs_{30} as a strain proxy basing on the derivation of deformation. In addition, as *PGA* related to the shear stress, these proxies would be able to represent the stress-strain relation of the soil.

In the first part of this article, the seismic interferometry by deconvolution method is presented along with the *PGV/Vs* as the nonlinear proxy. The relevancy of these two elements is validated in the second part using synthetic data computed by Cyclic1D software (http://www.soilquake.net/cyclic1d/ last consulted August 9th, 2013; Elgamal, et al., 2010)

and then tested on more realistic data produced by centrifuge tests. The classic nonlinear two-parameter hyperbolic model is then performed to characterize the nonlinear parameter. Finally, the application of this nonlinear proxy and material model to Japanese K-NET and KiK-net data is presented.

2.2. Methods

2.2.1. Seismic Interferometry by Deconvolution

Seismic Interferometry can be defined as a method to obtain seismic response by cross-correlating seismic responses from different receivers (Wapenaar et al., 2010). Snieder and Şafak (2006) developed a method to analyze the seismic response of a building using seismic interferometry by deconvolution instead of the traditional cross-correlation method. They considered the building as a resonant system where waves propagate in one dimension. This method is expressed as follows:

The response of deconvolved waves between signal recorded in receiver *i* and receiver reference, $D_{i\text{-}ref}(\omega)$ can be computed as

$$D_{i-ref}(\omega) = \frac{A_i(\omega)A^*_{ref}(\omega)}{\left|A_{ref}(\omega)\right|^2 + \varepsilon} \tag{2.1}$$

where ω indicates that the procedure are applied in frequency domain. $A_i(\omega)$ is the displacement wavefield recorded at the first reciever, $A_{ref}(\omega)$ is the displacement wavefield recorded at the second receiver that is also considered as the reference wavefield, the * symbol indicates the complex conjugate of the signal, and ε is the stabilization estimator to avoid instability caused by the $A_{ref}(\omega)$ value being too close to zero. In this article, we use the signal recorded at the top as a reference and, after testing the slight influence of the ε value, it was set to 10% of the average spectral power, as recommended by Snieder and Şafak (2006). This method has the advantage of being independent of the input signal and providing the propagation of upward (causal) and downward (acausal) shear deformation along the system, which can be related to the shear velocity of the system. Todorovska and Rahmani (2013)

stressed the importance of the frequency band used for this method, since a smaller band would result in a wider pulse that may diminish the accuracy of the localization estimate over time.

Since the soil column can be considered as a resonant system having a shear deformation (Dobry, 2013), this method can be applied to analyze the soil column response. In particular, thanks to vertical sensor arrays, *Vs* can be computed along the soil profile based on the time delay estimation. This method was first successfully applied by Mehta et al. (2007) to a Californian downhole array. Nakata and Snieder (2012) also observed seasonal influences on the shear wave velocity and shear wave splitting on Japanese KiK-net borehole data. Pech et al. (2012) also used Japan KiK-net borehole data to estimate shear wave velocity and the change in its time-lapse. Most of these results are focused on the top-to-bottom *Vs* assessment. By using a multi-sensor vertical array, the local *Vs* in depth can be computed and nonlinear response can be analyzed in detail by testing the relationship between the local variations of *Vs* with respect to local strain.

2.2.2. PGA-PGV/Vs as Nonlinearity Proxy

A simple way of observing nonlinear behavior is to trace its stress-strain curves (e.g., Pavlenko and Irikura, 2002; Pavlenko and Irikura, 2003). *PGA–PGV/Vs* has been introduced as a shear strain based on the wave propagation (Hill et al., 1993). Idriss (2011) recently proposed a proxy for representing the probable nonlinear effect, based on the representation of the Peak Ground Acceleration *PGA* versus Peak Ground Velocity (*PGV*) / Vs_{30} ratio, which can be compared to stress-strain. According to Idriss (2011) and DeMartin et al. (2012), shear stress is the spatial derivative of *PGA* following:

$$\tau = PGA \times \rho \times z \tag{2.2}$$

and *PGV/Vs* can be considered as a proxy of shear strain, as shown below:

$$\gamma = \frac{du}{dx} = \frac{du/_{dt}}{dx/_{dt}} = \frac{PGV}{Vs} \tag{2.3}$$

where τ is the shear stress, ρ is the mass density, z is the depth, and γ is the shear strain.

In addition to *PGA vs. PGV/Vs$_{30}$* proxy, in this paper we use the peak particle acceleration, *a*,* the peak particle velocity, *v*,* and the equivalent linear shear wave velocity, *Vs*,* where all of these are computed between two successive sensors performing *a* vs. v*/Vs** as stress-strain proxy. In the first part to validate this proxy, we focused on *v*/Vs** since it refers to actual deformation instead of average S-wave velocity along the first 30m (*Vs$_{30}$*). Using a vertical geotechnical array, we can compute the depth variation of *Vs* locally using the deconvolution method. Since we compute the equivalent linear S-wave velocity *Vs**, it may have a lower value than the initial *Vs* (G/Gmax<1), due to nonlinearity. Otherwise, the test of *Vs$_{30}$* instead of *Vs* is primary for the prediction of soil nonlinear behavior, since *Vs$_{30}$* is the site condition parameter used for site classification. It will therefore be computed hereafter, considering the soil type classification given in the building code as the initial *Vs$_{30}$*.

In addition, we fit the classic two-parameter nonlinear hyperbolic model (Seed et al., 1984; Ishihara, 1996) to our data, following Equation 2.4.

$$\tau = \frac{G_0 \gamma}{1 + \frac{\gamma}{\gamma_r}} \tag{2.4}$$

where τ is the shear stress, γ is the shear strain, G_0 (or G_{max}) is the initial/maximum shear modulus, and γ_r (or γ_{ref}) is the reference strain according to the Equation 2.5.

$$\gamma_{ref} = \frac{\tau_{max}}{G_{max}} \tag{2.5}$$

where τ_{max} is the maximum shear stress. By extracting *Vs* and γ_r from our model, it allows us to compute other dynamic soil parameters, such as shown in Equations 2.6 and 2.7.

$$\frac{G}{G_{max}} = \frac{1}{1 + \frac{\gamma}{\gamma_r}} \tag{2.6}$$

$$D = \frac{4}{\pi}\left(1 + \frac{1}{\gamma/\gamma_r}\right)\left[1 - \frac{1}{\gamma/\gamma_r} ln\left(1 + \frac{1}{\gamma/\gamma_r}\right)\right] - \frac{2}{\pi} \tag{2.7}$$

where G is the shear modulus, G/G_{max} is the degradation of shear modulus, and D is the damping ratio.

Being that stated, extracting the Vs_{30} and γ_r basically means predicting soil nonlinearity behavior for different site conditions classified following Vs_{30} and according to the earthquake engineering code.

2.3. Numerical Validation using a Synthetic Model

To validate the interferometry method for soil response analysis, we first compute the elastic response of a synthetic and homogenous soil column using nonlinear finite element Cyclic1D software (Elgamal, et al., 2010). This simulates nonlinearity using incremental plasticity models. The characteristics of the cohesionless soil proposed in Cyclic1D are indicated in Table 2.1.

Table 2.1. Soil Properties for the synthetic models tested in Cyclic1D (Elgamal et al., 2010)

Cohesionless soil	*Vs* at 10m depth (m/s)	Friction angle (degrees)	Possion's ratio	Permeability coefficient (m/s)	Mass density (kg/m3)
Loose	185	29	0.4	$6.6x10^{-5}$	$1.7x10^{3}$
Medium	205	31.5	0.4	$6.6x10^{-5}$	$1.9x10^{3}$
Medium-dense	225	35	0.4	$6.6x10^{-5}$	$2.0x10^{3}$
Dense	255	40	0.4	$6.6x10^{-5}$	$2.1x10^{3}$

The thickness of the soil model considered herein is 300 m and the acceleration time-history response is computed every 10 m, considering a single Ricker-like wavelet as the input signal with a predominant frequency of 2.5Hz and 1 mg amplitude (Fig. 2.1)

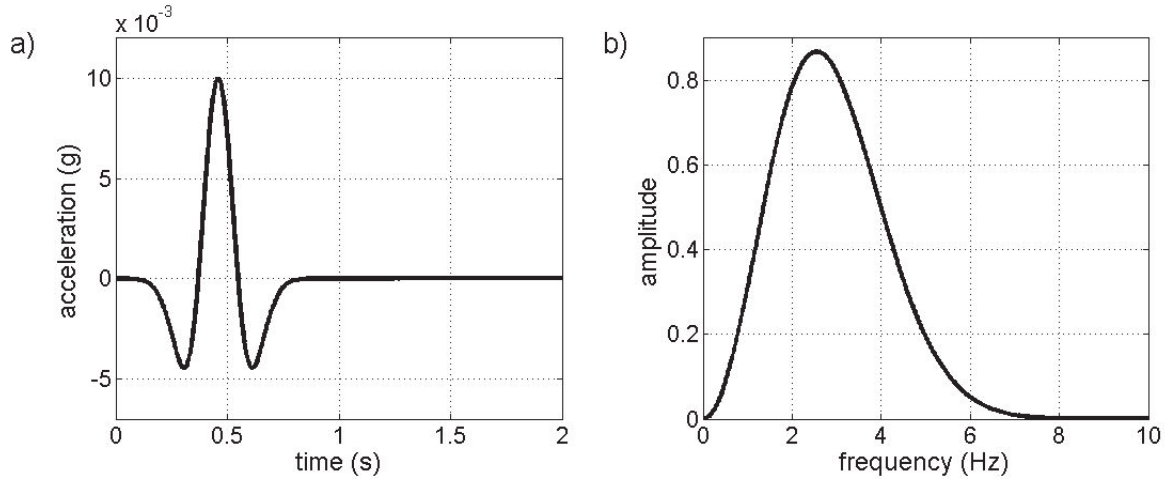

Figure 2.1.a. Time history of Ricker signal; b. Fourier spectra of Ricker signal

First, the column is composed of a homogenous dry-loose cohesionless soil (Tab. 2.1, first row) and the reference value of shear wave velocity (*Vs*=185 m/s) is given at a depth of 10 m. Velocity varies according to depth following the increment $(\mathrm{p_m})^{0.25}$, where p_m is the effective mean confinement corresponding to the reference dotted line in Figure 2.2.b with $Vs = 1.73(p_m)^{0.25}$.

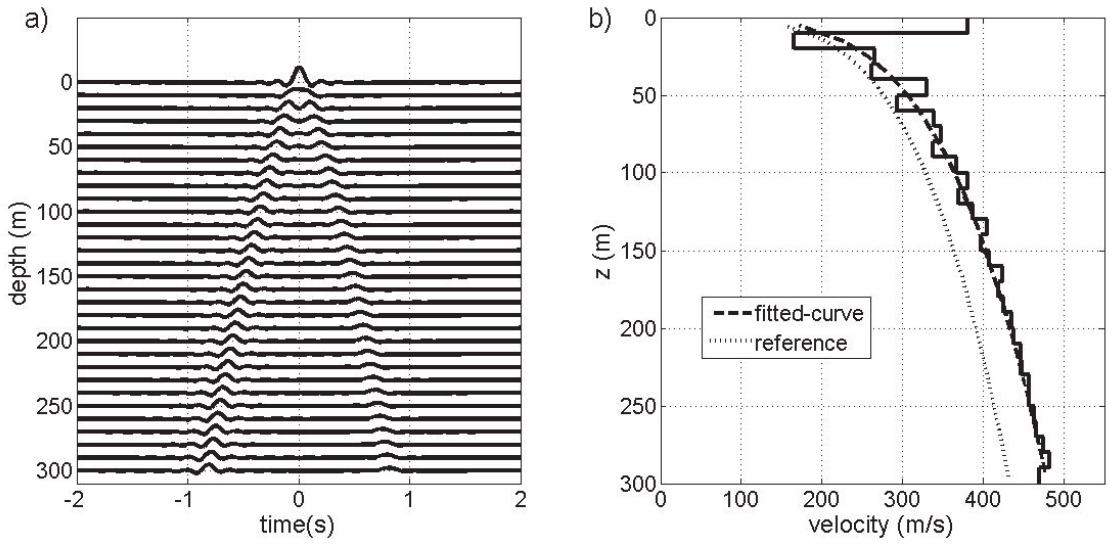

Figure 2.2. Results of a synthetic model of a 300m depth soil column with Ricker input signal (loose cohesionless soil). a. Interferogram of deconvolved waves; b. Velocity profile construction

The time histories computed along the profile are deconvolved using Eq. 2.1, considering the top first layer as a reference. Figure 2.2.a displays the interferogram of the deconvolved waves for the 300m deep soil column. The upward and downward waves are clearly observed, allowing computation of the *Vs* profile by dividing the distance between two sensors by the arrival time delay between two successive accelerograms. The *Vs* profile computed by interferometry fits the theoretical Cyclic1D profile (Fig. 2.2.b): $\mathrm{Vs} = 1.92(\mathrm{p_m})^{0.25}$. A global 10% shift to the reference profile is observed, due to inaccurate assessment of the velocity value for the surface layers. In fact, we note (Fig. 2.2.a) a mixing of upward and downward waves in the first layer, resulting in confusion on the time delay estimate. This difficulty affects the result of *Vs* at the top, where nonlinear behavior is expected to be strongest. Nonetheless, the shape of the *Vs* variation with depth is well reproduced. The damping effect in the downward (acausal) waves is also apparent, reducing amplitude with depth, and used by Newton and Snieder (2012) for damping assessment in buildings. Nevertheless, some caution must be applied when using this technique for damping assessment, since radiation damping is not accounted for, even though it may be predominant in the case of a slight impedance contrast between two systems. This parameter will not be discussed in the following.

We continue the modeling process using more realistic seismic signals including nonlinear response. Two different input signals are used, representing weak and strong excitation, used in the framework of the French ARVISE research program for conducting an experimental project on centrifuge tests (see below) (Fig. 2.3). The first accelerogram is a strong synthetic ground motion, generated using the Green's Function method for a hypothetical Mw 5.5 earthquake occurring 15km from a RAP (French Accelerometric Network) station (OGDH code, Péquegnat et al., 2008) located in the center of the Grenoble valley (Guéguen et al., 2007; Causse et al., 2008) and having a *PGA* of 0.43g (dominant frequency close to 1.86Hz). The second motion is a weak seismic ground motion recorded at the JARA rock station of the RAP during the Mw 7.3 earthquake in Martinique in 2007. Peak ground acceleration (*PGA*) corresponds to 0.07g and dominant frequency is close to 2.7Hz. This record is scaled to 10% of the weak motion (leaving the phase unchanged), giving a third accelerogram for numerical application, ensuring a pure elastic and linear consideration. Pre-processing is applied to the three signals, with mean and trend removal, applying a 5% Tukey taper window and filtering the signal in a frequency band between 0.33 and 13.8Hz (3-order Butterworth filter). For the

two first accelerograms (and by consequent for the third), this frequency band corresponds to a signal-to-noise (S/N) ratio over 3 (Fig. 2.3.b). This frequency band is wide enough to avoid the problem of time-delay assessment accuracy in the seismic interferometry method (Todorovska and Rahmani, 2013).

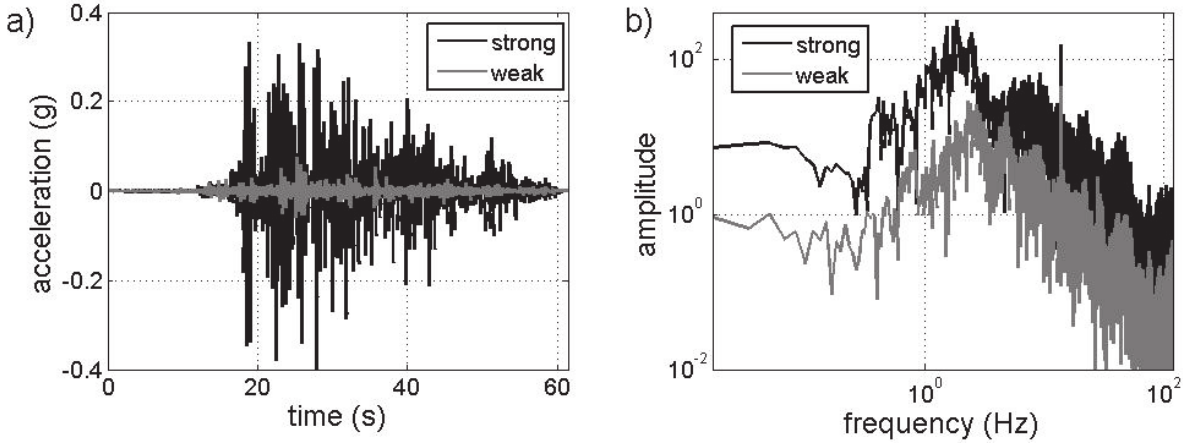

Figure 2.3.a. Time History of Input Signals; b. Fourier Spectra of Input Signals

Figure 2.4 shows the Cyclic1D stress-strain curves of the loose soil response at the surface for the three accelerograms.

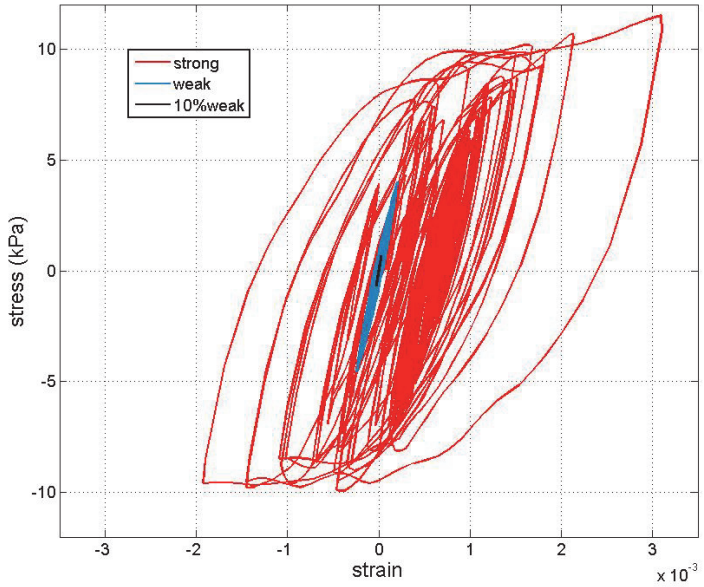

Figure 2.4. Stress Strain Relationship of loose cohesionless soil response computed by CYCLIC 1D at a depth of 1.15m for strong, weak and 10% weak input motions.

The hysteresis curve for the strong motion confirms the nonlinear simulation of the soil response, while the 10% weak motion remains within the elastic and linear domain. Synthetic interferograms of the deconvolved waves for the three input signals for the loose sand type are shown in Figure 2.5.

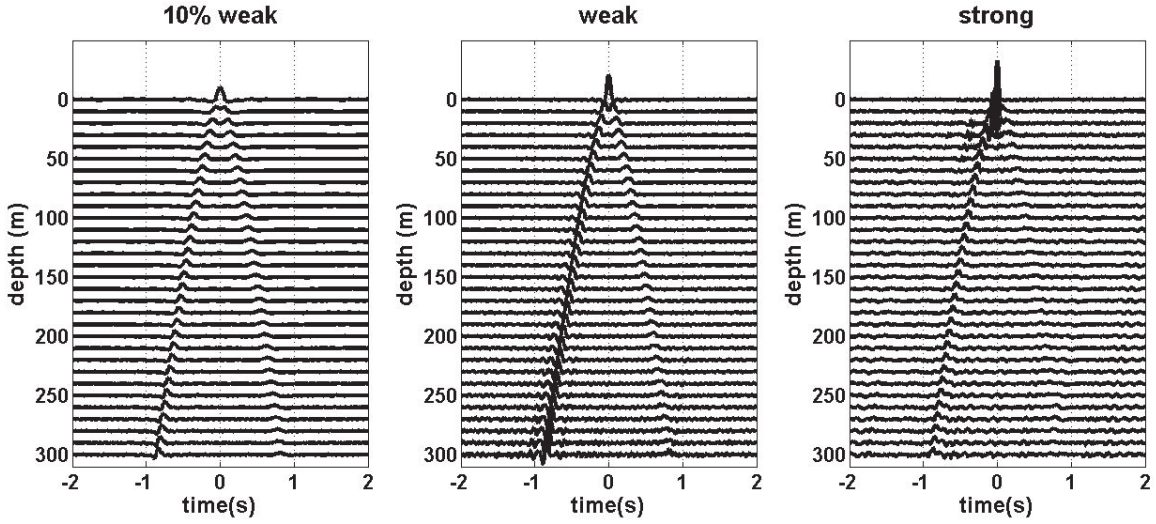

Figure 2.5. Interferogram of deconvolved waves for 10% weak, weak and strong events on a 300m depth synthetic soil column model (loose cohesionless soil).

The most visible effects are the increasing amplitudes of deconvolved waves as input moves from 10% weak to strong. Furthermore, the effect of the attenuation is observed, also increasing from weak to strong motion on the acausal wave, in relation to the increase in damping with nonlinearity.

Figure 2.6 shows the velocity profiles obtained for the three different input signals compared with the initial *Vs* profile obtained for the elastic analysis. The 10% weak and weak inputs give very similar results compared with the elastic analysis, with a variation of less than 1%. The nonlinear effect of strong motion is also clearly shown by the reduction of *Vs* along the profile. The reduction is not regular with depth, providing some information on the location of the nonlinearity. Up to a depth of 230 m, *Vs* is reduced by around 1.5% and beyond 230m depth, *Vs* increases by around 8.6%. We notice the largest increase in *Vs* (17.3%) at a depth of around 230 m under strong excitation. This increase is related to the contracting behavior of the soil due to dynamic compaction/consolidation effects (Sirles, 1988; Bernardie et al., 2006). From a rheology point of view, the contracting behavior of the soil corresponds to the value of its characteristic angle defining the limit between the soil's tendency to dilate and to

contract. (Lopez-Caballero et al., 2007). In conclusion, the models validate the reliability of the interferometry method used for *Vs* assessment along the soil profile and its use for depth monitoring in nonlinear site response analysis.

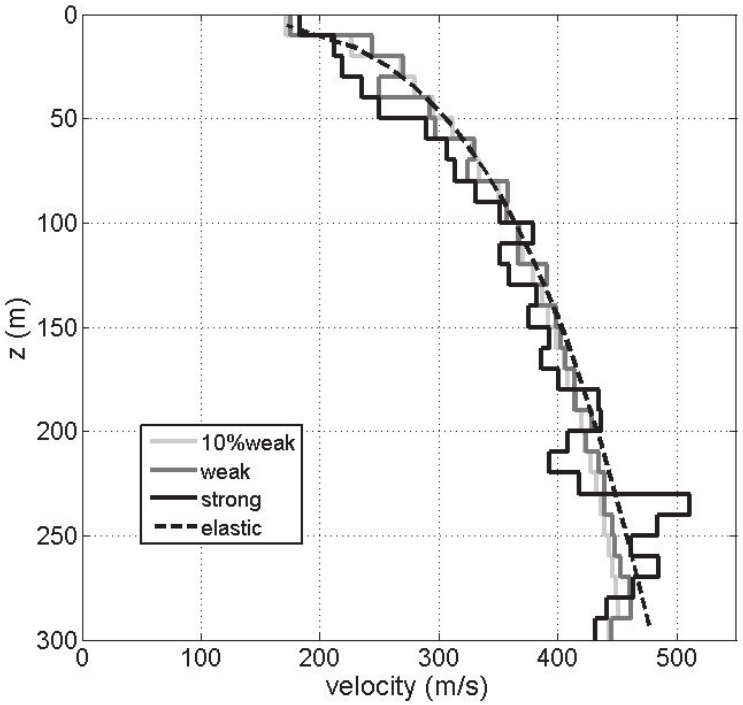

Figure 2.6. Velocity profile of a 300m depth synthetic soil column model for 10% weak, weak and strong events (loose cohesionless soil).

Using the *Vs* assessed by the interferometry by deconvolution method, the stress-strain proxy *a* vs. v*/Vs** is computed to evaluate the nonlinear behavior of the soil. Figure 2.7.a displays the *a** versus *v*/Vs** value computed using synthetic data and considering now all the soil types shown in Table. 2.1. If nonlinear effects exist, *V*s* changes with respect to the initial value, according to *a**. The soil is therefore grouped according to the *Vs** obtained using the seismic interferometry method rather than the initial value. On this 300 m depth soil column, *Vs** ranges from less than 300 m/s to more than 600 m/s. Linear and nonlinear behavior are clearly distinguished for each class of *Vs** for stiffer (>600 m/s) and softer (<300 m/s) soils, the latter showing a clear nonlinear response at higher *v*/Vs** values. Since *a** and *v** increase simultaneously, resulting in a decrease of *Vs**, the rate of variation of *v*/Vs** must be higher than *a**, giving a typical elastoplastic-like curve.

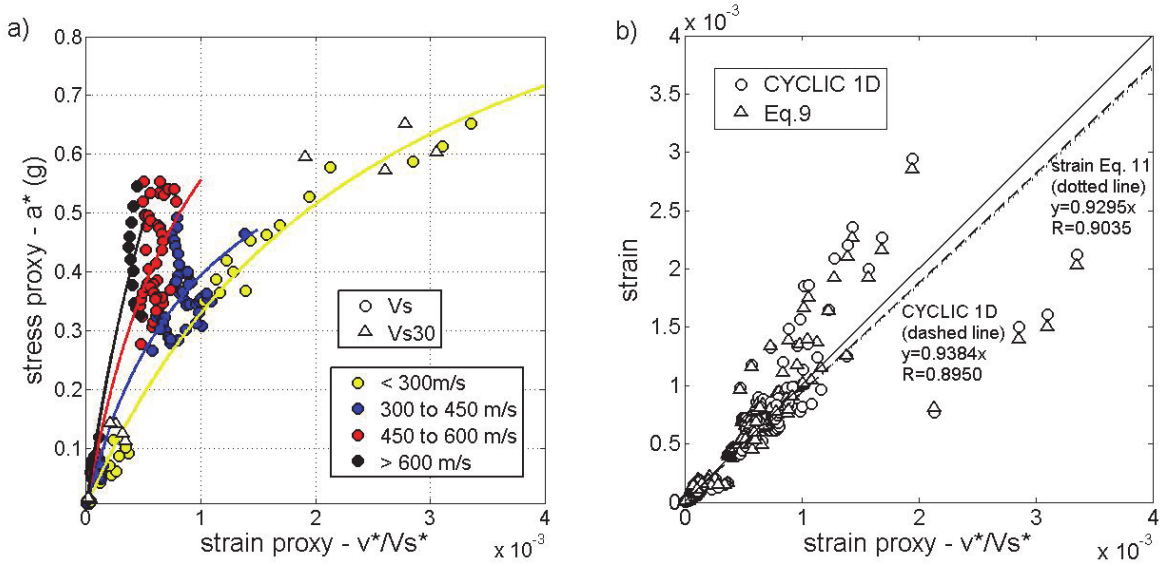

Figure 2.7. (a). Nonlinear behavior of synthetic models using *a*-v*/Vs** representation as a stress-strain proxy. Data are taken from all soil type analysis results. The solid line represents the hyperbolic model adjusted to the numerical model data (see Tab. 2.2). (b): Comparison between *v*/Vs** as a strain proxy and deformation (strain) extracted from CYCLIC 1D and Eq. 2.5; Dashed Line indicates the linear fit of the data from CYCLIC 1D, and Dotted Line indicates the linear fit of the data from Equation. 2.9.

We form the classic hyperbolic model, commonly used for nonlinear stress and strain relationships (Seed, et al., 1984; Yu, et al., 1992; Ishihara, 1996; and Beresnev and Wen, 1996), given by the following model

$$y = \frac{ax}{1 + \frac{a}{b}x} \tag{2.8}$$

where y and x correspond to shear stress τ and shear strain γ, respectively, and a and b represent the regression coefficients of the proxy model. Finally, the non-linear proxy according the hyperbolic model can be expressed by:

$$a^*(g) = \frac{a\,\frac{v^*}{Vs^*}}{1 + \frac{a}{b}\frac{v^*}{Vs^*}} \tag{2.9}$$

assuming a^* and v^*/Vs^* as the shear stress and the shear strain, respectively. Table 2.2 shows the coefficient values of our hyperbolic models, including the R (coefficient of correlation) and the average residual values between the model and the data. Following Eq.2.6, γ_r can be computed simply by b/a value. The discussion on this value and proxy will be discussed in the next section.

Table 2.2. Coefficients values, *R* and residuals for our nonlinear synthetic models using numerical modeling. a, b and b/a correspond to the coefficients of the model fitted to the data, according to Eq.2.9.

	Velocity Group			
	< 300 m/s	300-450 m/s	450-600 m/s	> 600 m/s
a (x 10^{3})	0.4586	0.7871	1.1120	1.3988
b	1.1744	0.7871	1.1154	1.5560
R	0.9631	0.9641	0.9647	0.9695
Res	0.0192	0.0187	0.0262	0.0244
b/a (x 10^{-3})	2.5609	0.9994	1.0031	1.1124

Fig. 2.7a also displays the value of $PGA\text{-}PGV/Vs_{30}$ (in a triangle) for comparison. Vs_{30} is computed as the average value of *Vs* over the first 30m, for the four soil types (Tab.2.1) and the three excitation levels using seismic interferometry. Vs_{30} range from 193 m/s to 447 m/s with an average value of 277 m/s. According to Cyclic1D's soil characteristics (Tab. 2.1), the PGV/Vs_{30} corresponds to the <300m/s velocity class, comparable to the *Vs* value at a depth of 10m since Vs_{30} only takes into account the average value of the first 30m. PGV/Vs_{30} provides relevant information on the nonlinear site response, requiring only ground motion parameters (*PGA* and *PGV*) and the site classification.

Figure 2.7b shows a comparison between strain, given by the *PGV/Vs* proxy with the Cyclic1D deformation calculated directly from the strain profile of the soil response, and deformation computed from the displacement time histories calculated along the soil profile as follows (Brennan et al., 2005):

$$\gamma_{ij} = \frac{(u_j - u_i)}{(z_j - z_i)} \tag{2.10}$$

where γ_{ij} is the deformation (strain) between two successive points i and j, u_i and u_j are the displacements at points i and j, respectively, calculated from the double integration of acceleration values, and z_i and z_j are the depth positions of points i and j, respectively. The double integration from acceleration to displacement value was done including some signal processing as follows: mean removal, trend removal, 5% Tukey tapering, 3-order Butterworth filter between 0.33-13.8Hz, first integration to velocity value, 3-order Butterworth filter between 0.33-13.8Hz, and second integration to displacement value. *v*/Vs** shows a linear relationship compared to Cyclic1D and computed deformation, with a good coefficient of correlation, lead us assume that the *v*/Vs** is relevant proxy for soil strain. We can therefore assume that *a*-v*/Vs** represents the stress-strain relationship that can be used for the nonlinear site response assessment or prediction.

2.4. Application to the Centrifuge Test

Taylor (1995) noted that the first idea of a centrifuge test came from Edouard Phillips, who presented the elastic theory limitation on complex structure analysis in 1869. Since then, interest in this method has grown significantly and spread to other dynamic geotechnical fields. It consists in creating a scaled-down model that can reproduce actual scale behavior of soil by increasing the gravity-scaled acceleration fields. Scaling from model to real object respects the established scaling factors shown in Tab. 2.3.

Table 2.3. Scaling factors considered in centrifuge tests from model to real object dimension under N time the gravity.

Parameter	Real Object/Model
Length, Displacement	N
Area	N^2
Volume, Mass	N^3
Velocity	1
Stress	1
Acceleration	1/N
Time	N
Frequency	1/N

Various applications for centrifuge tests have been published, including the evaluation of soil dynamic properties (Brennan et al., 2005), the observation of wave propagation by drop ball arrangement test (Semblat and Luong, 1998), the measurement of shear wave velocities using a bender element system (Brandenberg et al., 2006), assessment of shallow foundation rocking (Gajan et al., 2005), the seismic analysis of dam response (Yang et al., 2004, Saleh and Madabushi, 2010), the study of dynamic response in piles (Escoffier, 2012), assessment of soil-structure interaction effects (Ghosh and Madabhushi, 2007), soil-foundation-structure interaction effects (Mason et al., 2013), and site-city interaction (Chazelas et al., 2003).

In this study, the centrifuge test was performed at the IFSTTAR (Institut Français des Sciences et Technologies des Transports, de l'Aménagement et des Réseaux) facility (Chazelas, 2010) at the 60 g scale (Figure 2.8).

Figure 2.8. Centrifuge instrumentation at IFSTTAR Nantes.

The typical model, dimensions and sensor distribution of the setups are presented in Figure 2.9. We use equivalent shear-beam (ESB) containers, dimension 800x350x416mm, thus representing a soil mass 48 m long, 21 m wide, and 25 m deep.

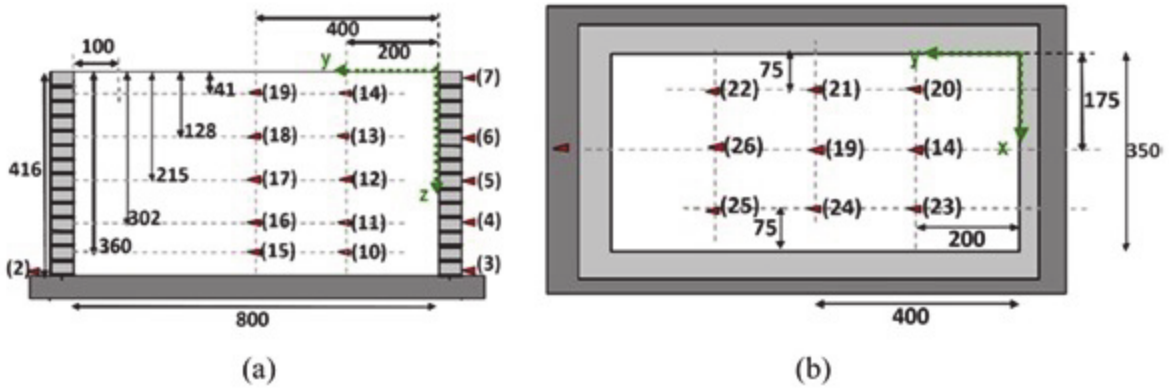

Figure 2.9. Typical model, dimension and sensor distribution of the centrifuge test. Sensor numbers are in brackets and the numbers without bracket are model dimensions in mm. (a). Y-Z plan view (b). X-Y plan view. (modified after Chazelas, 2010)

The boundary condition is considered to be one of the most important issues of centrifuge tests, since with ordinary testing methods, this condition cannot be conserved. For this reason, two ESB containers were used in our experiments. Zeng and Schofield (1996) reported that ESB is the most recent solution to recreate vertical boundary conditions approximately, i.e. behaving like a soil column and having the same stress-strain condition on any position in the soil mass.

The solid triangle shows the sensor locations with each reference number. The material used is dry Fontainebleau sand, whose properties are shown in Table 2.4, where e is void ratio, γ_d is material weight and D_r is relative density. The soil mass was constructed using the dry pluviation method and the sensors were placed manually along the pluviation in the desired positions. The pluviation is done with a drop height of 57cm and recalibrated to this height after each return. This soil filling technique is used to recreate the initial stress in granular soil.

Table 2.4. Soil properties used in the experiment (Chazelas, 2010)

Soil	e_{min}	e_{max}	$\gamma_{d\,min}$	$\gamma_{d\,max}$	D_r (%)	γ_d
Fontainebleau Sand NE34	0.86	0.55	13.93 kN/m^3	16.78 kN/m^3	57.00	15.42 kN/m^3

Piezoelectric horizontal accelerometers (PCB type 200 A1 and Bruel & Kjaer type 4317) were used, attached to a thin plate to ensure direction and position. The exact position before and after the experiments are done is measured to consider the soil settlement due to the earthquake shaking.

The weak and strong ground motions previously used for the modeling step were applied as inputs for the centrifuge tests at the bottom of the container, using a shaker driven in displacement. Figure 2.10 shows one example of the signals recorded by sensors 15 and 19 for both input motions. All signals were pre-processed before analysis, as mentioned previously. As expected, the signals recorded by the top sensor are amplified compared to the signals from the bottom sensor (Fig. 2.10a), related to soil column amplification. The Fourier spectra (Fig. 2.10b) show the dominant frequency of the signal and the relevant signals are contained between 0.33 and 13.8Hz as mentioned previously. Moreover, the shift of the predominant frequency to the low frequencies is clearly visible for the strong input, indicating the presence of nonlinear effects as expected at the beginning of the experiment.

Figure 2.11 displays the PGA value of the signals recorded by the top and bottom sensors for the weak and strong inputs, compared to Idriss' (1990) representation. In the first approximation, considering the bottom input signal as rock motion, we observe roughly comparable amplification for the weak motion and the nonlinear response of the soil column. The centrifuge experiment provides an acceleration limit close to 0.4g, above which the nonlinear process is effective, with reduction of amplification with respect to the rock site motion. This limit value is similar to Idriss (1990), however, the threshold values (the starting limit of the nonlinear process) are different, which could be explained, as suggested by Cua and Heaton (2012), by saturation characteristics of the ground (not reproduced here) and the frequency content of the input signal.

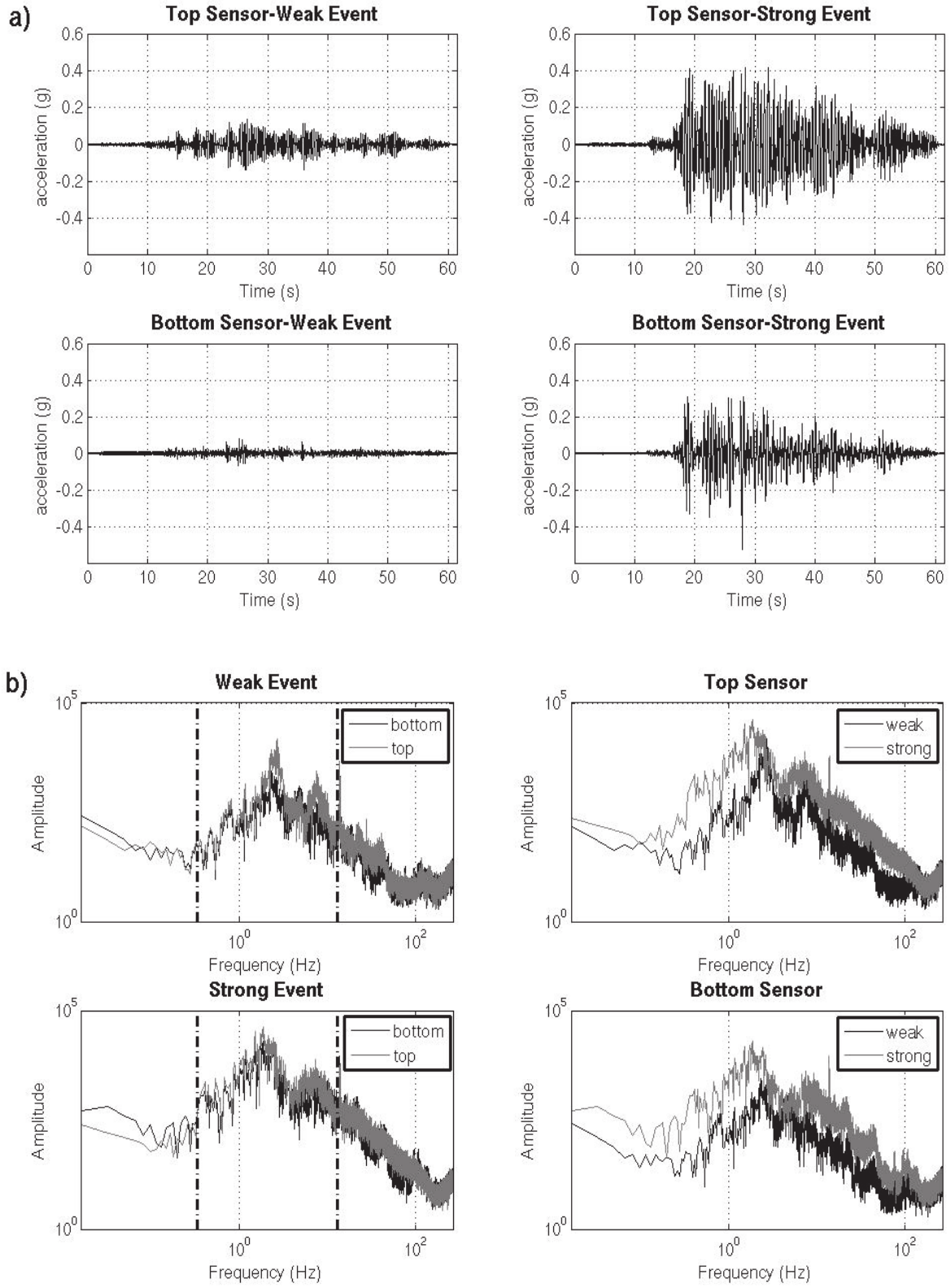

Figure 2.10.(a). Time history of signal recorded for indicated excitation and position; (b). Fourier Spectra of signal recorded for indicated excitation and position. (Top sensor = sensor 19 ; Bottom sensor = sensor 15) The dotted-dash lines are the frequency band in which the energy is maximum.

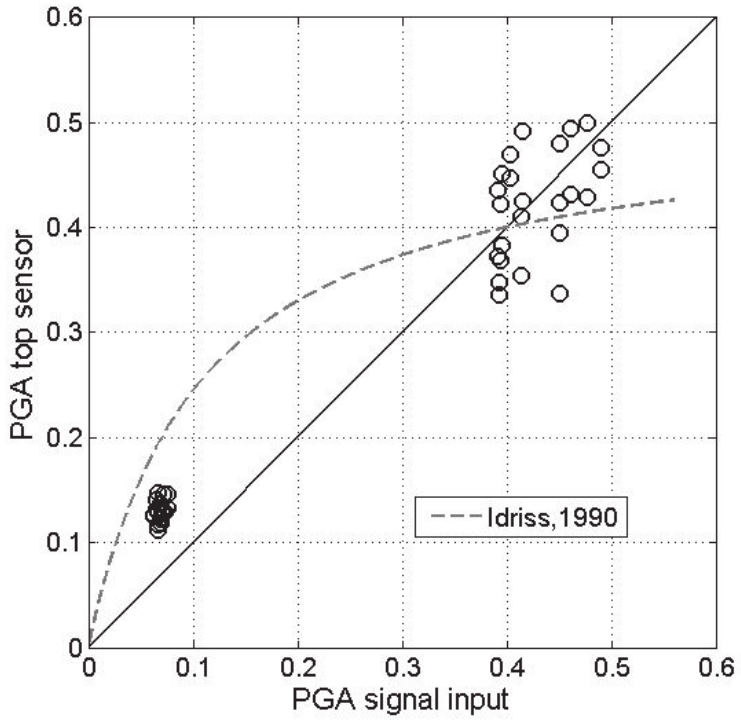

Figure 2.11. Approximate relationship between the PGA of signals recorded by top sensors and the PGA of signals recorded by the sensor located at the bottom of the container. Black circles show the results obtained from centrifuge test with the black dashed line as the approximate relationship, and gray dashed line as the approximate relationship from Idriss (1990).

2.4.1. Validation of the Centrifuge Test

To check the repeatability and stability of the tests, several sets of experiments (trials) were carried out (between 5 and 6) for each input, applied to two containers with the same geotechnical and instrumental characteristics, in order to limit unusable data. Figure 2.12 shows the high level of experiment repeatability, the time history of the strong and weak signals being the same for all trials (Fig. 2.12 top). Moreover, the variability of PGA along the profile is as slight as possible (Fig. 2.12 bottom). We note that the variability observed at the top of the container is of the same order of magnitude as the input signal, which explains why the vertical waves are not contaminated by reflection at the vertical boundaries. This confirms the efficiency of the ESB box.

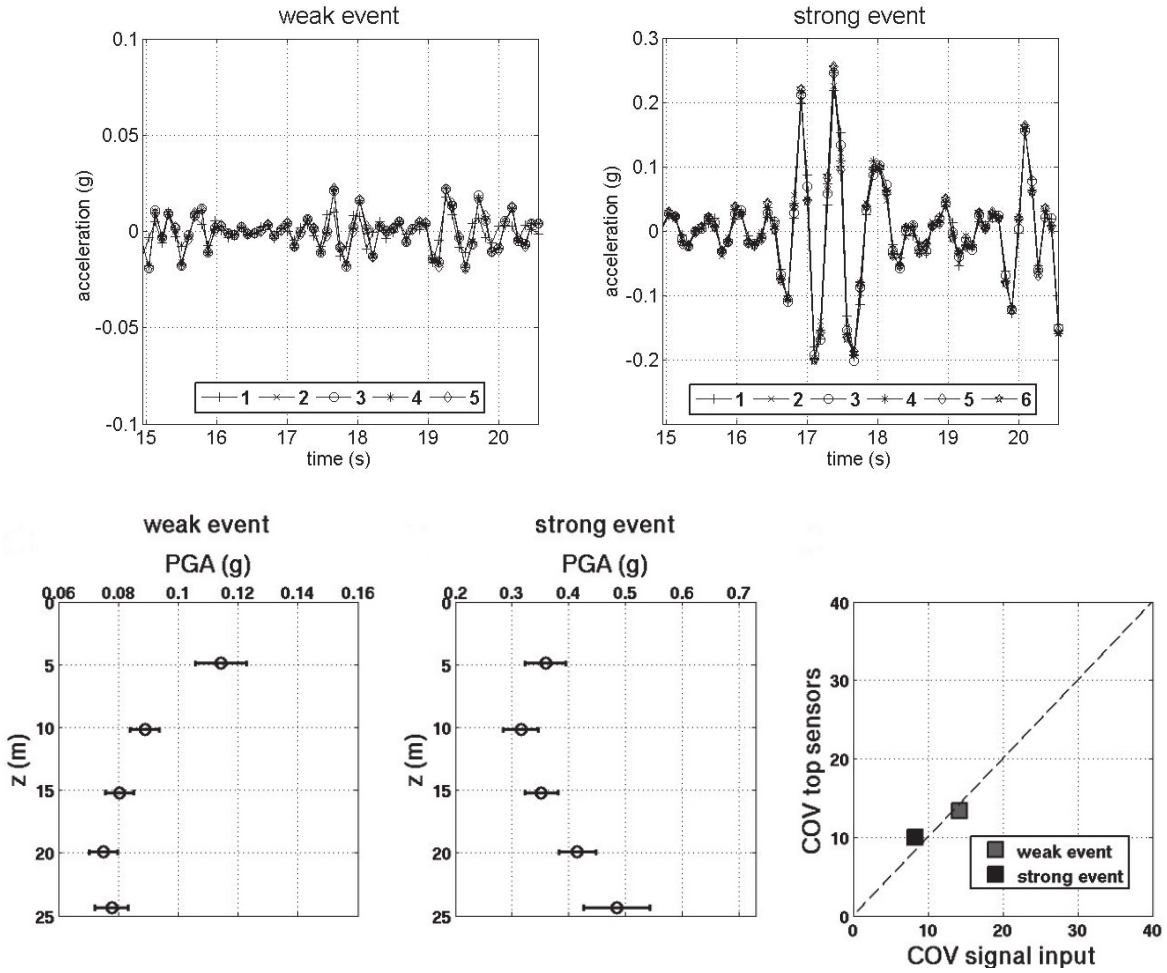

Figure 2.12.(Top). Zoom of Time Histories of input signals for weak and strong events. (Bottom). Mean and Standard Deviation of PGA values recorded on the vertical array of middle soil column (sensor 15-19) for weak and strong events (left and middle). Right: PGA variation coefficient on top sensors and bottom sensors.

Figure 2.13 shows an example of the Anderson (2004) multi-criteria evaluation of two signals recorded at the surface of one container, considering the center (sensor 19) as the reference sensor. According to Anderson, and as applied recently by Roullé et al. (2007) and Perrault et al. (2013), goodness-of-fit is computed in different frequency bands (0.33-13.8Hz in our case) for the following ten parameters: Arias Duration (SDa), Energy Duration (SDe), Arias Intensity (SIa), Energy Integral (SIv), Peak Acceleration (Spga) Peak Velocity (Spgv), Peak Displacement (Spgv), Response Spectra (Ssa), Fourier Spectra (Sfs) and Cross Correlation (C*). These parameters range from 0 to 10, scores below 4 corresponding to poor fit, scores of 4-6 to fair fit, scores of 6-8 to good fit, and scores over 8 to excellent fit. Considered as a reference, the center sensor shows perfect correlation.

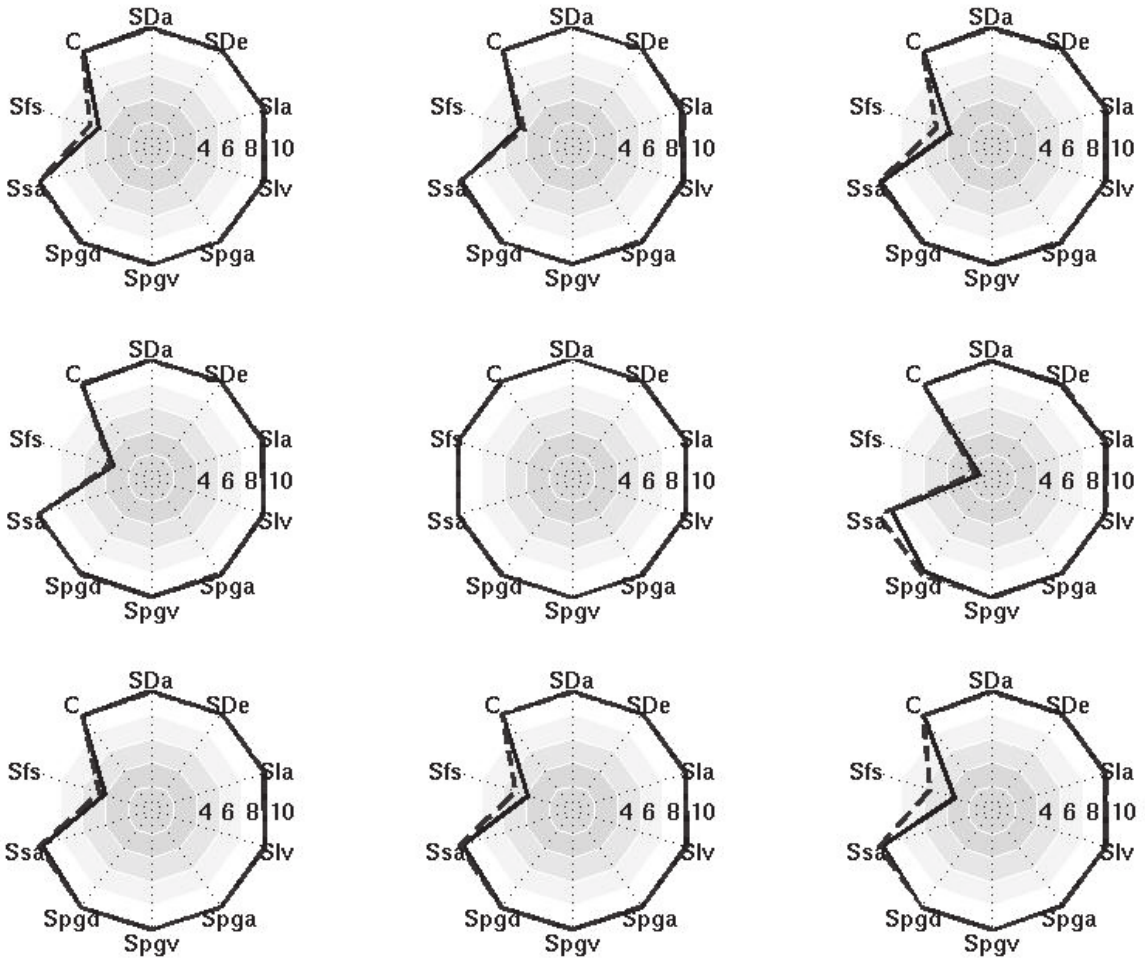

Figure 2.13. Goodness-of-fit between signals recorded on the surface taking the middle sensor as a reference. The solid line indicates the results for weak events and the dashed line indicates the results for strong events.

The comparison (Fig. 2.13) results in excellent fit with values of almost 10 for every criterion, except the Fourier Spectra. Anderson indicates that this is the most difficult criterion to fit because the Sfs criterion compares the Fourier amplitude at all frequencies. Except for this parameter, the results show that there are no obvious boundary effects, also considering that for the half space problem reproduced in centrifuge tests, the surface waves are not dispersive. In conclusion, the high repeatability and the negligible boundary effects lead us to assume that the observation of the processes described in the rest of this paper are not due to experimental issues but to physical phenomena. Finally, as many trials as possible are considered in this study, combining data from the two containers and the two lines of the vertical arrays.

2.4.2. Shear Wave Velocity, Nonlinear Behavior Assessment, and Soil Nonlinearity Prediction

We apply the seismic interferometry by deconvolution method to extract the soil shear wave velocity, using the same procedure as for the synthetic data. An example of a deconvolved wave interferogram is shown in Figure 2.14, along the main (center) vertical line of the centrifuge array.

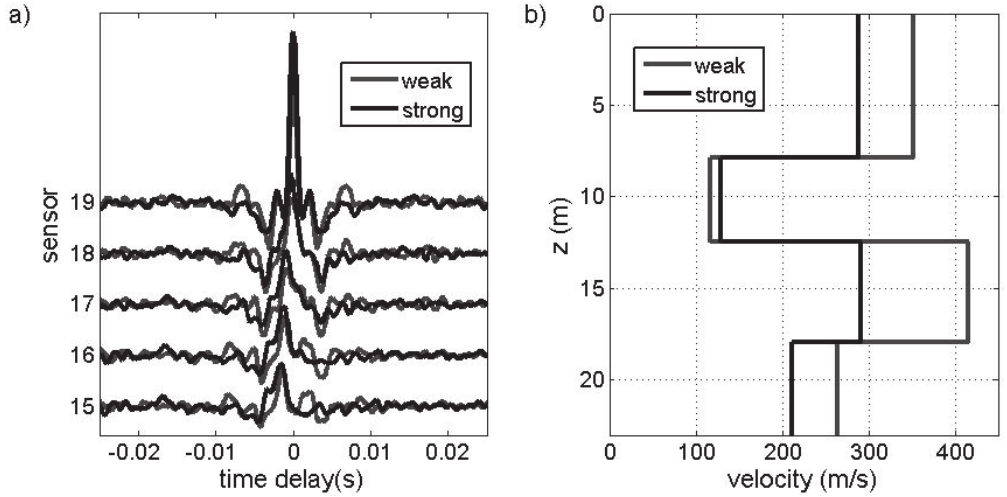

Figure 2.14. (a). Interferogram of deconvolved waves for weak and strong events from the centrifuge test; (b). Velocity profile for weak and strong events from the centrifuge test.

The upward and downward waves are clearly visible for the weak and strong events, enabling estimation of *Vs** by setting the time-delay between two successive sensors. The results are not as clean as for the synthetic data, due to experimental noise and the difficulties inherent to experimental data. Nevertheless, we observe the same differences between weak and strong inputs, i.e. stronger attenuation due to energy dissipation on the acausal wave for the strong input, and stronger amplitude at the top of the soil column. This is shown in Fig. 2.14b by the reduction of *Vs** along the soil profile, providing some information on the nonlinear effects, which are not homogeneous in depth. The average shear wave velocities obtained are 242 m/s and 197 m/s for weak and strong motions, respectively.

a–v*/Vs** curves for all centrifuge data, i.e. all containers, all depth measurements, all levels of excitation, all trials and the two vertical lines of sensors, are shown in Figure 2.15a, along with the strain-*v*/Vs** curves (Fig. 2.15b).

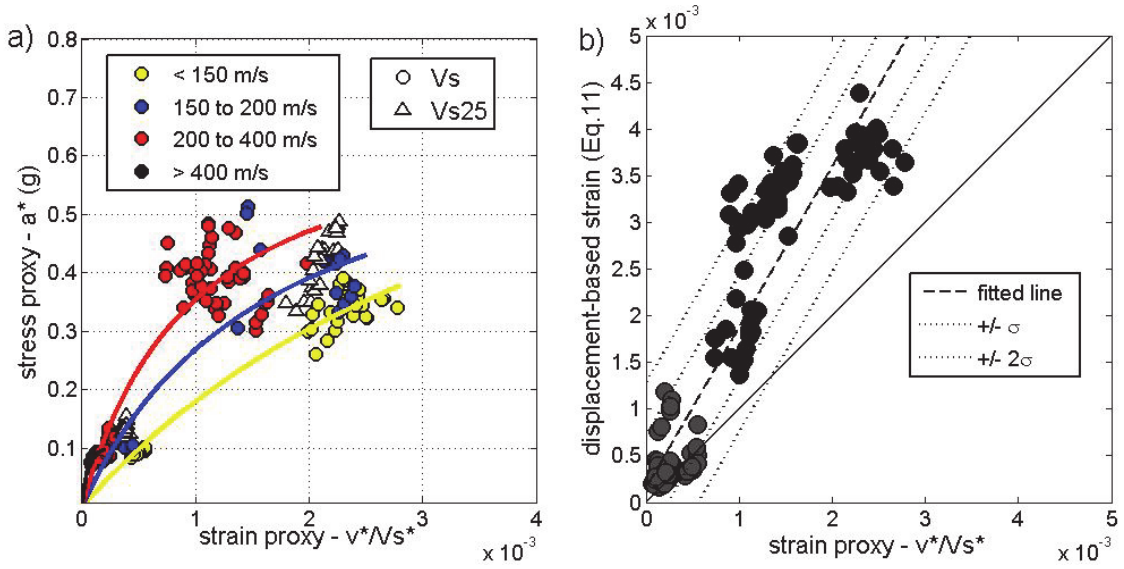

Figure 2.15. (a). Centrifuge test: nonlinear behavior using a*–v*/Vs* representation as a stress-strain proxy. Data are taken from all soil type analysis results. The solid line represents nonlinear regression for observed data (see Tab. 2.5); (b). Comparison between v*/Vs* as a strain proxy and percentage deformation (strain) extracted from centrifuge data. The grey circles are the weak event data and the black circles are the strong event data.

Different classes of soil are considered, grouped according to *Vs**, ranging from less than 150m/s (softer soil) to more than 400m/s (stiffer soil). These ranges are different from those of the synthetic data since depth is shallower. We observe the evolution of soil behavior as a function of seismic input motion. Again, it is evident that for the lower velocity group, higher strains are observed, i.e. higher nonlinearity, and for the higher velocity group, lesser nonlinear behavior is observed.

The values of coefficients *a* and *b* of Eq. 2.8 for centrifuge data can be found in Tab. 2.5, along with the correlation coefficient *R* and residuals values. Our experimental data have lower values of *R* compared with synthetic results, due to the experimental dispersion of results, but correlation remains good nonetheless.

Table 2.5. The same as Tab. 2.2, for centrifuge data

	Velocity Group			
	< 150 m/s	150-200 m/s	200-400 m/s	> 400 m/s
a (x 10^3)	0.2205	0.4289	0.7118	2.5072
b	0.9748	0.7188	0.7042	0.1223
R	0.9776	0.8218	0.8857	0.7819
res	0.0171	0.0553	0.0406	0.0035
b/a (x 10^{-3})	4.4206	1.6761	0.9894	0.0488

Compared to the average velocity value Vs_{25} (since we have a soil depth of just 25m), *PGA-PGV/*Vs_{25} fits our nonlinear curve ranges and shows an average value of the strain proxy, useful for practical issues (Fig. 2.7a). Our Vs_{25} values range from 194 m/s to 242 m/s with an average value of 217 m/s. Figure 2.15b compares the strain proxies extracted from the value of *PGV/Vs* with the deformation extracted from Eq. 2.5. Our data provide a good fit between the range of +/- sigma. This figure offers further confirmation of effectiveness of *PGV/Vs* as a strain proxy. Validation of this representation on centrifuge results shows that *PGA-PGV/Vs* can be used for predicting the stress-strain relationship of soils as discussed in the following sub-section.

Applying the same hyperbolic model to our Vs_{25} data, we get the *a* value of 0.412 10^3 and *b* value of 0.820, giving the *b/a* value of 1.991 10^{-3}. Li et al. (2013) tested the same Fontainebleau sand and they proposed equations to find the corresponding confining pressure as written in equation 2.11 and 2.12.

$$K_0 = -\frac{1}{2.9}D_r + 0.63 \tag{2.11}$$

$$\sigma_c = \frac{(1 + 2K_0)\gamma_d z}{3} \tag{2.12}$$

where K_0 is the lateral soil pressure coefficient at rest, D_r is the soil relative density, σ_c is the confining pressure, γ_d is the soil weight, and z is the depth which equal to 12.5m in our case of Vs_{25}. Using values in Tab. 2.4, our confining pressure is 120 kPa and we report on Fig. 2.16 our model compared to Delfose-Ribay et al. (2004) and Li et al. (2013) results for

Fontainebleau sand, with confining pressure of 100 kPa and 117 kPa, respectively. Be reminded that our shear strain is the scaled PGV/V_{s25} value. Our results are comparable to the data corresponding to 117 kPa, let us assume the PGV/Vs or PGV/Vs_{30} as a relevant proxy for assessing or predicting the soil strain.

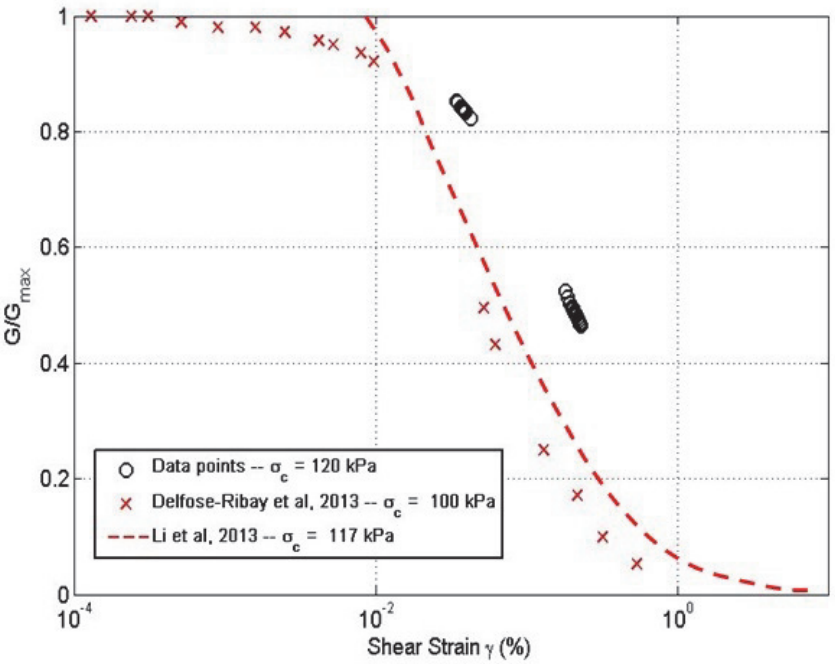

Figure 2.16. Shear degradation modulus computed from Eq. 2.6, for soil depth of 25m using γ proxy (PGV/Vs_{25}) and γ_{ref} (a/b) value from hyperbolic model fitted to the centrifuge data, compared with other references having similar confining pressure. σ_c is calculated from Eq.2.11-2.12.

2.5. Soil Nonlinearity Prediction: Application to the Japanese K-NET and KiK-net Data

We apply our nonlinear proxy to the Japanese K-NET and KiK-net Data. Japan is a high seismicity area having a quality digital data that are recorded and made available to the scientific community. After the destructive 1995 Kobe earthquake, Japanese scientists installed dense and uniform networks that cover the whole of Japan, among them the KiK-net and K-NET strong motion networks (Okada et al., 2004). The two networks were deployed in two different geomorphological contexts, the K-NET stations were mainly constructed on sedimentary sites, and the KiK-net stations are on weathered rock or on thinner sediment

sites. Thus, on average, the site conditions of KiK-net are harder than those of K-NET (Aoi et al., 2004). One advantage of the Japanese network is that the site characterization was performed homogeneously (downhole measures). For the K-NET network the surveys were made down to 20 m in depth, the Vs_{30} is then extrapolated (Boore et al., 2011). In the case of the KiK-net network, with the sites characterized by velocity profiles ranging from 30 to 200 m, Vs_{30} was directly computed from them. In addition, the KiK-net network offers the advantage of combining pairs of sensors (one at the surface and one installed at depth in a borehole). In the present study, the KiK-net and K-NET strong-motion records were collected up to the end of 2009. For both networks, only data with a *PGA* larger than 0.01 m/s2 are retained with no conditions on distance and magnitude. For more details on the data processing see the papers by Regnier et al. (2013) and Laurendeau et al. (2013).

The accelerograms were processed following the procedure depicted by Boore (2005) in order to integrate to reliable velocity and displacement time histories. Then the *PGV* was obtained and the strain proxy as PGV/Vs_{30}. For the KiK-net data, we also computed the strain at the middle of the layer by considering the top and bottom sensors according to Eq. 2.10. The Eurocode 8 (CEN, 2003) soil classification is considered, i.e. Class A (Vs_{30} > 800m/s), Class B (Vs_{30} of 360 to 800 m/s), Class C (Vs_{30} of 180 to 360 m/s), and Class D (Vs_{30} < 180 m/s).

Figure 2.17-2.18 show the $PGA–PGV/Vs_{30}$ for each class of soil class as well as the corresponding hyperbolic model for K-NET and KiK-net data, respectively. We found similar results as with centrifuge and numerical modeling, i.e. our proxy describes well the nonlinear response according to the site classification. For the stiffer soils (Classes A and B), the nonlinear behavior appears for high value of *PGA* (or stress) corresponding to low PGV/Vs_{30} (strain) values, while for soft soil (Classes C and D), the nonlinear behavior starts at very early stage on the stress-strain curve. In addition, the K-NET data may be more non-linear than the KiK-net data in agreement with the site conditions discussed by Aoi et al. (2004). This observation should be confirmed in the future with more specific comparison

The values of coefficients a and b along with the correlation coefficient R and residuals values for the hyperbolic model of Eq. 2.9 for K-NET and KiK-net data can be found Tab. 2.6 and 2.7, respectively.

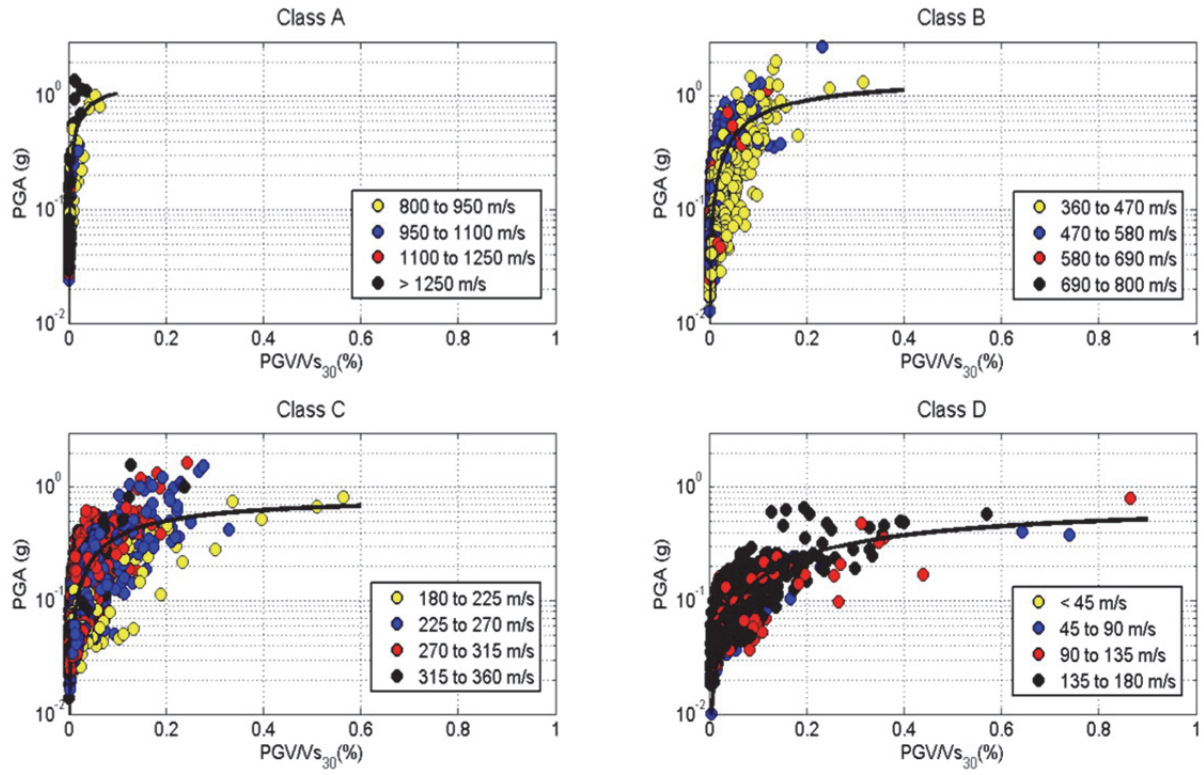

Figure 2.17. Nonlinear behavior of Japanese sites according to the EC8 site classification, using *PGA–PGV/Vs30* as the stress-strain proxy for K-NET data. The solid lines represent the hyperbolic model for each class given by Eq. 2.9 and corresponding to the values of Tab. 2.6.

Table 2.6. The same as Tab. 2.2, for K-NET data and according to the EC8 site classification

	Eurocode 8 Soil Group			
	Class A (> 800 m/s)	Class B (360-800 m/s)	Class C (360-800 m/s)	Class D (< 180 m/s)
a ($x10^3$)	4.7572	1.1931	0.6363	0.1874
b	1.3422	1.4790	0.8306	0.7534
R	0.7511	0.7892	0.7488	0.7940
res	0.0068	0.0164	0.0110	0.0089
b/a ($x10^{-3}$)	0.2821	1.2396	1.3053	4.0203

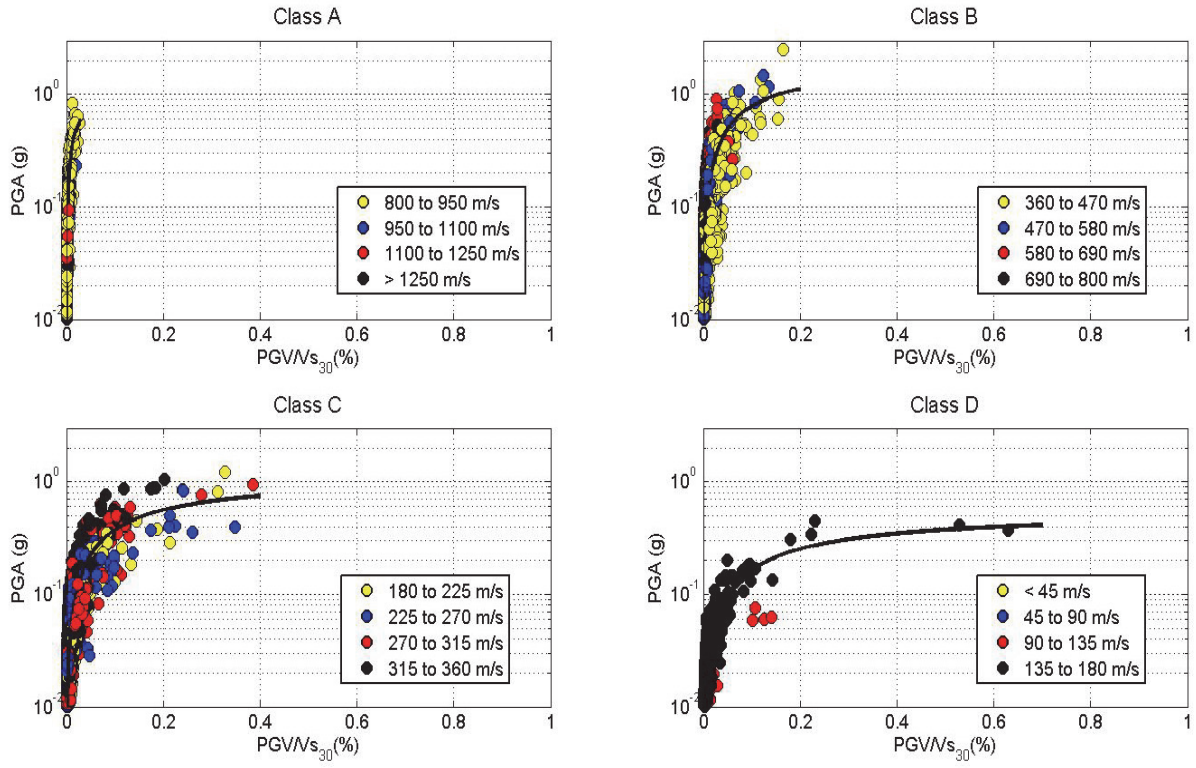

Figure 2.18. Nonlinear behavior of Japanese sites according to the EC8 site classification, using *PGA–PGV/Vs30* as the stress-strain proxy for KiK-net data. The solid lines represent the hyperbolic model for each class given by Eq. 2.9 and corresponding to the values of Tab. 2.7.

Table 2.7. The same as Tab. 2.2, for KiK-net data and according to the EC8 site classification

	Eurocode 8 Soil Group			
	Class A (> 800 m/s)	Class B (360-800 m/s)	Class C (360-800 m/s)	Class D (< 180 m/s)
a ($x10^3$)	4.2131	1.3041	0.5542	0.2326
b	1.1364	1.9475	1.1317	0.5522
R	0.9043	0.8375	0.8583	0.9102
res	0.0046	0.0075	0.0064	0.0048
b/a ($x10^{-3}$)	0.2697	1.4934	2.0420	2.3740

Figure 2.19 represents for the KiK-net data the correlation between the strain and the *PGV/Vs* proxy of strain, considering the Vs_{30} and the Vs_0 as *Vs*. The reason of considering Vs_0 is because the sensor is located at the top of the soil column, and then the *PGV* is obtained at the top rather than at 30m depth. We observe a good correlation between strain and *PGV/Vs*, the two values of Vs providing similar trends. Of course, because of an increase of *Vs* in depth, PGV/Vs_0 is higher than PGV/Vs_{30} (2.20b) leading to a better coefficient of correlation for *Vs30*. This tends to confirm the nonlinear strain is representative of the 30-meter depth rather by only the uppermost soft layer. This conclusion should be confirmed in further studies.

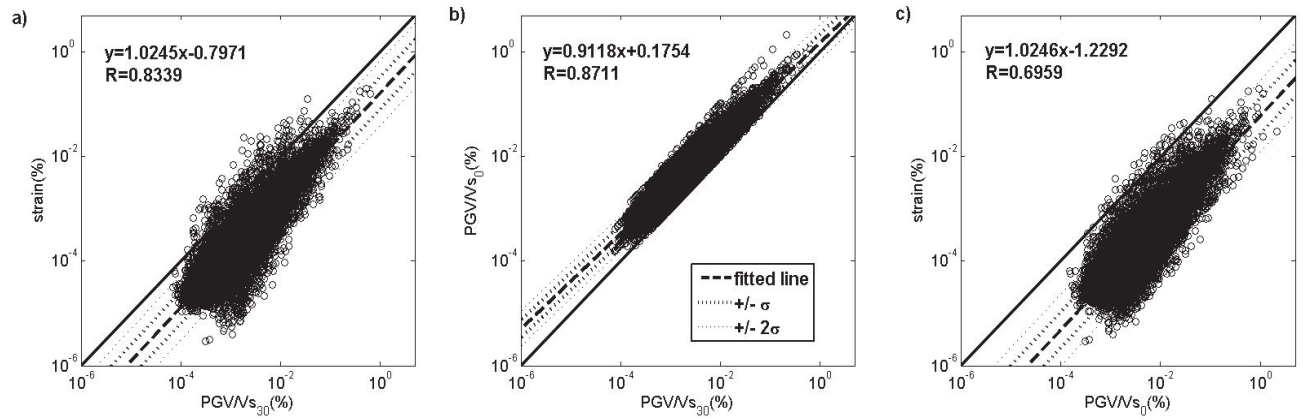

Figure 2.19. Comparison of the strain and the *PGV/Vs* proxy of strain computed for the KiK-net data. a) Strain vs PGV/Vs_{30}; b) PGV/Vs_0 vs PGV/Vs_{30}; c) Strain vs PGV/Vs_0. The strain is computed as the difference of the top and the bottom displacement divided by the distance between the two sensors (Eq. 2.9).

2.6. Conclusion and Perspectives

Near-surface geology effects, particularly soil nonlinear response, are key issues related to ground motion hazards. This nonlinear response depends on the soil properties and excitation variations over time, one of the most crucial being asymmetric cyclic loading (i.e. earthquake motion). Nonlinear behavior is characterized by alteration of the shear wave velocity *Vs* related to shear modulus *G* and damping ζ during excitation, representative of different types of soil and it is usually difficult to assess or predict the nonlinear response on site. In this paper we propose a strain proxy of soil based on v^*/Vs^* coefficient and represented according to the a^* values.

First, we use seismic interferometry by deconvolution to extract the seismic response of our systems using equivalent linear shear wave velocity Vs^*. The Vs^* and proxy were first validated by numerical modeling, using Ricker-like signals and more realistic accelerograms. We observe a fairly good correlation between the estimated and initial Vs^* profiles, allowing depth assessment along the soil profile. The proxy also gives a good estimation with respect to the strain provided by modeling. Even though the proxy does not give a direct estimation of strain, it provides an approximation of strain variation with respect to excitation, offering a good means of estimating nonlinearity. We also note that PGV/Vs_{30} related to the site classification found in the seismic code gives also a good estimate of nonlinearity.

This observation is further confirmed by experimental data of dynamic centrifuge tests. These tests enable the creation of a scaled-down model that can reproduce actual object behavior by applying gravity acceleration fields and preserving the initial stress-strain conditions of the soil thanks to the equivalent-shear-beam box. We observe similar phenomena with synthetic results for shear wave velocity and nonlinear representation. The comparison with the Vs_{25} proxy confirms the practical advantage of using Vs_{30} (or Vs_{25} in our case).

We built the nonlinear two-parameter hyperbolic model and compute the γ_{ref} of our soil model by inverting our data. This finding is then applied to Japanese K-NET and KiK-net data. The Vs_{30} related to Eurocode 8 site classification is chosen for practical reason of engineering code. We show that only by knowing the site classification, we are able to assess and then to predict the nonlinear behavior corresponds to a specific soil. If the correct parameter was incorporated to the hyperbolic model, we could define the shear degradation modulus and damping ratio for specific soil, thus it could be incorporated furthermore in the ground motion prediction equation. This would be the scope of further studies.

This page intentionally left blank

Chapter 3

In-situ Assessment of the G-γ Curve for Characterizing the Nonlinear Response of Soil: Application to the Garner Valley Downhole Array (GVDA) and the Wildlife Liquefaction Array (WLA)

Johanes CHANDRA, Philippe GUEGUEN, Jamison H. STEIDL, Luis Fabian BONILLA

From a submitted paper to the Bulletin of the Seismological Society of America (In review)

Summary

In this chapter, we analyze the nonlinear and near-surface geological effects of two NEES@UCSB instrumented sites, i.e. Garner Valley Downhole Array (GVDA) and the Wildlife Liquefaction Array (WLA). The seismic interferometry by deconvolution method is applied to earthquake data recorded by the multi-sensor vertical array between January 2005 and September 2013. Along the cross-section, local shear wave velocity is extracted by estimating travel time between the surface and the bottom, and also between each sensor. The S-wave velocity profiles are constructed and compared with classical in-situ geophysical surveys. We show that velocity values change according to amplitude of the the ground motion and we find anisotropy between EW and NS directions between different levels at the GVDA site. A v^*/Vs^* ratio between peak particle velocity v^* and equivalent linear S-wave velocity Vs^* between each sensor is then tested as a deformation proxy, and the a^*-v^*/Vs^* plot is displayed as the stress-strain curve for observing the nonlinear response of the sites under different levels of excitation, where v^* is the peak particle acceleration. Nonlinearity is observed from quite low shear strain levels ($\sim 10^{-6}$) and a classic hyperbolic model is derived from the data. Magnitude and maximum acceleration are shown not to be the only parameters governing nonlinearity and V^*/Vs^* (and similarly PGV/VS_{30}) proves to be a good deformation proxy. Finally, the shear modulus degradation curves are constructed for each depth and test site, and they are similar to previous laboratory measurements or in-situ geophysical surveys.

3.1. Introduction

The effects of near-surface geology has been documented for many previous earthquakes such as the 1985 Michohacan earthquake (e.g., Campillo et al., 1989; Chávez-Garcia and Bard, 1994), the 1989 Loma Prieta, California earthquake (Chin and Aki, 1991; Rubinstein and Beroza, 2004), or the 1994 Northridge, California earthquake (Field et al., 1997; Beresnev, et al., 1998; Hartzell, 1998). One consequence is the amplification of seismic ground motion in sedimentary sites compared to rock sites, which normally has the maximum amplification at the fundamental frequency, the f_0 of the soil column. Under a 1D assumption, f_0 of a sedimentary layer overlaying stiff bedrock depends on the shear wave velocity, *Vs*, and the thickness, *H*, of the layer, and is often approximated by $f_0=Vs/4H$. For strong ground motion, nonlinear soil response may occur. In this case, the soil response depends on the strength of the material and the strain induced by the incoming wavefield. Many authors have reported observations of nonlinear response by examining changes in f_0 (e.g., Beresnev and Wen, 1996; Bonilla et al., 2003; Tsuda and Steidl, 2006; Wu et al., 2009), the variation of mode shape (Guéguen et al., 2011), or reduction of amplification of the sediment response (Assimaki et al., 2006). This nonlinear response is mainly driven by the strain-dependent dynamic parameters of the soil, i.e. shear modulus *G* and damping D. Variations in these parameters is the consequence of the increase in shear strain related to the increase in shear stress that occurs during strong shaking. *G* is related to shear stress τ and shear deformation γ according to the classical formula: $\tau = G(\gamma) \times \gamma$. For the largest deformation expected during strong ground motion, degradation of shear modulus is observed as damping increases. Assuming constant density, ρ, this implies that shear wave velocity, *Vs*, decreases with the reduction in shear modulus, G, through the relation:

$$Vs = \sqrt{G/\rho} \tag{3.1}$$

For earthquake engineering applications involving soil nonlinearity, the site is generally characterized by establishing the *G*-γ curve, using data from cyclic laboratory tests that are performed on samples collected in-situ. Based on laboratory tests (Fig 1.4), Vucetic (1994) distinguished two different shear strain thresholds related to soil nonlinearity: linear cyclic γ_{tl} and volumetric γ_{tv} shear strains. For $\gamma < \gamma_{tl}$ the soil behaves in a linear manner, for $\gamma_{tl} < \gamma < \gamma_{tv}$, the soil exhibits nonlinear elastic behavior with negligible permanent deformation, and for $\gamma >$

γ_{tv}, the soil shows hysteretic nonlinear behavior with major permanent deformation. The order of magnitude of γ_{tv} is around 10^{-4} (Hardin and Black, 1968; Drnevich and Richart, 1970; Dobry and Ladd, 1980) or $2x10^{-4}$ (Youd, 1972; Vucetic, 1994). Johnson and Jia (2005), using compressional waves reported ε_{tl} around 10^{-7} to $5x10^{-6}$ associated with a Young's modulus degradation of 5% at a strain level of 10^{-6}. Furthermore, Vucetic (1994) observed a PI (plasticity index) dependence on γ_{tl} starting around $5x10^{-6}$. Because of the lack of *in-situ* data covering wide range of strain levels for assessing the *G-γ* curve, the significance of laboratory tests compared with *in-situ* conditions is seldom discussed. Due to the high cost of collecting in-situ vertical array data combined with the time between significant earthquakes, there is a paucity of in-situ data to compare with laboratory tests. Moreover, the competing effects of ground motion amplification due to the presence of different impedance contrasts at different depths and ground motion deamplification due to near-surface nonlinearity, induces further complexity (Archuleta et al., 1992; Bonilla et al., 2011).

An effective solution for observing *in-situ* nonlinear response consists in measuring the shear wave velocity variation under different levels of excitation (Haskell, 1953; Ohmachi et al., 2011; Dobry, 2013). Using a vertical array having a series of accelerometers located at different depths, the measurement of the wave's arrival time provides an estimation of *Vs*, assuming the soil column undergoes shear deformation. The classical methods to compute these velocities use cross-correlation analysis (Rubinstein and Beroza, 2004; Rubinstein and Beroza, 2005) and cross-spectral analysis (Coutant, 1996). Recently, the seismic interferometry by deconvolution method has been successfully applied (Mehta et al., 2007, Sawazaki et al., 2009; Nakata and Snieder, 2012; Pech et al., 2012) to detect very small changes in velocity. In addition, the representation of soil nonlinearity by the *G-γ* curve also relies on the measurement of deformation directly estimated by instantaneous relative displacement along the borehole (e.g. Zeghal and Elgamal, 1994).

This study aims to test the efficiency of the seismic interferometry by deconvolution method to assess of the nonlinear response of a site, applied to the Garner Valley (GVDA) and the Wildlife (WLA) test sites, at moderate or strong strain levels. For that, a proxy of the stress-strain relationships is proposed by computing the ratio between the maximum average particle velocity and the equivalent-linear shear wave velocity, as used for example by Hill et al. (1993) and Idriss (2011) and validated on synthetic results and centrifuge tests by Chandra et

al. (2014). The description of the GVDA and WLA test sites and the data selection criteria used in this study are presented in the first part. The seismic interferometry by deconvolution method is then applied to the vertical arrays, and the shear wave velocity (*Vs*) profiles are obtained, along with the variation of *Vs* with respect to the level of shaking. Finally, the stress-strain relationship is acquired through the wave-based nonlinear proxy *PGV/Vs* for strain, and the *in-situ* nonlinear response is discussed in the last part.

3.2. The NEES@UCSB GVDA and WLA Test Sites

The Garner Valley Downhole Array (GVDA) and the Wildlife Liquefaction Array (WLA) are part of the George E. Brown Jr. Network for Earthquake Engineering Simulation (NEES) operated by the University of California, Santa Barbara (UCSB), USA. The GVDA test site (33°40.127'N, 116°40.427'W) is situated in a narrow valley within the Peninsular Ranges batholith, 23km east of Hemet and 20km south-west of Palm Springs, California. It is located 7km and 35km from the San Jacinto Fault (SJF) and the San Andreas Fault (SAF), respectively. The SJF is historically the most active strike-slip fault in the SAF system, with a slip rate of ~10 mm/year, and the southern SAF is an active fault with a slip rate of ~25 mm/year.

Figure 3.1. Test site location (source: https://www.google.com/maps/, last consulted on February 28th, 2014)

The WLA test site (33°05.843'N, 115°31.827'W) is situated in California's Imperial Valley on the west bank of the Alamo River, 13km north of Brawley and 160km east of San Diego. It is located south-east of the southernmost terminus of the SAF. For more extensive details on these sites, readers are referred to Youd et al (2004), Steidl and Seale (2010), Steidl et al (2012), Steidl et al (2014), and the NEES@UCSB website (http://nees.ucsb.edu/ last consulted in March 3, 2014).

The GVDA near-surface geological conditions consist of soft alluvial lake deposits to a depth of 18-25 meters overlaying weathered granite (Fig. 3.2a). The cross-section of GVDA shows multiple impedance contrasts at several depths, resulting in a complex amplification of ground motion. The fundament frequency is found to be around 1.7Hz (Archuleta et al., 1992; Theodulidis et al., 1996; Steidl et al., 1996; Bonilla et al., 2002) and several higher resonance frequencies exist at 3, 6, 8 and 12Hz. According to Pecker (1995) and Bonilla et al. (2002), we assumed a 1D model of the site. Furthermore, Coutant (1996) detected velocity anisotropy in the shallow layers, confirming the complexity of the site in terms of seismic response. In-situ surveys have been performed, providing an extensive description of the site in terms of geotechnical and geophysical characteristics (Pecker and Mohammadioun, 1991; Archuleta et al., 1992; Gariel et al., 1993; Pecker, 1995; Steidl et al., 1998; Youd et al., 2004; NEES@UCSB website). The shear-wave velocity ranges from 90m/s in the uppermost layer to 3,500m/s at the bottom (500m depth). Furthermore, Stokoe and Darendeli (1998) performed laboratory tests to extract the G-γ curve of the surficial sediments; these results will be used as a reference for our analysis. Moreover, Lawrence et al. (2008) studied the nonlinear response of GVDA using induced vibration with acceleration of more than 1g. By inverting the dispersion curves, they observed the greatest change in S-wave velocity nearest the surface (up to a depth of 4m) related to the nonlinear response of the uppermost layers. Since its installation in 1989, GVDA's instrumentation has been upgraded and enhanced several times (Steidl et al., 2012). In this paper, we consider data recorded using the most recent configuration, which was updated in 2004. The seismic vertical array consists of seven accelerometers located at GL-0m (GL: ground level) and at GL-6m, GL-15m, GL-22m, GL-50m, GL-150m and GL-501m. Data from these accelerometers is collected using continuous data acquisition at 200sps (samples per second), transmitted back to UCSB in real-time, and archived.

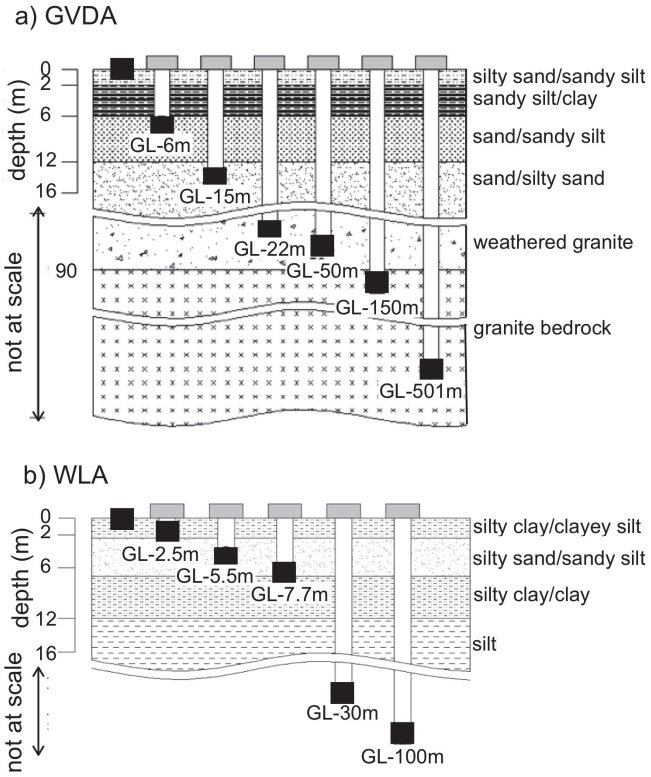

Figure 3.2. Geotechnical cross-section of the GVDA (a) and WLA (b) test sites, including the position of the accelerometers used in this study (black squares).

The WLA test site was first instrumented in 1982. The near surface geology of this site consists of a layer of saturated silty sand of around 2-7m in-between silty clay layers (Fig. 3.2b). The presence of the sandy layer in addition to a shallow water table at around 1.2m render the site liquefiable, as observed from field evidence during regional earthquakes (e.g., 1979 Imperial Valley earthquake, M_w=6.5; 1981 Westmorland earthquake, M_w=5.9), and from instrumental evidence of liquefaction or strain hardening (Bonilla et al., 2005) during the 1987 Superstition Hills M_w=6.6 earthquake. No observations at bedrock are available at this site due to the thickness of the Imperial Valley sedimentary basin. In 2002, 20 years after the site was first instrumented, the original sensors had failed and the datalogger had become obsolete. New instrumentation was deployed, 65m north of the original site under the NEES program in 2004 is now operated by UCSB. The current vertical array, used in this study, is composed of six accelerometers at GL-0m, GL-2.5m, GL-5.5m, GL-7.7m, GL-30m and GL-100 m (Fig 3.2b). Information from geophysical surveys has been reported by Cox (2006) providing shear-wave velocity ranging from 100m/s at the surface to 300m/s at the bottom (100m depth).

In total, data from 5,080 events with magnitudes ranging from $1.0 \leq M_L \leq 5.5$ were recorded during the period from January 2005 to September 2013 from GVDA test site and data from 8,515 events with magnitudes ranging from $1.0 \leq M_L \leq 5.5$ were collected from WLA test site during the same period. Hypocentral distances vary from 1 to 100km. The recorded data are mostly from weak to moderate events, with Peak Ground Acceleration (PGA) of 0.12g and 0.30g for GVDA and WLA, respectively. For all of the events used in this study, the observed pore pressure data showed that liquefaction has not occurred.

3.3. Deconvolution Method

The seismic interferometry by deconvolution method is applied to the selected data for the assessment of shear wave velocity. Seismic interferometry obtains the Green's function by cross-correlating the seismic motion between different receivers, thus removing the propagation from the source to the first receiver (Wapenaar et al., 2010). Instead of using single cross-correlation, Snieder and Şafak (2006) proposed the seismic interferometry by deconvolution method for application to buildings assuming a 1D shear model (see Chapter 1.3). By deconvolving these waves, the causal and acausal propagation of wave within the system is obtained as well as a better estimation of the arrival times and amplitudes (Clayton and Wiggins, 1976). Depending on the frequency content of the signal, in some cases a mixture of upward and downward deconvolved waves is unavoidable in the uppermost layers. Assuming the soil to be a shear deformation system, several authors (Mehta et al., 2007; Nakata and Snieder, 2012, Pech et al., 2012) have applied this method to vertical soil profiles to extract the shear wave velocity. They monitored small variations of *Vs* related to environmental changes or seismic shaking. In Chapter 2, we also applied this method to extract the soil response on centrifuge testing.

We deconvolved each earthquake record along the soil profile in depth with the GL-0m record. The response of the deconvolved waves $D_{i\text{-}0m}(\omega)$ is computed as:

$$D_{i-0m}(\omega) = \frac{A_i(\omega)A_{0m}^*(\omega)}{|A_{0m}(\omega)|^2 + \varepsilon} \tag{3.2}$$

where $A_i(\omega)$ is the i^{th} wavefield in the frequency domain recorded at receiver i, $A_{om}(\omega)$ is the reference signal at GL-0m, ω is the angular frequency, * is the complex conjugate symbol, and ε (set at 10% of the average spectral power) is the stabilization parameter to avoid instability caused by deconvolution (Clayton and Wiggins, 1976). Having computed the response, travel time between each receiver, Δt, is obtained by the inverse Fourier transformation of $D_{i\text{-}0m}(\omega)$ and the equivalent linear shear wave velocity Vs* is obtained as $V_s^* = \Delta h/\Delta t$, where Δh is the distance between receivers.

3.4. Data Processing

An initial data selection is made from the GVDA and WLA databases, taking only events recorded at all accelerometers in the two horizontal directions (EW and NS) with a signal-to-noise (S/N) ratio greater than 3 for frequency bands between 0.1 and the Shannon frequency (i.e., 100Hz). These criteria give 401 and 1,066 recordings at GVDA and 7,146 and 6,864 recordings at WLA for the EW and NS directions, respectively. The data has been rotated to true north direction by the standard NEES@UCSB processing procedures, for the borehole sensors that are not already aligned to north (GVDA sensors GL-6, GL-15, GL-22, GL-50). We use the complete records collected from the NEES@UCSB database, including P- and S-waves without applying magnitude criteria, the time window varying from 72 seconds to 252 seconds, depending on the original data available at the NEES@UCSB website. Before deconvolution, the mean and trend of the data were removed, we applied a 5% Tukey tapering function and zero-padding was applied up to 2^{16} samples. Finally, we applied a 3-order Butterworth filter between 0.5 – 10Hz and 0.5 – 20Hz for GVDA and WLA, respectively, which is large enough to ensure accurate travel time estimation (Todorovska and Rahmani, 2013) and covers the fundamental frequency of the sites. Having computed the deconvolution, the inverse Fourier Transform of the $D_{i\text{-}0m}$ (Eq.3.2) is resampled eighty times to increase the accuracy of the travel time picking using a polyphase implementation. By doing this we are able to increase the sample rate by eighty times for the same length of signal. We use the complete record collected from the NEES database, thus the time window varying from 72 seconds to 252 seconds, depending on the events.

Three typical examples of deconvolved waves are shown in Figure 3.3, corresponding to three earthquakes recorded at GVDA in the east-west direction: (a) a weak earthquake (June 9, 2006, M_L=1.24 and R = 23.88 km); (b) a moderate earthquake (February 9, 2007, M_L=4.73 and R = 74.8 km); and (c) the strongest earthquake (July 7, 2010, M_L=5.43 and R = 32.53 km).

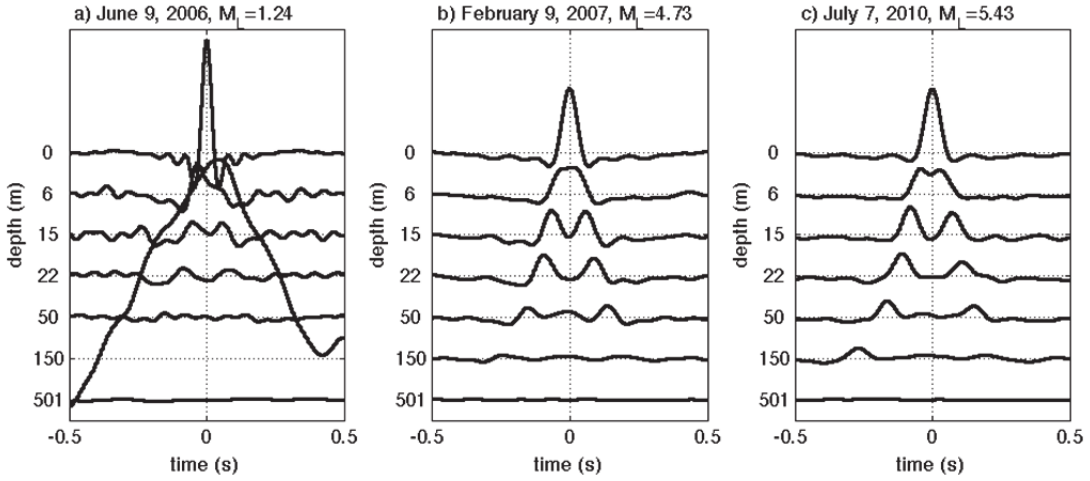

Figure 3.3. Three typical examples of interferograms of deconvolved waves for GVDA east-west data recorded at GL-0m, GL-6m, GL-15m, GL-22m, GL-50m, GL-150m and GL-501m. (a) June 9, 2006 M_L 1.24, R = 23.88 earthquake. (b) February 9, 2007 M_L 4.73, R = 74.8km earthquake. (c) July 7, 2010 M_L 5.43, R = 32.53km earthquake.

For the first event (Fig. 3.3a), the deconvolved data at GL-150m resulted on an erroneous estimation of Vs^* at this level due to sensor malfunction. For the second and third events (Fig. 3.3b and 3.3c), we obtain clear traveling waves and the shear fundamental mode. Interferometry by deconvolution produces a virtual source that excites the system at *t=0* (Snieder and Şafak, 2006), causal and acausal waves referring to the waves in the positive and negative times, respectively. The waveforms in Figure 3.3b and 3.3c are almost symmetric in time and, as shown by Nakata and Snieder (2012), the estimated velocity in the positive or negative parts provides similar values. However, to avoid attenuation in the downward waves, we estimate the equivalent linear velocity from the upward wave in the negative time by automatic picking of arrival times applied to the GVDA and WLA event databases. For the second event (Fig. 3.3b), because the upward and downward waves overlap in the uppermost layer, we cannot pick their arrival accurately. For the third event (Fig. 3.3c), the wave arrival

time cannot be picked accurately at the bottom (GL-501m) where some technical issues related to the instrumentation was occurred, thus this sensor is removed from our analysis. These three cases are also found for WLA recordings, and a second selection of data is then applied to both GVDA and WLA data for automatic computation of *Vs*.

In order to limit the artificial time-delay or the picking inaccuracy due to the lack of separation between the upward and downward waves at close sensor spacing near the surface, the GL-6m sensor at GVDA and the GL-2.5m and GL-5.5m sensors at WLA are not used in our analysis. The GL-501m sensor at GVDA is also not used as previously mentioned, and the analysis focuses on the uppermost layers between the GL-0m and GL-150m sensors at GVDA and GL-0m and GL-100m sensors at WLA. The resulting usable GVDA and WLA event databases considered in this study correspond to 368 EW and 956 NS events, and 6,461 EW and 6,012 NS events, respectively (Fig. 4). In Fig. 4 the data truncated at lower magnitude are the result of the pre-selection carried out by NEES@UCSB in order to consider the most relevant ground motion for earthquake and geotechnical engineering applications. This truncation is due to the fact that the NEES@UCSB team does not segment out events from the continuous data when the magnitude is small and the distance is large, as the signal-to-noise ratio is assumed to be insufficient.

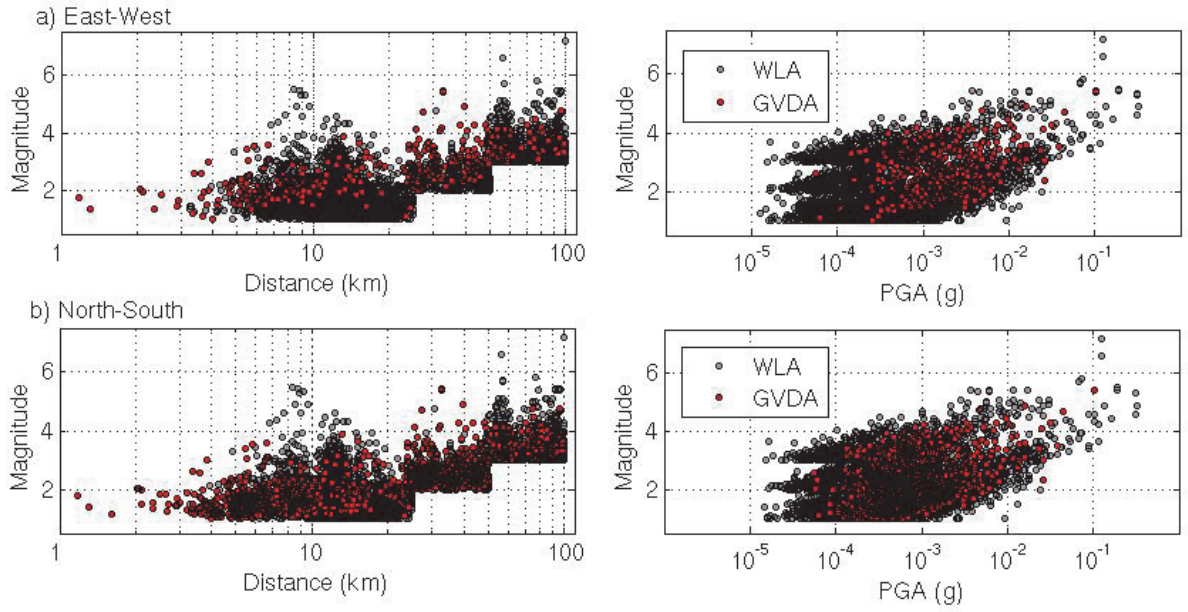

Figure 3.4. Distribution of the data selected for this study displayed as function of magnitude and distance (left) and magnitude and PGA (right) in the (a) EW and (b) NS components.

3.5. Velocity Profile and Site Anisotropy

The seismic interferometry by deconvolution process is applied to the overall dataset selected for NS and EW recordings and the velocity profiles for GVDA and WLA are shown (Fig. 3.5) considering east-west and north-south directions separately. The results are compared with reference velocity profiles proposed by Stellar (1996) at GVDA and Cox (2006) at WLA. In our case, *Vs** is computed between two GL sensors, smoothing the velocity contrasts found by Stellar. (1996) and Cox (2006). This is why we also show (Fig. 3.5) the average *Vs* profile (called *avg.*) derived from the references, assuming constant *Vs* between each GL sensors.

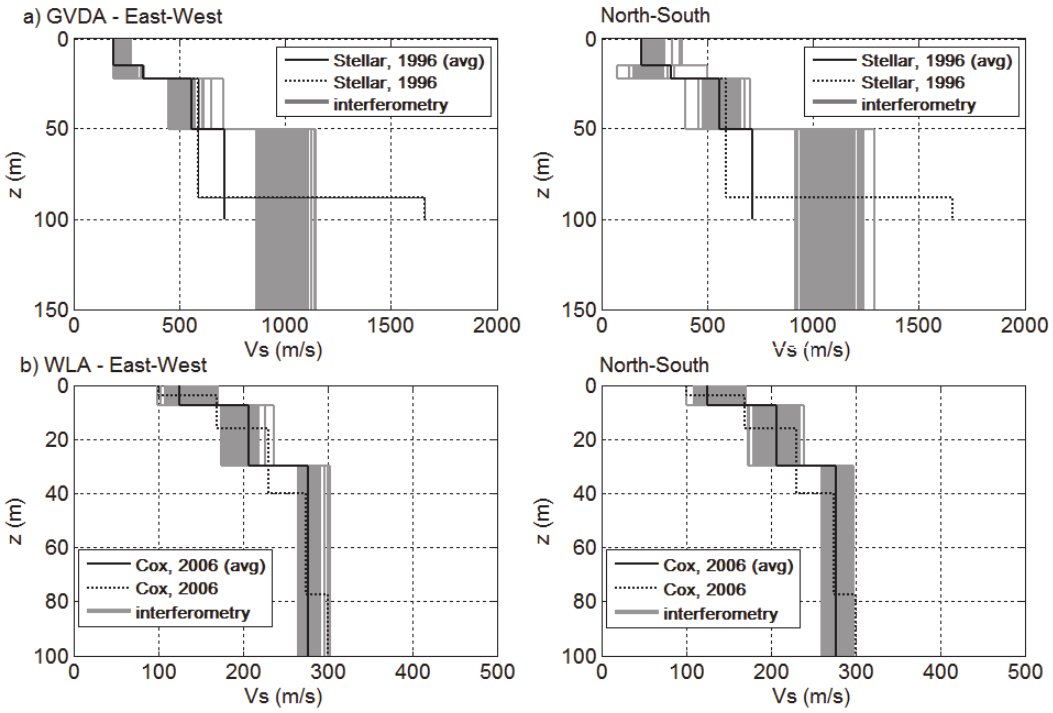

Figure 3.5. Velocity profiles computed by seismic interferometry (in gray) for the GVDA (a) and WLA (b) sites using EW (left) and NS (right) horizontal recordings. Dotted black lines correspond to original velocity profiles from Stellar (1996) and Cox (2006) for the GVDA and WLA sites, respectively. Solid black lines represent their equivalent averaged velocity profiles derived from the original profile and considering the position of the GL sensors.

At GVDA (Fig. 3.5a), the results are compared with the velocity profile provided by Stellar (1996) from suspension log results. In the uppermost layers (GL-0m-GL-50m), our results provide a good match with the reference velocity profile, with *Vs** equal to 175-260m/s down

to GL-15m, around 175-500m/s down to GL-22m and 400-700 m/s between GL-22m and GL-50m. Differences are observed below GL-100m (Vs^* between 900 and 1,300 m/s) due to the interface between the weathered granite (V_s ~400-700 m/s) and crystalline bedrock (V_s ~3000 m/s) between 90-110 meters, and the lack of suspension log data beyond 94m in Stellar (1996) since the drilling encountered the crystalline bedrock. At WLA (Fig. 3.5b), our results match the reference velocity profile provided by Cox (2006) quite well, with *Vs** equal to 100-170 m/s down to GL-7.7m, around 170 -230m/s down to GL-30m and 265-300m/s between GL-30m and GL-100m.

Depending on the earthquake, *Vs** profiles show variability at the two sites and in each layer. At WLA, the variability is largest in the uppermost layers. On the contrary, the GVDA test site manifests an inverse trend, where the variability seems to be largest in the lowermost layers. Therefore, we found that our *a priori* knowledge of the nonlinear response of sites, assuming the strongest nonlinear effects near the surface of the soil column, might not manifest in all the cases. We also observe velocity anisotropy between EW and NS directions at GVDA regardless of the layer, as previously reported by Coutant (1996). In this previous study, anisotropy at GVDA is observed between GL-22m and GL-220m, and seems to persist in the upper layers (GL0-22m) despite data dispersion, thus avoiding a definitive conclusion. One possible explanation is that the fast and slow axis in the deeper layers (weathered granite and granite) had to do with the preferred fracture orientation related to the tectonic stress field. This would likely be less prevalent in the soil than in the rock, supported by our results and those of Coutant (1996). The origin of the anisotropy may also be related to the in-homogenous properties of the soil between two sensors, but as for classical geophysical and geotechnical surveys, the differences between EW and NS direction reflects different soil properties in both directions. In Figure 3.5a, below GL-50m the interferometry profile in the NS direction shows results centers on values above the reference profile at 1,000m/s while in the EW direction, velocity profiles are centered below 1,000m/s. The same observations are possible in the uppermost layers. According to Coutant (1996), the percentage of anisotropy can be computed along the GVDA and WLA profiles as the difference of travel time between both horizontal directions, expressed in velocity in our case as:

$$a(\%) = \frac{Vs^*_{NS} - Vs^*_{EW}}{Vs^*_{NS}} \tag{3.3}$$

In Fig. 3.6, anisotropy is plotted as a function of the average peak particle velocity *v** recorded by the two sensors bordering each layer and the equivalent linear shear wave velocity *Vs** computed by interferometry in each layer. As proposed by Chandra et al. (2014a), and discussed later in this paper, this ratio provides a proxy for strain and it will be used as a nonlinear criterion.

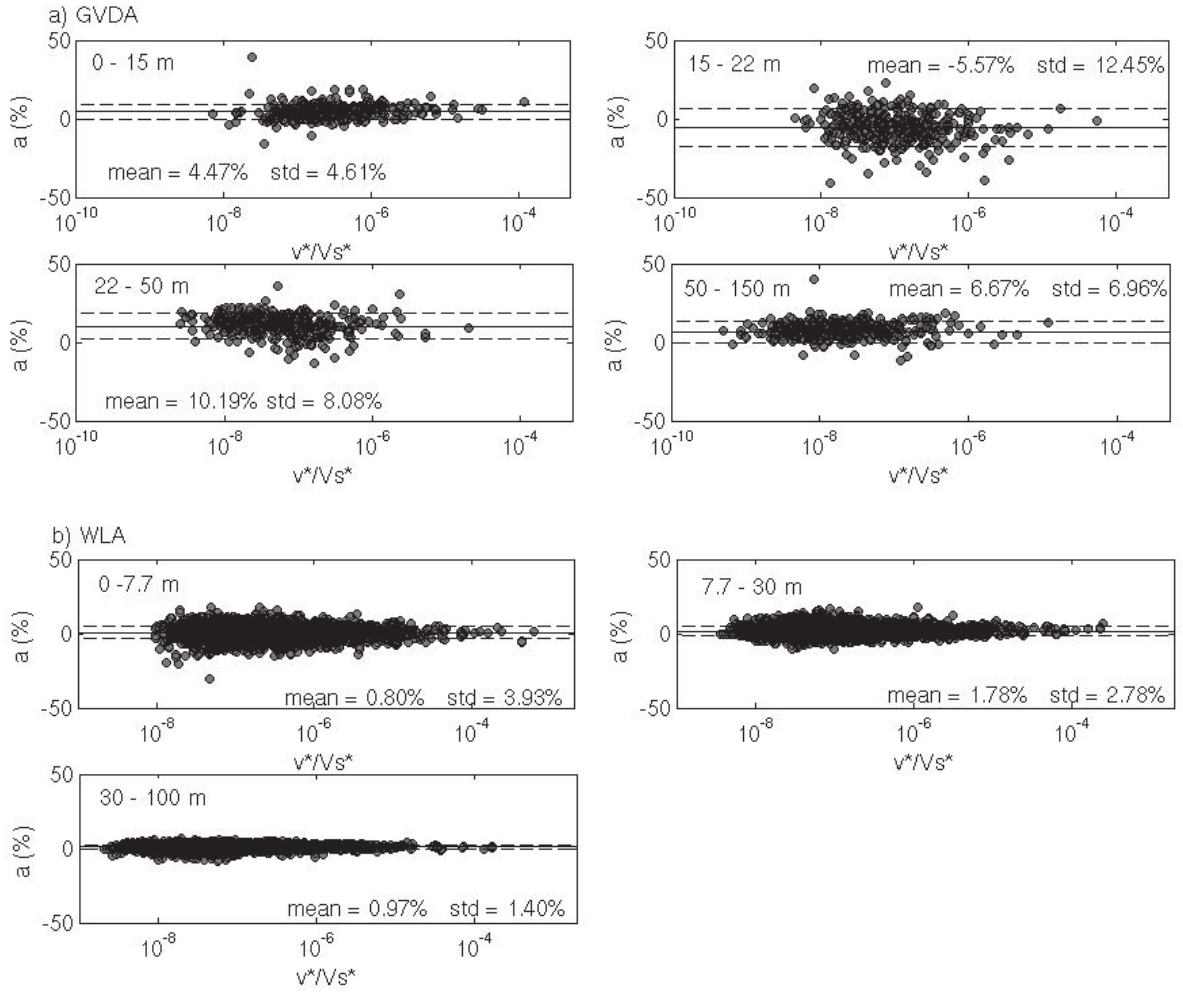

Figure 3.6. Variation of anisotropy a(%) at different depths displayed as a function of the v*/Vs* ratio at the GVDA (a) and the WLA (b) sites.

At GVDA, we observe anisotropy variations at depth (Fig. 3.6a), consistent with the values provided by Coutant (1996) especially for below 22m of depth. Anisotropy occurs at all depth levels, equal to 4.5% between GL-0m and GL-15m, -5.6% between GL-15m and GL-22m. The strongest values are found between GL-22m and GL-50m, equal to 10.19%, and finally 6.67% below GL-50m. At WLA (Fig. 3.6b), no strong anisotropy is observed, the maximum value being equal to 1.78% between GL-7.7m and GL-30m, and less than 1% otherwise.

Furthermore, regardless of depth and site, at least for our collected data, no variation of anisotropy is observed with respect to *v*/Vs*,* which suggests that at least for the set of data used in this study there is no relationship between the anisotropy and the level of deformation, the site's nonlinear response (if present) being the same in both directions. The stability of the *Vs* and the good correlation when compared with *Vs* profiles coming from other studies (Cox, 2006 and Stellar, 1996) support that the method allows a good estimation of *Vs in-situ*. Therefore, this method can be applied to detect changes in elastic properties during earthquake shaking in relation to the level of strain and nonlinearity.

3.6. Assessment of Nonlinear Site Behavior

Assuming shear stress τ as the spatial derivative of *PGA* according to $\tau = PGA \times \rho \times z$, and that the displacement-based shear strain γ_{DB} is the derivative of the displacement as follows:

$$\gamma_{DB} = \frac{du}{dz} = \frac{du/dt}{dz/dt} = \frac{PGV}{Vs} \tag{3.4}$$

where *PGV* is the Peak Ground Velocity, *PGA–PGV/Vs* is considered herein as the representation of the stress-strain relationships that can be used to test the nonlinear susceptibility of a site under seismic loading. *PGA–PGV/Vs* was first introduced as a stress-strain proxy based on wave propagation by Hill et al. (1993), Rathje et al. (2004) and Cox et al. (2009). Idriss (2011) proposed a stress-strain proxy using the PGV/Vs_{30} ratio, where Vs_{30} is the average shear wave velocity for the first 30m of depth used in the seismic codes. The efficiency of this proxy has been successfully demonstrated by Idriss (2011) on NGA datasets, De Martin et al. (2012) on KiK-net data, and Chandra et al. (2014a) on K-NET and KiK-net data. In this study, because we use an estimation of *Vs**, the peak ground accelerations and velocities along the borehole are replaced by the peak particle velocity, *v*,* and peak particle acceleration, *a*,* recorded between each pair of sensors. For all the strain computation, we assumed homogeneity of the soil layer between two successive sensors in the vertical array.

In order to test the validity of the plane shear wave propagation proxy for strain, v^*/Vs^* is first compared with the displacement-based shear strain γ_{DB} calculated by Equation 3.5:

$$\gamma_{DB} = \gamma_{ZZ-ij} = \frac{du_z}{dz} = \frac{(u_{zj}(t) - u_{zi}(t))}{(z_j - z_i)} \tag{3.5}$$

where $\gamma_{zz\text{-}ij}$ is the vertical deformation between two successive sensors i and j, u_{zi} and u_{zj} represent horizontal displacement at points i and j, respectively, and z_i and z_j are the respective depths of sensors i and j. Velocities and displacements were calculated by integrating and double integrating acceleration following the procedure proposed by Boore (2005). This method implicitly transforms the signals to have the same length by applying zero-padding before filtering and integration. To compute the stress and strain in each layer, several options can be considered depending on whether maximal strain is assumed to arrive (or not) at the same time as maximal displacement $u_{zj}(t)$ and $u_{zi}(t)$ and maximal velocity. Hence, in our study, we test two solutions for computing shear strain using displacement-based methods and three definitions of maximum particlevelocity.

The first strain value γ_{DB-1} is computed as the absolute value of the average maximal displacement between two sensors z_i and z_j divided by the distance $(z_j - z_i)$, as follows:

$$\gamma_{DB-1} = \left| \frac{(max[u_{zj}(t)] + max[u_{zi}(t)])}{(z_j - z_i)} \right| \tag{3.6}$$

The second strain value γ_{DB-2} is computed as the maximal relative displacement as follows:

$$\gamma_{DB-2} = max\left[\left| \frac{(u_{zj}(t) - u_{zi}(t))}{(z_j - z_i)} \right| \right] \tag{3.7}$$

Simultaneously, the maximum particle velocities v_1, v^* and v_3 are computed as the average value of the maximal velocities V in a layer between sensors i and j (Eq. 3.8), the maximal absolute value of velocity (Eq. 3.9) and the absolute average velocity (Eq. 3.10) at the time corresponding to maximal strain γ_{DB-2}, respectively, as described in Eqs. 3.8 to 3.10:

$$v_1 = \left[\frac{(max[V_i(t)] + max[V_j(t)])}{2} \right] \tag{3.8}$$

$$v^* = \max\left[\left|\frac{V_i(t)+V_j(t)}{2}\right|\right] \quad (3.9)$$

$$v_3 = \left|\frac{V_i(t=t(\gamma_{DB-2}))+V_j(t=t(\gamma_{DB-2}))}{2}\right| \quad (3.10)$$

Fig. 3.7 displays the comparison between displacement-based strain (γ_{DB-1} and γ_{DB-2}) and wave-based strain represented by the proxy *v*/Vs** (Fig. 3.7a), as well as the distribution of the residual values (Fig. 3.7b). We observe a slight dispersion of the data around the 1:1 line shown on Figure 3.7a. The lowest residual values are obtained considering *v*/Vs**.

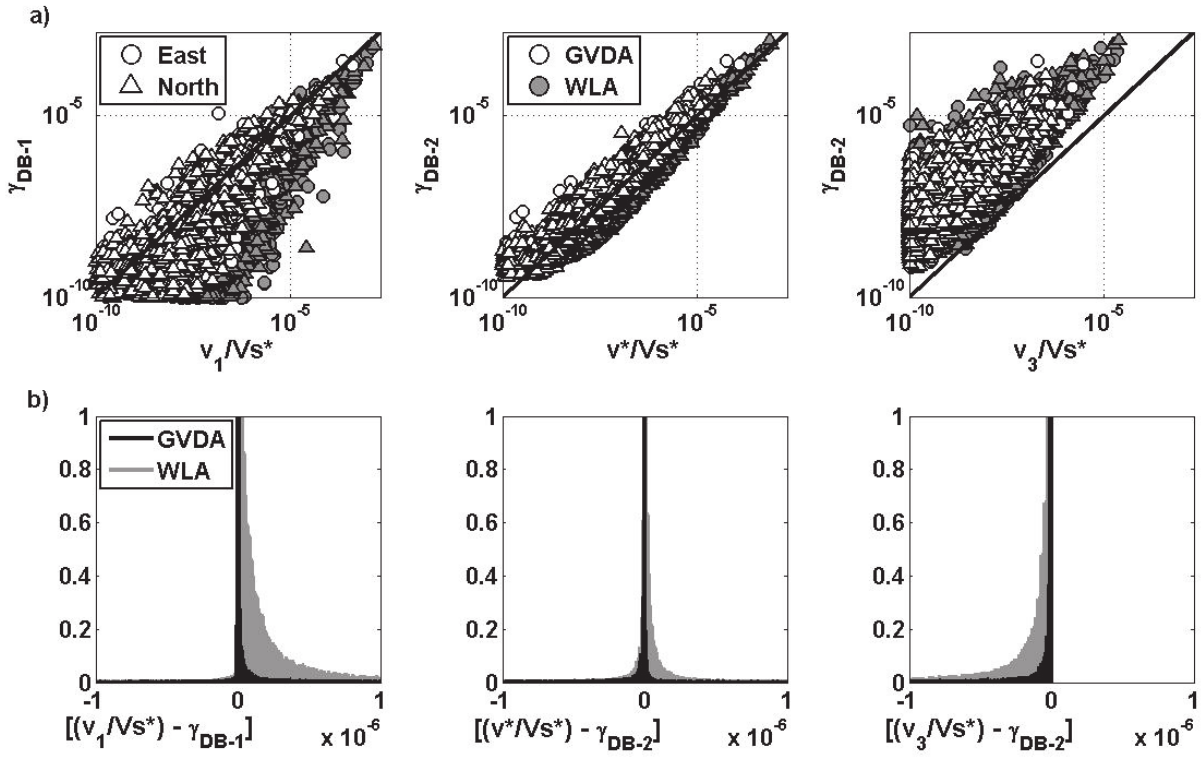

Figure 3.7. (a) Comparison and (b) residual values of displacement-based strain and wave-based strain proxies at the GVDA and WLA test sites. (left) γ_{DB-1} versus v_1/Vs*, (middle) γ_{DB-2} versus v*/Vs*, (right) γ_{DB-2} versus v_3/Vs* (see text for definition).

Rathje et al. (2004) reported that shear strain computed using plane shear wave propagation over-predicts displacement-based shear strain. . In our case, as shown in the residual distribution (Fig. 7b), the *v*/Vs** strain proxy under-predicts the displacement-based

strain: the mean and standard deviation values of the residues are $-4.78\text{x}10^{-7}\pm6.34\text{x}10^{-6}$ and $-1.66\text{x}10^{-7}\pm4.71\text{x}10^{-6}$ at GVDA and WLA, respectively. These values are very small and v^*/Vs^* may be therefore considered as the strain proxy in this study. To be consistent with this definition, we also defined acceleration-based shear stress, a^* used for the stress-strain curve as follows:

$$a^* = \max\left[\left|\frac{A_i(t)+A_j(t)}{2}\right|\right] \tag{3.11}$$

Vs^* may change during loading due to the nonlinear response of the soil layers and the strain, v^*/Vs^* along the borehole might change with the amplitude of the loading represented herein by a^*. The nonlinear response can be studied at various depths along the vertical array thanks to shallow and intermediate-depth strain (i.e. between two successive sensors).

Finally, the a^*–v^*/Vs^* results are inverted to fit the classic two-parameter nonlinear hyperbolic model proposed by Seed et al (1984), and Ishihara (1996):

$$\tau = \frac{G_0\gamma}{1+\frac{\gamma}{\gamma_r}} \tag{3.12}$$

where G_0 (or G_{max}) is the initial/maximum shear modulus, and γ_r is the reference strain that is the ratio between maximum shear stress τ_{max} and maximum shear modulus G_{max}. An equivalent shear modulus degradation can be obtained using Vs^{*2}/Vs_0^{*2} representing G/G_0. The nonlinear model is derived from Eq. 3.12 by:

$$\frac{G}{G_0} = \frac{1}{1+\gamma\frac{\tau_0}{\gamma_0}} \tag{3.13}$$

Finally, a function of the nonlinear representation is fitted to our results, derived from Eq. 3.13 as:

$$y = \frac{ax}{1+\frac{a}{b}x} \tag{3.14}$$

where y and x correspond to shear stress τ (i.e. a^*) and shear strain (i.e. v^*/Vs^*), respectively, and a and b are the initial shear modulus G_0 and shear strength a_0^*, respectively. In the rest of the chapter, only the hyperbolic model was used to fit data based on physical justification of the geotechnical models and valid from low to large strain levels.

3.7. Results and Discussion

In order to evaluate the validity of the v^*/Vs^* strain proxy, we plot (Fig. 3.8) the variation of the proxy with respect to acceleration for the GVDA (a) and WLA (b) test sites, i.e. a^*-v^*/Vs^*curve. Figure 3.9 plots the zoom of Figure 3.8 to display the results in small strain area. Vs^*, v^* and a^* values are computed in each layer and for all events. In addition, the degradation of local Vs^* along the borehole with strain (v^*/Vs^*) is studied. In these figures, assuming that a^* represents shear stress, the curve can be considered as equivalent to the in-situ stress-strain curve. Because of the degradation of shear-wave velocity during the earthquake, data are grouped according to the value of Vs_{30} found in Eurocode8 (CEN, 2003). The average velocity in each layer Vs^* is obtained by deconvolution and thus accounts for the degradation of the S velocity with respect to strain. We also group the data in terms of magnitude in order to introduce the possible consideration of source effects, associated, for example, with the frequency content of the waveforms recorded along the borehole, rather than only considering the peak values. Finally we consider the engineering representation of the stress-strain curve, PGA-PGV/Vs_{30}^* for all events, where PGA and PGV represent acceleration and velocity at GL-0m for NS and EW directions, and Vs_{30}^* is the average velocity over the 30m depth layer computed from the equivalent linear shear-wave velocity Vs^*. This figure shows the nonlinear behavior of the GVDA and WLA sites by fitting the hyperbolic model (Eq. 3.13) to the data: as for all theoretical nonlinear stress-strain curves, for a certain level of strain corresponding to the yield point, the slope of the curve decreases up to a horizontal line.

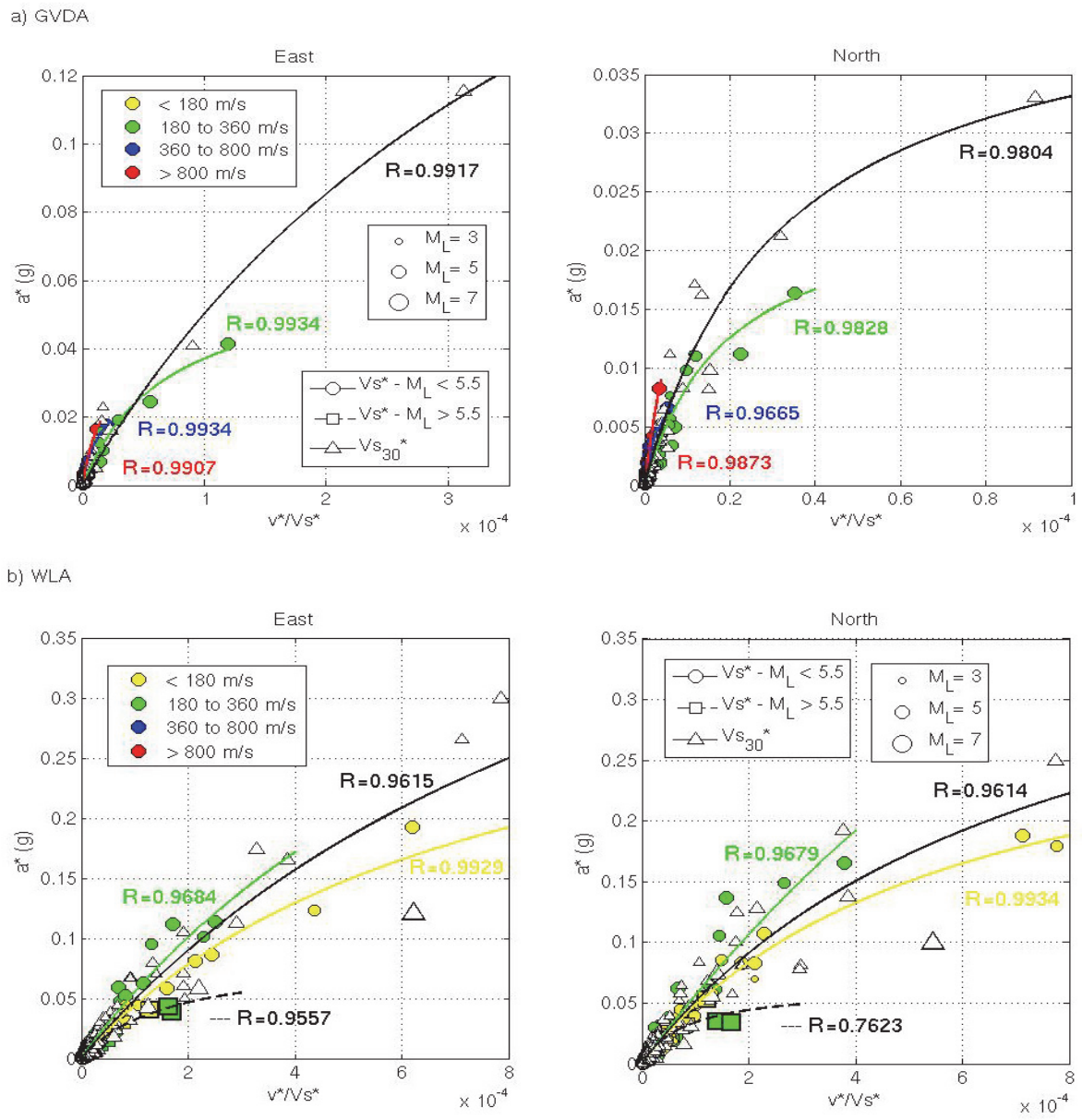

Figure 3.8. Equivalent stress (a^*) strain (v^*/Vs^*) results at (a) GVDA and (b) WLA test sites in the east-west (left) and north-south (right) directions, color-ranked according to the EC8 Vs_{30}-based site classification. The type of symbol represents the v^*/Vs^* proxy computed using M<5.5 (circle) or M>5.5 (square) events. The size of the symbol is proportional to the magnitude. The triangles correspond to the $PGA\text{-}PGV/Vs_{30}^*$ stress-strain proxy. Solid lines represent the hyperbolic models (Eq. 3.13) fitted to data within each Vs range. The dashed line at WLA is the hyperbolic model for M>5.5 data regardless of Vs due to the small number of events. Note that the x and y-axis scales for GVDA are different in the north and east directions.

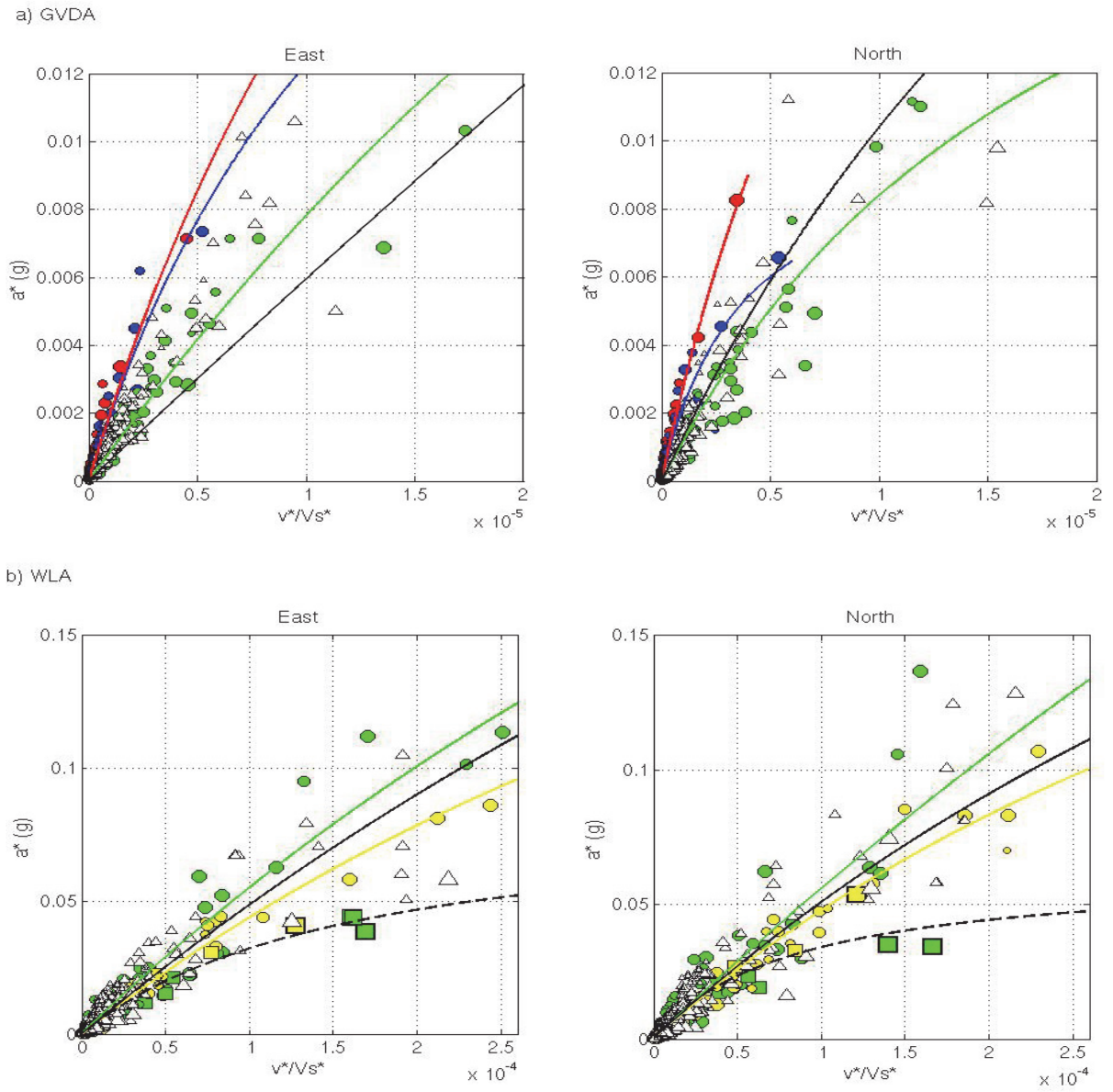

Figure 3.9. Zoom of Figure 3.8 for strain level up to $2x10^{-5}$ and $2.7x10^{-4}$, for (a) GVDA, and(b) WLA, respectively (different scale). For legends, see Figure 3.8.

It is not clear at which strain level the nonlinearity starts. Nevertheless we observed that at GVDA, nonlinearity appears at $2.5x10^{-5}$ in the EW direction and at 10^{-5} in the NS direction for the 180<Vs<360 class of soil. Few data at large strain are available but as shown by Chandra et al. (2014) using K-Net and KiK-net Japanese data, nonlinearity seems to be directly related to the velocity class. In fact the equivalent stiffest (*Vs*>800m/s) and softest (180<*Vs*<360m/s) soils border the nonlinear models at GVDA (180<Vs<360 and Vs<180m/s for WLA). During shaking, the degradation of *Vs** can be directly related to acceleration and strain. Owing to the *Vs** computed in each layer and taking into account the shear degradation

during shaking (not only from the elastic *Vs* profile provided by in-situ survey), the strain proxy (*v*/Vs**) points out the in-situ nonlinear behavior of the soil: the hyperbolic models for the stiffest soil are more linear compared with the softest soil models. If we consider Vs_{30}* as the proxy and Peak Ground Velocity as Idriss (2011) did, we observe at GVDA and WLA that the hyperbolic model smoothes the strain between the classes of soils, averaging the stiffest and the softest soil hyperbolic models.

At GVDA the Vs_{30}* hyperbolic model fits the data according to the magnitude level, as expected from the strongest acceleration. The same observation is made at WLA, for M<5.5 events. No clear dependence on magnitude is seen when M>5.5 and M<5.5 classes of events are compared, as the strongest nonlinear effect is not always apparent for the strongest events. With WLA M<5.5 data for instance, several larger magnitude events give smaller values of *v*/Vs** for equivalent acceleration with smaller magnitude inside the same class of soil (for example the last two yellow circles that correspond to the largest strain). Gélis and Bonilla (2012) discussed the frequency dependence of the nonlinearity. At WLA, for the largest magnitude events (M>5.5 - square), *a* vs. v*/Vs** represented by the dashed line in Fig. 8b (without soil classification) shows greater nonlinearity compared with lower magnitude event. These M>5.5 events correspond to distant large events, for example the April 4, 2010 El Mayor earthquake (M=7.2, distance of 99.93 km) and June 15, 2010 event (M=5.7, distance of 77.43 km). The PGA on the site reached only 0.12g and 0.07g for the April 2010 and June 2010, respectively. Nevertheless, these events produced a moderate strain.

The coefficient of correlation, R, is provided in Figure 3.8. The R value is ranged from 0 to 1, where 1 represents a perfect correlation between the fit and the data. The R value is computed following:

$$R = \sqrt{1 - \frac{\sum_{i=1}^{n}(y_i - yfit_i)^2}{\sum_{i=1}^{n}(y_i - \bar{y})^2}} \tag{3.15}$$

where n is the number of data, y_i is the data of the dependent variable, $yfit_i$ is the vector values of the fit, and $\bar{y}$ is the mean value of the dependent variable. For example, R values for *PGA vs. PGV/*Vs_{30} fit are 0.9917 and 0.9804 for GVDA and 0.9615 and 0.9614 for WLA in the NS and EW direction, respectively. Despite the lack of large strain values, the high values of R show a good estimation of the nonlinear hyperbolic model using the strain proxy (*PGV/*Vs_{30} or *v*/Vs**) derived from in-situ data.

Finally, as shown in Fig. 3.6 and contrary to WLA (Fig. 310b), we observe (Fig. 3.10a) differences in the hyperbolic models used in the two horizontal directions at GVDA for equivalent deformation. These differences might suggest anisotropy of soil nonlinearity, as also supported by the *Vs** values (Fig. 3.6a) but the lack of data at large strain does not allow to definitively conclude on this effect. The anisotropy issue may raise some questions about the velocity profile derived from in-situ geotechnical or geophysical surveys, usually performed in one direction and considered for nonlinear analysis of the site response. Moreover, starting from the elastic velocity given by classical geophysical and/or geotechnical surveys, the in-situ nonlinear response of the site may be underestimated because the degradation of *Vs** with the level of shaking is not taken into account. Finally in Fig. 3.10c, a simple comparison of the GVDA and WLA sites shows that even for the EW direction (showing less nonlinearity at the GVDA site), the nonlinear response seems to start at a lower strain value compared to the WLA site, that must be confirmed in the future with higher strain data.

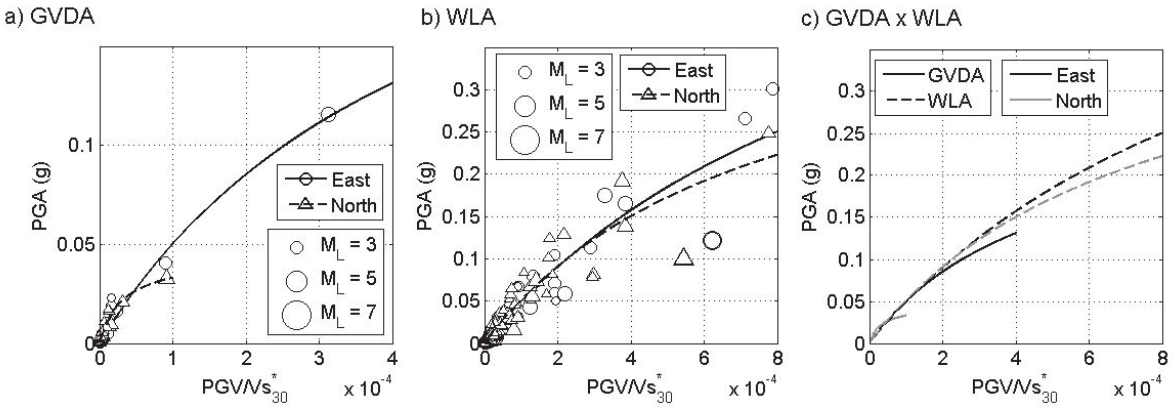

Figure 3.10. *PGA–PGV/Vs30** data for (a) GVDA, (b) WLA, and (c) comparison between both sites. The solid and dashed lines are the hyperbolic model fitted to the data for the east (circle) and north (triangle) direction data, respectively.

Since *v*/Vs** represents strain, one interesting solution to define the in-situ nonlinear response of the site is to derive the shear modulus degradation with respect to the strain, i.e. the so-called *G-γ* curve, from the site data. Using this method, it is possible to obtain the nonlinear curves at different depths. However, we have no direct value for *G*, and only the *Vs* value. Nevertheless, by discerning the relation between *Vs** and *G* (Eq. 3.1), the G/G_0 value can be substituted by Vs^2/Vs_0^2. (Eq. 3.13). Vs_0 is defined as the average shear wave velocity

corresponding to the smallest deformation for which a linear response is expected, i.e. between $5x10^{-8}$ and $5x10^{-7}$ of strain. The *Vs* degradation analysis is carried out at different depths, and moreover the data is inverted to fit the model according to Eq.3.14.

Figures 3.11 and 3.12 display the Vs^2/Vs_0^2 variation according to the v^*/Vs^* proxy computed in the east-west (a) and north-south (b) directions for the GVDA and WLA test sites, respectively. The smallest deformation shows the largest discrepancy of data but overall, the figures show rather limited scattering of data. As expected, the uppermost layers exhibit stronger nonlinear behavior than the lower layers. In the uppermost layers, we found that nonlinear behavior starts at a very low level of deformation ($\sim10^{-6}$) and corresponds to the cyclic γ_{tl} threshold, becoming more significant above the γ_{tv} threshold ($\sim10^{-4}$). For example, G degradation starts at a level of strain equal to 10^{-6} and $2x10^{-6}$ at GVDA for the north-south and east-west directions between GL-0m and GL-15m, and at 10^{-5} at WLA in both directions, which confirms that GVDA is more nonlinear than WLA. Comparing the different depths at each site, we observe an increase in the strain threshold for the nonlinear response (i.e., shift of the fitted model to the largest deformation), in accordance with the fact that the lowermost layers are less nonlinear. As discussed previously, the degradation of *G* is much more sensitive to the strongest PGA (circles) than to the strongest magnitudes (size of the symbols), as systematically observed at the WLA site, confirming that magnitude is not sufficient as a parameter to reflect the possibility of an event generating nonlinearity. This is understandable since a large magnitude event could generate a low intensity level due to the distance. Conversely, a small magnitude event could produce a large intensity value due to the proximity between the source and the site. Even though nonlinearity is less present at greater depths, nonlinear response is also observed: for example at $3x10^{-6}$ of strain between GL-15m and GL-22m at GVDA or at 10^{-5} of strain between GL-7.7m and GL-30m at WLA. Although the data are not sufficient, we observe a slight nonlinear trend in the fitted curve below 30m, suggesting that nonlinearity may occur at depth, even for moderate deformations generated by moderate earthquakes.

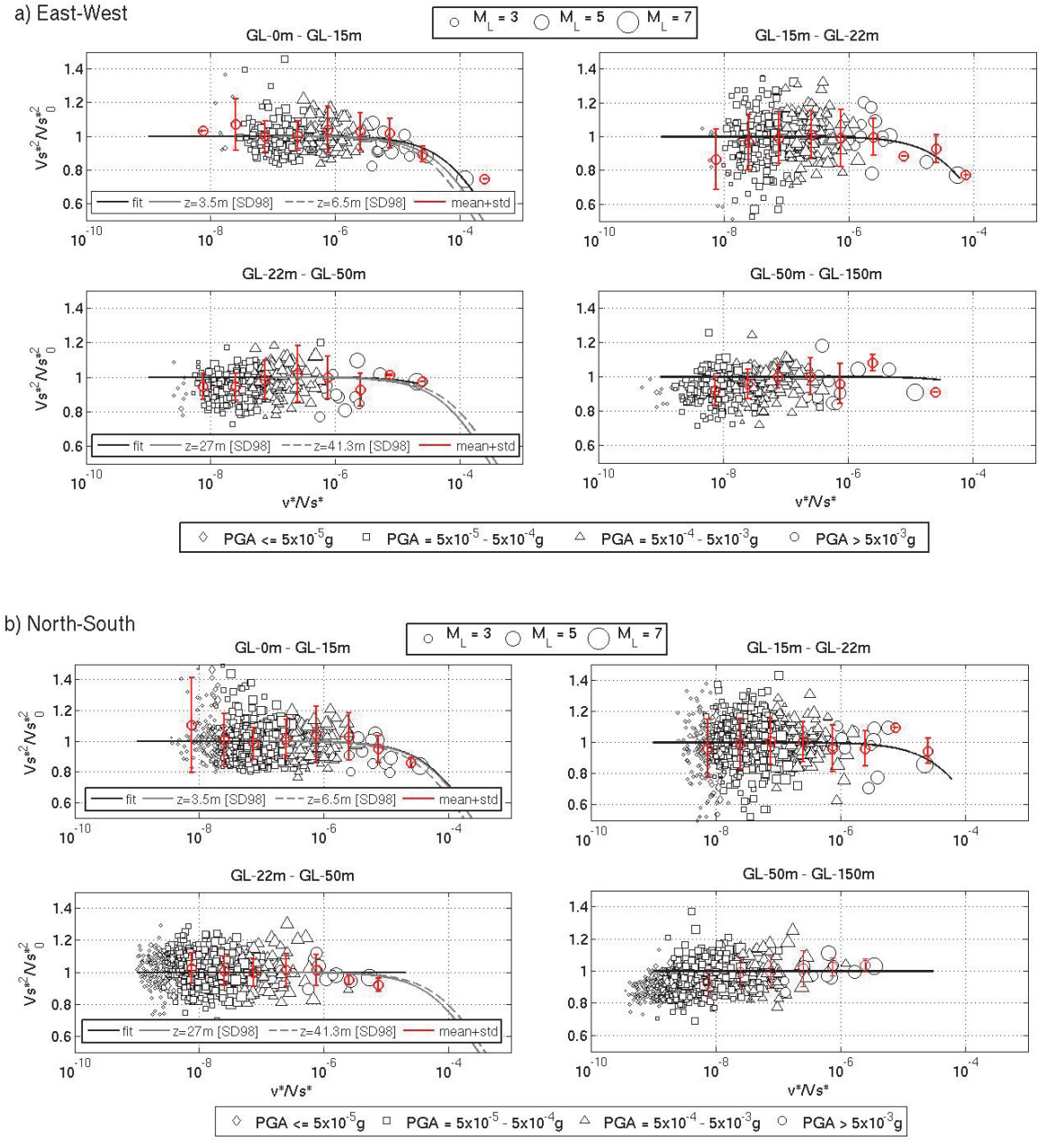

Figure 3.11. Equivalent shear modulus degradation curve for different depths at the GVDA test site (a) EW and (b) NS directions. The solid black line represents the fitted-curve of our data, and the grey lines represent (when available) the results from laboratory tests performed by Stokoe and Darandeli (1998) on samples taken at different depths. The red circle indicates the mean value of the measured data as well as the sigma for different band of strain, i.e. below 10^{-8}, 10^{-8}-$5x10^{-8}$, $5x10^{-8}$-10^{-7}, 10^{-7}-$5x10^{-7}$, $5x10^{-7}$-$x10^{-7}$, 10^{-7}-$5x10^{-6}$, $5x10^{-6}$-$x10^{-5}$, 10^{-5}-$5x10^{-5}$.

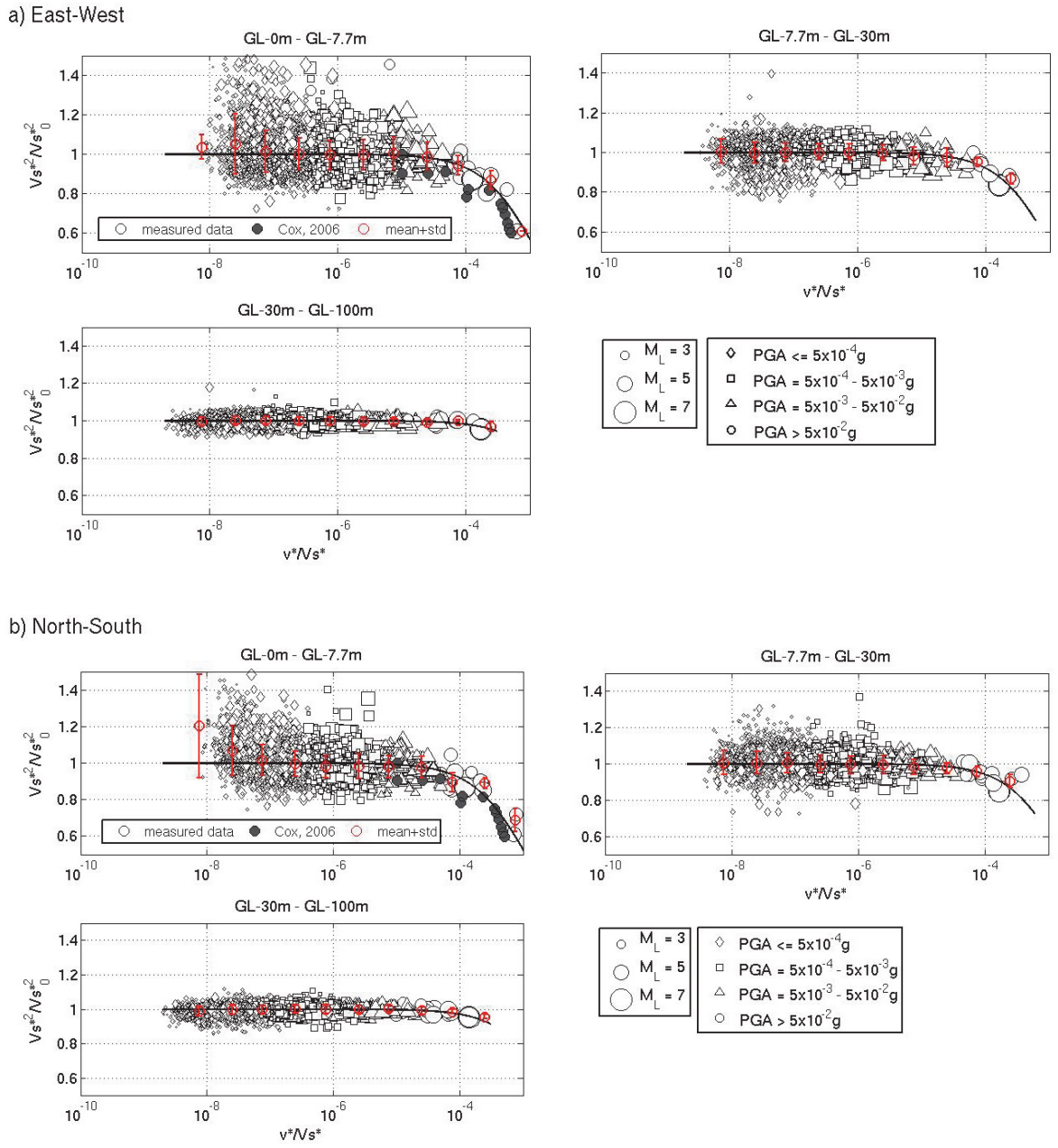

Figure 3.12. Equivalent shear modulus degradation curve for different depths at the WLA test site. (a) EW and (b) NS directions. The solid black line represents the fitted-curve of our data, and the grey filled circles represent the results from Cox, 2006. The red circle indicates the mean value of the measured data as well as the sigma for different band of strain, i.e. below 10^{-8}, 10^{-8}-$5x10^{-8}$, $5x10^{-8}$-10^{-7}, 10^{-7}-$5x10^{-7}$, $5x10^{-7}$-$x10^{-7}$, 10^{-7}-$5x10^{-6}$, $5x10^{-6}$-$x10^{-5}$, 10^{-5}-$5x10^{-5}$, $5x10^{-5}$-$x10^{-4}$, 10^{-4}-$5x10^{-4}$, $5x10^{-4}$-$x10^{-3}$.

Stokoe and Darandeli (1998) performed laboratory Resonant column and Torsional Shear tests on samples extracted at GL-3.5m, GL-6.5m, GL-27m and GL-41.3m at the GVDA test site and provided the G-γ curve. The laboratory tests are compared in Tab. 3.1 with the degradation values found using vertical arrays in this paper. Furthermore, the curves at different depths are given for comparison on Fig. 3.11-3.12 with the average strain computed for different ranks of strain (average value +/- standard deviation in red).

Table 3.1. Comparison of *G* reduction values between in-situ assessment and laboratory tests from Stokoe and Darendeli (1998) for equivalent shear strain values provided by laboratory tests or by the strain proxy

Stokoe and Darandeli (1998)		Shear strain	In-situ (this study)		
depth (m)	*1-G/G0* (%)	(γ)	direction	depth (m)	*1-Vs*/Vs*$_0$* (%)
3.5	28	10^{-4}	East	0 – 15	28
6.5	15	$3.3x10^{-5}$	North		17
27	9	$2x10^{-5}$	East	22-50	11
41.3	7				
27	1	$9x10^{-6}$	North	22-50	8
41.3	1				

We observe that for larger deformations (10^{-4} to 10^{-5}), our results match very well with the laboratory measurements, whatever the depth. Scattering of results may be due to the smaller number of events having a statistical representation of strain and degradation, or to the natural variability of the nonlinear response for different types of seismic loading. Since the laboratory tests were performed considering only cyclic loading, we can also assume that the site's nonlinear response may depend on ground motion characteristics, producing real *in-situ* uncertainties concerning the dynamic response, not included in laboratory-induced curves. This also applies to the consideration of anisotropy, which is not provided by *in-situ* classical surveys.

Cox (2006) performed *in-situ* dynamic loading tests at three different locations of the WLA test site. In this paper, we compare our results with his results at Test Location C (Cox, 2006) for which more information is available. Two dynamic loading experiments with multiple loading stages were carried out for his study using T-Rex apparatus to apply dynamic shear load to the surface array. The comparison of the results is shown in Figure 3.12 only at the first 7.7m depth measurement since non-invasive methods are available for the uppermost

layers. Our results in WLA test site, match Cox's results (2006) very well. At the WLA test site, the degradation modulus may be the result of both the nonlinear behavior of the site and the pore water pressure generated (Cox, 2006), as indeed the largest event at WLA has excess pore pressure generation, with the largest having an Ru of 60% (Steidl et al., 20014). In this study, however, pore water pressure generation is not discussed. It is also important to note that nonlinearity does not occur only at shallow depth, but also in the lowermost layers, at strain of 10^{-4}. Therefore, nonlinearity may be generated not only near the surface. However, this is rarely investigated due to the difficulty of extracting samples at greater depths and to reproduce in lab the in-situ stress level.

Finally, we compare (Fig. 3.13) the results from the two test sites. Since the site characteristics are different, we use the strain parameter PGV/Vs_{30}* to compare the behavior between the two sites. Shear modulus degradation is represented by Vs_{30}*/Vs_{30}*$_{max}$, where Vs_{30}* corresponds to the instantaneous average particle velocity computed using v* between GL-0m and GL-30m and Vs_{30}*$_{max}$ corresponds to the average Vs_{30}* for the smallest deformation at which a linear response is expected, i.e. between $5x10^{-8}$ and $5x10^{-7}$ of strain. Despite the fact that liquefaction is expected at WLA, with the data collected at GVDA so far, nonlinear behavior appears to start at a lower strain level than at WLA. Since GVDA has not suffered significant deformation, preventing us from being able to compare the results for the highest levels of deformation. Once again, we observe that both v*/Vs* and PGV/Vs_{30} are reliable proxies for predicting nonlinearity, the degradation of the equivalent shear modulus being related to the increased values of the proxy.

In Fig. 3.13 we also plot the volumetric strain $\gamma_{tv}=10^{-4}$ (Hardin and Black, 1968; Drnevich and Richart, 1970; Dobry and Ladd, 1980) and linear strain $\gamma_{tl}=10^{-6}$ (Vucetic, 1994; Johnson and Jia, 2005). The nonlinear response close to 10^{-6} and corresponding to the cyclic strain is less visible compared to Figs. 3.11 and 3.12. This is due to fact that corresponding PGV (rather than instantaneous v*) and Vs_{30}* (rather than intermediate depth Vs*) smooth the results and do not represent the actual stress-strain relationship. Nevertheless, above 10^{-4} the nonlinear response is clearly observed and estimated by the PGV/Vs_{30} proxy, allowing us to assume an efficient prediction of the nonlinear response from the ratio between peak ground velocity and Vs_{30}.

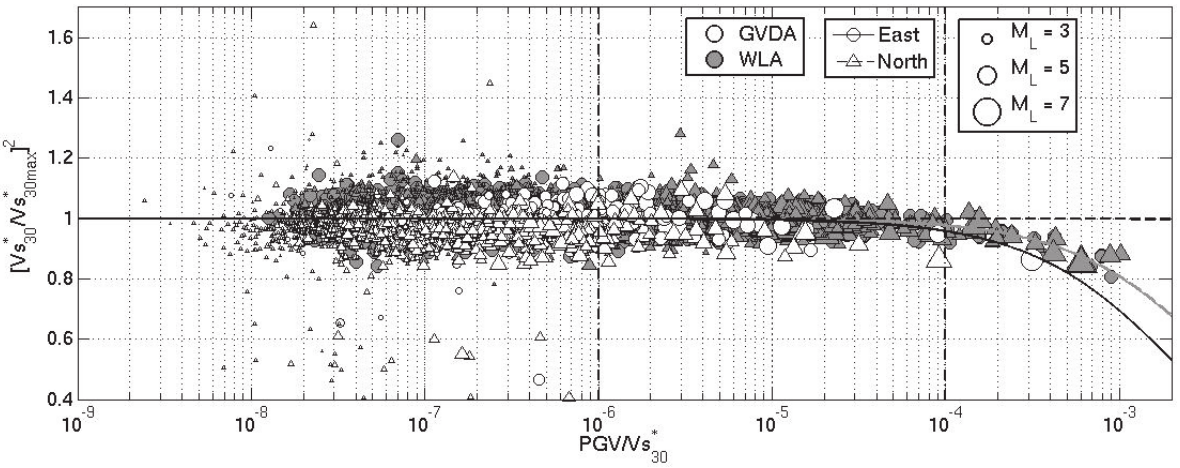

Figure 3.13. Comparison of equivalent shear modulus degradation curve between the GVDA (blank) and WLA (filled) test sites. The circle represents the east direction data and the triangle the north direction data. The solid (east direction) and dashed (north direction) lines represent the fitted hyperbolic model from Eq. 3.4 for GVDA (black) and WLA (grey) test sites. The dot-dashed lines represent the γ_{tl} of 10^{-6} and γ_{tv} of 10^{-4}.

3.8. Conclusion

The near-surface geology effects of the Garner Valley Downhole Array (GVDA) and the Wildlife Liquefaction Array (WLA), both situated in the active San Andreas Fault system, are analyzed for nonlinearity assessment using in-situ data. We monitor the changes in the *in-situ* shear wave velocity measured using the seismic interferometry by deconvolution technique.

We are able to estimate the velocity profile and to monitor the nonlinear response of the sites with respect to the level of shaking. In our case, we consider the loading using the strain proxy *v*/Vs*,* reproducing in each layer the shear strain accounting for the degradation of shear-wave velocity. At the GVDA test site, slight anisotropy is clearly demonstrated between east and north components, in agreement with previous studies. The anisotropy at the WLA test site is negligible and anisotropy is not influenced by deformation (shear strain) level at either site.

We show that the v^*/Vs^* ratio is a deformation proxy, as well as PGV/Vs_{30}. In the first case, deformation is accurate enough to observe in the uppermost layers the cyclic deformation due to the nonlinear elastic behavior of the soil at values close to 10^{-6}, as reported by Vucetic (1994), and Johnson and Jia (2005). The a^*-v^*/Vs^* curve represents the evolution of the stress-strain relationship of the soil column under different levels of excitation. For the lowest S-wave velocities (softer soil), typical nonlinearity trends are observed compared with the higher velocity group (stiffer soil). The magnitude and the peak ground acceleration are shown to be complementary for predicting nonlinearity and source effects of the ground motion (such as the frequency of the seismic energy) may also influence the nonlinear behavior of the site. By comparing a^*-v^*/Vs^* with PGA-PGV/Vs_{30}, we show that although the use of Vs_{30} is convenient in practice, the results are more dispersive compared with the use of Vs^*. Nevertheless, in both cases the inverted classic hyperbolic model offers a good fit with the data and, with further study, could be used for nonlinear prediction.

This study has shown a possible solution for in-situ estimation of the shear modulus degradation curve of each layer located at different depths. The results are comparable with the laboratory measurements obtained previously when available. Nonlinear behavior starts at a low level of deformation (~10^{-6}) inside the soil column and becomes more significant at a deformation of around ~10^{-4}. The data is also inverted with the classic hyperbolic model that fits the data with moderate scattering using Vs_{30} and/or Vs^*. We demonstrated that despite the lack of large strain values, the high values of the correlation coefficients, R, confirm the good prediction of the nonlinear hyperbolic model using the strain proxy (PGV/Vs_{30} or v^*/Vs^*) derived from *in-situ* data. This type of analysis might finally be integrated to the prediction of the ground motion including nonlinearity. Analysis of the efficiency of our method with other classical methods (e.g. based on f_0, mode shape variation, and amplification reduction) might be performed in further studies for comparison.

3.9. Data and Resources

Garner Valley and Wildlife data used in this study were collected as part of the NEES@UCSB program. Data can be obtained from the NEES@UCSB website at http://nees.ucsb.edu/ (last consulted in March 3, 2014).

3.10. Acknowledgements

The authors wish to acknowledge the California Department of Fish and Wildlife that provides access to the monitoring site at the Wildlife Liquefaction Array and the Lake Hemet municipal Water district that provides access to the monitoring site at Garner Valley. The NEES@UCSB field site facility received supported from the George E. Brown, Jr. Network for Earthquake Engineering Simulation program through CMS-0217421 and CMMI-0927178. The authors are grateful to Marco Mucciarelli and an anonymous reviewer for their comments that helped to improve this work. The authors would also like to gratefully thank the NEES@UCSB and ERI UCSB team for all the helps and discussions during the data collection and processing, in particular Paul Hegarty and Francesco Civilini. We thank the ED TUE-Université de Grenoble for the travel grant in order to collect the necessary data. We also like to thank IFSTTAR, France for funding this research.

Chapter 4

Nonlinear Soil-Structure Interaction model with coupled Horizontal and Rocking response: Application to Centrifuge Testing

Summary

In addition to the soil nonlinearity that has been discussed in Chapters 1.1, 2 and 3, the presence of surface heterogeneities, especially surface structures, influence the response of soil-structure systems in urban areas through the nonlinear Soil-Structure Interaction (SSI). SSI is responsible for the modification of the responses of the soil, structures and soil-structure systems. Using the centrifuge test, we apply two different excitations (weak and strong) to identify and separate the nonlinear soil-structure system responses. In the first part, the nonlinear soil responses due to presences of different type of building are discussed by computing the deformation level inside the soil column. In the second part, the contribution of each element of SSI is determined using a nonparametric system identification procedure based on a 1D wave propagation technique. The modal parameters, i.e. frequency and damping are observed to analyze the responses of different type of structures. The nonlinear responses are analyzed by quantifying the changes of these parameters when strong motion is introduced. In the third part, the responses when two adjacent buildings present are observed as a simplification of what happens in an urban environment. Finally, the free-field contamination due to presence of the structure is analyzed. The governed parameters that are modified by this phenomenon are identified and the modification is quantified to see how far this contamination affects the free-field responses.

4.1. Introduction

In urban areas, the presence of heterogeneities at the surface including structures and their foundation, through their dynamic interaction produce a strong coupling between soil and structure (Kausel, 2010). When seismic waves travel through soil to foundation of the structure, the impedance causes scattering of the incident waves (kinematic soil-structure interaction). Detailed study on the impedance functions and dynamic soil-foundation interactions can be found in Gazetas (1991), Gazetas and Makris (1991), and Makris and Gazetas (1992). The waves transmitted to the structure are modified by its intrinsic properties, and the structure starts shaking with vibrating energy that is diffracted back into the ground as seismic waves (inertia soil-structure interaction). This soil-structure coupling manifests through rocking and horizontal motion of the building (Luco et al., 1987; Bard, 1998; Guéguen and Bard, 2005; Todorovska, 2009a). After propagating inside the building seismic waves are diffracted back into the ground and contaminate the incident seismic waves recorded in the free field. This modification is known as Soil-Structure-Soil Interaction (SStSI) and has been discussed mostly from experimental *in-situ* observations. Several active tests were done, for example by Jennings (1970) using resonance tests in Millikan Library Building, Gueguen et al. (2000) and Gueguen and Bard (2005) at the Volvi test site, Mucciarelli et al. (2003) in Potenza, Italy, and Ditommaso et al. (2010) in Bagnoli, Italy, all using an active release test. Other indirect observations came from Kanamori (1992) who observed the generation of seismic waves by high-rise buildings forced into vibration by the return of the Columbia space shuttle, and Kim et al. (2001) who observed similar phenomenon by aircraft impacts and building collapses after the 2001 World Trade Center, USA, tragedy. Other numerical models analyzed this effect (Wong and Trifunac, 1975; Wirgin and Bard, 1996; Guéguen, et al. 2002; Boutin and Roussillon, 2004; and Mucciarelli et al., 2009). Their results confirm the contamination of the seismic ground motion in the presence of surface structures.

In presence of two adjacent buildings, multi-interactions appear named Structure-Soil-Structure Interaction (StSStI). Numerical works by Luco and Contesse (1973) using two parallel infinite shear walls showed that these effects are important at low frequencies, and around the fixed-base natural frequencies of the second structure. Trombetta et al. (2014) examined this problem using the centrifuge experiment and showed the high coherency between two roof motions of adjacent structures. In presence of identical buildings, Kitada et

al. (1999) with experimental data, Guéguen (2000) with finite-element model and Chazelas et al. (2003) with centrifuge tests showed the splitting of the resonance frequency of adjacent buildings, and that the effects vary as a function of the inter-building distance (Padrón et al., 2009). Efraimiadou et al. (2012) also reported an amplification of these effects on multiple earthquake sequences. Lou et al. (2011) provided a literature review focusing more on the numerical study of this phenomenon. In urban areas where more than two buildings present, multi-interaction between buildings is generated, which refers to Site-City Interaction (SCI). This effect has been studied extensively, especially after the 1985 Mexico City earthquake (Wirgin and Bard, 1996; Guéguen et al., 2002; Chávez-García and Cárdenas-Soto, 2002). Some numerical works on SCI have been done for example by Kham et al. (2006), Semblat et al. (2008), and Padrón et al. (2009) showing the contamination of the waves due to the presence of a resonator as the excitation source. This point was also studied physically by Rupin et al. (2014) and Colombi et al. (2014).

The difficulty in the SSI model is to separate the effects of each contributing element of the interaction (Stewart and Fenves, 1998) which may have the same importance as the building characteristics on the damage that is observed after earthquakes. A classical approach is to determine the frequencies of vibration and the corresponding mode shapes where the structural response can be represented as a superposition of the modal responses (e.g., Paolucci, 1993; Meli et al., 1998; Guéguen and Bard, 2005). An alternative approach is to identify the time domain characteristics, such as wave travel times through the structure (e.g. Kanai, 1965; Safak, 1998a, 1999; Kawakami and Oyunchimeg, 2003, Snieder and Şafak, 2006; Kohler et al., 2007; Todorovska and Trifunac, 2009a, 2009b). In the time domain, the response of the structure is represented as a superposition of waves that propagates in the structure with the same transmission and reflection properties as those of the soil. Using this assumption, Snieder and Şafak (2006) considered the 1D wave propagation model in a building and soil as equivalent.

Most of these studies are focused on the linear elastic behavior of the SSI and the contamination of the wave-field by the presence of the building (kinematic and inertial SSI). However, under strong excitation, building would have a nonlinear behavior (Celebi et al., 1993; Clinton et al., 2006; Todorovska and Trifunac, 2008; Michel and Guéguen, 2010) producing changes in frequency and damping values of the modes. The nonlinear behavior of the structure and the soil modifies the behavior of the soil-structure interface, resulting in the

nonlinear SSI response that changes the dynamic response of the structures (Todorovska, 2009a; Trifunac et al., 2010). In addition, the soil-structure coupling changes as well the soil responses. Leroueil and Vaughan (1990) reported that regardless the nature of the structure, its presence increases strength and enlarges the stress domain in the soil. Gicev (2009) showed that at the boundary between soil and foundation, spatial distribution of permanent nonlinear soil strain depends on the incident angle, the amplitude and the duration of the pulse. In addition, the waves diffracted back into the soil may also introduce nonlinear effects, and they may sometimes produce induced-liquefaction due to the soil cyclic loading triggered by the vibration of the structures.

In this section, we use the dynamic centrifuge to analyze the wave propagation problem (Kutter, 1995; Semblat and Luong, 1998; Brandenberg et al., 2006; Chandra et al., 2014a) and the multi-coupling between the soil and the structure (Ghosh and Madabhushi, 2006, Mason et al., 2013; Chazelas et al., 2003, Trombetta et al., 2013, 2014; Ha et al., 2014). Frequency and time-domain methods were employed under weak and strong motion. The interest of the centrifuge test is first, to compare the soil, SSI, and structure responses for different level of shaking, and second, to test the responses of different models of structure while the majority of the papers that were published usually only considered one case-study structure. In the first part, the centrifuge test and the data used are presented. Then the influence of the presence of the structure to the soil resonance is analyzed. Later, different building responses including the SSI are analyzed by considering different stand-alone building models and two adjacent buildings. The nonlinear free-field contamination caused by the building is finally discussed in the last part.

4.2. Centrifuge Test and Data

The centrifuge test was performed at the IFSTTAR facility (Nantes, France) (Chazelas, 2010). The description of the centrifuge test was previously given in chapter 2.4, including the characteristics of the soil, the type of containers, the type and the distribution of sensors and the feature of the input signals. The container is an equivalent shear-beam (ESB) container. Zeng and Schofield (1996) reported that ESB is the most recent solution to limit the reflection at the container boundaries so that it behaves like a soil column and having the same stress-strain condition at any position in the soil mass.

In Chapter 2, Chandra et al. (2014a) have tested the influence of the boundary condition on the wave propagation and they have concluded the efficiency of the ESB used in this study. The dimension of the ESB box is 800x350x416mm representing a soil column of 48m long, 21m wide, and 25m deep at 60g scale factor. The different types of structures resting at the top of the soil column are presented in Figure 4.1. These models represent a low rigid structure (LRS, 4.1b), a rigid structure (RS, 4.1c), a flexible structure (FS, 4.1d), a 2-DOF flexible structure (2DOFS, 4.1e), and two flexible buildings (2FS, 4.1f).

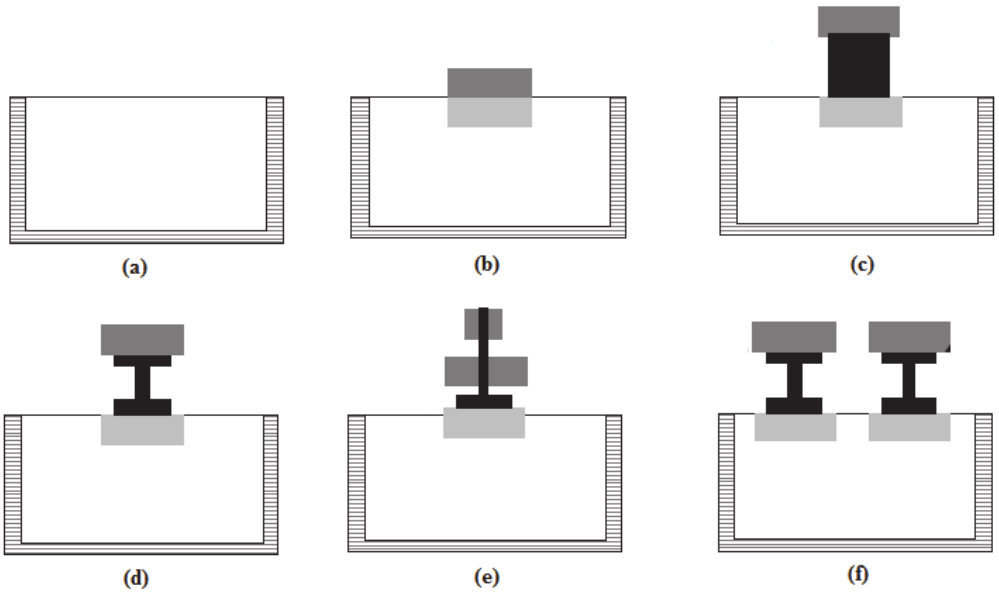

Figure 4.1. Different types of models presented in the experiment. (a). Soil Only ; (b). Low Rigid - LRS; (c). Rigid - RS; (d). Flexible - FS; (e). Two degree-of-freedom flexible - 2DOFS; (f). Two adjacent flexible - 2FS. (Modified from Chazelas, 2010)

The LRS is represented by a steel mass, the RS is composed by steel-aluminum-oak materials, and FS and 2DOFS are by composite steel-aluminum materials. The real dimensions of the structures are shown in Figure 4.2, correspond to the 1/60 scaled dimension in the centrifuge tests performed at 60g. The frequency of the FS was chosen to be similar to the response frequency of the soil, i.e. around 2.5-2.7Hz (see Chap. 2.4), and the dimensions of the RS were chosen to have the center of gravity at the same height as the FS with respect to the surface of the soil column. All structures are founded with a shallow foundation, reducing the kinematic interaction. The foundations were made by two aluminum and pinewood (laminated) plates. The mass of the foundation is 0.156 kg, the LRS has 0.98kg, the RS has 0.976kg, the FS has 1.0716kg, and the 2DOFS has 1.018kg.

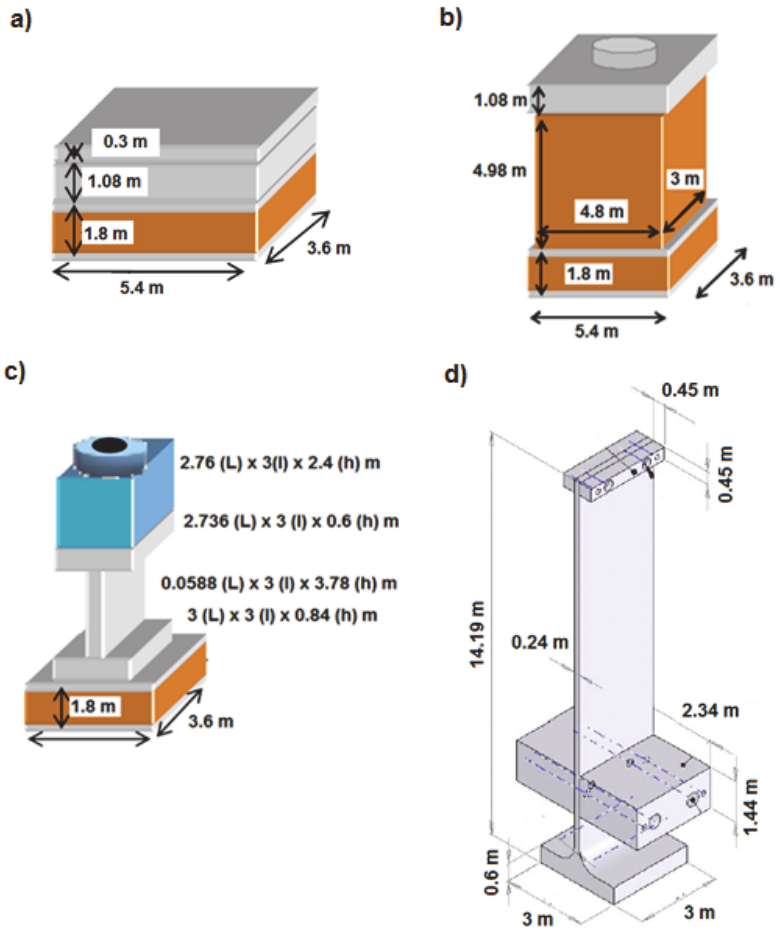

Figure 4.2. Real dimension of the structures. (a). LRS; (b). RS; (c). FS; (d). 2DOFS; (modified from Chazelas, 2010)

The sequence of each experiment was done using two different containers, as also discussed for the soil-only analysis (Chap 2.4.1) and about three to six tests were carried out for each [building/container/input signal] pairs of configuration. The acquisition was performed using sensors described in Chap. 2.4. Piezoelectric horizontal and vertical accelerometers (PCB type 200 A1 and Bruel & Kjaer type 4317) were used, attached to a thin plate to ensure direction and position. The localization of the sensor is shown in Fig. 4.3, and after checking the data and keeping only the sensors that worked, the list of sensors that is not used in this study is presented Tab. 4.1 for each experiment. This table presents also the number of sequences and container that were used.

Table 4.1. Detailed containers, trials and working sensors for different experiments

Structure	Container Number	Number of Sequences		Not Working/Not Deployed Sensors Number
		weak	strong	
SO	1	3	6	11
	2	5	6	
LRS	1	5	6	10, 11, 15, 22
	2	5	6	
RS	1	6	6	10, 11, 15, 16
FS	1	3	15	10, 11, 15, 16, 20, 25
	2	4	4	
2 DOFS	1	3	6	20, 21, 22, 26
	2	3	4	
2FS	1	3	6	20, 21, 22, 23, 24, 25, 26

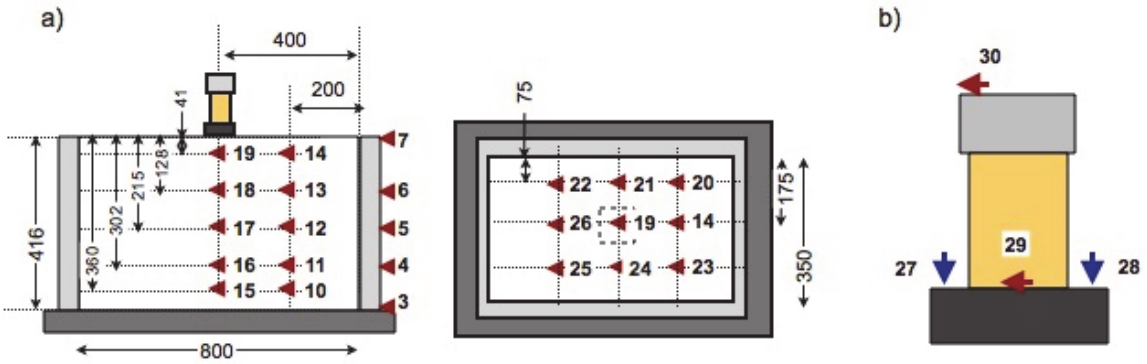

Figure 4.3. General dimension of the container and the localization of the sensors in the soil (a) and in the structure (b). Horizontal red arrows indicate horizontal sensors and vertical blue arrows indicate vertical sensors. The dashed square represents the position of the building model in plan. (modified from Chazelas, 2010). Unit: mm.

The experiment can be divided in two sequences. The first sequence was only interested in the soil and the distribution of the sensors which is the same as in Chapter 2, keeping the same numbers of sensors (Fig. 4.3a). The soil was first analyzed with the same method as presented in Chapter 2. The material used is dry Fontainebleau sand, whose properties are shown in Table 2.4. The soil mass was constructed using the dry pluviation method to reproduce the initial stress in granular soil. The second sequence was to analyze the dynamic response of each structure model, with almost the same instrumental schema for all experiments (Fig. 4.3b).

Two different input signals were used, representing weak and strong excitation, and applied as inputs for the centrifuge tests at the bottom of the container using a shaker that was driven in displacement. The first signal is a synthetic accelerogram representing a strong ground motion with a realistic phase corresponding to Mw 5.5 earthquake recorded at 15km (Causse et al., 2008) and having a Peak ground acceleration (*PGA)* of 0.43g (dominant frequency close to 1.86Hz). The second signal is a real accelerogram of a weak seismic ground motion recorded during the Mw 7.3 earthquake in Martinique in 2007 by one station of the French Accelerometric Network. The *PGA* corresponds to 0.07g and dominant frequency is close to 2.7Hz. In all of our processing, the signals were zero-padded as proposed by Boore (2005) to assure the completeness of the signals when integrating, deriving or transforming from time to frequency domain. The mean and trend were removed from the signals, tapered using a 5% Tukey window, and the signals were filtered using a 3rd order of Butterworth filter between 0.3 to 13.8 Hz where the maximum of energy is focused as reported by Chandra et al. (2014a) (Fig. 2.4b). We performed multiple trials applied to all the models and Chandra et al. (2014a) has reported the stability of the input signal from one trial to another one. We used Konno-Ohmachi function of smoothing factor (B=40 Konno and Ohmachi, 1998) in order to avoid the unrealistic large peaks due to high-frequency errors (Şafak, 1999). An example of a propagating strong signal from input to the top of the soil column to the top of the building for 2DOFS is shown in Fig. 4.4.

4.3. Resonance Frequency of the Soil

In the time domain, as described in Chapter 1.3, the 1D soil response can be represented as a superposition of waves that enter the column. Incoming waves reflect from the surface boundaries and from internal boundaries with impedance contrast, applying the reflection and transmission coefficients at each interface (Thomson, 1950; Haskell, 1953; Kennett, 1974). In the time domain, Chandra et al. (2014a) (see Chap 2.4) analyzed the soil response in the centrifuge container through the wave velocity obtained from pulse travel time measured from broader band impulse response functions (Mehta et al, 2007; Nakata and Snieder, 2012).

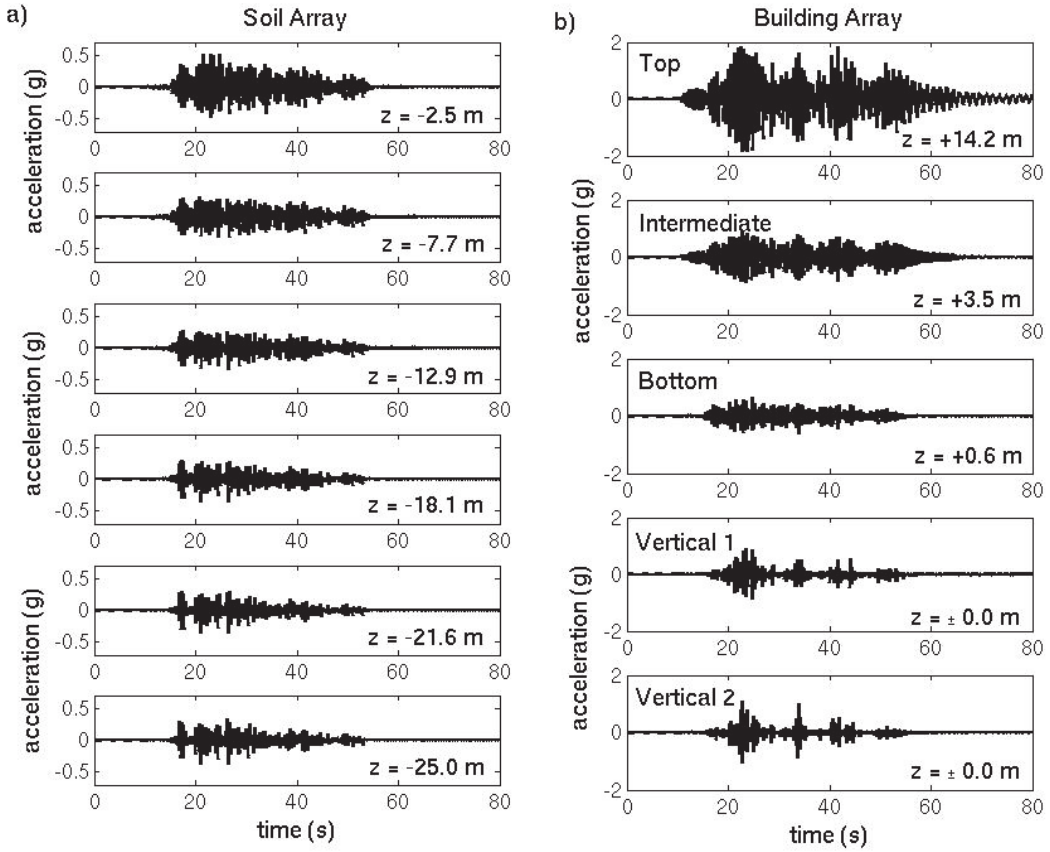

Figure 4.4. Example of a strong signal propagating from input to the top of the soil column to the top of the building on the centrifuge test. *z* indicates the vertical position of the sensor. a) propagation through the soil column. b) propagation in the building.

The theoretical resonance condition for the shear deformation gives fundamental resonance frequency $f_0 = Vs/4H$. The shear wave velocity Vs was obtained by picking the time for the input pulse to travel a distance H from bottom to the top. This method, recently named the seismic interferometry by deconvolution method by Snieder and Safak (2006) has been applied in Chapter 2 and 3, and is summarized by Equation 4.1:

$$D(\omega) = \frac{U_1(\omega)U_2^*(\omega)}{|U_2(\omega)|^2 + \varepsilon} \tag{4.1}$$

where $U_1(\omega)$ is the displacement wavefield in the frequency domain recorded at receiver 1, $U_2(\omega)$ is the reference displacement signal recorded at receiver 2, ω is the angular frequency,

* is the complex conjugate symbol, and ε (set at 10% of the average spectral power) is the stabilization parameter to avoid instability caused by deconvolution (Clayton and Wiggins, 1976). In our study the deconvolution is computed following the Clayton and Wiggins (1976) formulation as follows:

$$H(\omega) = \frac{O(\omega)}{max\left\{I(\omega), k.\left(|I(\omega)|.\frac{I(\omega)}{|I(\omega)|}\right)_{max}\right\}} \tag{4.2}$$

where $H(\omega)$ is the transfer function of the soil column, $O(\omega)$ and $I(\omega)$ the Fourier transforms of the top (output O) and bottom (input I) signal and k the water level parameter ($0 \leq k \leq 1$). By computing the inverse Fourier transform of $H(\omega)$, the pulse travel time gives Vs. Chandra et al. (2014a) computed Vs along the soil profile between two sensors, and in the uppermost layer in the container the Vs was estimated at 242m/s and 197m/s under weak and strong input signals, respectively. In presence of the structures, the soil-structure coupling modifies the strength and stress applied to the soil and dynamic effects may appear during the shaking (Leroueil and Vaughan, 1990), leading to changes of the response of the soil-structure system.

Figure 4.5 shows the average transfer function $H(\omega)$ of the soil, considering all sequences of trials including the two containers and the weak and strong input signals for nonlinear assessment. Using Eq. 4.2, the soil system frequency, f_s, is computed as the peak frequency of the deconvolution between the signal recorded at the top of the soil column (sensor 19 Fig. 4.3a) and the input signal at the bottom of the containers (sensor 2, Fig. 4.3a). For the 2FS cases, two transfer functions are computed using sensor 14 (Fig. 4.3a) instead of sensor 19 for 2FS-2. The damping, D, was estimated using the classical half-power bandwidth method applied to 1D resonant system (Eq. 1.30).

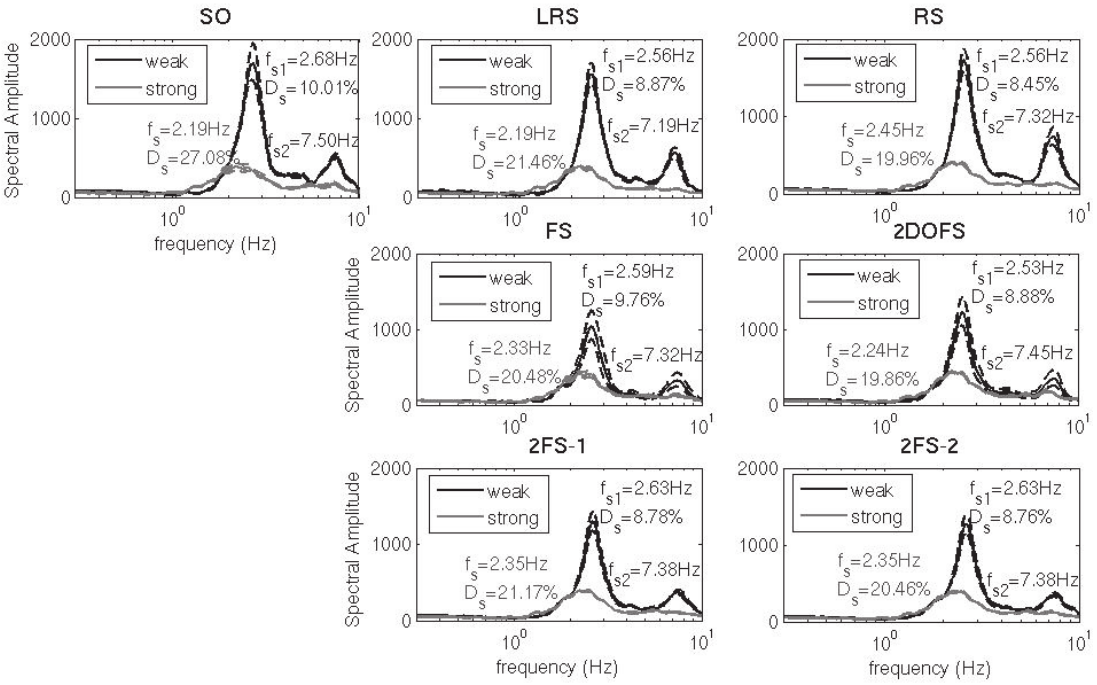

Figure 4.5. Transfer function of the soil computed by deconvolution between signals recorded at the top (sensor 19) and the bottom (sensor 2) of the column considering weak (black) and strong (gray) input motion. fs and D represent the system frequency of the soil and the damping value computed by the half-power bandwidth method. Solid layers are the mean transfer function considering all the trials and dashed layers are mean+/standard deviation computed as proposed by Ktenidou et al. (2011). (SO: Soil Only; LRS:Low Rigid; RS: Rigid; FS: Flexible; 2DOFS: Two degree-of-freedom flexible; 2FS-1 and 2FS-2: two adjacent flexible).

All the results show shift of the frequency to a lower value and an increase of damping between weak and strong input signals, classic of the nonlinear response of the soil (Bonilla et al, 2005; Wu et al, 2009). Under weak motion, $H(\omega)$ show a system fundamental frequency f_{s1} of around 2.6Hz (close to the reference value of 2.7Hz) and a second mode f_{s2} at around 7.5Hz that fits the theoretical shear model (f_k/f_1=3, 5, 7..., k=2:n modes). Under strong motion, the second mode is also observed, however it is less pronounced, reflecting a large increase of damping. In the rest of the manuscript, due to the proximity between the fundamental system frequency of the soil and the expected frequency of the building models, only the fundamental mode will be considered. At this frequency, the amplitude of the transfer function is comparable for all the models. For 2FS model, $H(\omega)$ computed with the first (sensors 2 and 19) or the second (sensors 2 to 14) vertical array gives exactly the same transfer function under weak or strong motion with the same values of frequencies and similar

values of damping. No boundary effects are thus observed that validate the efficiency of the ESB boundary condition as already reported by Chandra et al. (2014a). For each experiment, the soil column in the container is set up following the same procedure (dry pluviation) but slight changes may exist along the soil profile. In the rest of the manuscript for comparing configurations "with or without buildings", we will assume that the soil profile remains the same for all trials. All the results are summarized in Tab. 4.2. and 4.3, including the variation between weak and strong (Δ) and the variation between with and without building models (Δ^*).

Table 4.2. Summary of the frequency and damping of the soil models and percentage of variation (Δ=(strong-weak)/weak) between weak and strong input signals.

		f_s (Hz)	D (%)			f_s (Hz)	D (%)
SO	weak	2.68	10.01	FS	weak	2,59	9,76
	strong	2.19	27.08		strong	2,33	20,48
	Δ	***-22%***	***170%***		***Δ***	***-10%***	***110%***
LRS	weak	2.56	8.87	2DOFS	weak	2,53	8,88
	strong	2.19	21.46		strong	2,24	19,86
	Δ	***-14%***	***142%***		***Δ***	***-11%***	***125%***
RS	weak	2,56	8,45	2FS-1	weak	2,63	8,78
	strong	2,45	19,96		strong	2,35	21,17
	Δ	***-4%***	***136%***		***Δ***	***-11%***	***141%***
				2FS-2	weak	2,63	8,76
					strong	2,35	20,46
					Δ	***-11%***	***134%***

Table 4.3. Summary of the variation Δ^* of frequency, f, and damping, D, due to the presence of the building models. Δ^* = (Building-SO)/SO for weak and strong input signals.

		LRS	*RS*	*FS*	*2DOF*	*2FS-1*	*2FS-2*
$\Delta^* f$	weak	-4%	-4%	-3%	-6%	-2%	-2%
	strong	0%	12%	6%	2%	7%	7%
$\Delta^* D$	weak	-10%	-20%	0%	-10%	-10%	-10%
	strong	-22%	-26%	-26%	-26%	-22%	-26

A clear peak is observed for SO model, moving from 2.68Hz to 2.19Hz (Δ=22% of softening) with increase damping from 10% to 27% between weak and strong input signals. Between weak and strong motion the reduction factor (Δ, Tab. 4.2) for f_s is less important in the presence of buildings than for SO model (22%). This shows that the presence of the building changes the soil conditions, for example by increasing the confining pressure by static loading due to the building weight. Keep in mind that all the models have the same mass (close to 1kg). However, the reduction of frequency is less pronounced in presence of rigid structures (Tab. 4.2), i.e. of about 4% and 11% for rigid (RS) and flexible (FS, 2DOFS and 2FS) structures, respectively. The difference must be explained by the motion of the structure since the dynamic SSI may increase the stress and strain in the uppermost layer during shaking in different way for rigid and flexible buildings.

Under weak motion, we observe slight modification of the site response in presence of structures, f_s moving from (Tab. 4.3) 2.68Hz to 2.56Hz for the rigid structures (Δ*=-4% for LRS and RS), to 2.59Hz for FS (Δ*=-3%) and 2.53Hz for 2DOFS (Δ*=-6%), and to 2.63Hz for 2FS-1 and 2FS-2 (Δ*=-2%). For strong motion (Tab. 4.3), the variation of the frequency (Δ* f_s,), goes in the opposite way, where SO being smaller than other building models, i.e., 0% for LRS, 12% for RS, 6% for FS, 2% for 2DOFS, 7% for 2FS-1 and 2FS-2. The presence of the structure, and consequently the dynamic SSI, contributes to the modification of the site response by limiting the nonlinear strain. Moreover, this modification is not linear since Δ* for weak are completely different from those of strong motion. Furthermore, we observe that Δ* varies with the building model: LRS has no impact on f_s (0%), FS and 2FS have moderate impact, where their presence reduces the nonlinear response of the soil (6 and 7%) and the RS has the strongest impact by reducing of about 12% the nonlinear response of the site in term of frequency shift. Under strong motion, buildings vibrate with largest amplitude due to the inertial effect. In this case, the dynamic loading of the soil due to SSI rocking increases, increasing thus the confining pressure. This is especially the case for RS model where soil nonlinear behavior is less pronounced at high confining pressure.

For the damping, the values are more coherent with the nonlinearity. First, equivalent observations with the frequency variations are found (Tab. 4.2), giving Δ equal to 170% for SO, and smaller Δ values in presence of building (i.e., 142% for LRS, 136% for RS, 110% for FS, 125% for 2DOFS and 141% and 134% for 2FS) with more than 100% of damping

increase whatever the building type. Moreover, A^* increases with the level of shaking, from about 10-20% to 22-26% for weak and strong motion, respectively.

A classical way to further observe the nonlinear behavior of the soil column is to trace the stress-strain curves (e.g., Pavlenko and Irikura, 2002; Pavlenko and Irikura, 2003). Beside the common displacement based stress-strain, the *PGA–PGV/Vs* can be used as wave propagation based stress-strain proxy (Hill et al., 1993; Chandra et al., 2014a). Here we used instantaneous *PGA-PGV/Vs* as a stress-deformation proxy already applied in Chapter 2 and 3. Using a vertical array, we computed the local variation of instantaneous *Vs (Vs*)* in depth by picking the time delay of the pulse travel time between two sensors, and the instantaneous *PGA* and *PGV* values (A^* and V^*) were computed as the average values between two successive sensors in the same manner as in Chapter 3.5 following:

$$A^* = \max\left[\left|\frac{A_i(t)+A_j(t)}{2}\right|\right] \tag{4.3}$$

$$V^* = \max\left[\left|\frac{V_i(t)+V_j(t)}{2}\right|\right] \tag{4.4}$$

where i and j indicate two successive sensors, and A and V indicate the acceleration and velocity time histories.

We traced in Figure 4.6, the $A^* – V^*/Vs^*$ curve for the model tested, ranging the *Vs* according to the velocity classes of Eurocode 8 (<180m/s; 180-360 m/s; 360-800 m/s; and >800m/s). Hyperbolic models are fitted to the weak and strong data, reproducing the nonlinear response of the site (Chap. 2.3, 2.4, and 3.6). As for the analysis of the transfer function, we see modification of the soil nonlinearity response depending on the type of structures. For SO model, a nonlinear response is observed, the slope of the hyperbolic model changing with the value of instantaneous *Vs* measured along the soil profile. Nonlinearity is clearly observed as previously reported by Chandra et al (2014a). For rigid buildings (LRS and RS), equivalent hyperbolic models are computed with different slopes for each soil class. For flexible buildings, the nonlinearity is less pronounced, much more data being finally classified in stiff soil ($360<Vs<800$ m/s).

Once again, the presence of the building reduces the nonlinear response of the soil by artificially increasing the confining pressure of the soil, reducing then the soil strain for equivalent stress. As shown in Tab. 4.3, in case of the LRS model nonlinear response does not change significantly (e.g. Δ*=0% for strong motion), hyperbolic model being equivalent to SO model. For the RS model, the hyperbolic model is close to a straight line suggesting a reduction of the nonlinear response in presence of a rigid structure. This suggests a strong coupling due to SSI that increases the confining pressure below the footing during strong motion through the rocking motion. Finally, for flexible structures *Vs** is larger, more data ranging in the 360-800 m/s class of soil. Green and blue classes have the same hyperbolic model slope, as well as the yellow class for FS model, the difference of the nonlinear response Δ* between SO and flexible structure (Tab. 4.3) being moderate.

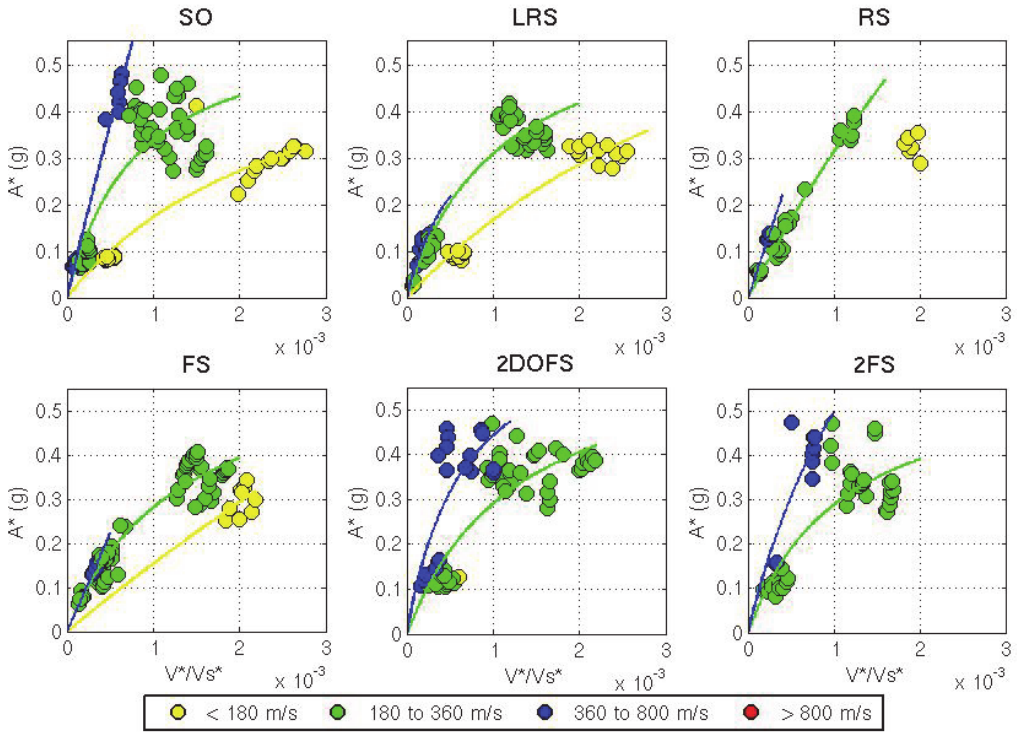

Figure 4.6. *A*–V*/Vs** curves for different velocity groups and type of structures. (SO: Soil Only; LRS:Low Rigid; RS: Rigid; FS: Flexible; 2DOFS: Two degree-of-freedom flexible; 2FS-1 and 2FS-2: two adjacent flexible).

The damping estimated in Fig. 4.5 and the corresponding strain displayed in Fig. 4.6 are comparable to the results from Li et al. (2013) for Fontainebleau sand. For strains between 1 and $3x10^{-3}$, damping are ranged between 20-25% (20-27% in our results) and for strain value

around 2-5x10^{-4}, damping are ranged between 5-15% (9-10% in our results). Li et al. (2013) also showed that the variation of damping values of the soil response was smaller for larger confining pressures. In our analysis, these effects are also shown (Tab. 4.2), the variation of damping moving from 170% to around 136% between SO and RS models, and to around 128% (mean value) for flexible models. This confirms also the confining pressure induced by the building.

These observations question the validity of nonlinear models extracted from samples collected in-situ free-field and the nonlinear response of the site once the buildings constructed. The effects may be non-negligible as in our case the nonlinear effects of the soil response can be doubled (in terms of frequency variation) between the free-field and urban-field (Tab. 4.2). The type of the structure also affects the nonlinear response of the soil due to the dynamic soil-structure interaction. In this example, rigid structure reduces the most the nonlinear response compared to the SO model. This effect is strongly nonlinear between weak and strong motion, suggesting a nonlinear SSI effect changing the response of the building and then of the soil. This must be confirmed by analysis the response of the building models.

4.4. Fixed-base, Rigid-body, Rocking and System Frequency of Vibration

In this section, the soil-foundation-structure interaction models from centrifuge tests with coupled horizontal and rocking response are analyzed in the frequency and time domains under weak and strong motion. The identified parameters in both domains are related. Under seismic excitation, the total horizontal motion of the structure x_{tot} can be expressed as:

$$x_{tot} = x_g + x_1 + x_H + h\phi \tag{4.5}$$

where x_g is the ground displacement, x_H is the foundation translation, $h\phi$ (h: height of the building) is the displacement due to the rocking of the foundation around the axis perpendicular to the horizontal motion, and x_1 is the structural displacement of the structure. In this equation we assumed a null vertical displacement at the top of the structure. Finally, the damage in the building will depend only on x_1 equivalent to the relative structural drift between the top and the bottom of the structure. The soil-structure coupling system model is reported in several scientific papers such as Stewart and Fenves (1998), Todorovska and

Trifunac (2008), Todorovska (2009a, 2009b), Pecker (2007), and Trifunac et al. (2010), in which the identification is done by processing input and output signals recorded in the soil-structure system. Two specific cases of the model in Eq (4.5) are the flexible structure on rigid soil, named fixed-base, and the rigid structure on flexible soil. In the first case, the anchoring condition at the soil-foundation is perfectly clamped and the ground and the foundation move in the same way. The frequency of the building f_1 is considered as the fixed-base frequency. For the second case, the soil is modelled as spring and dampers for each degree-of-freedom and the building vibrates at its rigid-body frequency f_{RB}. It is also assumed that the rotation (rocking) of each floor was equal to the rocking of the foundation. Usually, structure and soil are flexible and the total motion of the building vibrates at the system frequency (f_{sys}), below the fixed-base frequency due to the flexibility and the deformability of the soil. Luco et al. (1988) proposed the approximate equation relating the component of the soil-structure system as:

$$\frac{1}{{f_{sys}}^2} = \frac{1}{f_1^2} + \frac{1}{f_{RB}^2} \tag{4.6}$$

According Eq. 4.5, the horizontal and rocking stiffness of the foundation correspond to the rigid-body motion of the foundation. Consequently, Eq. 4.6 can be rewritten as:

$$\frac{1}{{f_{sys}}^2} = \frac{1}{f_1^2} + \frac{1}{f_\phi^2} + \frac{1}{f_H^2} \tag{4.7}$$

where f_H and f_ϕ are the frequencies related to the horizontal and rocking foundation motion. This equation implies that if the building is very stiff ($f_1=\infty$), the system frequency f_{sys} is equivalent to the rigid-body frequency f_{RB}.. Furthermore, if the soil is very stiff, the system frequency is equal to the building frequency. An exceptional situation also exists: if the foundation is very stiff in the horizontal direction, the horizontal foundation can be neglected. The pseudo-flexible body frequency is equal to:

$$\frac{1}{{f_{app}}^2} = \frac{1}{f_1^2} + \frac{1}{f_\phi^2} \tag{4.8}$$

named apparent frequency f_{app} herein. This situation is found in the case of a very specific system of foundation or when we can remove the horizontal motion of the foundation to the total building motion. For example, Snieder and Şafak (2006) showed that the system identification by deconvolution between top and bottom of the building corresponded to the fixed-based frequency, even though the rocking was not removed from the horizontal recordings. To the contrary, Todorovska (2009a) asserted that the deconvolution gives apparent frequency rather than fixed-base frequency. Stewart and Fenves (2008) summarized (Tab. 4.4) the input and output signals of the soil-structure system that actually represent the information required for system identification.

Table 4.4. Input and output signals for system identification procedures (Stewart and Fenves, 2008)

System	Input	Output
Flexible base	x_g	$x_g + x_H + h\phi + x_1$
Pseudo-fixed base	$x_g + x_H$	$x_g + x_H + h\phi + x_1$
Fixed base	$x_g + x_H + h\phi$	$x_g + x_H + h\phi + x_1$

In fact, the identification of the system can be directly derived from seismic recordings done in suitable localization in the structure. For the identification of centrifuge models, we computed the component of building motion with the sensors described in Fig. 4.3 (number of sensor is noted in brackets):

- the total system frequency, $f_{tot,}$ is the peak frequency of the total signal x_{tot} recorded at the top of the building, using [30];
- the system frequency, f_{sys}, is the peak frequency of the motion recorded on top, reduced by the free-field motion assuming that the free-field is not contaminated by the building vibration. Herein the system frequency will be obtained by deconvolution between the top [30] and the free-field [14] signals, according the Clayton and Wiggins (1976) formulation (Eq. 4.2);
- the apparent frequency, f_{app}, is the peak frequency of the transfer function obtained by deconvolution (Eq. 4.2) between the signal recorded on top [30] and bottom [29] of the building;

- the rocking frequency, f_ϕ, is computed as proposed by Paolucci (1993) and Guéguen and Bard (2005) by dividing the vertical motion of the two opposite extremities of the foundation as :

$$f_\phi = max\left(FFT\left[\frac{(V_1(t) - V_2(t))h}{B}\right]\right) \tag{4.9}$$

with FFT means the Fast Fourier Transform, $V_1(t)$ and $V_2(t)$ are the time histories of the vertical foundation motion, i.e. sensors [27] and [28], B is the distance between V_1 and V_2.

- the horizontal frequency, f_H, is the peak frequency of the deconvolution (Eq. 4.2) between the horizontal signal recorded on the foundation [29] and on free-field [14]. This motion reflects the kinematic interaction due to scattering of waves on the footing and is expected to be the same for all the models because of similar footings.
- the fixed-base frequency, f_1, is computed using several ways:
  - First, the time delay τ of the pulse travel time along the building was computed by Todorovska and Trifunac (2008) and they assumed the relationship between frequency and time delay if the building responses primarily in shear:

$$f_1 = \frac{1}{4\tau} \tag{4.10}$$

In our case f_1 is obtained by manually picking the time delay of the pulse between the bottom [29] and the top [30] obtained by inverse Fourier Transform of deconvolved function (Eq. 4.2).

  - The fixed-based frequency can also be computed as the peak of the function $\Psi(\omega)$ obtained after removing the rocking motion from the rigid-body motion, as proposed by Paolucci (1993). Herein, the deconvolution is then computed following Eq. 4.2 in which we considered the total motion at the top x_{tot} [30] and the rigid-body motion of the foundation $x^{tot}_{RB} = x_g + x_H + h\phi$ [29 + 27&28], i.e. (capital letters mean Fourier transform):

$$\psi(\omega) = \frac{X_{tot} X_{RB}^{tot*}}{|X_{RB}^{tot}|^2 + \varepsilon} \tag{4.11}$$

In addition, damping was estimated by the half-power bandwidth method (Eq. 1.30).

4.5. Results and Analysis

Similar to the soil only model, two containers, several trials, and weak and strong input signals were considered for centrifuge tests. For each building model, the mean results +/- standard deviation of the trials are presented and the effect of the nonlinearity on each component of the model is compared using the SSI models described above. Chazelas (2010) gave the expected fixed-base frequency used as reference, i.e. 2.65Hz for FS and 2FS, and 0.78Hz and 2.99Hz for the first two modes of the 2DOFS. The reference f_1 for RS is calculated from the mass and the stiffness (using equivalent Young's modulus) of the structure, i.e. 4.05Hz. In addition, we focused our analysis on the nonlinear response of the SSI model. Finally, the importance of the SSI was also analyzed by computing the coherence between rocking and structural drift as proposed by Bard (1988). All the values of frequency are summarized in Tab. 4.5. The damping analysis is only detailed in the text.

Table 4.5. Summary of the frequency values (in Hz) obtained in centrifuge tests*.

		1	*2*	*3*	*4*	*5*	*6*	*7*	*8*	*9*	*10*
		f_{tot}	f_{sys} (1)	f_H	f_ϕ	f_{app} (1)	f_1	f_{app} (2)	f_{sys} (2)	Δf_{app}	Δf_{sys} (1)
RS	weak	2.51	2.69	2.69	2.46	2.64	2.72	1.82	1.51	-45%	-78%
	strong	1.82	2.33	2.42	1.83	2.13	2.23	1.41	1.22	-51%	-91%
	Δ	**-27%**	**-13%**	**-10%**	**-26%**	**-19%**	**-18%**	**-23%**	**-19%**		
FS	weak	2.15	2.05	2.87	2.30	1.99	2.34	1.64	1.42	-21%	-44%
	strong	1.50	1.59	2.45	1.83	1.58	1.88	1.31	1.16	-21%	-37%
	Δ	**-30%**	**-22%**	**-15%**	**-20%**	**-21%**	**-20%**	**-20%**	**-18%**		
2DOFS mode 2	weak	2.61	2.70	2.59	2.60	2.74	2.73	1.88	1.52	-46%	-78%
	strong	2.43	2.54	2.42	2.39	2.60	2.73	1.80	1.44	-44%	-76%
	Δ	**-7%**	**-6%**	**-7%**	**-8%**	**-5%**	**0 %**	**-4%**	**-5%**		

* Columns 1 to 6 are obtained from the data, with f_1 is computed using Eq. 4.11. Columns 7 and 8 are obtained from equations 4.7 and 4.8. Columns 9 to 11 (gray zone) are the error between direct estimation of frequency using data and empirical equations (9=7-5/7; 10=8-2/8). The rows labelled ***Δ*** correspond to the percentage of variation between weak and strong motion (strong-weak)/weak.

4.5.1. Total Motion - x_{tot}

Fig. 4.7 presents the horizontal total motion, x_{tot}, for the RS, FS and 2DOFS models. The nonlinear effect is observed through the shift of the frequency and the increase of the damping of the soil-structure-footing system between weak and strong input signal. Since the input ground motion x_g is included in the total motion, the amplitude of the Fourier spectra increases between weak to strong motion.

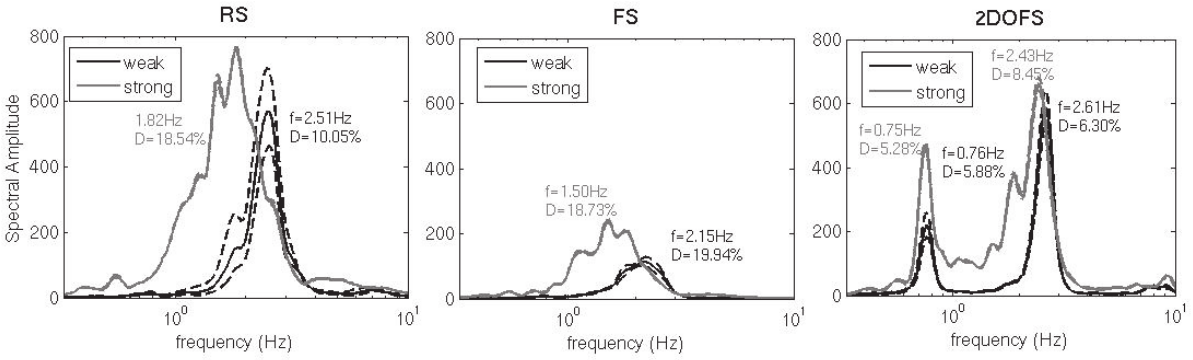

Figure. 4.7. Fourier transform of the total motion of the rigid (RS), flexible (FS) and two DOF flexible (2DOFS) structures. The black and gray lines are for the weak and strong input signals, respectively. Continuous and dashed lines represent the mean and the mean+/-standard deviation of the transfer function, respectively, computed from all the trials performed in centrifuge tests.

The total frequencies move from 2.51Hz to 1.82Hz (Δf=-27%), 2.15Hz to 1.50Hz (-30%) and 2.61Hz to 2.43Hz (-7%) for the RS, FS and the second mode of 2DOFS model, respectively. Damping increase with values moving from 10.1% to 18.5% ($\Delta\zeta$=8.4%) and 6.3% to 8.5% (2.2%) for the RS and the second mode of 2DOFS model, respectively. For the FS model, the damping increases from 19.9% to 18.7% (-1.2%) this variation nevertheless is not significant compared to the accuracy of the method. Frequency and damping show that RS and FS buildings have the same sensitivity to the nonlinearity in term of total frequency, even though the response of the soil for RS was less nonlinear (Δfs=4%, Tab. 4.2). This observation may be explained either by different nonlinear response of the fixed-base systems or by the increase of the nonlinear SSI for RS. We observe also that the first mode of the 2DOFS is not affected by the nonlinearity, with equivalent frequency and damping for weak and strong motion. This may be due to the proximity between the soil resonance frequency (2.5Hz, see

Tab. 4.2) and the model frequency of the second mode, or to the lesser soil-structure coupling of the first mode.

4.5.2. Horizontal Motion - x_H

Fig. 4.8 presents the horizontal motion of the SSI model for the LRS, RS, FS and 2DOFS cases. As expected for this motion, the functions are very similar in amplitude and in shape regardless the model.

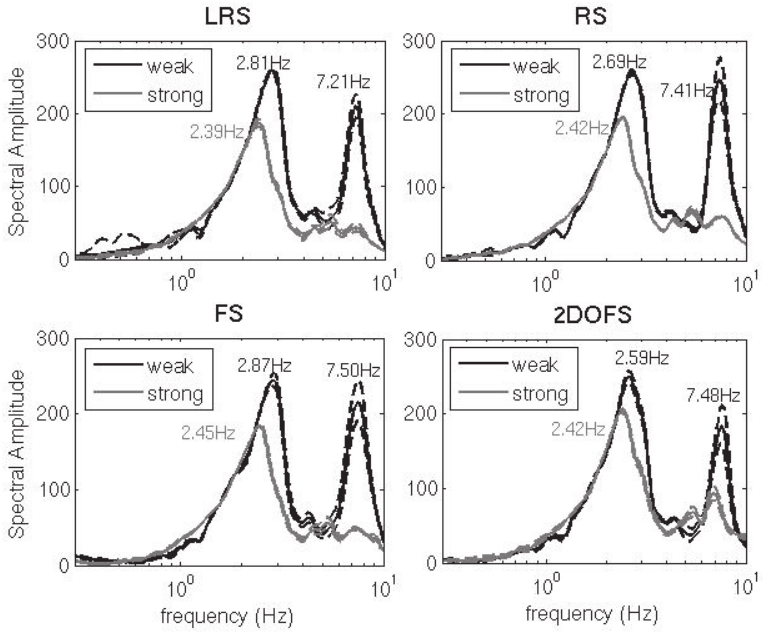

Figure 4.8. Transfer function of the horizontal motion x_H for the low rigid (LRS), rigid (RS), flexible (FS) and two DOF flexible (2DOFS) structures. The black and gray lines are for the weak and strong input signals, respectively. Continuous and dashed lines represent the mean and the mean+/-standard deviation of the transfer function, respectively, computed from all the trials performed in centrifuge tests.

This motion represents the kinematic interaction influenced by the type of the footing. In our case, all the footings are the same and LR model corresponds to the reference model for the kinematic interaction. Moreover, Lai and Martinelli (2013) noticed that for shallow foundations struck by vertically propagating S-wave (which corresponds to the centrifuge test), the kinematic interaction is negligible. For all cases, two frequencies are observed at

around 2.7Hz and 7.5Hz, close to the natural frequencies of the soil. The effect of the strong motion is also well observed, the amplitude of the function being reduced, i.e. the first frequencies moves to around 2.4Hz corresponds to a softening of Δf=15% for LR, 10% for RS, 15% for FS and 7% for 2DOFS. This nonlinear effect is of the same order of magnitude with the nonlinear effect observed for SO model (Tab. 4.2).

4.5.3. Motion of the Soil-Structure System - $x_1+x_H+h\phi$

Fig. 4.9 displays the spectra of the soil-structure system motion and the peak of the frequency correspond to f_{sys}. Nonlinearity is observed by (1) a shift of the frequency from 2.69Hz to 2.33Hz (Δf=*-13%)* for RS, from 2.05Hz to 1.59Hz (*-22%)* for FS and from 2.70Hz to 2.54Hz (*-6%)* for the second mode of the 2DOFS; (2) an increase of the damping from 13% to 17% ($\Delta\zeta$=4%) for RS, from 13% to 16% (3%) for FS and from 6% to 10% (4%) for the second mode of 2DOFS; (3) a reduction of the spectral amplitude between weak and strong motion once the input signal removed from the total motion of the structure; (4) no effect of the magnitude of the input signal on the 2DOFS first frequency (0.76Hz) and damping (5.5%).

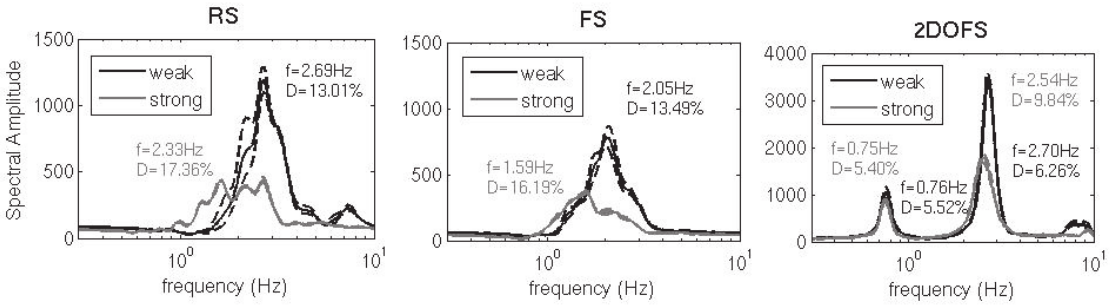

Figure. 4.9. Transfer function of the system motion $x_1+x_H+h\phi$ for the rigid (RS), flexible (FS) and two DOF flexible (2DOFS) structures. The black and gray lines are for the weak and strong input signals, respectively. Continuous and dashed lines represent the mean and the mean+/-standard deviation of the transfer function, respectively, computed from all the trials performed in centrifuge tests.

The system response of RS model is less affected than for FS model in terms of frequency (13% versus 20% of softening), consistent with the nonlinearity observed for the soil response (Tab. 4.2 and 4.3). The nonlinear soil-structure interaction may then affect the system motion through the nonlinearity of the soil and of the coupling, RS reducing the nonlinearity of the

soil through the dynamic rocking loading. The second mode of 2DOFS model is less affected in term of frequency while in term of damping it is strongly influenced by the strong shaking. The variation of the system damping is much smaller than the damping of the soil observed in Tab. 4.2 (Δ>100%), system damping being finally less influenced by the soil nonlinearity.

4.5.4. Rocking motion - hϕ

Fig. 4.10 displays the spectra of the rocking motion and the peak of the frequency corresponds to f_ϕ. We neglected in this part the rotation of the soil that can contribute also to the total rocking of the footing.

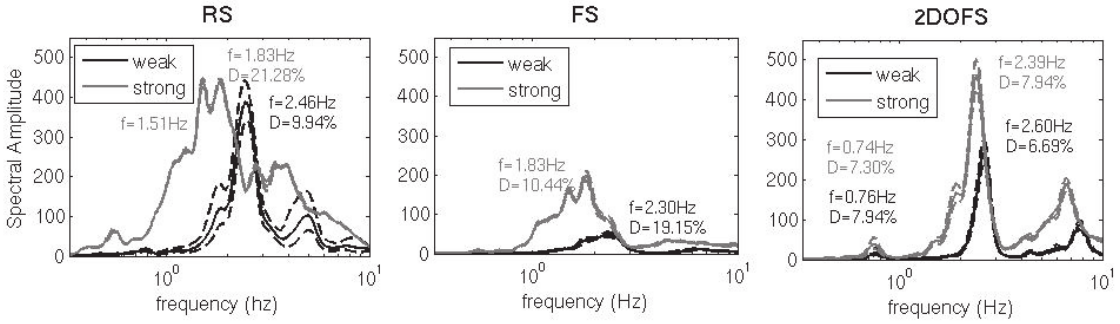

Figure. 4.10. Spectrum of rocking motion $h\phi$ for the rigid (RS), flexible (FS) and two DOF flexible (2DOFS) structures. The black and gray lines are for the weak and strong input signals, respectively. Continuous and dashed lines represent the mean and the mean+/-standard deviation of the transfer function, respectively, computed with all the trials performed in centrifuge tests.

We observe that the importance of the rocking increases with the level of shaking for FS and 2DOFS models, therefore reflecting the importance of the rocking in the total motion of the structure under strong ground motion. For the rigid building, the amplitude of the rocking motion is comparable for weak and strong motion. The nonlinear response is observed also between weak and strong input signals, the rocking frequency moving from 2.45Hz to 1.83Hz (Δf=-26%), 2.30Hz to 1.83Hz (-20%) and 2.60Hz to 2.39Hz (-8%) for the RS, FS and 2DOFS (second mode) models. Damping increase from 10% to 21% ($\Delta\zeta$=11%) and 7% to 8% (1%) for RS and 2DOFS while the damping is reduced for FS model from 19% to 10% ($\Delta\zeta$=-9%). If we compare with the total motion of the structure (Fig. 4.7), we observe that the rocking

spectra are very similar, both in terms of shape and frequency and damping values. We also note that the frequency variations from weak to strong are very similar for rocking and total motion, and to the same order of magnitude for damping. We can conclude on the importance of rocking in the total motion of structures with shallow foundation as also reported by Bard (1988). Furthermore, the amplitude of the rocking under strong and weak motion is more pronounced for RS than FS, in favor of the explanation given for the soil nonlinear response observed Fig. 4.5. Dynamic soil loading through SSI rocking is thus confirmed as being the main origin of the modification of the nonlinear response of the soil. Once again, the strong motion does not affect the first mode of 2DOFS model and the amplitude of the rocking is very small compared to the second mode, the proximity of the soil resonance frequency and the second mode amplifying the rocking motion.

4.5.5. Pseudo-flexible Motion - $x_1+h\phi$

Fig. 4.11 displays the spectra of the pseudo-flexible motion and the peak of the frequency corresponds to f_{app}. According to Todorovska (2009b), f_{app} corresponds to the system neglecting the horizontal motion of the foundation. We observe Figs. 4.9 and 4.11 equivalent functions between system and pseudo-flexible motions in term of shape, peak frequency and damping, allow us to assume a small contribution of x_H.

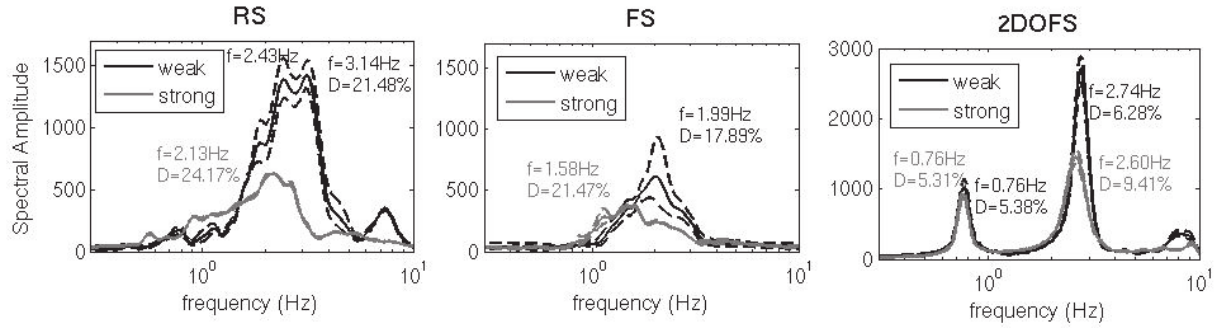

Figure. 4.11. Spectrum of the pseudo-flexible motion x_{sys}/x_H for the rigid (RS), flexible (FS) and two DOF flexible (2DOFS) structures. The black and gray lines are for the weak and strong input signals, respectively. Continuous and dashed lines represent the mean and the mean+/-standard deviation of the transfer function, respectively, computed from all the trials performed in centrifuge tests.

The pseudo-flexible frequencies move from 2.64Hz (mean of the double peaks, see Fig. 4.11) to 2.13Hz (Δf=-19%), 1.99Hz to 1.58Hz (-21%) and 2.74Hz to 2.6Hz (-5%) for the RS, FS and 2DOFS (second mode) models. Damping increases from 21% to 24% ($\Delta\zeta$=12%), 18% to 21% (20%) and 6% to 5% (14%) for RS, FS and 2DOFS, the values of variation being of the same order of magnitude as for the system motion. Once again, the first mode of the 2DOFS model is not affected by the strong motion.

4.5.6. Fixed-base motion - x_1

The fixed-base motion is certainly the most difficult element to assess. In this manuscript we considered Eq. 4.11 based on the deconvolution formulation. Fig. 4.12 shows the fixed-base response spectrum and the frequency peak of the function corresponds to f_1. For 2DOFS model, the fixed-base motion computed both by model and equations are quite the same. We observe no significant shifts of the 2DOFS model response, the fixed-base frequency for mode 1 (0.82 to 0.80 Hz) and mode 2 (3.04 to 3.07Hz) being almost exactly the same under weak and strong motion, and close to the theoretical frequencies provided by Chazelas (2010), i.e. 0.78 and 2.99Hz. The variation of the damping is also not significant in term of nonlinearity, and finally we can assume a perfect linear and elastic response of the fixed-base structure. For RS, the fixed-base frequency moves from 2.72 to 2.23Hz (Eq. 4.11) with equivalent damping values (about 15%). For FS, we observe a shift of the frequency from 2.34 to 1.88Hz but much dispersion is observed in the data (Fig. 4.12).

Finally, Tab. 4.5 also compares the frequency values that are extracted directly from the data using deconvolution or Fourier transform processes and the based-model empirical relationships (Eqs. 4.7 and 4.8). As we can see, the error is quite large, keeping the same order of magnitude between weak and strong shaking. For rigid building, the error is around 40-50% for apparent frequency (pseudo-flexible motion) and 75-90% for system frequency. But the empirical equation proposed by Luco et al. (1987) supposes several assumptions, for example a shear response of the structure, the same rotation (rocking) at the foundation and at the top of the structure, an in-phase motion for the rocking, horizontal, structural and system motion, etc. These hypotheses can be accepted in specific and actual buildings but not in all cases, such as in these centrifuge test models. For example, the equivalent continuous beam model used for the centrifuge tests suggest a response of the structure not in shear as

confirmed by the ratio of the second and first mode of the 2DOFS model. Moreover, Fig. 4.13 shows the comparison of the fixed-base frequency computed from the time delay of the pulse travel time (Eq. 4.10) and the deconvolution (Eq. 4.11). We observe a bias using the time delay, similar with Michel et al. (2013) who showed that this empirical relationship does not represent most of the actual buildings and need to be modified for building that does not have a pure shear deformation.

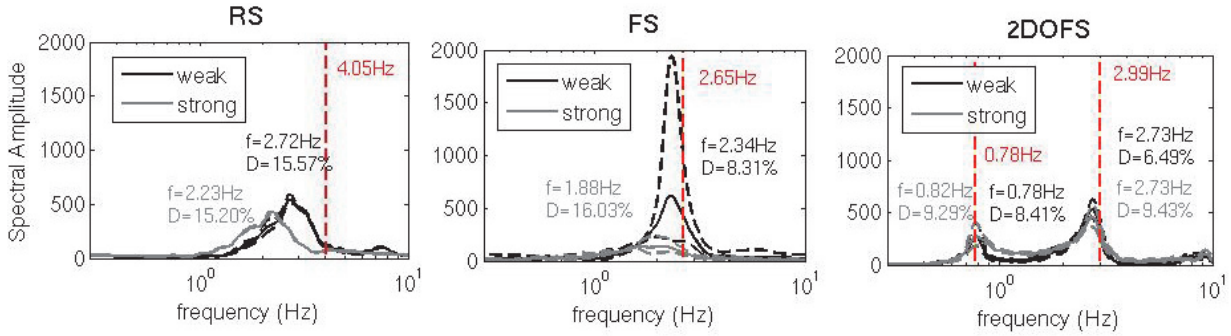

Figure 4.12. Spectrum of the fixed-base motion x_1 for the rigid (RS), flexible (FS) and two DOF flexible (2DOFS) structures. The black and gray lines are for the weak and strong input signals, respectively. Continuous and dashed lines represent the mean and the mean+/-standard deviation of the transfer function, respectively, computed from all the trials performed in centrifuge tests. The red dashed lines show the reference fixed-base frequency value from Chazelas (2010).

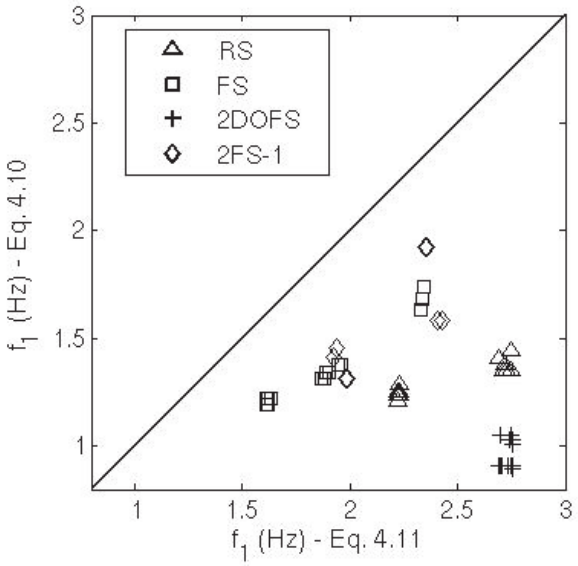

Figure 4.13. Comparison of fixed-base frequency computed from Eq. 4.10 and from deconvolution method (Eq. 4.11).

4.5.7. Nonlinear Soil-Structure Interaction

The nonlinearity observed for the building response is with the same order of magnitude as the variation of the soil response between the weak and strong motion. The nonlinearity of the soil reduces the shear wave velocity and increases its deformability. Hence, the soil nonlinearity partially controls the soil-structure interaction.

The importance of the SSI is confirmed Fig. 4.14, showing the coherency between rocking and fixed-based motion as proposed by Bard (1988).

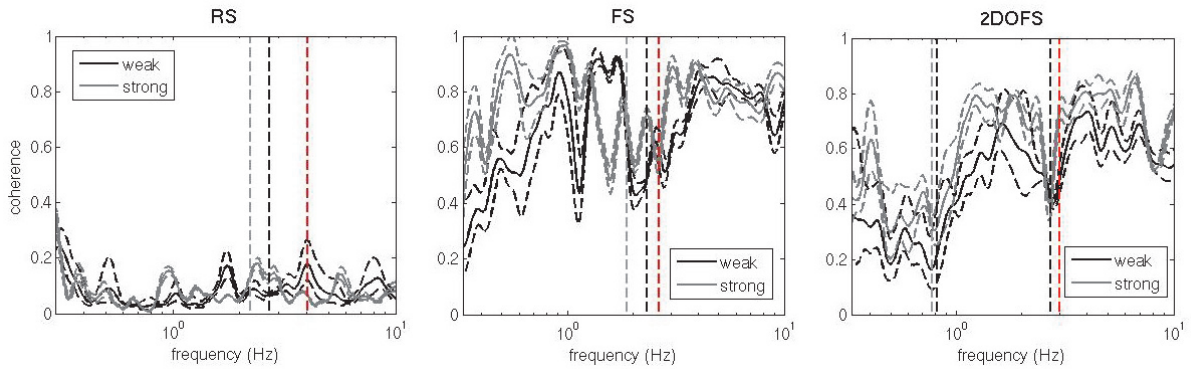

Figure 4.14. Coherency between fixed-base and rocking motion for the rigid (RS), flexible (FS) and two DOF flexible (2DOFS) structures. The black and gray lines are for the weak and strong input signals, respectively. Continuous and dashed lines represent the mean and the mean+/-standard deviation of the transfer function, respectively, computed from all the trials performed in centrifuge tests. The red dashed lines show the reference fixed-base frequency value from Chazelas (2010) and the vertical gray and dashed lines correspond to the fixed-frequencies computed for weak and strong motion, respectively.

We observe that for rigid structure RS, the coherence is very low suggesting a small SSI contribution to the total motion of the structure. This is in contradiction with the fact that rocking is dominant in the total motion of the structure. But the building is very stiff and it moves as a rigid body resting on a soft soil. Structural drift is rather limited and the coherency between drift and rocking as no sense in this case. For FS model, the coherency is over 0.6 at the frequencies of the structure (fixed-based), more important than for the 2DOFS (0.4). The nonlinear behavior of the soil may then control the nonlinear response of the system, through

the nonlinear rocking of SSI: at the fixed-base frequency, the coherency increases slightly with the amplitude of shaking that confirms the predominance of the nonlinear SSI, the nonlinear rocking being less pronounced for 2DOFS (-8%) than FS (-20%). For 2DOFS, the first mode has a small coherency (less than 0.2). This is related to the frequency deviation between soil and the first mode, confirming that the small predominance of SSI when building frequency is below the soil frequency.

We observe that the first mode of the 2DOFS is not affected by the nonlinearity (Figs. 4.7 to 4.12) and its frequency value remains the same. The first mode is far from the resonance frequency of the soil and the coupling is less at this frequency. The second mode reacts slightly and by comparing the variation of the fixed-base frequency and the frequencies of the interaction (f_H and f_ϕ) we note that the nonlinearity of the system is mainly dominated by the soil-structure coupling with a softening of around 5% while the site response (Tab. 4.2) is of about 11%. At this second mode, the structure may move out-of-phase with the foundation and the coupling remains limited.

The rigid and flexible models (RS and FS) show a softening of the total frequency of about 27% and 30%, respectively. Flexible buildings show more nonlinear total response compare to rigid buildings if we compare the frequency reduction, either for fixed-base, system or total frequencies. This finding is in agreement with Nader and Astaneh (1991) who showed similar results on steel-frame buildings. Moreover the differences between weak and strong motion for fixed-base and system frequencies are respectively equal to -18% for RS and -20% for FS; -13% for RS and -22% for FS, suggesting RS reduce the nonlinear response of the system. In addition, total frequency variation is the smallest for RS and assuming the same experimental condition for FS and RS (i.e., same input signal and same soil) the nonlinear response of the system is controlled by the soil-structure interaction. In fact, the rocking is the most important component of the soil-structure interaction and moreover it is the most sensitive parameter to the nonlinearity compared to fixed-base and horizontal motion (Tab. 4.5). Figure 4.10 has showed that this is the component that controls the building motion whatever the type of structure. The nonlinearity of the rocking is more pronounced for RS model than for other models, with a largest softening of the rocking frequency compared to the other motion. We can conclude that the rocking motion produces a positive effect for reducing the nonlinear response of the soil and of the SSI. This can be due to a dynamic local loading of the soil. This is also confirmed looking at the site response in the presence of rigid structure. This

phenomenon is dominant in case of RS. Nevertheless, it is also reported for FS, the rocking being more nonlinear, reducing then the nonlinearity of the site response in the presence of FS compared to SO model.

Finally we can conclude on the role of the nonlinear response of the soil and of the soil-structure interaction during earthquake:

(1) The rocking motion is dominant in the total motion of the structure and this is the component the most sensitive to the nonlinearity. The soil nonlinearity is thus the parameter controlling the nonlinear response of the system, impacting more the rocking motion even if the other motion must not be definitively neglected.

(2) The presence of the building changes the site response as well as its nonlinear response. In presence of structure, the nonlinear response of the soil is less pronounced: the rocking motion increases then the confining pressure and reduces the deformation of the soil. This phenomenon is larger for rigid building.

This observation questions the reliability of the nonlinear model of soil defined without building consideration. In order to improve the prediction of the building response for design, the site response must integrate the effect due to the presence of the structure with the nonlinear response of the soil and of the soil-structure interaction. But also the dynamic loading of the soil produced by the building motion through the rocking must be integrated, which can increase the cyclic stress in the uppermost layer. In presence of saturated soil, the response could be different, the dynamic and cyclic loading due to the rocking being able to increase the liquefaction.

4.5.8. The Case of the Adjacent Stand-alone Buildings

The centrifuge test was performed to analyze the behavior of two adjacent buildings. A similar attempt has been carried by Chazelas et al. (2003) and Trombetta et al. (2013, 2014), however considering different types of buildings. In our setup (Fig. 4.15), building 2FS-1 was similar to the 2FS-2 in terms of frequency response. The 2FS-1 was exactly the same as the FS. In addition, even though the 2FS-2 has a different design, it was assembled so that the center of mass and rigidity, as well as the theoretical fixed-base frequency were similar with

2FS-1. The distance between 2FS-1 and 2FS-2 was 200mm at the centrifuge scale (60g), corresponding to 12m in the reality, i.e. half of the footing dimension.

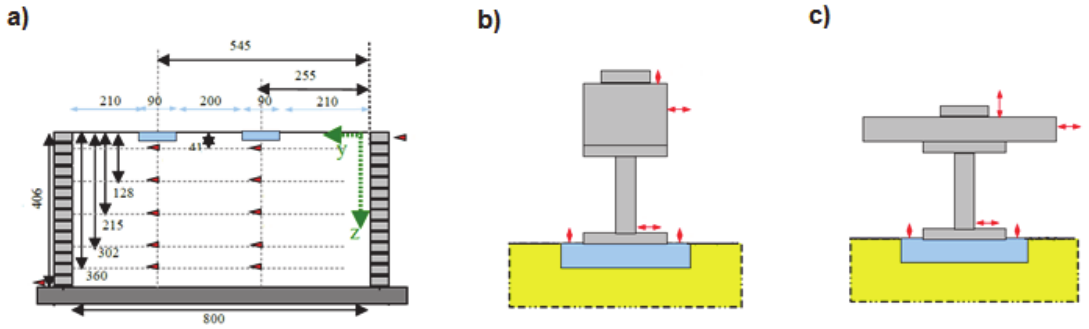

Figure 4.15. Description of the 2FS model (modified from Chazelas, 2010). The number indicates model dimension in mm. (a). Y-Z plan view (b). 2FS-1 model localized on the left in the container (c). 2FS-2 model localized in the right side. Red arrows show the sensor installed on the building, both horizontal and vertical.

The SSI model analysis is done as for stand-alone single buildings carried out in the previous section. Figs 4.16-4.19 show the results for total, apparent, fixed-base, and rocking frequency of the two adjacent buildings. The system and horizontal frequency are not able to be computed due to non-existence of free-field sensors on the setups.

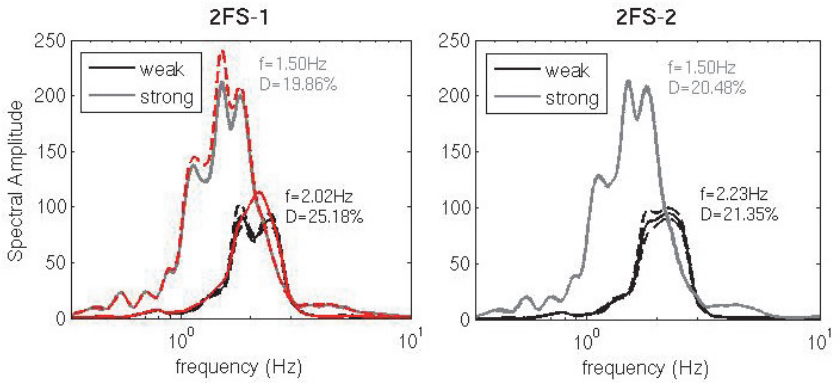

Figure 4.16. Total frequency of the two adjacent stand-alone and flexible buildings (2FS) obtained by computing the FFT of the recording at the top of the structure. The black and gray lines are for the weak and strong input signals, respectively. Continuous and dashed lines represent the mean and the mean+/-standard deviation of the transfer function, respectively, computed from all the trials performed in centrifuge tests. Solid and Dashed red lines represent the mean of total responses of FS for weak and strong, respectively

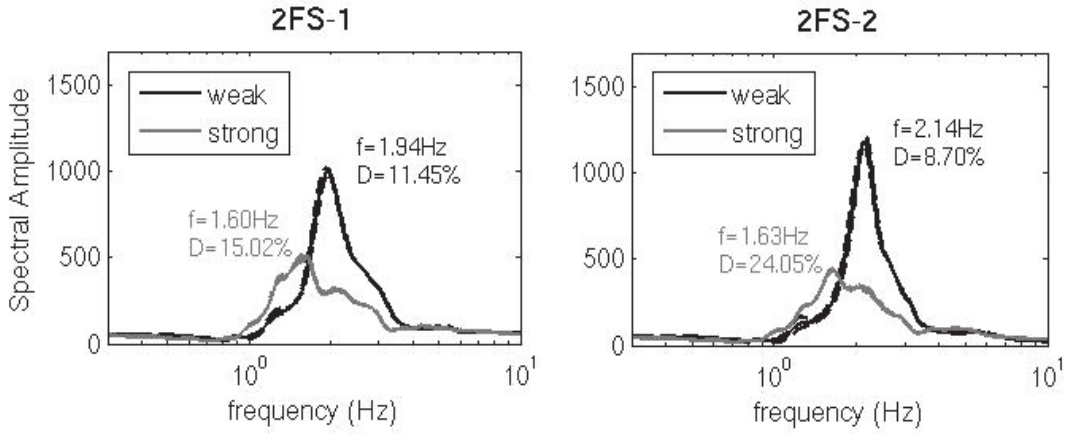

Figure 4.17. Apparent (pseudo-flexible) frequency of the two adjacent stand-alone and flexible buildings (2FS) obtained by top/bottom deconvolution. The black and gray lines are for the weak and strong input signals, respectively. Continuous and dashed lines represent the mean and the mean+/-standard deviation of the transfer function, respectively, computed from all the trials performed in centrifuge tests.

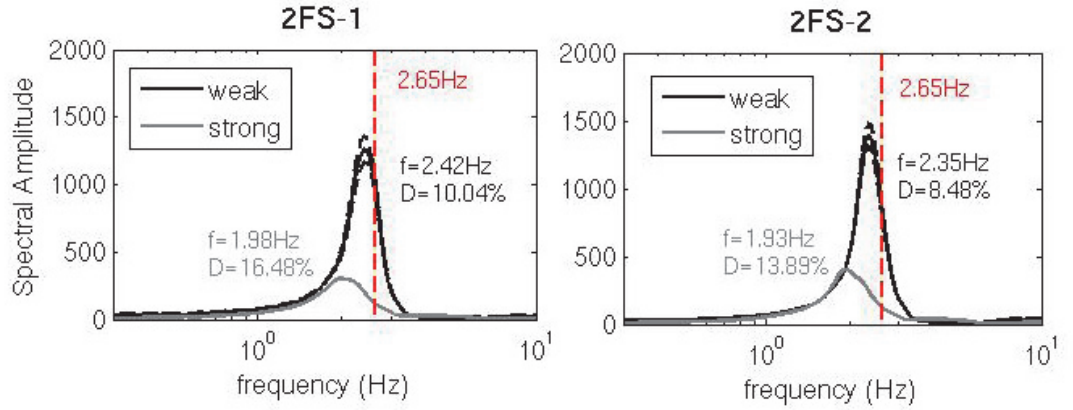

Figure 4.18. Fixed-based frequency of the two adjacent stand-alone and flexible buildings (2FS) obtained with Eq. 4.11. The black and gray lines are for the weak and strong input signals, respectively. Continuous and dashed lines represent the mean and the mean+/-standard deviation of the transfer function, respectively, computed from all the trials performed in centrifuge tests.

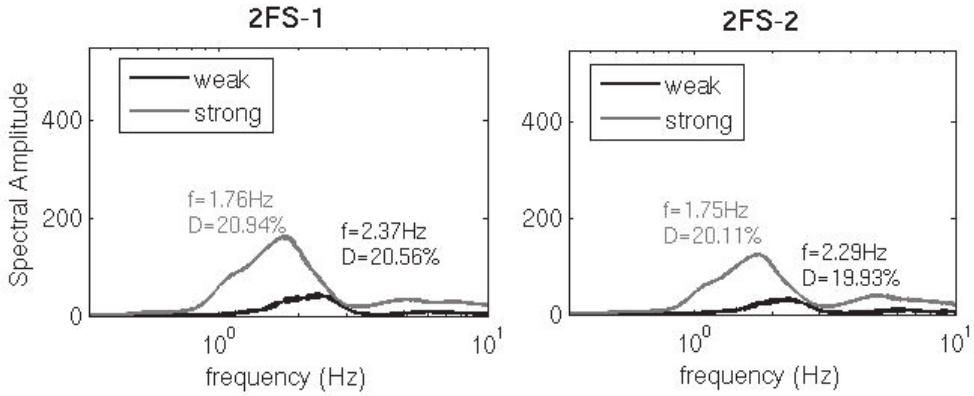

Figure 4.19. Rocking frequency of the two adjacent stand-alone and flexible buildings (2FS) obtained with Eq. 4.9. The black and gray lines are for the weak and strong input signals, respectively. Continuous and dashed lines represent the mean and the mean+/-standard deviation of the transfer function, respectively, computed from all the trials performed in centrifuge tests.

We observe that the results are very similar with the FS results shown before, the SSI being quite strong as for FS. The synthesis of the frequency values is shown Tab. 4.6.

Table 4.6. Summary of the frequency values (in Hz) obtained in centrifuge tests for 2FS models. The rows labelled Δ correspond to the percentage of variation between weak and strong motion (weak - strong)/strong.

		f_{tot}	f_{ϕ}	f_{app} (1)	f_1
2FS-1	weak	2.23	2.37	1.94	2.42
	strong	1.50	1.76	1.60	1.98
	Δ	**-49%**	**-25%**	**-18%**	**-18%**
2FS-2	weak	2.43	2.29	2.14	2.35
	strong	1.50	1.75	1.63	1.93
	Δ	**-38%**	**-24%**	**-24%**	**-18%**

2FS-1 and 2FS-2 have the same nonlinear response, regardless the elements of motion. Shifting energy towards lower frequency and increased damping for the strongest excitation indicate the nonlinear behavior of the SSI system. While the buildings are 1-DOF model, the total frequency showed a double peak frequency (Fig 4.16). Kitada et al. (1998), and Guéguen (2000) have also observed this phenomenon in numerical simulation. Although in the stand-alone building case, this splitting frequency has occurred on RS and FS for total (Fig. 4.7),

and rocking (Fig 4.10), as well as on RS in apparent (Fig 4.11) responses due to strong excitation, this splitting frequency is more pronounced and clear on weak excitation when 2 adjacent buildings present. On the other hand, this splitting disappears on the rocking (Fig 4.19) and apparent (Fig 4.17) responses. This splitting phenomenon has been also known in acoustic or solid state physics as the "tight binding" phenomenon that is used to compute the electronic band structure (Kittel, 2005). Since this phenomenon only remains on the total responses of buildings, we can assume that it is influenced directly by the soil-structure coupling.

We observe that 2FS models have the same influence on the site response (Ta. 4.2 and 4.3) as the FS model (about 11%). However, we observe Tab. 4.6 a larger reduction of the total frequency (-49% and -38%) than for FS (-30%) and the nonlinear rocking has equivalent reduction (about -25%). While 2FS-1 and FS are exactly the same, this results shows that the response of stand-alone or adjacent buildings is different and the design must integrate the urban environment in the design of new building.

The variation of the response due to the proximity of another building questions the significance of the dynamic, numerical or experimental analyses that consider stand-alone building only even though the results are to be integrated into urban environment where more than one building presents. At this stage, it is not possible to evaluate how the splitting of frequency may change the seismic risk of the structure but it must be considered for further analysis on real case studies.

4.6. Contamination of Surface Wave Field due to Presence of Different Structures

Finally, the contamination of free-field ground motion is analyzed to find the governing parameters that control the perturbation. We used the centrifuge data since the free-field are equipped with surface sensors (Fig. 4.3). The in-plane sensors (y-axis) regarding to the excitation direction are separated by 12m distance and the out-of-plane sensors (x-axis) are separated by 10.5m. The foundation dimension is 5.4m x 3.6m. Hence, the in-plane sensors are actually located 9.3m horizontally from the edge of foundation and the out-of-plane sensors are located 8.7m vertically from the edge of foundation (Table 4.7). Sensor 19 is in

the center of the soil surface, below the foundation and the rest of the surface sensors are considered as free-field sensors.

Table 4.7. Directions and distances from foundation edge of the surface sensors

Sensor Number	Direction	Distance from foundation edge (m)
19	Center	0
21, 24	Out-of-Plane	8.7
14, 26	In-Plane	9.3
20, 22, 23, 25	Diagonal	12.7

Taking advantage of the symmetric configuration of the surface array and since there are some sensors that are not deployed in certain tests (Tab. 4.1), we only analyzed the results from half of the configuration including sensor 25 (s-25), 24 (s-24), 23 (s-23), 19 (s-19), and 14 (s-14). Furthermore, since the 2FS does not have any surface sensors, it is excluded from these analyses.

4.6.1. The Anderson's Criterion Analyses

To evaluate the contamination of free-field ground motion, we used the Anderson's criterion (see Chap. 2.4.1) in order to evaluate the variability induced by the driven input signal of the centrifuge. We compared (Fig. 4.20) the variability of the Anderson's global values (average of all parameters) at the surface of the soil column with those of the input, considered herein as the signal recorded by sensor 2 (Fig. 4.3). We compute the coefficient of variation (CoV) from the mean (μ) and sigma (σ) of the Anderson's global value for all building models following:

$$CoV = \sigma/\mu \tag{4.12}$$

Fig. 4.20a shows that for both excitation levels, the variability at s-19 (center of the container) is very low, i.e. around 0.08 and 0.04 for the weak and strong excitation, respectively. The variability of the s-19 is more or less the same (aligned with 1:1 line) with those of input

signal (s-2) showing that the small variability at the surface sensor comes from the variability of the input.

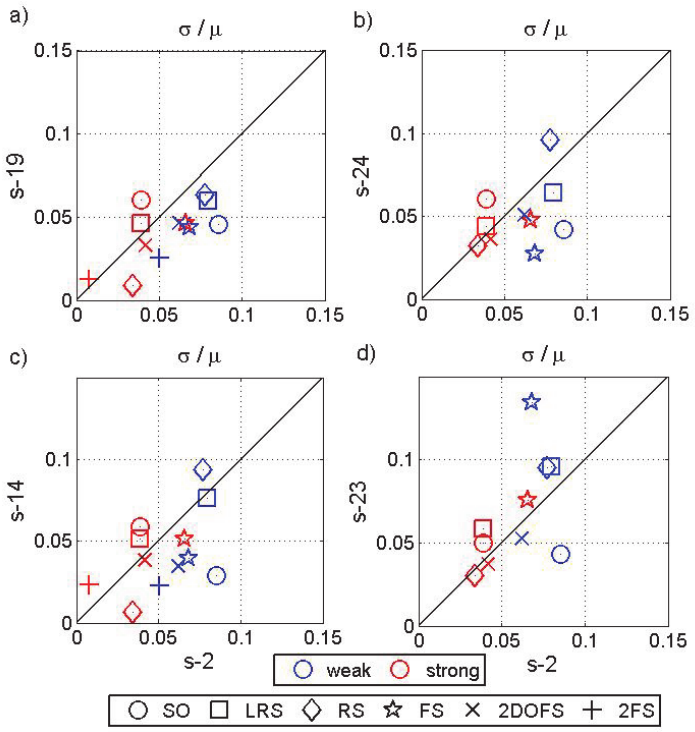

Figure 4.20. Coefficient of variation of Anderson's global values at the surface (a. sensor 19/center; b. sensor 24/out-of-plane; c. sensor 14/in-plane; d. sensor 23/ diagonal) compared with coefficient of variation of Anderson's global values of the input signal (sensor 2).

When we compare the *CoV* of the in-plane sensor (s-14. Fig 4.20c) with the input signal s-2, we found slight differences, indicating slight modification of the coefficient of variation in the in-plane direction. More modification can be found for the out-of-plane direction (s-24. Fig 4.20b) and the diagonal direction. For weak excitation, we see a decrease of *CoV* for FS from 0.05 to 0.03, and increase of *CoV* for RS from 0.06 to 0.1. For strong excitation, only the RS is modified from 0.035 to 0.008. Fig 4.20d shows that the biggest modification has occurred in the diagonal direction, especially for FS due to weak excitation that change from 0.05 to 0.14. We did not show the results for s-25 since the s-23 represents already the diagonal direction comparison.

Table 4.8 summarizes the results of the Anderson's global value for each model. The results at the surface sensors (s-14, s-24, s-25, and s-23) are compared with the results at s-19, and the changes are presented as Δ, where larger delta represents more modification.

Table 4.8. Anderson's Global Values for different type of model (SO, LRS, RS, FS, 2DOFS, and 2FS) under weak and strong excitation for reference sensor (s-19), out-of-plane sensor (s-24), in-plane sensor (s-14), and diagonal sensors (s-23 and s-25).

	SO		LRS		RS		FS		2DOFS		2FS	
	weak	strong	weak	Strong	weak	strong	weak	strong	weak	strong	weak	strong
s-19	8.99	8.96	8.38	9.06	7.48	8.85	8.02	8.28	7.55	8.55	7.95	7.75
s-24	8.82	8.72	8.39	9.08	8.20	9.11	8.27	8.34	7.65	8.55		
Δ(%)	**-1.89**	**-2.68**	**0.12**	**0.22**	**9.63**	**2.94**	**3.12**	**0.72**	**1.32**	**0.00**		
s-14	8.45	8.91	8.18	8.85	7.63	8.86	8.38	8.38	7.79	8.50	7.96	7.77
Δ(%)	**-6.01**	**-0.56**	**-2.39**	**-2.32**	**2.01**	**0.11**	**4.49**	**1.21**	**3.18**	**-0.58**	**0.13**	**0.26**
s-25	8.78	8.87	7.84	8.73					7.70	8.62		
Δ(%)	**-2.34**	**-1.00**	**-6.44**	**-3.64**					**1.99**	**0.82**		
s-23	9.06	8.91	8.02	8.83	7.46	9.08	6.98	8.03	7.70	8.61		
Δ(%)	**0.78**	**-0.56**	**-4.30**	**-2.54**	**-0.27**	**2.60**	**-12.97**	**-3.02**	**1.99**	**0.70**		

We observe in this table that for SO the variation of this value can reach 6%. Hence to show if there is any contamination of the ground motion due to the presence of the structure, *Δ* values should be larger than 6%. RS at out-of-plane sensor and FS at diagonal sensor have *Δ* values larger than 6% under weak excitation, i.e. 9.63% and -12.97% respectively. In addition, we found that the weak excitation gives *Δ* values larger than for the strong excitation: for example between 9.63% and 2.34% for RS in s-24, -12.97% and -3.02% for FS s-23, and 3.18% and -0.58% in 2DOFS for s-14. Nevertheless, the results do not lead to any clear conclusion since the variability is weak. The averaging of all parameter values that have different behavior may cause these insignificant results. Therefore, further investigation on each parameter needs to be done.

4.6.2. Ground Motion Parameter Analyses

We analyzed different ground motion parameters to see which parameters may be sensitive to the free-field contamination. Ditommasso et al. (2010) asserts that Peak Ground Acceleration (PGA) and Spectral Acceleration (Sa) are the most sensitive parameters while Housner Intensity (HI) is less affected by the contamination of free-field motion. Here, we analyzed 8

ground parameters (GMP), which are the Peak Ground Acceleration (PGA), Peak Ground Velocity (PGV), Peak Ground Displacement (PGD), Cumulative Absolute Velocity (CAV), Arias Intensity (Ia), Housner Intensity (HI), Trifunac Duration (D-Tnac), and Effective Duration (D-Eff).

Cumulative Absolute Velocity (*CAV*) is defined as the integral of the absolute value of ground acceleration over total earthquake duration:

$$CAV = \int_0^T |a(t)|dt \tag{4.13}$$

where *a(t)* is the acceleration time history and *T* is the earthquake total duration. This parameter was proposed by EPRI(1988) and used as governing parameter for nuclear power plant by Reed and Kassawara (1990). It is assumed to correlate better to structural damage, compared to peak response parameters, since it incorporates damage given within total seismic duration (Reed and Kassawara, 1990; Campbell and Bozorgnia, 2010).

Arias Intensity (*Ia*) was proposed by Arias (1970) as an energy measure to define earthquake damage potential.

$$Ia = \frac{\pi}{2g}\int_0^T [a(t)]^2 dt \tag{4.14}$$

and Housner Intensity (*HI*) was proposed by Housner (1952) which is the mean value of the pseudo-velocity response spectrum (PSV) between period of 0.1 to 2.5 s.

$$HI = \int_{0.1}^{2.5} PSV(\xi, T_n)dT_n \tag{4.15}$$

where ξ is the damping ratio and T_n is the natural period of a SDOF system. These periods were chosen since most of the structures have fundamental periods between these ranges.

Campbell and Bozorgnia (2010) discussed the use of CAV as a parameter for Ground Motion Prediction Equation (GMPE). Danciu and Tselentis (2007) showed that *CAV* has the least error compared to other ground motion parameters when used in the attenuation model. *CAV* has also better stability compared to CAV_{STD} and CAV_5, which is the reason why we don't used the later in our study. In this work, we aligned *CAV* with *Ia* and *HI* since they are related to each other (Koliopoulos et al., 1998; Martinez-Rueda et al., 2008).

Finally, two parameters of duration are computed. There are many definitions of ground motion duration and the studies of duration are detailed for example by Kramer (1996), and Bommer and Martínez-Pereira (1999). In general, we distinguish four types of durations: Bracketed Durations (total duration of when the threshold is exceeded for the first and last time), Uniform Durations (sum of duration where the threshold is exceeded), Significant Durations (based on accumulation of energy in the accelerogram), and Structural Response Duration (based on structural response when subjected to earthquake). In this study, we will compare the Trifunac Duration (D-Tnac) and Effective Duration (D-Eff). Trifunac duration is proposed by Trifunac and Brady (1975) and belongs to Significant Duration group. This duration is based on the time interval between the points at which 5% and 95% of the total energy is achieved. Effective Duration is proposed by Bommer and Martínez-Pereira (1999) and could also be considered to be belonging to Significant Duration group. In this duration, the strong motion is considered for *Ia* between 0.01 m/s and 0.135 m/s. D-Eff is considered to be stable for multi-event and contains more energy on some parts.

4.6.2.1. Mean Values of GMP

To study the wave propagation contamination by surface structures, we first compared GMP in the presence of the building model to GMP of free-field (soil only) reference. Tabs. 4.9-4.13 present the average values of all GMP for reference (s-19), out-of-plane (s-24), in-plane (s-14), and diagonal (s-23 and s-25) sensors, respectively. These tables also indicate the rate of contamination by quantifying the Δ value, i.e.

$$\Delta = \frac{P_{si}^{ei}(Bi) - P_{si}^{ei}(SO)}{P_{si}^{ei}(SO)} \tag{4.16}$$

where *P* is the average value of the GMP tested (i.e. PGA, PGV, PGD, CAV, Ia, HI, D-Tnac, or D-Eff), *ei* is the given excitation (weak or strong), *si* is the sensor tested, *Bi* is the building model (i.e. LRS, RS, FS, 2DOFS, 2FS), and SO is the Soil Only reference model. This delta represents the physical variation between "with and without building" models, with respect to the position of the observation (diagonal, out-of-plane or in-plane) and the level of shaking. However, we have to keep in mind that variations also exist coming from the driven input signal of the centrifuge as shown Fig.4.20. Although we showed that this variation could be neglected (Fig 4.20) in terms of overall parameters, it might not be the case for each parameter. In order to give information on the experimental variation of the ground motion, we compute Δ^* as:

$$\Delta^* = \frac{P_{si}^{ei}(SO) - P_{19}^{ei}(SO)}{P_{19}^{ei}(SO)} \tag{4.17}$$

that represents the variation of the parameter values between free-field sensors (s-24, s-14, s-25, and s-23) and reference sensor (s-19) for soil only and we assume that the experimental variability is the same between each trial.

Table 4.9. Comparison of the GMP (PGA, PGV, PGD, CAV, Ia, HI, DTnac, and DEff) for weak (W) and strong (S) excitation of the signals recorded at sensor 19. *Δ* indicates the values obtained by Eq. 4.16.

	PGA (g)		PGV (m/s)		PGD (m)		CAV (cm/s)		Ia (m/s)		HI (m)		DTnac (s)		DEff (s)	
	W	S	W	S	W	S	W	S	W	S	W	S	W	S	W	S
SO	1.29	3.89	0.09	0.43	0.0066	0.0549	13.10	47.42	0.98	13.14	0.34	1.87	32.85	28.55	41.22	47.30
LRS	1.36	4.02	0.10	0.42	0.0078	0.0541	14.71	47.83	1.23	13.39	0.39	1.88	33.68	28.22	41.96	47.27
***Δ*(%)**	**5.94**	**3.32**	**12.70**	**-3.91**	**18.18**	**-1.46**	**12.26**	**0.86**	**25.00**	**1.87**	**14.83**	**0.39**	**2.54**	**-1.17**	**1.80**	**-0.07**
RS	1.55	4.17	0.11	0.41	0.0082	0.0487	18.35	47.59	1.81	13.46	0.42	1.83	33.63	28.67	42.81	45.89
***Δ*(%)**	**20.72**	**7.18**	**21.05**	**-4.79**	**24.24**	**-11.29**	**40.07**	**0.35**	**84.24**	**2.42**	**21.99**	**-1.90**	**2.37**	**0.44**	**3.84**	**-2.98**
FS	1.03	3.95	0.08	0.42	0.0069	0.0516	15.36	48.32	0.85	12.93	0.34	1.84	36.30	28.40	54.95	51.42
***Δ*(%)**	**-20.14**	**1.56**	**-8.70**	**-3.10**	**4.55**	**-6.01**	**17.20**	**1.91**	**-13.01**	**-1.60**	**-1.32**	**-1.48**	**10.48**	**-0.54**	**33.30**	**8.72**
2DOFS	1.10	5.08	0.09	0.41	0.0082	0.0510	16.25	49.49	1.20	14.68	0.37	1.86	34.28	27.87	47.99	41.77
***Δ*(%)**	**-14.39**	**30.33**	**1.72**	**-5.93**	**24.24**	**-7.10**	**24.04**	**4.36**	**21.92**	**11.74**	**7.63**	**-0.65**	**4.34**	**-2.39**	**16.41**	**-11.70**

Table 4.10. Comparison of the average value of GMP (PGA, PGV, PGD, CAV, Ia, HI, DTnac, and DEff) for weak (W) and strong (S) excitation recorded at sensor 24. *Δ* indicates the values obtained by Eq. 4.16. *Δ** indicates (s-24–s-19)/s-19 for SO model.

	PGA (g)		PGV (m/s)		PGD (m)		CAV (cm/s)		Ia (m/s)		HI (m)		DTnac (s)		DEff (s)	
	W	S	W	S	W	S	W	S	W	S	W	S	W	S	W	S
SO	1.25	4.12	0.08	0.41	0.0067	0.0546	12.52	45.70	0.91	12.46	0.33	1.84	32.90	27.58	40.93	47.21
***Δ**(%)**	**-2.54**	**5.74**	**-3.20**	**-4.98**	**1.52**	**-0.55**	**-4.42**	**-3.62**	**-6.98**	**-5.19**	**-2.43**	**-1.48**	**0.16**	**-3.41**	**-0.70**	**-0.20**
LRS	1.38	4.31	0.10	0.42	0.0075	0.0542	14.25	47.76	1.13	13.39	0.38	1.88	32.97	27.63	43.30	48.27
***Δ*(%)**	**9.65**	**4.59**	**15.13**	**2.00**	**11.94**	**-0.73**	**13.79**	**4.49**	**23.55**	**7.45**	**14.90**	**2.25**	**0.20**	**0.18**	**5.80**	**2.25**
RS	1.35	4.20	0.10	0.42	0.0078	0.0526	17.59	47.79	1.58	13.35	0.40	1.86	34.32	28.08	49.44	51.29
***Δ*(%)**	**8.01**	**1.88**	**21.99**	**2.27**	**16.42**	**-3.66**	**40.44**	**4.56**	**72.93**	**7.15**	**19.03**	**0.83**	**4.31**	**1.82**	**20.78**	**8.64**
FS	1.01	3.98	0.08	0.43	0.0068	0.0522	15.82	50.77	0.90	13.75	0.34	1.87	36.88	28.21	56.28	61.54
***Δ*(%)**	**-19.87**	**-3.27**	**-7.45**	**4.48**	**1.49**	**-4.40**	**26.35**	**11.09**	**-1.04**	**10.41**	**0.75**	**1.30**	**12.07**	**2.30**	**37.49**	**30.36**
2DOFS	1.04	3.97	0.08	0.42	0.0082	0.0517	15.59	49.12	1.10	13.74	0.36	1.86	34.20	27.52	46.57	44.52
***Δ*(%)**	**-17.01**	**-3.63**	**-0.95**	**1.97**	**22.39**	**-5.31**	**24.50**	**7.48**	**20.75**	**10.33**	**7.85**	**1.07**	**3.94**	**-0.20**	**13.78**	**-5.70**

Table 4.11. Same as Tab. 4.10 for s-14.

	PGA (g)		PGV (m/s)		PGD (m)		CAV (cm/s)		Ia (m/s)		HI (m)		DTnac (s)		DEff (s)	
	W	S	W	S	W	S	W	S	W	S	W	S	W	S	W	S
SO	1.22	4.39	0.09	0.43	0.0076	0.0553	13.13	46.61	0.95	13.14	0.36	1.89	33.96	27.24	44.52	49.03
Δ*(%)	**-4.99**	**12.83**	**1.49**	**-0.49**	**15.15**	**0.73**	**0.22**	**-1.71**	**-3.49**	**-0.03**	**6.64**	**1.06**	**3.36**	**-4.57**	**8.01**	**3.65**
LRS	1.43	4.58	0.11	0.45	0.0080	0.0569	15.39	51.38	1.30	15.33	0.41	1.98	33.36	27.54	45.04	54.84
Δ(%)	**17.29**	**4.34**	**19.62**	**4.98**	**5.26**	**2.89**	**17.24**	**10.24**	**37.10**	**16.69**	**12.42**	**4.60**	**-1.76**	**1.09**	**1.16**	**11.86**
RS	1.64	4.62	0.11	0.44	0.0080	0.0550	18.05	50.94	1.77	15.01	0.43	1.94	33.50	27.65	42.52	52.78
Δ(%)	**34.18**	**5.26**	**27.62**	**3.47**	**5.26**	**-0.54**	**37.44**	**9.29**	**86.30**	**14.28**	**16.70**	**2.93**	**-1.33**	**1.49**	**-4.51**	**7.66**
FS	1.13	4.28	0.08	0.45	0.0071	0.0532	15.34	56.26	0.99	15.28	0.35	1.94	33.70	28.61	47.59	101.68
Δ(%)	**-7.54**	**-2.65**	**-4.40**	**5.19**	**-6.58**	**-3.80**	**16.86**	**20.69**	**4.65**	**16.30**	**-3.07**	**2.64**	**-0.75**	**5.00**	**6.89**	**107.38**
2DOFS	1.10	4.25	0.09	0.45	0.0081	0.0527	16.05	51.08	1.16	14.77	0.37	1.91	34.08	27.39	46.32	46.54
Δ(%)	**-9.93**	**-3.26**	**-0.23**	**4.82**	**6.58**	**-4.70**	**22.26**	**9.58**	**22.95**	**12.47**	**1.54**	**0.95**	**0.35**	**0.53**	**4.03**	**-5.08**

Table 4.12. Same as Tab. 4.10 for s-25.

	PGA (g)		PGV (m/s)		PGD (m)		CAV (cm/s)		Ia (m/s)		HI (m)		DTnac (s)		DEff (s)	
	W	S	W	S	W	S	W	S	W	S	W	S	W	S	W	S
SO	1.20	3.93	0.08	0.40	0.0064	0.0533	12.54	45.15	0.89	12.21	0.33	1.81	32.90	27.14	40.76	47.09
Δ*(%)	**-7.13**	**0.91**	**-3.89**	**-6.53**	**-3.03**	**-2.91**	**-4.29**	**-4.80**	**-8.95**	**-7.09**	**-3.51**	**-3.10**	**0.13**	**-4.93**	**-1.12**	**-0.44**
LRS	1.44	4.84	0.11	0.46	0.0079	0.0600	15.36	52.38	1.28	16.37	0.42	2.08	33.21	27.31	48.15	52.77
Δ(%)	**20.74**	**23.25**	**26.67**	**14.12**	**23.44**	**12.57**	**22.49**	**16.03**	**42.97**	**34.13**	**25.95**	**15.05**	**0.94**	**0.63**	**18.13**	**12.05**
2DOFS	1.00	4.42	0.08	0.42	0.0081	0.0528	15.22	49.06	1.06	14.13	0.36	1.89	34.88	27.21	45.01	43.71
Δ(%)	**-16.72**	**12.50**	**0.00**	**4.46**	**26.56**	**-0.94**	**21.39**	**8.68**	**18.64**	**15.74**	**8.64**	**4.60**	**6.04**	**0.25**	**10.44**	**-7.19**

Table 4.13. Same as Tab. 4.10 for s-23.

	PGA (g)		PGV (m/s)		PGD (m)		CAV (cm/s)		Ia (m/s)		HI (m)		DTnac (s)		DEff (s)	
	W	S	W	S	W	S	W	S		W	S	W	S	W	S	W
SO	1.19	4.13	0.09	0.41	0.0066	0.0531	12.61	45.42	0.91	12.46	0.33	1.81	32.90	26.99	40.82	47.18
Δ*(%)	**-7.18**	**6.02**	**-1.72**	**-4.33**	**0.00**	**-3.28**	**-3.76**	**-4.22**	**-7.77**	**-5.19**	**-2.08**	**-3.28**	**0.16**	**-5.48**	**-0.96**	**-0.26**
LRS	1.48	4.87	0.11	0.47	0.0081	0.0593	15.46	52.71	1.34	16.55	0.42	2.06	32.83	27.39	42.02	46.66
Δ(%)	**24.00**	**17.90**	**26.89**	**13.28**	**22.73**	**11.68**	**22.56**	**16.04**	**48.19**	**32.87**	**25.63**	**13.98**	**-0.22**	**1.48**	**2.93**	**-1.10**
RS	1.45	4.65	0.11	0.46	0.0081	0.0570	17.91	51.75	1.73	16.01	0.43	2.01	33.20	27.39	42.39	45.31
Δ(%)	**21.28**	**12.55**	**31.20**	**10.19**	**22.73**	**7.34**	**42.03**	**13.93**	**90.60**	**28.55**	**27.51**	**11.04**	**0.90**	**1.51**	**3.83**	**-3.96**
FS	1.09	4.32	0.09	0.43	0.0083	0.0529	15.15	48.99	0.73	13.48	0.35	1.89	57.41	28.67	79.62	60.61
Δ(%)	**-8.36**	**4.67**	**3.96**	**4.14**	**25.76**	**-0.38**	**20.14**	**7.87**	**-19.47**	**8.17**	**4.72**	**4.62**	**74.46**	**6.24**	**95.04**	**28.46**
2DOFS	1.08	4.28	0.09	0.45	0.0081	0.0535	15.82	50.77	1.14	15.00	0.36	1.92	34.06	27.28	46.31	45.06
Δ(%)	**-9.93**	**3.55**	**0.70**	**9.05**	**22.73**	**0.75**	**25.44**	**11.78**	**25.71**	**20.41**	**8.90**	**6.13**	**3.52**	**1.09**	**13.45**	**-4.50**

In Tabs 4.10-4.13, we see that Δ^* values are quite low, with largest variation for the in-plane sensor (s-14) with 15.15% on the PGD value under weak excitation. This low variation shows that without structures, the modification of the free-field signals can be neglected and the ground motion of SO model can be considered as reference.

Since Δ is computed using the average value of GMP with or without buildings, the value can be positive or negative and in this first analysis we considered only the amount of contamination with respect to the building model, the level of shaking and the position of the sensor. In Table 4.9, we observe that the presence of the structure modifies the GMP at s-19. This modification confirms the phenomena explained in previous chapters and due to the strain increase at the soil-footing boundary through the rocking motion induced by the soil-structure coupling. In general, PGA and CAV show the largest variation of the ground motion, whatever the building model. For RS, largest variations are observed with 20.72%, 21.05%, 24.24%, 40.07%, 84.24%, and 21.99% increases for PGA, PGV, PGD, CAV, Ia, and HI, respectively, which allow us to suppose that rigid structure contaminates the ground motion to a greater extent. Moreover, for LRS the contamination is important, related to the kinematic interaction of the input signal with the presence of rigid diffracting footing.

For both rigid structures (LRS and RS), the duration is less affected (around 2%) while for FS, the biggest variation is shown for D-Eff (33.3%). The same trend is found for 2DOFS with 16.41% increase for D-Eff. In addition, the PGD, CAV, and Ia are also modified of about 20%. In conclusion, rigid structures seem to have more impact on the GMP, except the duration that is more sensitive to the flexible structures: these structures have a strong rocking motion that must control the lengthening of the ground motion close to the structure. PGA, CAV and Ia are three parameters more sensitive to the presence of the structure. All these phenomena are more pronounced under weak motion that suggests an attenuation of the propagation due to nonlinear response of the soil or a reduction of the soil-structure coupling.

The observations are the same for in-plane, diagonal of out-of-planes sensors. Nevertheless, comparing diagonal (s-23 and s-25) sensors to in-plane (s-14) or out-of-plane (s-24) sensors, we observed a different rate of contamination. For example, under weak motion for RS model, the variation of PGA, CAV and IA are 24.00, 22.56 and 48.19% at s-23, and 34.18, 37.44 and 86.30 at s-14. The same trend is also observed for strong motion. These observations indicate that kinematic interaction induced by the rigid structure is more

pronounced along the diagonal position of observation than in-plane. Moreover, for flexible and RS models the contamination in-plane and out-of-plane is generally smaller than along the diagonal. This confirms the inertial interaction is more pronounced along the diagonal direction.

4.6.2.2. Variability of GMP

In order to have a more accurate evaluation of the contamination, we calculated Δ considering each value of the trials so that we can get the mean and sigma value for each test. This comparison is considered to be less biased thanks to the use of reference free-field (SO), where no structure is present. We called this delta Δ^o, expressed as follows:

$$\Delta^o_{t,r} = \frac{{}^{t=1:T}_{Bi}P^{ei}_{si} - {}^{r=1:R}_{SO}P^{ei}_{si}}{{}^{r=1:R}_{SO}P^{ei}_{si}} \tag{4.18}$$

where T is the number of trials for Bi and R is the number of trials for SO, and T may be different than R, then $\Delta^{o}_{t,r}$ represents all possible combination of the variation. The mean and sigma of $\Delta^o_{t,r}$ are shown in Figures 4.21-4.23 which also summarize the Tables 4.9-4.13. If there is no contamination, these values are equal to 0, and if there is attenuation these values are negative. Figures 4.21-4.23 also show the value of Δ^o for s-19 to give the variation of the GMP due to the presence of the building model.

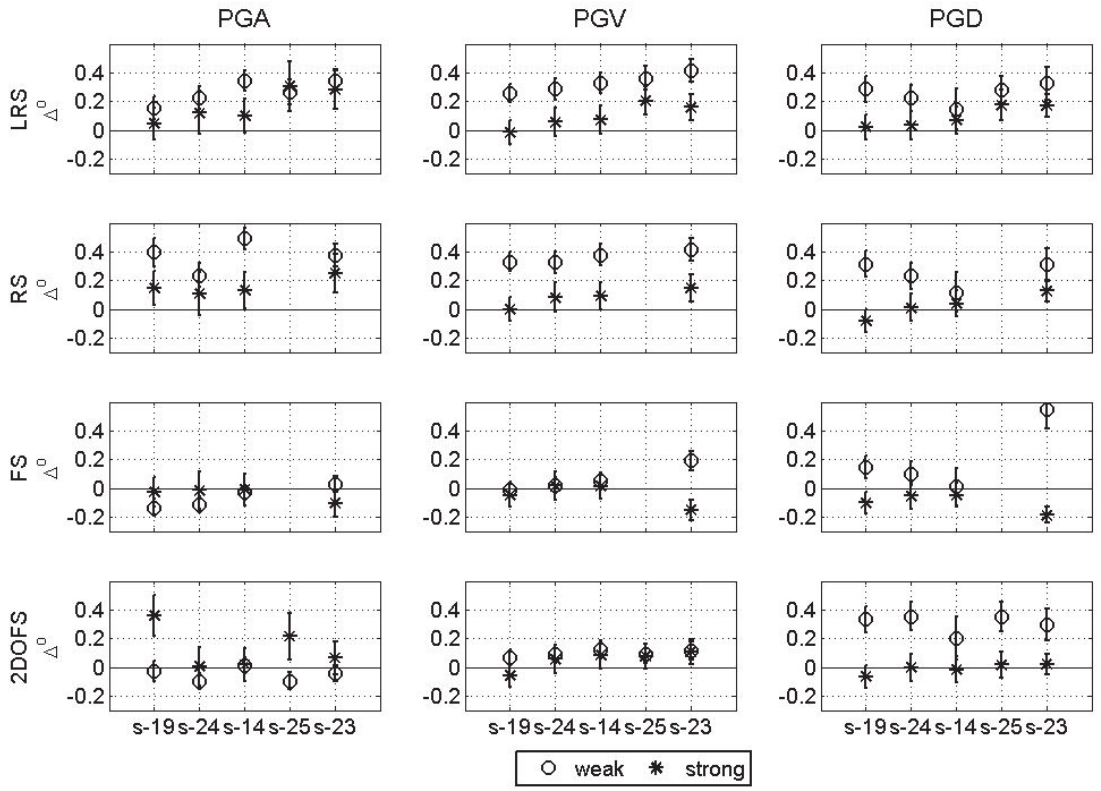

Figure 4.21. Δ^o of the PGA, PGV, and PGD of the free-field sensors for LRS, RS, FS, and 2DOFS. Vertical lines are the standard derivation of the Δ^o. The black line indicates the zero value. The circle shows the weak excitation and asterisk shows the strong excitation

Fig. 4.21 shows the results for PGA, PGV and PGD. We see differences between weak and strong motion. The weak excitation gives the largest variation of GMP whatever the building and the sensor position. The difference between weak and strong traduces the nonlinear effect of the soil-structure interaction and of the soil that impact the strong ground motion contamination through attenuation of the coupling. We note that rigid models, i.e. LRS and RS, have similar pattern of variation, and the flexible models also, i.e. FS and 2DOFS. PGA is very sensitive to the model and to the position of the sensor. This observation confirms the difference of the nature of the interaction, kinematic interaction being more pronounced for rigid buildings while inertial interaction being more pronounced for flexible buildings, as reported previously. As the contamination is more important for the rigid model, we can conclude that the kinematic interaction dominates the ground motion contamination to the detriment of inertial interaction. For flexible models, negative variations are observed which indicates the presence of the building attenuates the ground motion and reduces the contamination. Finally, the contamination varies from one position to others. For PGD and

weak motion, diagonal sensors s-25 and s-23 have the same perturbation as out-of-plane s-24 sensor while in-plane s-14 is less perturbed. For PGA, the trend is not so clear. For rigid and weak motion, in-plane s-14 has the more pronounced variation but it is not the case for strong motion. The PGV seems to be more stable, the variation increasing for diagonal sensor, whatever the building model and in-plane s-14 is more perturbed than out-of-plane.

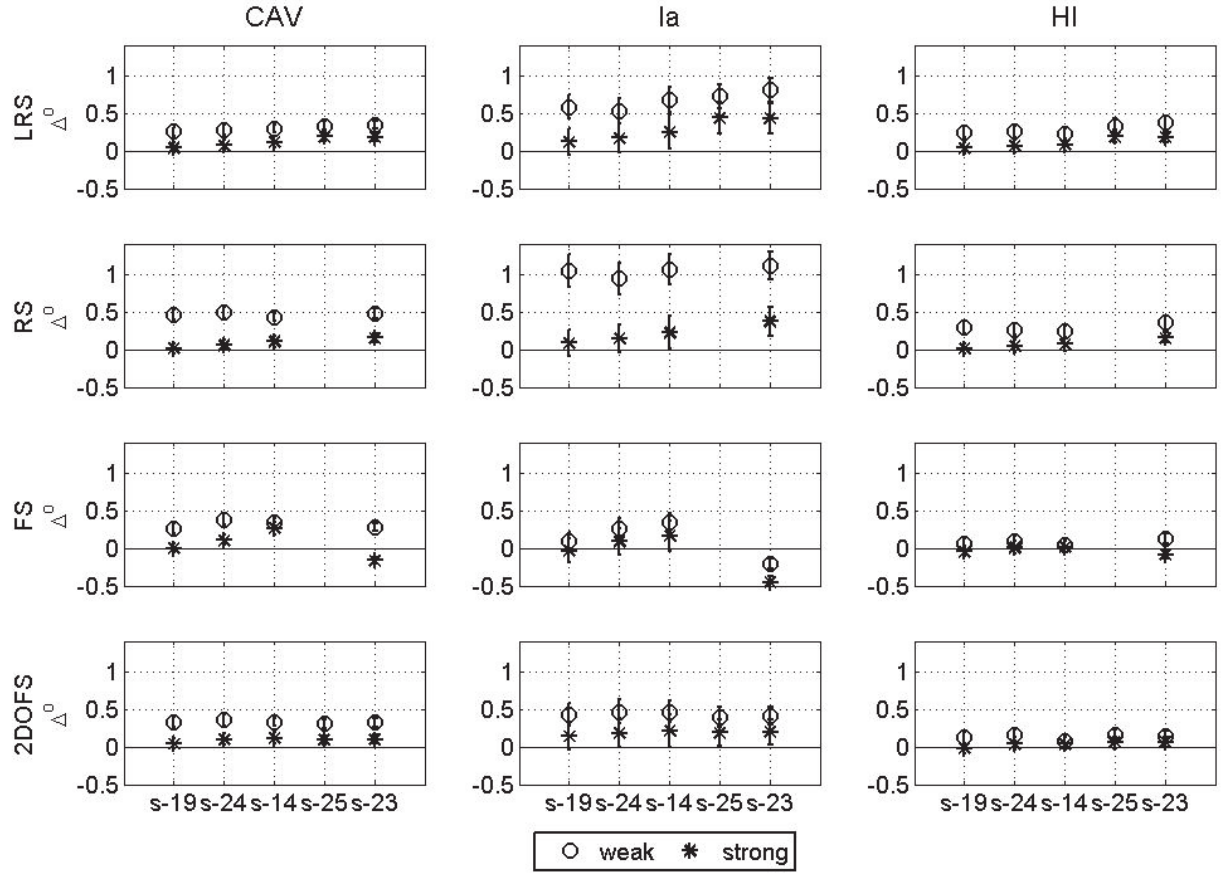

Figure 4.22. Δ^o of the CAV, Ia, and HI of the free-field sensors for LRS, RS, FS, and 2DOFS. The black line indicates the zero value. The circle shows the weak excitation, and asterisk shows the strong excitation

In Fig. 4.22, we show that HI is less contaminated than CAV and Ia, for weak and strong motion and whatever the building model. Ia is the more sensitive parameter but also the more sensitive to the level of shaking for rigid structures. Moreover, the variation of CAV and HI are roughly of the same order of magnitude as the PGA variation, while Ia has larger variation. We observe the variation is the largest for rigid buildings. Once again, the kinematic interaction increases the energy of the signal produced by the contamination and

the nonlinear behavior of the soil and of SSI attenuate the ground motion contamination. Flexible buildings have less impact and the out-of-plane s-24 is less perturbed than other sensors. The variation of CAV is less pronounced for weak and strong motion. The variation is not large enough to distinguish the effect of the position.

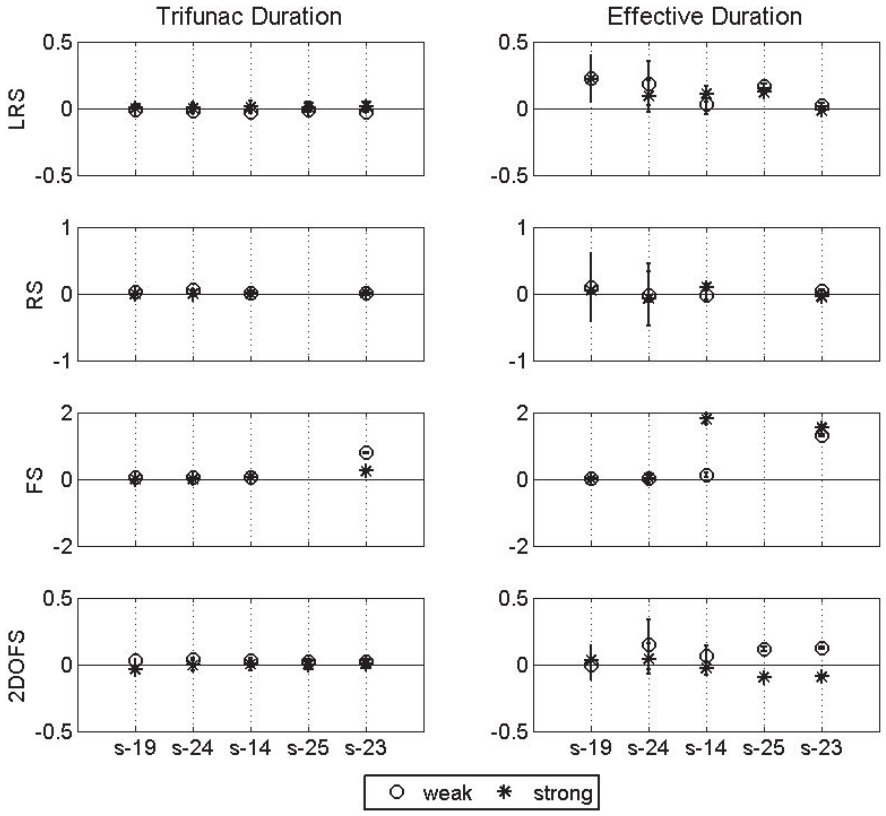

Figure 4.23. Δ^o of the Trifunac duration and effective duration of the free-field sensors for LRS, RS, FS, and 2DOFS. The black line indicates the zero value. The circle shows the weak excitation, and asterisk shows the strong excitation. The plots have different scales.

Finally, we compare the variation of the duration due to the presence of the structure (Fig. 4.23). First, we observe that effective duration is more sensitive to the contamination than the Trifunac duration. Then, as reported in Tabs. 4.9-4.13, the duration is the most perturbed in case of flexible structure for in-plane and diagonal positions. This is directly related to the inertial SSI, as reported by Guéguen et al. (2000) and given as one explanation for the lengthening of the seismic ground motion observed in Mexico City (Wirgin and Bard, 1996; Guéguen et al., 2002). Rigid structures do not contaminate the duration of the ground motion. The amount of the variation can be the double as those observed for Ia.

No strong dependency with the level of excitation is noted on this figure, which suggests the duration is more controlled by the flexible building vibration than by the wave propagation in the soil. Guéguen et al. (2000) reported also the same observation since they noted the attenuation in time of the wave diffracted back into the ground by the building was equivalent to the damping of the building. For FS model, the effective duration is however larger for strong motion, multiplying by 4 the duration of other building models and confirming the duration is controlled by the building. Finally, for 2DOFS the duration of the ground motion is not clearly perturbed.

4.7. Conclusion and Perspectives

We used centrifuge tests to attempt to understand and to analyze the different mechanisms included in the modification of the soil, soil-structure and structure response under strong and weak motion. The modal parameters, i.e. frequency and damping, are computed to analyze the variation of the soil response and the building response under weak and strong motion as well as the nonlinear interaction that may be present between the soil, the interaction and the structure.

First, the presence of structures modifies the site response and the nonlinear behavior of the soil in terms of frequency shift to the lower values (-22% for SO, -4% for RS, and -11% for FS, 2DOFS, and 2FS). This effect is particularly important for rigid structures but non negligible for flexible structures. The role of the nonlinear response of the soil and of the soil-structure interaction during earthquake is then a key issue. The soil nonlinearity is thus the parameter controlling the nonlinear response of the building system, impacting more the rocking. Simultaneously, the nonlinear response of the soil is less pronounced in presence of a structure, the rocking motion increasing the confining pressure and reducing the deformation of the soil. The site response computed using the proxy of the strain PGV/Vs confirms the reduction of the nonlinear response of the soil in the presence of structures. We show that these effects may be non-negligible doubling the nonlinear effects (in terms of frequency variation) between the free-field and urban-field, with smaller damping in the presence of structure. We show that when coupling existed, the nature of the structure affects the nonlinear response of the soil, and *vice-versa* the soil nonlinearity partially controls the soil-structure interaction.

We showed that at the fixed-base frequency the coherency increases slightly with the amplitude of shaking which confirms the predominance of the nonlinear rocking. Flexible buildings show more nonlinear responses compare to rigid buildings if we compare the frequency reduction, either for structural frequency, system or total frequency. The soil nonlinearity is thus the parameter controlling the nonlinear response of the system, impacting more the rocking motion. The presence of the building changes also the site response as well as its nonlinear response. In presence of structure, the nonlinear response of the soil is less pronounced: the rocking motion increases then the confining pressure and reduces the deformation of the soil. This phenomenon is larger for rigid buildings but non negligible for flexible buildings, with critical consequences in case of saturated sand material that may produce induced-liquefaction due to the rocking motion.

Moreover the response of the structure changes with its environment, as shown with the adjacent building case study. The soil is less nonlinear but the nonlinear response of the building system is larger than for stand-alone building, the coupling between both structures changing the system response. Finally, the ground motion in the vicinity of the building is contaminated by the structure. The kinematic interaction seems to be more predominant to explain this phenomenon, with the largest contamination observed for rigid structures. This contamination is essentially observed on Arias intensity, this one reflecting the redistribution of the vibrating energy from the building vibration to soil vibration. The nonlinear response of the soil and/or of the building system reduced also the contamination. In presence of flexible motion, the inertial interaction produces the lengthening of the seismic ground motion, not negligible for seismic ground motion prediction in urban environment.

These observations question the reliability of the seismic risk analysis in urban environment without integrating the presence of the buildings not only as passive elements but also as active elements of the seismic response of the city. To improve the prediction of the building response for design, the site response must integrate the effect due to the presence of the structure with the nonlinear response of the soil and of the soil-structure interaction. But also the dynamic loading of the soil produced by the building motion through the rocking must be integrated, that can increase the cyclic stress in the uppermost layer. In presence of saturated soil, the response could be different, the dynamic and cyclic loading due to the rocking being able to increase the liquefaction. Moreover, the response of a stand-alone building and an

urban environment is completely different and this must be integrated in the seismic risk assessment. Finally, the ground motion can be perturbed by the presence of the structures.

All these findings need to be justified with more data and testing to verify their applicability to the urban environment. More data are required to be able to draw further conclusions and numerical simulations can be done to supplement the findings of these experimental results.

This page intentionally left blank

Chapter 5

Nonlinear Soil-Structure Interaction model with coupled Horizontal and Rocking response: Application to the Garner Valley Downhole Array Soil-Foundation-Structure-Interaction (GVDA-SFSI) Structure

Summary

We apply the non-parametric system identification procedures by deconvolution that has been applied in chapter 4 to the NEES@UCSB GVDA Soil-Foundation-Structure-Interaction (GVDA-SFSI) structure. This method is applied to earthquake data recorded from August 2010 to February 2014. Using this method, the flexible base, pseudo-flexible base and the fixed base responses of the system can be extracted after computing the horizontal and rocking responses. Comparing the results, we test the validity of the analytical expressions that have been used previously to relate the fixed base, rocking, and horizontal responses with the flexible base and pseudo-flexible base responses. The variation of frequencies and damping for different excitation are observed, first, to find the origin of the nonlinearity of the system, and second, to analyze the nonlinear behavior of the system related to the intensity of the earthquake (PGA) and structural deformation (drift). In this nonlinear Soil-Structure Interaction (SSI) observation, the soil nonlinearity is integrated through the use of the Vs_{30} of the site. We show at moderate excitation of 0.045g, the nonlinear behavior occurs at the system. Time window monitoring during the strongest event confirms this process of nonlinear elasticity.

5.1. Introduction

Building responses and structural deformations are essential in determining the seismic demand that is used in most of the earthquake resistance building codes (e.g. IBC-ICC 2000, Eurocode 8-CEN 2003, SNI-BSN 2002). In these codes, the base shear force is computed by multiplying the building mass with corresponding response spectral (associated with building damping) at the fundamental period of the building. However, due to Soil-Structure Interaction (SSI) effects, the modal parameters of the system (f_{sys} and ξ_{sys}) are different with the fixed-base model (f_1 and ξ_1). Stewart et al (2002) explained the role of SSI on the inertial interactions due to induced-base shear and moment and rocking motion relative to the free-field. In fact, kinematic interaction reduces the foundation motions relative to the free-field, particularly at high frequencies of excitation. As a consequence, spectral accelerations are smaller than the fixed-base structure, especially for medium-to-long period buildings (T > 0.5 sec) and they can exceed those of fixed-base structure in case of very stiff structures. Pecker and Chatzigogos (2010) showed that the nonlinear SSI effects seem beneficial by drastically reducing the ductility demand in the structure, although on the other hand displacement and rotation of the foundation became larger which gave more variability in the responses. Hence, Pecker et al (2014) proposed to take into account the nonlinearity of the structure, foundation, and soil by using a controlled shared ductility demand between the superstructure and the foundation. Bard (1988) noticed the importance of rocking in building motion, being the most important signature of the SSI effect (Paolucci, 1993; Guéguen and Bard, 2005).

Therefore, system identification is a key issue in order to evaluate the contribution of the SSI to the global response of the structure and also to evaluate eventual local damage through the monitoring of the fixed-base structure frequency. In fact, frequency and damping are known to be sensitive to the changes of the structural stiffness and mass (Doebling et al, 1996). These changes can appear daily due to the fluctuations of the temperature such as shown by Clinton et al (2006), Mikael et al (2013), and Stinson (2013) or due to nonlinear behavior when subjected to strong ground motion as discussed in Celebi et al (1993), Todorovska and Trifunac (2008), and Todorovska (2009b). The nonlinearity can come from the nonlinear response of the structure, of the soil or of the soil-structure interface related to SSI.

System identification methods have been applied to vibrating structures for some 40 years (Ljung, 1987). Şafak (1992) resumed that the identification procedures are input-output

methods, where the input and the output are the recording inside the building system. Stewart et al. (1998) and Tileylioglu et al. (2008) divided identification methods into two categories, parametric and nonparametric. Safak [1992, 1995] published an early works of the system identification using nonparametric procedures for which the results were relevant with those from parametric procedures. For nonparametric methods, signal processing must be done carefully and hence many researchers opt for parametric procedures (e.g., Stewart and Fenves, 1998; Stewart et al., 1999a; Tileylioglu et al., 2008). Recently, nonparametric system identification method using seismic interferometry by deconvolution instead of cross-correlation has been applied using accelerometric arrays in building (1) for system identification in the Milikan Library building (Snieder and Şafak, 2006; Todorovska 2009a, 2009b), and (2) for structural health monitoring in the Van Nuys hotel, Los Angeles (Todorovska and Trifunac, 2008). In these cases, the nonlinear response of the system is often attributed to the SSI (rocking or horizontal relative motion of the foundation) and the nonlinear response of the soil is not included in the analysis.

The Soil-Foundation-Structure-Interaction (SFSI) facility at the Garner Valley Downhole Array (GVDA) test site is one of the few test sites that has been well instrumented for the purpose of the SSI studies. The system identification of this steel-moment frame structure has been done by Tileylioglu et al (2008) using parametric procedures. In this study we aim to apply the deconvolution method that has been applied in Chapter 4 to do similar system identification on the GVDA-SFSI structure, and then compare it with the results of the parametric studies. The importance and separation of each contributing element of SSI effects are also discussed. In addition, the integration of soil-system observations to the SSI system observations allows us to investigate the nonlinear behavior of the SSI system and determine the importance of nonlinearities of different components of the motion.

5.2. The GVDA-SFSI Facility

The Soil-Foundation-Structure-Interaction (SFSI) facility is located at the Garner Valley Downhole Array (GVDA) test site as one of the test sites of The George E. Brown Jr. Network for Earthquake Engineering Simulation (NEES) at University of California, Santa Barbara (UCSB). The GVDA test site (33°40.127’N, 116°40.427’W) has already been detailed in Chapter 3.2. It is situated in high seismicity region of Southern California, and

located near San Jacinto Fault (SJF) and the San Andreas Fault (SAF). The GVDA near-surface geological conditions consist of soft alluvial lake deposits to a depth of 18-25 meters overlaying weathered granite. The water level is found at a shallow 0-3 m depth. The shear wave velocity, *Vs*, has been measured in situ using suspension logging (Stellar, 1996), SASW (Steidl et al, 1996), cross hole experiment (Steidl et al, 2012), and using the seismic interferometry method (Chandra et al, 2014b) where *Vs* is found to be varied between 175-260 m/s for the first 15m depth.

The SFSI structure was constructed in 2004 with the aim to study the soil-foundation-structure interaction problems. The conceptual location of the SFSI structure with respect to the GVDA test site is shown in Figure 5.1.

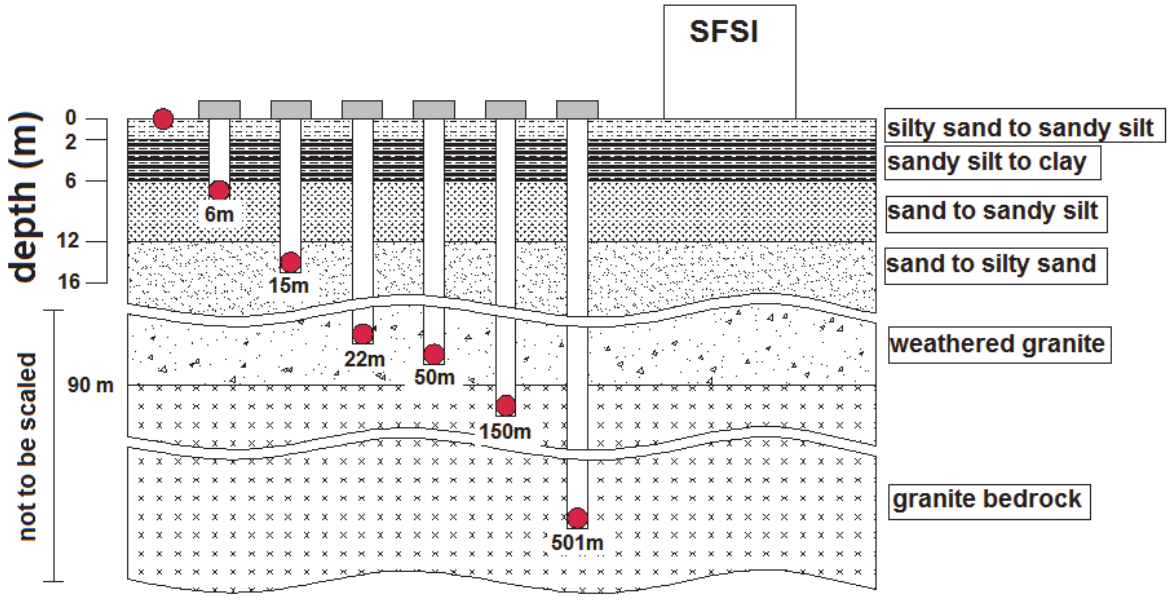

Figure 5.1. Conceptual diagram of GVDA test site cross-section. The red circles are the accelerometers performing a vertical array.

This figure also shows the complete cross section of the GVDA test site. The SFSI was planned to be a medium-scale reconfigurable steel moment frame flexible structure founded on a rigid massive concrete slab (simple spread footing) (Nigbor et al, 2004). This structure is comparable to the flexible structure of the centrifuge test (see Chapter 4). However, at GVDA-SFSI structure, about 50% of the mass is on the foundation to ensure significant SFSI. Roof slab is made from rigid reinforced concrete (RC).

The superstructure has 4x4 m of dimension and as-to-as height of 4m (Figure 5.2a). It is planned to have 7-10Hz fixed base natural frequency, and its frequency can be adjusted by putting or removing steel bracings, adding weight on the roof slab, even adding a second story. Bolt connections are used between columns and the top and bottom slabs. The final design specification shows the fixed-base frequency of 8.4 Hz and a flexible-base frequency of 5.56 Hz for the first mode (NEES@BYU, 2003). Figure 5.2b shows the actual photo of the unbraced SFSI structure taken in October 2013.

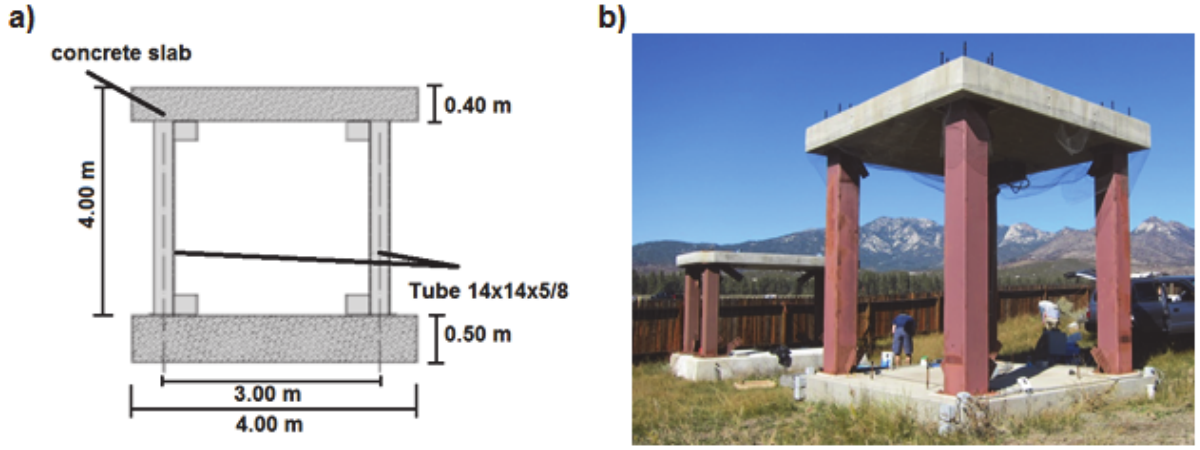

Figure 5.2. (a). Dimension of SFSI structure (modified from NEES@BYU, 2003); (b). The SFSI test structure at GVDA test site.

The GVDA-SFSI structure is equipped with uni-axial and tri-axial accelerometers, rotation sensors, pressure cell and sensors, and displacement transducers, as shown in Figure 5.3. In this work, we were only interested on using the vertical uni-axial sensors that is located at the corner of the structures (sensors no 7, 8, 10, and 11), the horizontal component of the tri-axial sensors located at the top of the footing (sensors no 1, and 2) and at the bottom of the top slab (sensors no 4, and 5). The sensors attached to the structure are positioned along the direction of the structure with 325° azimuth. Sensor signals are digitally recorded with 24-bits resolution and sampling frequency of 200 sps (samples per second). We can found a full description of the GVDA-SFSI test structure measurement and characterization for example in Tileylioglu (2008) who applied the parametric system identification method to GVDA-SFSI structure, in Asghari (2009) who characterized the environmental effects on the identified SFSI structure, and in Stinson (2013) who studied the seasonal fluctuations of the total frequency.

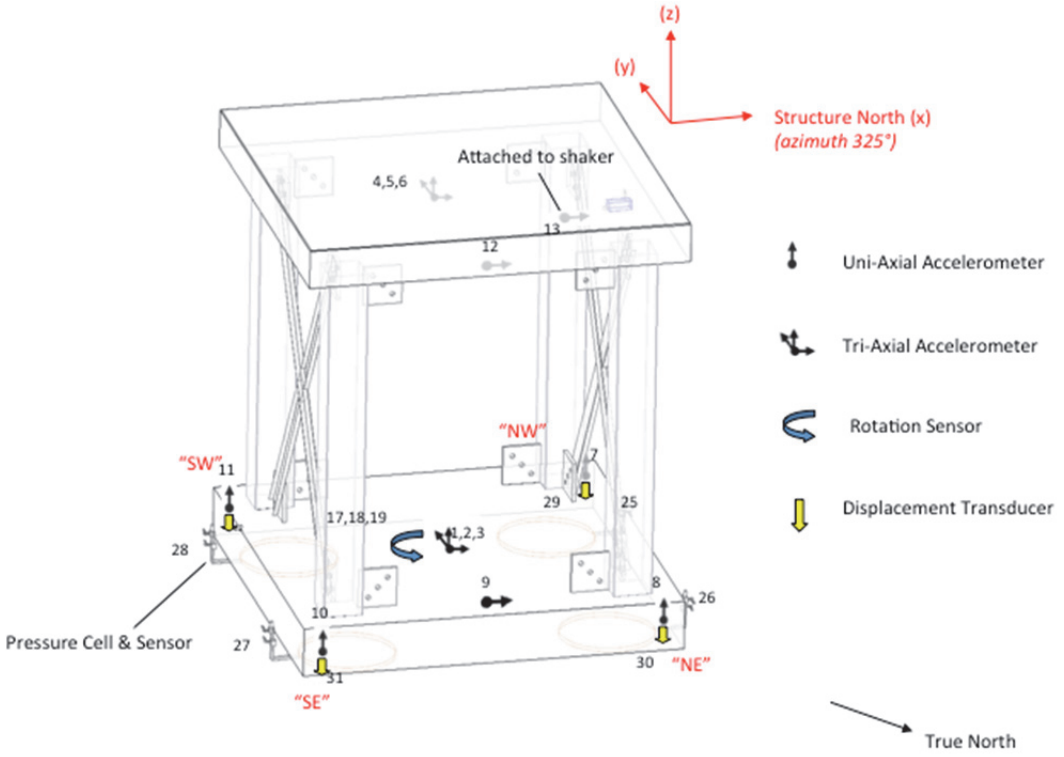

Figure 5.3. Instrumentation of the SFSI test structure (taken from http://nees.ucsb.edu/).

5.3. Data Processing

1,842 GVDA-SFSI events data were collected during the period from August 2010 to February 2014 (after the synchronization of GVDA data acquisition) with magnitudes ranging from $1.0 \leq M_L \leq 4.7$. Hypocentral distances vary from 1 to 100km. The recorded data are mostly from weak events, with largest Peak Ground Acceleration (PGA) of 0.045g. During all this period, the SFSI structure was unbraced.

Several data preprocessing were done including zero-padding (Boore, 2005), mean and trend removal, as well as a 5% Tukey window tapering. We applied a 3-order Butterworth filter between 0.5–10 Hz that covers the SFSI structure frequencies and the GVDA site response frequency as well (Chandra et al, 2014b). We used Konno-Ohmachi function of smoothing factor (B=40 Konno and Ohmachi, 1998) in order to avoid the unrealistic large peaks due to

high-frequency errors (Şafak, 1999). Furthermore, data selection was done to avoid the use of misleading events. Events that do not have complete recordings at all the required sensors to the system identification were rejected. Subsequently, events that have signal-to-noise (S/N) ratio below 3 for all frequency bands were also rejected. To avoid the problem due to deconvolution process such as found in Chandra et al (2014b), the events were finally checked manually.

At the end, 1,056 events were retained in this study (Figure 5.4). The truncated data on magnitude vs distance plot is due to the pre-selection events of NEES@UCSB team so that irrelevant events (small magnitude, large distance) were rejected.

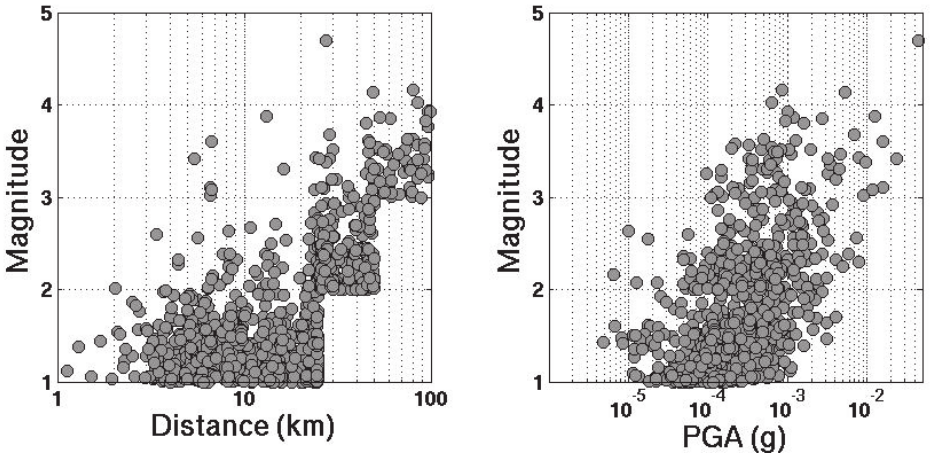

Figure 5.4. Distribution of the data selected for this study displayed as function of magnitude and distance (left) and magnitude and PGA (right).

5.4. System Identification of the Unbraced GVDA-SFSI structure

System identification of the unbraced GVDA-SFSI structure is performed following the nonparametric procedures in Chapter 4.3 and 4.4. The deconvolution process (Clayton and Wiggins, 1976) is the same with Equation 4.2, where

$$H(\omega) = \frac{O(\omega)}{max\left\{I(\omega), k.\left(|I(\omega)|.\frac{I(\omega)}{|I(\omega)|}\right)_{max}\right\}} \tag{5.1}$$

where $H(\omega)$ is the transfer function, $O(\omega)$ and $I(\omega)$ the Fourier transforms of the output motion (O) and input (I) signal, and k is the waterlevel parameter ($0 \leq k \leq 1$) that is used as stabilizer. Different input and output pairs are used according to Table 4.3 to extract the responses of the structure for different confinement case. The deconvolution process is done in displacement (double integrated) where it gives more stable results and then the transfer functions are brought back to the acceleration (double derived) wavefield to avoid the high frequency instabilities on the displacement results.

Similar to Chapter 4.4, the elements of SSI of the SFSI structure are extracted using sensors described in Figure 5.3 (number of sensor is noted in brackets):

- the total system frequency, $f_{tot,}$ is the peak frequency of the total horizontal signals x_{tot} recorded at the top of the building, using [4,5];
- the system frequency, f_{sys}, is the peak frequency of the horizontal motion recorded on top reduced by the free-field horizontal motion assuming. f_{sys} is obtained by deconvoluting (Eq. 5.1) between the top [4,5] and the free-field [0] signals;
- the apparent frequency, f_{app}, is the peak frequency of the transfer function obtained by deconvolution (Eq. 5.1) between the signal recorded on top [4,5] and bottom [1,2] of the SFSI structure;
- the rocking frequency, f_{ϕ}, is computed as proposed by Paolucci (1993) and Guéguen and Bard (2005) by dividing the vertical motion of the two opposite extremities of the foundation as :

$$f_{\phi} = max\left(FFT\left[\frac{\left(V_1(t) - V_2(t)\right)h}{B}\right]\right) \tag{5.2}$$

  with FFT means the Fast Fourier Transform, [$V_1(t)$ and $V_2(t)$] are the time histories of the vertical foundation motion, i.e. for EW direction, sensors [7 and 8] and [10 and 11], and for NS direction, sensors [7 and 11] and [8 and 10], B is the distance between V_1 and V_2.
- the horizontal frequency, f_H, is the peak frequency of the deconvolution (Eq. 5.1) between the horizontal signal recorded on the foundation [0,1] and on free-field [sensor 0 of Fig.5.1]. This motion reflects the kinematic interaction due to scattering of waves on the footing.

- the fixed-base frequency, f_1, is computed using two ways:
  - Since our building has primarily shear deformation, the pulse travel time method by Todorovska and Trifunac (2008) supposed to be able to be applied:

$$f_1 = \frac{1}{4\tau} \tag{5.3}$$

where τ is the time delay of the waves propagating from the bottom [1,2] to the top [4,5], obtained from the impulse response function Eq. 5.1.

  - The peak of the function $\Psi(\omega)$ is obtained after removing the rocking motion (Eq. 5.2) from the rigid-body motion, as proposed by Paolucci (1993). The deconvolution is computed following Eq. 5.1 where the total motion at the top x_{tot} [4,5] and the rigid-body motion of the foundation $x^{tot}_{RB} = x_g + x_H + h\phi$, with $x_g + x_H$ is the motion of the foundation [1,2], and $h\phi$ is the rocking motion using [7,8,10,11].

$$\psi(\omega) = \frac{X_{tot} X^{tot*}_{RB}}{|X^{tot}_{RB}|^2 + \varepsilon} \tag{5.4}$$

Again, the dampings were estimated by the half-power bandwidth method (Eq. 1.30). Considering the configuration of the site (Figure 5.1), the horizontal and system (flexible-base) responses require the recording from free-field sensor. Consequently, these two components were computed for events that had passed the data selection for SFSI (Chapter 5.3) and GVDA (Chapter 3.3). At the end, the total remaining events were 124 events in EW direction and 333 events in NS direction (Figures 5.7-5.8).

5.4.1. Total Motion - x_{tot}

Figure 5.5 shows the spectrum of the total motion in the two horizontal directions (East-West EW and North-South NS). The solid line corresponds to the mean of all selected events and the dashed line to the mean +/- standard deviation of the results. The total frequency f_{tot} corresponding to the peak of Figure 5.5 gives similar results of 5.82Hz for both directions that were expected due to the symmetric configuration of the structure. The standard deviation shows clear variation in terms of amplitude of Fourier spectra and only slight variation of the

peak frequencies. The amplitude variation is related to the amplitude of the ground motion but also to its frequency contents compared to the building frequency. The damping also shows similar results of around 5.8% for both directions. Our results give a good correlation with some minor differences to the results of Stinson (2013) who showed the first mode of 5.68Hz for the total frequency using in-situ dynamic tests with shaker.

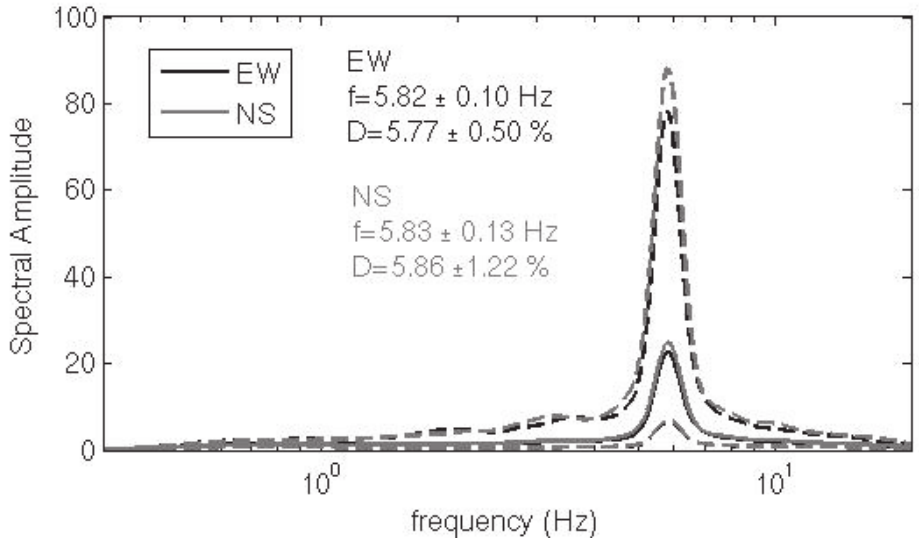

Figure 5.5. Fourier transform of the total motion of the SFSI GVDA structure (f_{tot}). The black and gray lines are for the EW and NS directions, respectively. Solid and dashed lines represent the mean and the mean+/-standard deviation of the spectra, respectively, computed with all 1,056 selected events.

5.4.2. Pseudo-flexible Motion - $x_1+h\phi$

Figure 5.6 shows the apparent response of the GVDA-SFSI structure. The peak of the spectra corresponds to f_{app} equal to 5.83Hz with damping around 5.8% in EW and NS. Stinson (2013) showed the peak of roof/base average amplitude spectral ratio of 9.93Hz, which corresponds to the second torsional mode. Nevertheless, with her spectral results, we may expect the pseudo-flexible (apparent) response at 5.67-5.68Hz and our results give similar values at 5.83Hz and 5.84Hz for EW and NS directions.

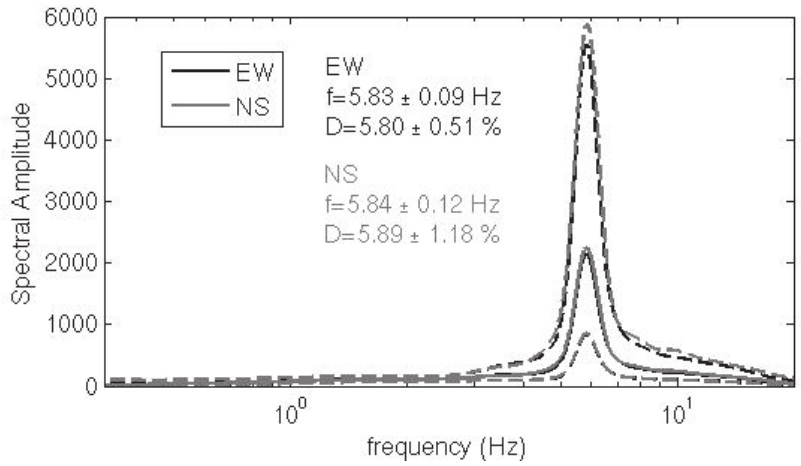

Figure 5.6. Spectrum of the apparent motion of the SFSI GVDA structure (f_{app}). The black and gray lines are for the EW and NS directions, respectively. Solid and dashed lines represent the mean and the mean+/-standard deviation of the transfer function, respectively, computed with all 1,056 selected events.

5.4.3. Horizontal Motion -x_H

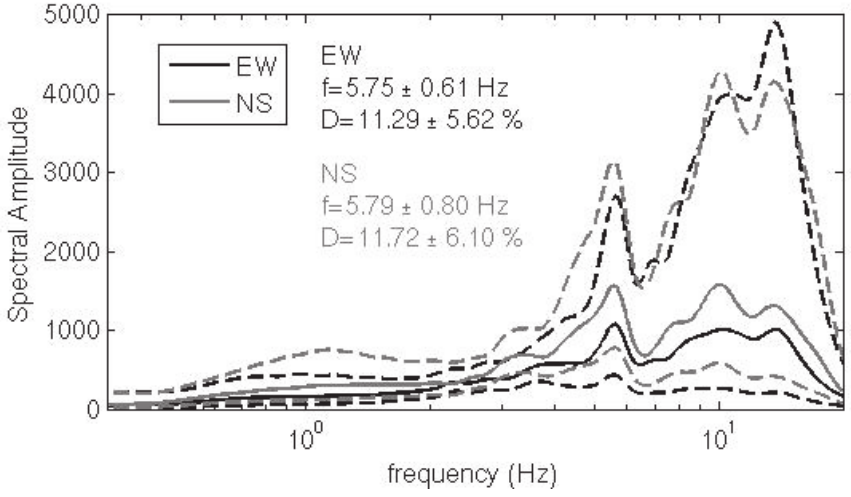

Figure 5.7. Spectrum of the horizontal motion x_H of the SFSI GVDA structure (f_H). The black and gray lines are for the EW and NS directions, respectively. Solid and dashed lines represent the mean and the mean+/-standard deviation of the transfer function, respectively, computed from all 124 EW and 333 NS selected events.

Stinson (2013) showed the free-field frequency at 5.66Hz and bottom frequency at 5.68Hz and we may expect the transfer functions between the bottom and the free-field would give us

similar results with our calculation, i.e. 5.75Hz and 5.79Hz for EW and NS directions, respectively. The horizontal response is related to the kinematic interaction of the GVDA-SFSI structure that is less important considering the shallow foundation of the structure, as shown by the small amplitude of the spectra (Fig. 5.7).

5.4.4. Motion of the Soil-Structure System - $x_1+x_H+h\phi$

In Fig 5.8, the peak of the spectra corresponds to f_{sys} equal to 5.78Hz with damping around 5.8% in EW and NS From parametric procedures. Tileylioglu (2008) found the flexible-base, f_{sys}, of the GVDA-SFSI structure from earthquake excitations at 5.81Hz for unbraced configuration, which are very close with our results. However Tileylioglu's damping estimations vary strongly: for two earthquakes (M_L 4.2 and M_w 5.4), he found the damping values of 1.25% and 4.11%, respectively. In addition, comparing to the shaker in-situ tests, he found a frequency equal to 6.04Hz with 1.68% of damping for unbraced configuration.

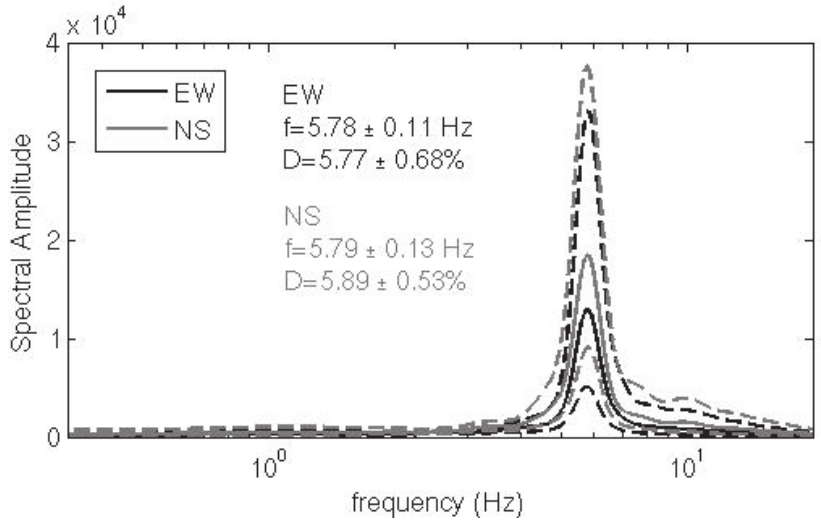

Figure 5.8.Response of the system motion $x_1+x_H+h\phi$ of the SFSI GVDA structure (f_{sys}).Spectrum of the apparent motion of the SFSI GVDA structure (f_{app}). The black and gray lines are for the EW and NS directions, respectively. Solid and dashed lines represent the mean and the mean+/-standard deviation of the transfer function, respectively, computed using 124 (EW) and 333 (NS) selected events.

5.4.5. Rocking Motion - hϕ

Asghari (2009) computed the rocking responses of the unbraced GVDA-SFSI structure, and his results of average 6.02Hz are very close to our results of around 5.85Hz (Fig 5.9) computed using the Eq. 5.2. In the two horizontal directions, the same value of rocking frequency is obtained and we observe a large difference as function of the event used. Moreover, in Asghari's dissertation, he showed that the rocking frequency has 3% daily variation due to the variation of temperature.

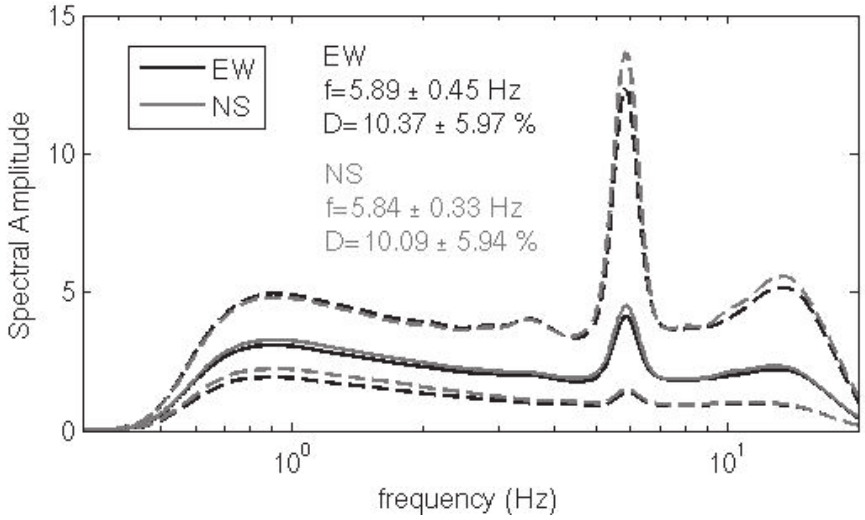

Figure 5.9. Spectrum of the rocking motion $h\phi$ of the SFSI GVDA structure (f_ϕ). The black and gray lines are for the EW and NS directions, respectively. Solid and dashed lines represent the mean and the mean+/-standard deviation of the transfer function, respectively, computed using all 1,056 selected events.

All the comparison done between our results and previous results show slight difference: the main reason is because in our study, we computed the average motion for each component and considering all the events. Differences can be due to the nonlinear response of the motion according to the level of shaking or to the temperature effect.

5.4.6. Fixed-base Motion- x_1

Similar with Chapter 4, the fixed-base responses are more difficult to obtain. Figure 5.10 shows the fixed base frequencies obtained using Eq. 5.4 that are equal to 5.83Hz and 5.82Hz,

with associated damping of 5.89% and 5.85% for EW and NS directions, respectively. These results are completely different with the design specification at 7-10 Hz, or with Tileylioglu (2008) that showed the fixed base frequencies of unbraced GVDA-SFSI structure at 6.70Hz.

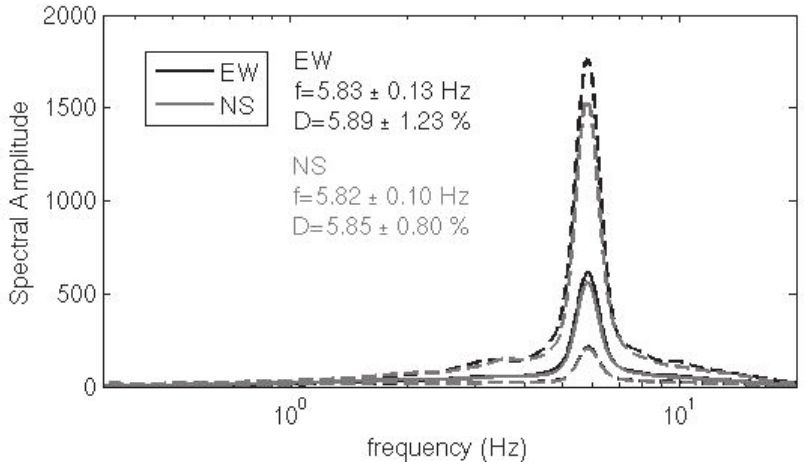

Figure 5.10. Spectrum of the fixed-base motion x_1 of the SFSI GVDA structure computed using Eq. 5.4. The black and gray lines are for the EW and NS directions, respectively. Solid and dashed lines represent the mean and the mean+/-standard deviation of the transfer function, respectively, computed for all 1,056 selected events.

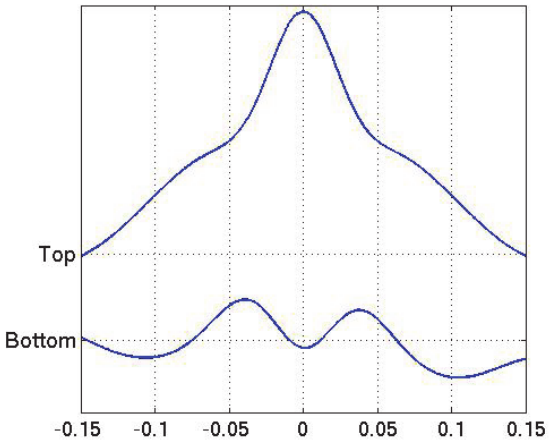

Figure 5.11. An example of an interferogram of the deconvolved waves.

Since the GVDA-SFSI structure can be considered as a shear-deformation structure, we expect that the fixed base responses could be computed using Eq. 5.3 from the travel time of the wave propagating from the base to the roof of the structure. An example of the

deconvolved waves can be seen in Figure 5.11. To gives more accurate estimation, the signals were resampled 4x using the same method such as explained in Chapter 3.3.

The example shows τ of 0.037sec that gives the fixed base frequency of 6.76Hz. Applying this method to all the events we obtained the average fixed base frequencies of 6.99Hz and 7.23Hz for EW and NS direction, respectively, which are closer to the expected fixed-base frequency of the structure ranged between 7 and 10Hz. However, in some cases, the upward and downward waves do not give a clear peak to enable us to do the estimation. Although the average of the fixed-base frequency by travel time method falls within the expected values, the variation (standard deviation) is very large (Fig 5.14). These variations could be related to the nonlinear response of the structure with respect to the seismic input level. In order to examine this, Fig. 5.12 displays the variation of f_1 (Eq. 5.3) with the Peak Ground Acceleration (*PGA*) values.

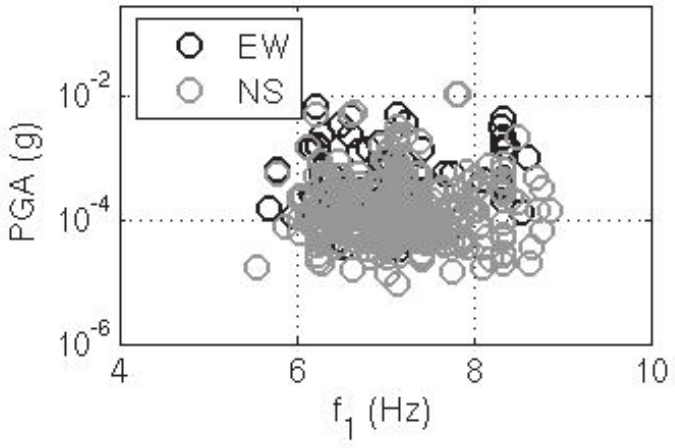

Figure 5.12. Variation of fixed-base frequency computed from Eq. 5.3 with variation of PGA

We observe in this figure that the variation is not coming from the excitation level, hence does not related to the nonlinearity. This dispersion also shows that even though we may expect the applicability of this method to our GVDA-SFSI test structure, its estimation may not be very accurate, and hence only accurate for certain type of structure allowing a good estimation of the time delay.

Finally, we computed the fixed-base frequency using Paolucci's (1993) method. This method is similar with Eq.5.4, but instead of doing deconvolution, the responses are estimated directly from the transfer function of the total motion at the top x_{tot} [4,5] with the rigid-body motion of

the foundation $x^{tot}_{RB} = x_g + x_H + h\phi$. Here, $x_g + x_H$ is the motion of the foundation [1,2], and $h\phi$ is the rocking motion using [7,8,10,11].

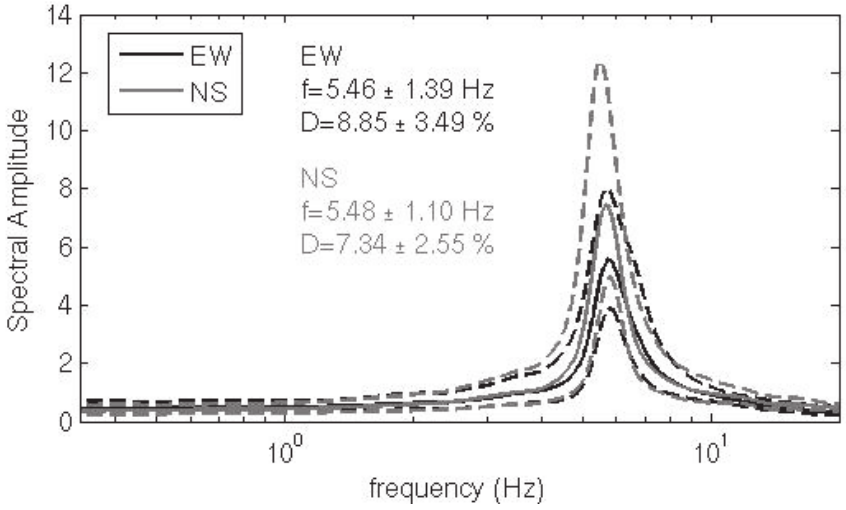

Figure 5.13. Spectrum of the fixed-base motion x_1 of the SFSI GVDA structure using Paolucci's (1993) transfer function (f_1). The black and gray lines are for the EW and NS directions, respectively. Solid and dashed lines represent the mean and the mean+/-standard deviation of the transfer function, respectively, computed from all 1,056 selected events.

Figure 5.13 shows the fixed-base responses extracted using Paolucci's transfer function. We see that the results are very close to the deconvolution method at around 5.8Hz for Eq. 5.4, and 5.5Hz for Paolucci's transfer function. Larger damping is observed, at 5.9% for Eq. 5.4 and around 8% for Paolucci's transfer function.

Fig 5.14 compares the fixed-base frequencies that are obtained from Eq. 5.3, Eq. 5.4, and Paolucci's transfer function. We show that the fixed base frequencies calculated from the deconvolution method (Eq 5.4) are more stable compare to other methods. The travel time analysis (Eq 5.3) gives the largest variation and Eq 5.4 gives close estimate with the Paolucci's transfer function. Nevertheless, the f_1 comes from deconvolution and Paolucci's methods under predict the fixed-base frequency given by the design and by Tileylioglu (2008).

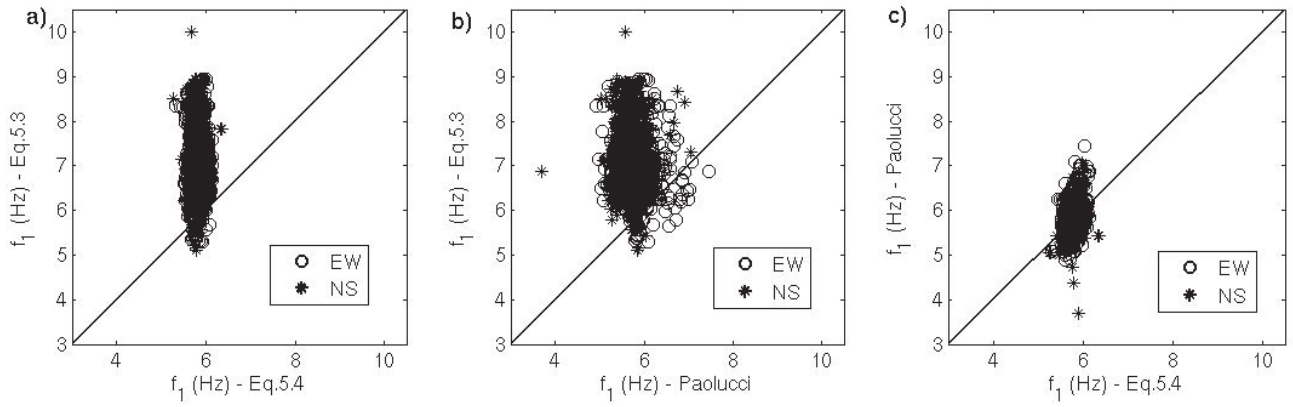

Figure 5.14. Comparison of fixed-base frequency computed from a) Eq. 5.3 (time delay travel time) and from Eq. 5.4 (deconvolution method); b) Paolucci's transfer function and Eq. 5.3; c) Paolucci's transfer function and Eq. 5.4.

5.4.7. Soil-structure Interaction

To observe the importance of the SSI effects, the coherence between rocking and the fixed-base responses are computed (Bard, 1988; Gueguen and Bard, 2005) and the results are shown in Figure 5.15.

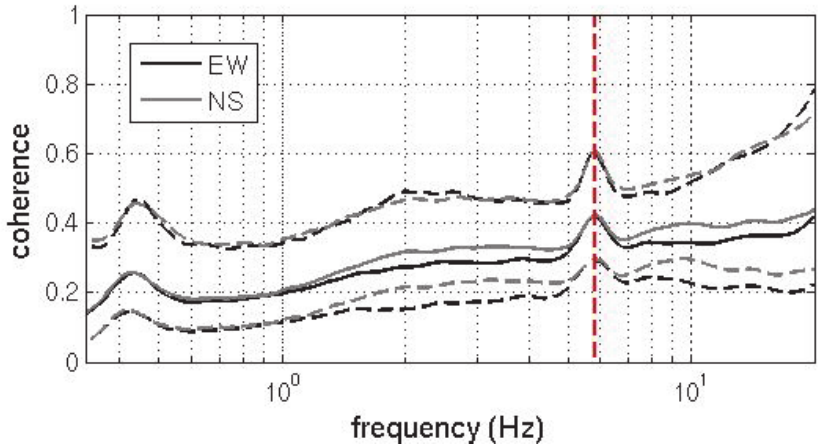

Figure 5.15. Coherency between fixed-base and rocking motion for the GVDA-SFSI structure. The black and gray lines are for the EW and NS directions, respectively. Continuous and dashed lines represent the mean and the mean+/- standard deviation of the transfer function, respectively, computed from all the trials performed in centrifuge tests. The red dashed line shows the rocking frequency value of 5.8Hz.

We see in Fig 5.15 that the coherency is relatively small (below 60%) and varies strongly from one event to another one (standard deviation of 0.2). We observe a peak at 5.8Hz, corresponding to the rocking frequency and that indicates the largest soil-structure interaction at this frequency. However, at this frequency the coherency remains low (below 60%) that indicates a moderate soil-structure interaction at GVDA-SFSI structure. The coherency is very similar for EW and NS directions, showing that the anisotropy of the GVDA test site (Chapter 3.4) does not influence the SSI.

Table 5.1 shows the comparison of the measured and computed pseudo-flexible (f_{app}) and flexible (f_{sys}) frequencies from analytical relationships (Chapter 4, Eqs 4.7-4.8) that link the rocking, horizontal and fixed-base motion. We found that the error is quite high, reaching up to 29% and 42% for pseudo-flexible and flexible responses, respectively. As shown in Chapter 4, the empirical relation is far from the reality when we compute each component of the motion (i.e., rocking, horizontal and fixed-base motion).

Table. 5.1. averaged (indicated by ~) f_1 (Eq. 5.4), f_ϕ, f_H, f_{app} (measured and computed from Eq. 4.7), and f_{sys} (measured and computed from Eq. 4.8) of GVDA-SFSI structure for EW and NS direction.

	$\tilde{f}_1$ (Hz)	$\tilde{f}_\phi$ (Hz)	$\tilde{f}_H$ (Hz)	$\tilde{f}_{app}$ (Hz)		error	$\tilde{f}_{sys}$ (Hz)		error
				Eq. 4.7	measured	(%)	Eq. 4.8	measured	(%)
EW	5.83	5.89	5.75	4.14	5.83	28.99	3.36	5.78	41.87
NS	5.82	5.84	5.79	4.12	5.84	29.45	3.36	5.79	41.97

Moreover, if we consider the empirical relationship (see Chapter 4, Eq. 4.7) using the reference values provided by the design of the building and the previous results (i.e., 5.81Hz for f_{sys}, 6.70Hz for f_1, and 6.02 for f_ϕ), this equation is actually not applicable since it gives negative value for the horizontal frequency. It means that although these analytic expressions have been used by several authors (e.g. Luco et al., 1987; Stewart and Fenves, 1998; Todorovska, 2009b), we showed here and in Chapter 4, that these equations are not representative of the full response of the SSI structure. These results question the validity of the analytical model that has been used for defining the empirical relationships and we cannot consider the displacement relationships equivalent to the frequency relationships.

5.5. Nonlinear Soil-Structure Interaction and Monitoring Analysis

During earthquakes, modal parameters can vary. Due to strong ground motion, the nonlinear behavior may occur. Although Pecker and Chatzigogos (2010) showed that the nonlinear SSI effects may be beneficial to the system, if the local nonlinear behavior of the structure reached the inelastic region, permanent deformation may occur. The nonlinear behavior is normally manifested by reduction of frequency and increase of damping. In the SSI system, the nonlinear behavior may come from its contributing elements, such as shown in Chapter 4.

After the synchronization with GVDA test site in 2010, the GVDA-SFSI structure has not yet been struck with a large earthquake. The events that we collected were small to moderate earthquakes, giving the largest PGA of 0.045g. Although nonlinear behavior is normally expected for stronger PGA, we showed in previous chapters that this behavior can also occur for weak excitation producing small deformation. To analyze the nonlinear behavior of the system, we plot the variation of the contributing components to the total motion thanks to the frequency response, i.e. f_1, f_{app}, and f_ϕ with two parameters: first, is the intensity measure of the ground motion corresponds to the PGA, and second, is the engineering demand parameter corresponds to the structural drift. The PGA is the peak of the acceleration of the free-field sensor and the drift reflects the deformation of the structure and is computed following:

$$drift = \frac{max|U_{top} - U_{bottom}|}{h} \tag{4.5}$$

Where U_{top} is the displacement of the structure at the roof level, U_{bottom} is the displacement of the structure at the foundation level, and h is the height of the building. In addition, to analyze the soil-structure system as a whole, the variation of the soil properties is considered through the variation of Vs_{30} that was taken from chapter 2. Figures 5.16 and 5.17 show the variation of each component of the motion as function of PGA and drift.

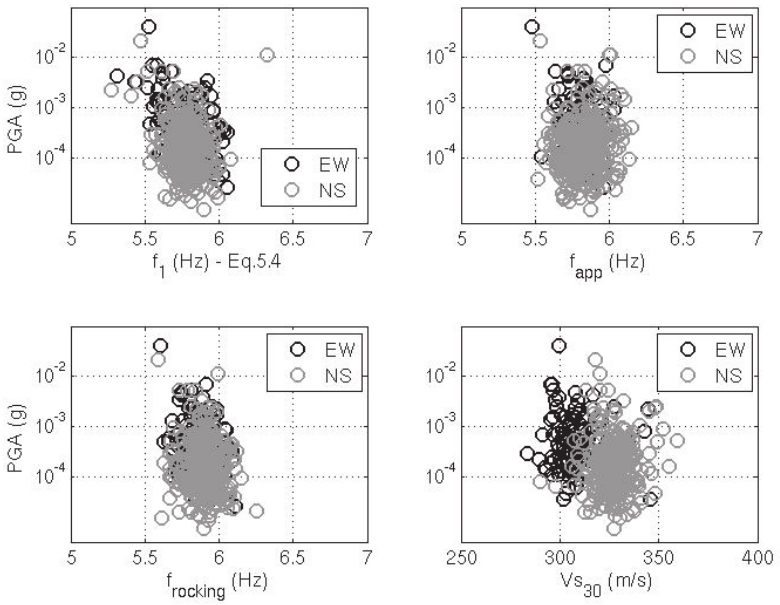

Figure 5.16. Variations of the fixed base (f_1, Eq. 5.4), apparent (f_{app}) and rocking (f_ϕ) frequencies of the GVDA-SFSI structure, and Vs_{30} of the GVDA test site with different values of PGA, correspond to the 124 EW and 333 NS selected events (see text).

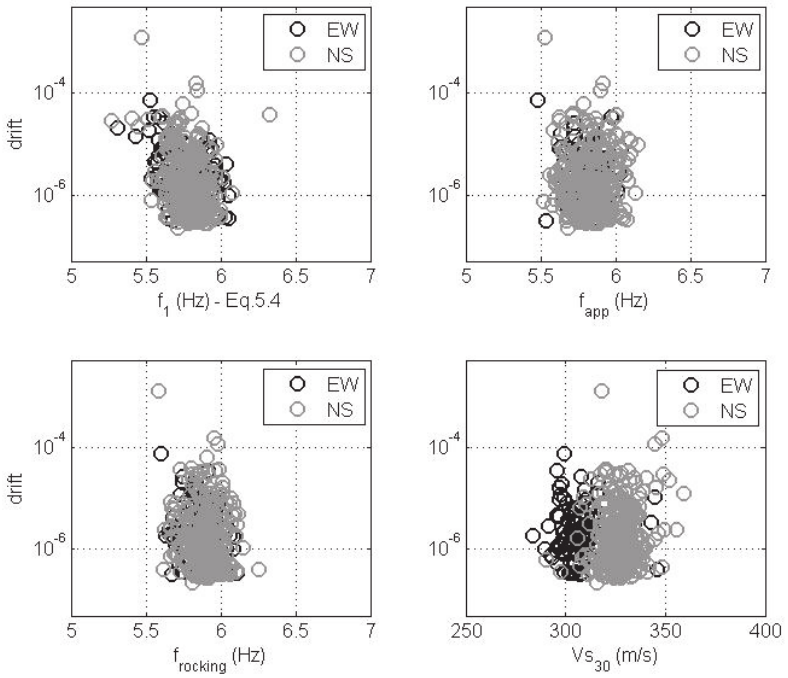

Figure 5.17. Variations of the fixed base (f_1, Eq. 5.4), apparent (f_{app}) and rocking (f_ϕ) frequencies of the GVDA-SFSI structure, and Vs_{30} of GVDA test site with different values of drift, correspond to the 124 EW and 333 NS selected events (see text).

We observe in Figures 5.16-5.17 that PGA and drift give equivalent trends. Apparent and rocking frequencies do not show clear variation with PGA or drift, except for the strongest event. The apparent frequency is reduced from around 6.1 to 5.5Hz (i.e. almost 10% of reduction). The rocking frequency has smaller reduction from around 6.1 to 5.7Hz (i.e. almost 6.5% of reduction). The fixed-base frequency shows the most important reduction from 6.1 to 5.2Hz, i.e. 14.75%. In addition we observe a trend of the f_1 variation showing the nonlinear response starting at very low value of PGA and drift.

The soil shows variation of Vs_{30} in the EW and NS direction, corresponding to the anisotropy discussed in Chandra et al. (2014b). If we consider the largest event (PGA=0.045g), the corresponding PGV and Vs_{30} are 0.029m/s and 300m/s, respectively, corresponding to PGV/Vs_{30} equals to 9.67×10^{-5}. From Figure 3.12 (see Chapter 3), this value corresponds to 4.3% of G reduction that indicates the nonlinearity of the soil. The fixed-base frequency thus is more sensitive to nonlinearity, the reduction of frequency being clearly observed for the strongest PGA even if it was considered as moderate motion (0.045g). From this value, we can suppose that the nonlinearity of the apparent system (f_{app}) is mostly coming from the nonlinearity of the structure (f_1) rather than the rocking motion. These results also justify the low coherency in Figure 5.15 that indicates moderate soil-structure interaction of the structure.

In the GVDA test site, the largest selected event happened in March 11th 2013 at 16:56 UTC with magnitude of 4.7. Figure 5.18 shows a zoom of the time window near the strongest event during 2.5 hours. It represents the variation of the frequencies compared to the value of PGA. The variation of the frequency for rocking, apparent and fixed-base motion are computed as the ratio between the value of the frequencies of event i normalized by the value of the elastic frequencies correspond to the smallest PGA. We observe that for the strongest PGA, the variation of the frequencies is also the strongest. Regarding the time variation, rocking variation is systematically over the fixed-base and the apparent frequencies, both having the same value of variations. Once again, this suggests that the apparent frequency correspond to the fixed-based frequency, supporting the Snieder and Safak (2006) explanation of frequency computed by deconvolution in opposition with the Todorovska (2008a) explanation. The relations for the smallest values of PGA are less clear and it is not possible to conclude on the importance of the rocking or the fixed-base motion in the total nonlinear response of the system. After the strongest ground motion, the frequency reduction due to nonlinear behavior

takes time to return to its elastic value (healing process). This healing process normally takes time and in the meantime, other events may occur and added transient variation of the elastic properties of the structure. It is then interesting to observe these variations through time such for example is done by Todorovska and Trifunac (2008) in the Van Nuys hotel building, Los Angeles.

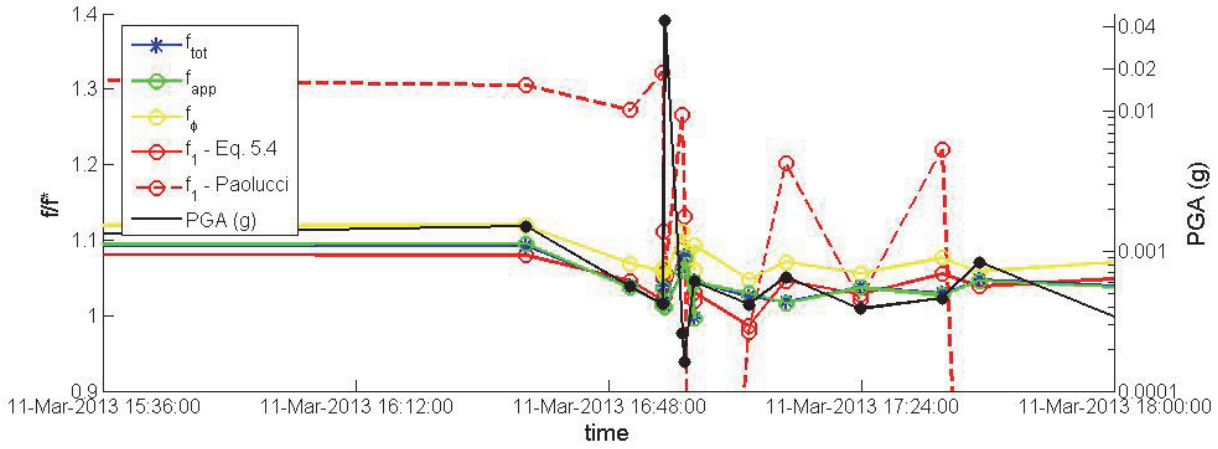

Figure 5.18. Variations of f_1 (Eq 5.4), f_1 (Paolucci), f_{tot}, f_ϕ, and f_{app} in the GVDA-SFSI structure during the events recorded from March 11th 15:36 to March 11th 18:00 2013. Largest event happened in March 11th 2013 at 16:56 UTC. The variation of frequencies corresponds to the variation (in %) with respect to the elastic values of the frequencies. (see text for explanation).

Figures 5.19 and 5.20 compared the variation of frequency of each component of the motion and the variation of Vs_{30} according to the PGA for all the events. We observe (Fig. 5.19) several trends related to the behavior of the building and the soil-structure interaction:

1. as expected, the variation of frequencies is directly related to the level of shaking, i.e. larger shaking corresponds to more softening of the system.
2. the total (d), apparent (b) and rocking frequencies have the same trend close to the linear, these three components being directly linked.
3. relative rocking variation is always smallest than the apparent and the total variation ($f/f^* < 1$ correspond to the largest variation, Fig. 5.19b and d). This allows us to assume that the nonlinear system response is less sensitive to the rocking motion, as expected by the low level of coherency (Fig. 5.15).

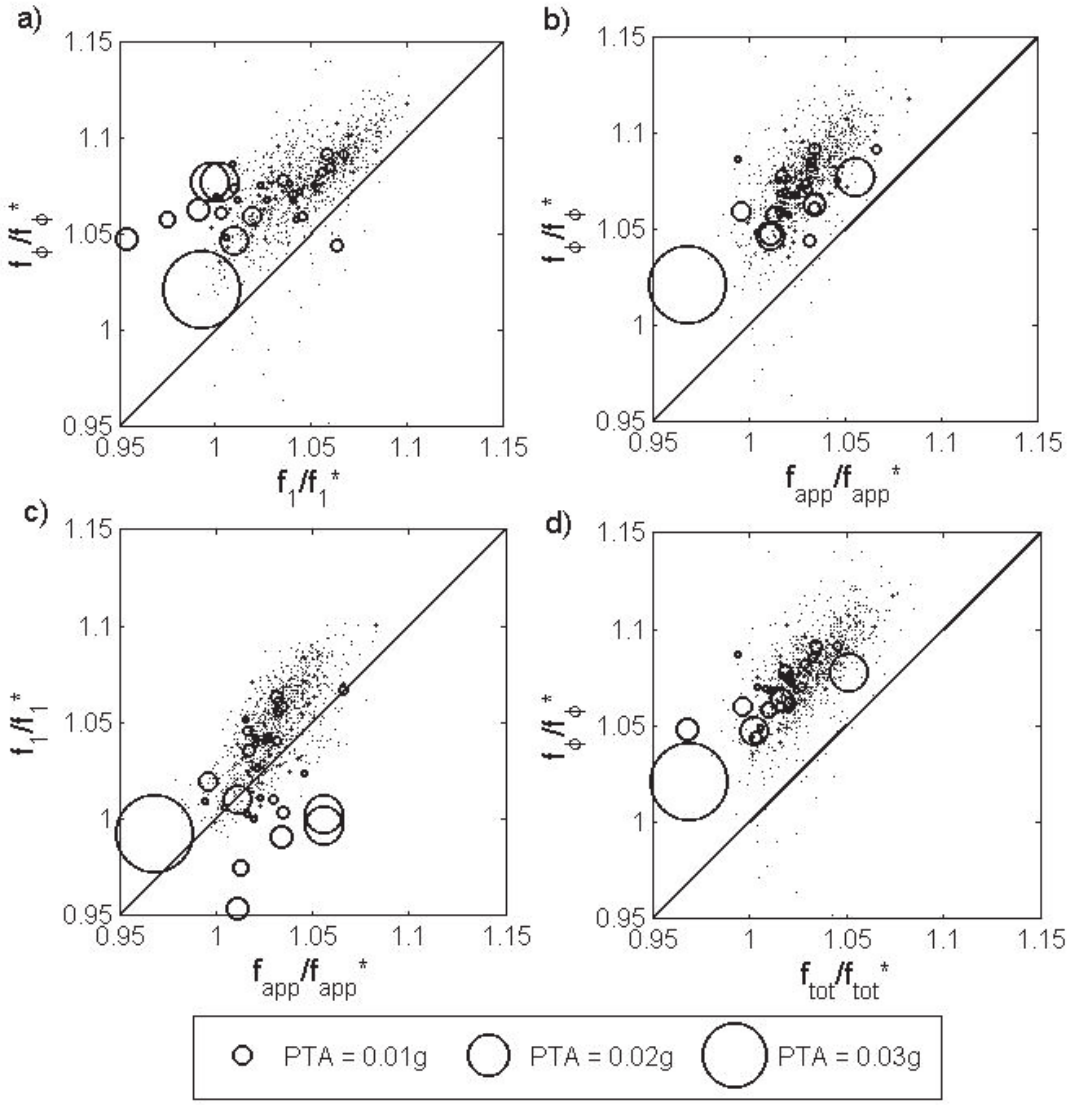

Figure 5.19. Variations of f_1 (Eq 5.4), f_ϕ ($f_{rocking}$), f_{tot} (f_t) and f_{app} in the GVDA-SFSI structure during the 1,056 selected events with respect to the Peak Top Acceleration recorded at the top f the structure. Variation is computed as the ratio between frequency recorded for each event and the elastic frequency (*) corresponding to the average frequency of the smallest 100 events.

4. variations of rocking and structural frequencies (5.19a) have less linear relationship, suggesting a small coupling effect between the soil and the structure.
5. variation of rocking is smaller ($f/f^* > 1$) than the variation of fixed-base frequency confirming that the nonlinear response of the system is mainly controlled by the nonlinear fixed-base response. Moreover, we observe a nonlinear trend of the rocking versus fixed-base comparison: stronger PGA gives faster variation of the fixed-base compared to the rocking.

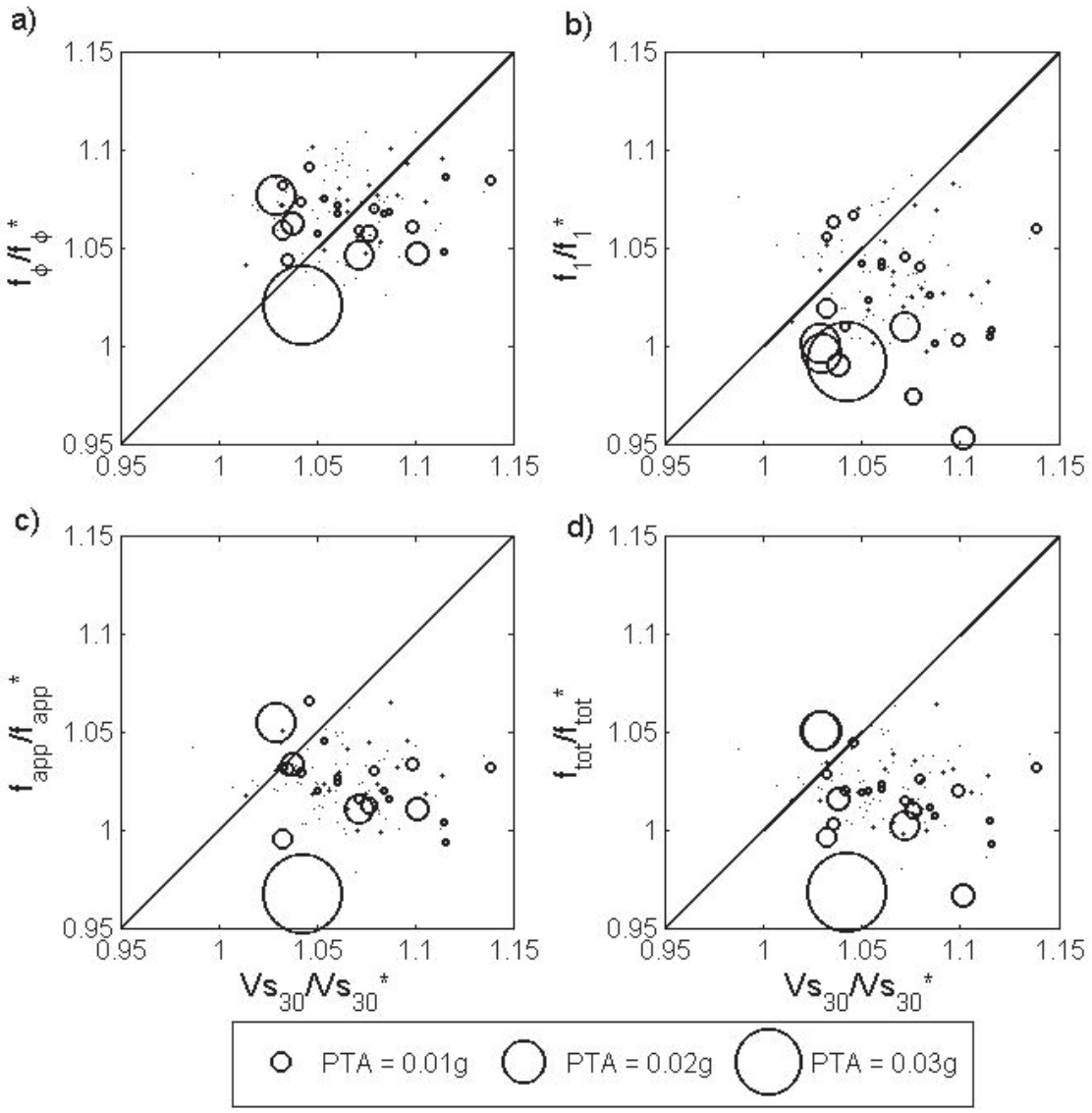

Figure 5.20. Variations of f_1 (Eq 5.4), f_ϕ, f_{app} and f_{tot} in the GVDA-SFSI structure and Vs_{30} of the soil during the 124 EW and 333 NS selected events (see text) with respect to the Peak Top Acceleration recorded at the top of the structure. Variation is computed as the ratio between frequency (or Vs_{30}) recorded for each event and the elastic frequency (*) (or Vs_{30}) corresponding to the average frequency (or Vs_{30}) of the smallest 100 events.

6. variation of apparent and fixed-base frequency (5.19c) is close to 1:1 slope suggesting that the assertion done by Snieder and Safak (2006) is correct (i.e. frequency obtained by deconvolution corresponds to the fixed-base frequency and not to the apparent frequency). This is less favorable for the strongest PGA.

Fig. 5.20 confirms the effect of the rocking motion related to the variation of the soil:

1. apparent, fixed-base and total frequencies does not show clear variation with the nonlinear response of the soil.
2. the soil is less sensitive to the nonlinear response ($Vs/Vs^* > 1$) than the fixed-base frequency (and by consequent the apparent and total frequency).
3. the rocking motion is directly linked to the soil nonlinearity, the variations being centered around the 1:1 curve.

5.6. Conclusion and Perspectives

Empirical relationships (see Chapter 4, Eqs. 4.7-4.8) have been used by several authors (e.g. Luco et al., 1987; Stewart and Fenves, 1998; Todorovska, 2009b) but in our case we showed here and in Chapter 4, that these equations are not representative of the full response of the SSI structure. These equations question on the validity of the analytical model used for defining the empirical relationships and we cannot consider the displacement relationship equivalent to the frequency relationship. Moreover, in the opposition of Snieder and Safak (2006) and Todorovska (2008) related to the frequency obtained by deconvolution, we conclude that the deconvolution process between top and bottom is roughly representative of the fixed-based frequency, even if small deviations are observed.

Nonlinear observation is done by monitoring the variation of different frequencies of the system with different level of excitation. The soil behavior is incorporated by comparing the variation of Vs_{30} of the GVDA test site where the structure was founded. We show that at GVDA-SFSI structure, the rocking motion does not give significant contribution to the global response of the structure. The fixed-base nonlinear response, rather than the rocking or the soil-structure interaction, mainly controls the nonlinear response of the system. We as well show that for a relative small excitation (0.045g), corresponding to a drift of 10^{-4}, the nonlinear behavior occurs in the soil-structure system. This nonlinear elasticity is also confirmed by the slow dynamic observed after the strongest event.

As expected, the nonlinear response of the rocking is directly related to the variation of the Vs_{30}, this information being obtained by the seismic interferometry by deconvolution method.

This page intentionally left blank

General Conclusion and Perspectives

General Reviews

Population concentration in an earthquake-prone urban region increases the seismic risks that may lead to greater damage and loss. Hence, the understanding of urban seismology is important in order to eventually reduce and minimize damages. One way to achieve this is by better predicting or assessing seismic hazard in the urban area. Since most casualties related to earthquakes are caused by building collapse, the prediction of near-surface response and deformation is fundamental for seismic hazard assessment. Near-surface response depends on the modification of seismic waves modification through site effects (site amplification and soil nonlinearity) and soil-structure coupling at the site.

Taking into account only the site amplification, the problem of soil nonlinearity and soil-structure coupling have not been integrated yet in the prediction of ground motion, resulting in increased epistemic uncertainty. Due to the complexities of the matter, most researchers have been approaching these problems separately, taking into account site effects but neglecting the soil-structure coupling, and *vice-versa*.

Within this context, this dissertation assesses the response of a soil-structure system by integrating the soil nonlinearity and soil-structure coupling at one site. Two experimental works were conducted in these works. These experimental works are important as a benchmark to the theoretical solutions and numerical simulations that exist.

The first experimental task is the laboratory scaled dynamic centrifuge test. This test computed approximately the response of both soil and structures, since the stress-strain state of the real conditions are conserved. Applying the acceleration on gravity scale to the model, the response can be scaled directly using the gravity value. The centrifuge test was performed

at IFSTTAR Nantes facility under the framework of ANR ARVISE. Different setups were experimented, first to extract the response of the soil only, and second to extract the response of the soil-structure system for different types of buildings.

The second experimental task uses the in-situ vertical array records of the Garner Valley Downhole Array (GVDA) and the Wildlife Liquefaction Array (WLA), which form part of the George E. Brown Jr. Network for Earthquake Engineering Simulation (NEES) operated by the University of California, Santa Barbara (UCSB), USA. GVDA and WLA test sites are two of the best-instrumented field sites worldwide that are equipped with vertical accelerometers array. Several geotechnical and geophysical measurements have been performed to characterize these sites. The GVDA test site is equipped with the Soil-Structure-Foundation-Interaction (SFSI) structure with aim to study the soil-foundation-structure interaction problems.

Thanks to the vertical array both inside the soil and within the structures of both configurations, we can apply a 1D wave propagation method to extract the response of these shear resonance systems. The waves are considered to propagate inside a 1D horizontally layered media that is subjected to anti-plane (*SH*) incident waves. The seismic interferometry by deconvolution method is applied in all the process to extract the impulse response function (IRF) of the 1D vertical system. The elimination of the source propagation in this method gives the advantage of being independent of the source, and moreover, provides information of the causal and acausal propagation within the system. This method also gives a better estimation of the arrival times and amplitudes. In the context of Soil-Structure Interaction (SSI), this method is independent of the soil-structure coupling, hence each contributing response of SSI can be separated.

General Findings and Conclusions

Chapters 2 and 3 discussed the matter of soil nonlinearity. The deconvolution method was first validated using a synthetic soil column. Computing the time delay between two consecutive signals, the instantaneous shear wave velocity, *Vs** was extracted. The shear wave velocity profile for the weak signal showed well correlated results with the elastic *Vs* profile, validating the method. Reduction of *Vs* was shown as nonlinear signature when subjected to strong input. This method was applied to the centrifuge data and the *in-situ*

GVDA and WLA data. We showed that as far as the downhole array exists, this method is applicable both in laboratory testing and *in-situ* data, giving similar velocity profile with the geotechnical and geophysical measurements for the *in-situ* data. During stronger excitation, similar *Vs* reduction was observed in both centrifuge and *in-situ* results. General *Vs* reductions were observed, changing with depth, showing that the nonlinear behavior is not the same at each depth. Anisotropy of the site could be captured using this method, showing clear anisotropy at the GVDA test site and negligible anisotropy at the WLA test site, at least from our selected data. Anisotropy was not influenced by deformation (shear strain) level at either site.

An equivalent *PGA-PGV/Vs*, i.e. *A*-V*/Vs** was proposed as a soil nonlinearity proxy at an instant depth of the soil column. *A** is the instantaneous maximum acceleration, *V** is the instantaneous maximum velocity between two consecutive sensors of the vertical array. The wave-based strain *V*/Vs** was compared to the displacement-based strain and gave a very similar results, validating the strain proxy. The results were grouped in different velocity groups, where higher values indicate stiffer soil and lower values indicate softer soil. This grouping (rather than using the soil's initial shear wave velocity) is because during excitation *Vs* changes depending on the excitation and soil behavior. We showed that using this proxy, the nonlinear behavior can be assessed showing more nonlinearity in softer soil and less nonlinearity in stiffer soil for either synthetic, centrifuge and *in-situ* data. The data were shown to fit well the classical hyperbolic model, and the reference strain, γ_r could also be estimated, providing the actual in-situ assessment of soil nonlinearity.

The *PGA-PGV/Vs*$_{30}$(or *PGA-PGV/Vs*$_{25}$) were also extracted for both synthetic and centrifuge results and were shown to average the results. This means that the instantaneous *Vs** gives a detailed estimation of the soil response while *Vs*$_{30}$ gives an average estimation of the soil responses. This proxy was also applied to the Japanese K-NET and KiK-net data. The *Vs*$_{30}$ (rather than *Vs*$_0$) is chosen, as it is related to Eurocode 8 site classification. We showed that only by knowing the site classification, we are able to assess and then to predict the nonlinear behavior corresponding to a specific soil. The K-NET data, which come from stations that lie on sedimentary sites, were shown to behave more nonlinearly, at least at the same level of deformation, than the KiK-net data, which come from stations on weathered rock. Nevertheless, although *Vs*$_{30}$ is convenient in practice, the results are more dispersive

compared with the use of Vs^*. The inverted classic hyperbolic model offers a good fit with the data for both Vs^* and Vs_{30}.

The magnitude and the Peak Ground Acceleration (PGA) are shown to be complementary for predicting nonlinearity and source effects of the ground motion (such as the frequency of the seismic energy) and may also influence the nonlinear behavior of the site. Nonlinearity was also shown to not occur only at shallow depth, but also in the deeper depth. It is thus possible that nonlinearity may be generated at great depths, but information is rarely available due to the difficulty in extracting samples from great depths. Moreover, due to anisotropy of the GVDA site, nonlinearity may affect different directions in different ways, however we do not have enough data to draw any definite conclusions.

The recorded *in-situ* data are mostly from weak to moderate events, with PGA up to 0.12g and 0.30g for GVDA and WLA respectively. Nonetheless, we showed that nonlinear elastic behavior could occur at such PGA values, at very low deformation level, i.e. close to 10^{-6}, typical of the nonlinear elasticity response observed in granular medium.

The shear modulus degradation for both centrifuge and in-situ GVDA and WLA data were computed using our method and were shown to be well correlated with previous results. For a given confining pressure, the centrifuge test yielded similar results with to other works under equivalent confining conditions. In general, the dynamic centrifuge tests captured the real condition response, although variability remains due to the experimentation process. At comparable low deformation levels, GVDA has stronger nonlinear site effects compared with WLA and this is without considering the liquefaction phenomena related to the pore pressure generation. However, we cannot compare at higher comparable deformation levels, due to the lack of strong data at GVDA.

In addition to the soil nonlinearity the presence of surface heterogeneities, another factor that influences the response of the soil-structure system is nonlinear Soil-Structure Interaction (SSI). In chapter 4, the dynamic centrifuge test was used to reveal the differences in nonlinear SSI behavior exhibited for different types of structures (i.e. rigid, flexible, 2DOF flexible, and 2 flexible structures) under weak and strong excitations. In chapter 5, recorded data from GVDA-SFSI were used to study the behavior of only one structure under multiple real

seismic events. In both approaches we used the deconvolution method to extract the responses of each contributing element using different input-output pairs of data.

The results from the centrifuge tests showed that, when surface structures are present, the soil nonlinearity affects the nonlinear soil-structure interaction in a way as to reduce the nonlinearity of the soil (less frequency reductions and less nonlinearity on stress-strain observations), however affecting the SSI through increase of rocking motion, and in the same time the confining pressure increases and the deformation of the soil decreases. This modification is more pronounced in rigid buildings compared to flexible buildings. Hence, when soil-structure coupling exist, the presence of the structure affects the nonlinear response of the soil, and *vice-versa* the soil nonlinearity partially controls the soil-structure interaction. This allows us to assume the reciprocity of the nonlinear effect between soil and structure.

We showed that using this method, we are able to do nonparametric system identification procedures. Each contributing element was extracted using different input-output recording pairs. Both from the centrifuge test and GVDA-SFSI results, we showed that the analytical equations linking different contributing elements of SSI are not representative of the full response of the SSI structure. This thus questions the validity of the analytical model used for defining the empirical relationships. Regarding the contradiction on the frequency obtained by deconvolution between Snieder and Safak (2006) and Todorovska (2008), we conclude that the deconvolution process between top and bottom is roughly representative of the fixed-based frequency, even if small deviations are observed.

From the centrifuge results, we showed that at the fixed-base frequency the coherency increases slightly with the amplitude of shaking, which confirms the predominance of nonlinear rocking. Flexible buildings show stronger nonlinear response compares to rigid buildings, in terms of frequency reduction, either for structural frequency, system or total frequency. In the case of two adjacent buildings, the soil is less nonlinear but the nonlinear response of the building system is larger than for stand-alone buildings, the coupling between both structures changing the system response.

Since both centrifuge and GVDA-SFSI structures are founded on shallow foundation, we showed that kinematic SSI interaction is not pronounced. The GVDA-SFSI structure showed a moderate level of SSI through a moderate level of coherency between rocking and fixed-

base responses. The nonlinear SSI response was assessed by monitoring the variation of the frequencies and damping of the system. The origin of this nonlinearity can be traced back by monitoring the variation of the frequencies of each contributing elements. The soil nonlinearity can be integrated by observing the variation of the shear wave velocity at the associated event. From both centrifuge and GVDA-SFSI results, we showed that the nonlinearity of the system came from the different proportion of each contributing element, as well as the soil nonlinearity.

From the centrifuge results, the kinematic interaction seems more predominant to explain the modification of free field motion, with the largest contamination observed for rigid structures. This contamination is essentially observed on Arias intensity, reflecting the redistribution of the vibrating energy from the building vibration to soil vibration. The nonlinear response of the soil and/or building system also reduced the contamination. In the presence of flexible motion, the inertial interaction produces the lengthening of the seismic ground motion, not negligible for seismic ground motion prediction in urban environment.

General Perspectives

More work would be beneficial in order to clarify certain aspects of the current work, which may have been inconclusive due to lack of data. Here we describe the perspectives of our work. The perspectives that are stated here maybe very specific but as well general to the urban seismology works.

Regarding the soil nonlinearity problem, in our computation, we took direct relation of A^* as a stress proxy. Although this does not change the importance of our findings, further study to compare A^* and the real stress level, especially in the recorded data, could be envisaged. Moreover, if the parameter γ_{ref} were incorporated in a more complex model, with or without additional parameters, we could define the shear degradation modulus and damping ratio for a specific soil, thus incorporating soil nonlinearity into the ground motion prediction equation (GMPE).

We showed that although *Vs30* is a practical soil parameter for engineering practice, it represents only the “average” characteristic of the first 30 m depth of the soil. Sometimes this

depth is not enough to explain the complex behavior of the soil, for example its contracting and dilatant behavior (Bonilla et al, 2005). Also, two sites that have the same Vs_{30} value may have completely different soil profile for example it is important if the impedance contrast is inside or outside these 30 m. Muciarelli (2014) presented the case of Christchurch, where the use of Vs_{30} overlooked a thin sedimentary layer that resulted into the damage of the building. However, in GMPEs, soil characteristics are often integrated using Vs_{30}. It is then important to encourage the use of instantaneous Vs*, which provides more detailed information about the characteristics of the near-surface soils and to integrate the *PGV/Vs* information into GMPEs.

Furthermore, in our study, the behavior of saturated soil was not taken into account. The pore pressure generation due to the existence of ground water was neglected. Nevertheless, this is one of the most important elements of soil nonlinearity that may lead into further destructive phenomena such as soil liquefaction or perhaps soil hardening due to cyclic mobility.

Since we used a 1D approach, any geometry effects such as 2D/3D effects, which are often manifested as the trapping of waves inside a sedimentary basin, was not taken into account. These effects together with the direct site effects (1D amplification), ultimately needs to be integrated into near-surface ground motion prediction.

Regarding soil-structure interaction phenomena, we focus our study on inertial interaction, and thus kinematic interaction was not discussed profoundly. This is simply because in our centrifuge study for example, for example, we used the shallow foundation which has less kinematic interaction compared to a deep or pile foundation. Nonetheless, for the construction of important or tall buildings, the use of pile foundations and even a pile groups cannot be avoided. Thus, nonlinear SSI response integrating both effects should be eventually studies.

On the system identification results, we showed that the computation of the fixed-base response of the building using the time delay estimation by Todorovska (2009a) needs to be clarified, since it may not always be applicable on all type of structures. Another parameter explaining the different behavior may be integrated into Todorovska's equation, either using analytical or empirical data. Furthermore, the often-used analytical expressions (Luco et al., 1988; Stewart and Fenves, 1998) linking the fixed-base, rocking, and horizontal responses with the system responses have never been tested on recorded data, at least in our knowledge.

Our results both on centrifuge tests and GVDA-SFSI structure showed that these expressions may not always be correct, hence we need to look back and clarify their limitation.

On the presence of two adjacent buildings, the splitting frequency phenomenon is worth investigating. Whether this phenomenon has any important effect (whether beneficial or detrimental) on urban response need is a question worth studying. Preliminary works using numerical models on COMSOL multiphysics using the same configuration as our centrifuge test was done by Matthieu Rupin in ISTerre (Personal communication) and is shown in Fig C.1. The model was made very thin so that it is comparable with our 1D approach.

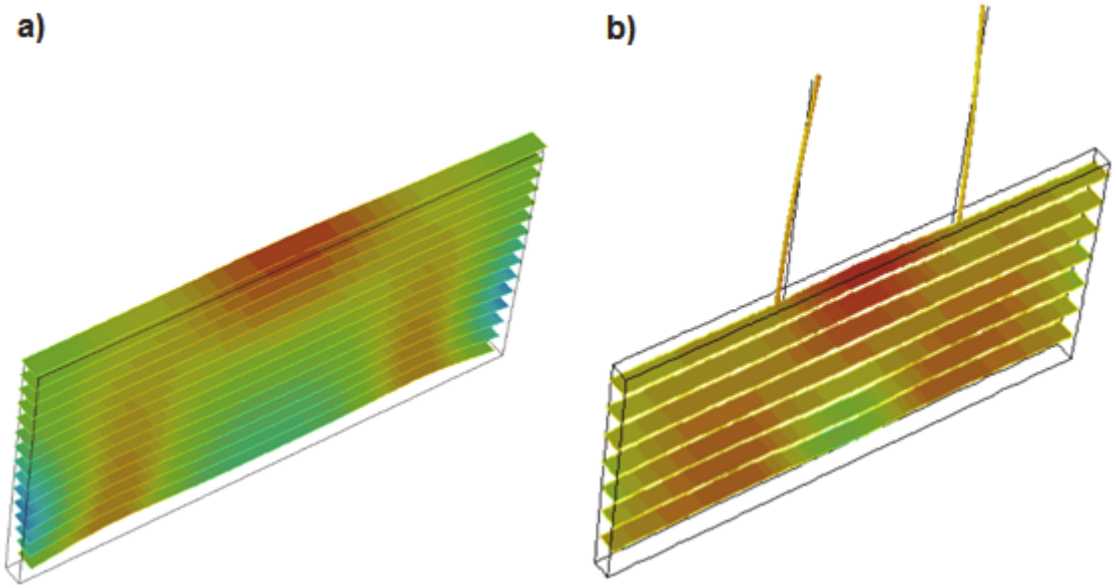

Figure C.1. Numerical model using COMSOL multiphysics of a) Soil Only, and b) Presence of two adjacent buildings using the same configuration of our centrifuge test.

In order to capture the complex phenomena of a city, we need to add more buildings, for example using the dynamic centrifuge test. These buildings could be realistic structures with degrees of freedom, or vibrating elements such as aluminum tubes. In this context, Rupin (2014) shows a band gap phenomenon on the meta-materials. He showed, using both uniformly or non-uniformly configured metal structures, that there exists a space between structures in the free-field, where the surface waves do not propagate. This is an interesting phenomenon to study in urban areas, in order to find whether similar phenomena occur and what would be their impact.

When we look at the modification of the free field, we find that even when surface structures are not presented, there is already some variability in the free-field, although negligible. This variation may relate to the spatial variability problem, and that may not be negligible for important or long structures.

Regarding the GVDA and WLA test sites, our data collection period does not provide sufficient strong ground motion recordings. The recent Napa Valley earthquake (August 24, 2014 with magnitude of 6.1) could, for example, be added to future datasets and may increase the robustness of our findings.

As general perspectives, integrating soil nonlinearity and soil-structure interaction to the GMPEs will become indispensable as we try to reduce epistemic uncertainties in our prediction models.

Numerical simulations are important tools in making a general model that could be used in the engineering practice. Hence, understanding the physics of seismic wave' propagation through simulations is important, so as not to rely only on empirical findings.

The dynamic centrifuge test is still one of the best laboratory scaled experiments that can be used for further analyses. However, limitations still exist, and borehole data are still considered the best data to explain the behavior of a soil-structure system on a specific site. The fact that very few well-instrumented sites exist means that we need more networks and arrays to study this matter.

This page intentionally left blank

Bibliography

Abrahamson, N. A., and Silva, W. (2008). Summary of the Abrahamson and Silva NGA ground-motions relations. *Earthquake Spectra*. 24(1): 67-97.

Akkar, S., and Bommer, J. J. (2010). Empirical equations for the prediction of PGA, PGV, and spectral accelerations in Europe, the Mediterranean, and the Middle East. *Seismological Research Letters*. 81(2): 195-206.

Aguirre, J., and Irikura, K. (1997). Nonlinearity, Liquefaction, and Velocity Variation of Soft Soil Layers in Port Island, Kobe, during the Hyogo-ken Nanbu Earthquake. *Bulletin of the Seismological Society of America.* 87(5): 1244-1258.

Aki, K. (1993). Local site effects on weak and strong ground motions. *Tectonophysics.* 218: 93–111.

Al Atik, L., and Abrahamson, N. (2010). Nonlinear Site Response Effects on the Standard Deviations of Predicted Ground Motions. *Bulletin of the Seismological Society of America.* 100(3): 1282-1292.

Al Atik, L., Abrahamson, N., Bommer, J. J., Scherbaum, F., Cotton, F., and Kuehn, N. (2010). The Variability of Ground-Motion Prediction Models and Its Components. *Seismological Research Letters*. 81(5): 794-801.

Anderson, D. G., and Richart, F. E. Jr. (1976). Effects of straining on shear modulus of clays. *Journal of Geotechnical Engineering Division*. 102(9): 975-987.

Anderson, J. G. Quantitative Measure of the Goodness-of-fit of Synthetic Seismograms. 13th World Conference on Earthquake Engineering., Vancouver, Canada., paper no.243 (2004).

Aoi, S., Kunugi, T., and Fujiwara, H. (2004). Strong-motion seismograph net- work operated by NIED: K-NET and KiK-net. *Journal of Japan Association for Earthquake Engineering.* 4(3): 65–74.

Archuleta, R.J., Seale, S. H., Sangas, P. V., Baker, L. M., and Swain S. T. (1992). Garner Valley Downhole Array of Accelerometers: Instrumentation and Preliminary Data

Analysis. Bulletin of the Seismological Society of America., Vol.82, No.4, pp. 1592-1621.

Arias, A. (1970). A measure of earthquake intensity. *Seismic Design for Nuclear Power Plants*. Hansen, R.J. (ed). Cambridge, MA, The M.I.T. Press, pp. 438 - 483.

Asghari, A. (2009). Characterizing of Environmental Variability in Identified Dynamic Properties of a Soil-Foundation-Structure System. *Dissertation*, University of Southern California.

Assimaki, D., Steidl, J., and Peng, C. L. (2006). Attenuation and Velocity Structure for Site Response Analyses via Downhole Seismogram Inversion. *Pure and Applied Geophysics*. 163: 81-118.

Assimaki, D., Li, W., Steidl, J. H., and Tsuda, K. (2008a). Site Amplification and Attenuation via Downhole Array Seismogram Inversion: A comparative Study of the 2003 Miyagi - Oki Aftershock Sequence. *Bulletin of the Seismological Society of America.* 98(1): 301-330.

Assimaki, D., Li, W., Steidl, J.H., and Schmedes, J. (2008b). Quantifying Nonlinearity Susceptibility via Site-Response Modeling Uncertainty at Three Sites in the Los Angeles Basin. *Bulletin of the Seismological Society of America.* 98(5): 2364-2390.

Atkinson, J. H. (2000). Non-linear soil stiffness in routine design. *Géitechnique* 50(5): 487-508.

Bankoff, G. (2001). Rendering the World Unsafe: 'Vulnerability' as Western Discourse. *Disasters*. 25(1): 19-35.

Bard, P. –Y. (1988). The importance of rocking in building motion: An experimental evidence. *Proceedings of Ninth World Conference on Earthquake Engineering, Japan, 1988*. 8: 333-338.

Beresnev, I. A, and Wen K. L. (1996). Review Nonlinear Soil Response - A Reality? *Bulletin of the Seismological Society of America*. 86(6): 1964-1978.

Beresnev, I. A., Atkinson, G. M., Johnson, P. A., and Field, E. H. (1998). Stochastic Finite-Fault Modeling of Ground Motions from the 1994 Northridge, California, Earthquake. II. Widespread Nonlinear Response at Soil Sites. *Bulletin of the Seismological Society of America.*, 88(6): 1402-1410.

Bernardie, S., Foerster, E., and Modaressi, H. (2006). Nonlinear site response simulation in Chang-Hwa region during the 1999 Chi-Chi earthquake, Taiwan. *Soil Dynamics and Earthquake Engineering*. 26: 1038-1048.

Bilham, R. (2004). Urban Earthquake Fatalities: A Safer World, or Worse to Come? *Seismological Research Letters*. 75(6): 706-712.

Bilham, R. (2009). The seismic future of cities. *Bulletin of Earthquake Engineering*. 7:839-887.

Bommer, J. J., and Martínez-Pereira, A. (1999). The effective duration of earthquake strong motion. *Journal of Earthquake Engineering*. 3(2): 127-172.

Bommer, J. J., Douglas, J., Scherbaum, F., Cotton, F., Bungum, H., and Fäh, D. (2010). On the Selection of Ground-Motion Prediction Equations for Seismic Hazard Analysis. *Seismological Research Letters*. 81(5): 783-793.

Bonilla, L. F., Steidl, J. H, Gariel, J. C., and Archuleta, R. J. (2002). Borehole Response study at the Garney Valley Downhole Array (GVDA), Southern California. *Bulletin of the Seismological Society of America.* 92(8): 3165-3179.

Bonilla, L. F., Cotton, F., and Archuleta, R. J. (2003). Quelques Renseignements sur Les Effets de Site Non-Linéaires en Utilisant des Données de Forgae: La Base de Mouvements Forts KiK-Net au Japon. *6eme Colloque National AFPS.* Ecole Polytechnique, Palaiseau.

Bonilla, L. F., Archuleta, R. J., and Lavallée, D. (2005). Hysteretic and dilatant Behavior of Cohesionless soils and their Effects on Nonlinear site Response: Field Data Observations and Modeling. *Bulletin of the Seismological Society of America.* 95(6): 2373-2395.

Bonilla, L.F., Tsuda, K., Pulido, N., Regner, J, and Laurendeau, A. (2011). Nonlinear Site Response Evidence of K-Net and KiK-net Records from the 2011 off the Pacific coast of Tohoku Earthquake. *Earth Planets Space.,* 63: 785-789.

Boore, D. (2005). On Pads and Filters: Processing Strong-Motion Data. *Bulletin of the Seismological Society of America*. 95(2): 745–750.

Boore, D., Thompson, E., and Cadet, H. (2011). Regional correlations of Vs_{30} and velocities averaged over depths less than and greater than 30 meters. *Bulletin of the Seismological Society of America*. 101(6): 3046–3059.

Boulanger, R. W., Meyers, M. W., Mejia, L. H., and Idriss, I. M. (1998). Behavior of a fine-grained soil during the Loma Prieta earthquake. *Canadian Geotechnical Journal.* 35(1): 146-152.

Boutin, C., and Roussillon, P. (2004). Assessment of the Urbanization Effect on Seismic Response. *Bulletin of the Seismological Society of America.*, 94(1): 251-268.

Brandenberg, S. J., Choi, S. L., Kutter, B. L., Wilson, D. W., and Santamarina, J. C. (2006). A Bender Element System for Measuring Shear Wave Velocities in Centrifuge Models. *6th International Conference on Physical Modeling in Geotechnics, Hong Kong.*

Brennan, A. J., Thusyanthan, N. I., and Madabhushi, S. P. G. (2005). Evaluation of Shear Modulus and Damping in Dynamic Centrifuge Test. *Journal of Geotechnical and Geoenvironmental Engineering*. ASCE. pp. 1488-1497.

BSN-Badan Standardisasi Nasional. (2002). *Tata cara perencanaan ketahanan gempa untuk bangunan gedung.* SNI 03-1726-2002. *in Indonesian*.

Calvi, G. M., Pinho, R., Magenes, G., Bommer, J. J., Restrepo-Vélez, L. F., and Crowley, H. (2006). Development of seismic vulnerability assessment methodologies over the past 30 years. *ISET Journal of Earthquake Technology*; 43(3): 75-104.

Campbell, K. W., and Bozorgnia, Y. (2008). NGA ground motion model for the geometric mean horizontal component of PGA, PGV, PGD and 5%-damped linear elastic response spectra at periods ranging from 0.1 s to 10.0 s. *Earthquake Spectra*. 24(1): 139-171.

Campbell, K. W., and Bozorgnia, Y. (2010). A Ground Motion Prediction Equation for the Horizontal Component of Cumulative Absolute Velocity (CAV) Based on the PEER-NGA Strong Motion Database. *Earthquake Spectra*. 26(3): 635-650.

Campillo, M, Gariel, J. C., Aki, K., and Sánchez-Sesma, F.J. (1989). Destructive strong ground motion in Mexico City : Source, path, and site effects during great 1985 Michoacán earthquake. *Bulletin of the Seismological Society of America.* 79: 1718-1735.

Causse, M., Cotton, F., Cornou, C., and Bard, P. -Y. (2008). Calibrating Median and Uncertainty Estimates for a Practical Use of Empirical Green's Function Technique. *Bulletin of the Seismological Society of America.* 98(1): 344-353.

Celebi, M., Phan, L. T., and Marshall, R. D. (1993). Dynamic characteristics of five tall buildings during strong and low-amplitude motions. *The Structural Design of Tall Buildings*. 2(1): 1-15.

Celebi, M., and Okawa, I. (Eds.). (1998). *Proceedings UJNR Workshop on Soil-Structure Interaction*. Menlo Park, California.

CEN-European Committee for Standardization. (2003). *Eurocode 8: Design of structures for earthquake resistance – Part 1: General rules, seismic actions and rules for buildings.*

Chandra, J., Guéguen, P., and Bonilla, L.-F. (2014a). On the use of PGV/Vs as a proxy for predicting nonlinear soil response. *Submitted to Soil Dynamics and Earthquake Engineering (in review).*

Chandra, J., Guéguen, P., Steidl, J. H., and Bonilla, L.-F. (2014b). In-situ assessment of the G-γ curve for characterizing the nonlinear response of soil: application to the Garner Valley Downhole Array (GVDA) and the Wildlife Liquefaction Array (WLA)."*Submitted to Bulletin of the Seismological Society of America (in review).*

Chávez-Garcia, F. J., and Bard, P. -Y. (1994). Site effects in Mexico City eight years after the September 1985 Michoacan earthquakes. *Soil Dynamics and Earthquake Engineering*. 13: 229-247.

Chávez-Garcia, F. J., and Cárdenas-Soto, M. (2002). The contribution of built environment to the 'free-field' ground motion in Mexico City. *Soil Dynamics and Earthquake Engineering*. 22: 773-780.

Chazelas, J. -L., Guéguen, P., Bard, P. -Y., and Semblat, J. -F. (2003). Modélisation de l'effet site-ville en modèle réduit centrifugé. Validation des techniques expérimentales. *6eme Colloque National AFPS.* Ecole Polytechnique, Palaiseau.

Chazelas, J. -L.(2010). *Program de recherché ANR ARVISE - Rapport Interne Final de la Contribution du LCPC.* (in French).

Chin, B., and Aki, K. (1991). Simultaneous study of the source, path, and site effects on strong ground motion during the 1989 Loma Prieta earthquake: A preliminary result on pervasive nonlinear site effects. *Bulletin of the Seismological Society of America.* 81: 1859-1884.

Chopra, A. K. (2007). *Dynamics of Structures*. New Jersey: Prentice Hall.

Clayton, R. W., and Wiggins, R. A. (1976). Source shape estimation and deconvolution of teleseismic bodywaves. *The Geophysical Journal of the Royal Astronomy Society.* 47: 151-177.

Clinton, J. F., Bradford, S. C., Heaton, T. H., and Favela, J. (2006). The observed wander of the natural frequencies in a structure. *Bulletin of the Seismological Society of America*. 96(1): 237-257.

Coburn, A., and Spence, R. (2002). *Earthquake Protection*. John Wiley & Sons, Ltd.

Cohen, B. (2006). Urbanization in developing countries: current trends, future projections, and key challenges for sustainability. *Technology in Society*. 28:63-80.

Colombi, A., Roux, P., and Rupin, M. (2014). Sub-wavelength energy trapping of elastic waves in a metamaterial. *The Journal of the Acoustical Society of America*, 136(2), EL192-EL198.

Cornou, C, Guéguen, P., Bard, P. –Y., and Haghshenas, E. (2004). Ambient noise energy busrts observation and modeling: Trapping of harmonic structure-soil induced-waves in a topmost sedimentary layer. *Journal of Seismology*. 8: 507-524.

Cotton, F., Scherbaum, F., Bommer, J. J., and Bungum, H. (2006). Criteria for selecting and adjusting ground-motion models for specific target regions: Application to Central Europe and rock sites. *Journal of Seismology*. 10: 137-156.

Coutant, O. (1996). "Observation of Shallow Anisotropy on Local Earthquake Records at the Garner Valley, Southern California, Downhole Array." *Bulletin of the Seismological Society of America.*, Vol.86, No.2, pp. 477-488.

Cox, B. R. (2006). Development of a Direct Test Method for Dynamically Assessing the Liquefaction Resistance of Soils In Situ. *Dissertation*. The University of Texas at Austin: May, 2006.

Cox, B. R., Stokoe, K. H., and Rathje E. M. (2009). An In-Situ Test Method for Evaluating the Coupled Pore Pressure Generation and Nonlinear Shear Modulus Behavior of Liquefiable Soils, *ASTM Geotechnical Testing Journal*, 32(1), 11-21.

Cua, G., and Heaton, T. H. (2012). Characterizing average properties of southern California ground motion amplitudes and envelopes. *submitted to the Bulletin of the Seismological Society of America.*

Danciu, L., and Tselentis, G. A. (2007). Engineering ground-motion parameters attenuation relationships for Greece. *Bulletin of the Seismological Society of America*, 97(1B): 162-183.

Delfose-Ribay, E., Djeran-Maigre, I., Cabrillac, R., and Gouvenot, D. (2004). Shear Modulus and damping ratio of grouted sand. *Soil Dynamics and Earthquake Engineering*. 24: 461-471.

De Martin, F., Kawase, H., and Bonilla, F. (2012), Inversion of Equivalent Linear Soil Parameters during the 2011 Tohoku Earthquake, Japan. *JST/ANR Joint Research ONAMAZU Project – International Symposium on Engineering Lessons Learned from the Giant Earthquake.*

Dimitriu, P., Theodulidis, N., Hatzidimitriou, P, and Anastasiadis, A. (2001). Sediment Nonlinearity and Attenuation of Seismic Waves; A Study of Accelerograms from Mefkas, Western Greece. *Soil Dynamics and Earthquake Engineering*. 21: 63-73.

Ditommaso, R., Mucciarelli, M., Gallipoli, M. R., and Ponzo, F. C. (2010). Effect of a single vibrating building on free-field ground motion: numerical and experimental evidences. *Bulletin of Earthquake Engineering.* 8:693-703.

Dobry, R., and Ladd, R. (1980). Discussion of 'Soil liquefaction and cyclic mobility evaluation for level ground during earthquakes,' by H. B. Seed and 'Liquefaction potential: science versus practice,' by R. B. Peck. *Journal of Geotechnical Engineering Division (ASCE)*. 106(6): 720-724.

Dobry, R. (2013). Radiation damping in the context of one-dimensional wave propagation: A teaching perspective. *Soil Dynamics and Earthquake Engineering*. 47: 51-61.

Doebling, S. W., Farra, C. R., Prime, M. B., and Shevit, D. W. (1996). Damage Identification and Health Monitoring of Structural and Mechanical Systems from Changes in Their Vibration Characteristics: A Literature Review. *Los Alamos National Lab*; Report LA-13070-MS.

Drnevich, V. P., and Richart, F. E. Jr. (1970). Dynamic prestraining of dry sand. *Journal of Soil Mechanics and Foundation Division (ASCE)*. 96(2): 453-469.

Efraimiadou, S., Hatzigeorgiou, G. D., and Beskos, D. E. (2012). Structural pounding between adjacent buildings: the effects of different structures configurations and multiple earthquakes. *Proceedings of the 15th World Conference on Earthquake Engineering, Lisbon, Portugal*. pp. 24-28.

Electrical Power Research Institute. (1988). A Criterion for Determining Exceedance of the Operating Basis Earthquake. *Report No. EPRI NP-5930.*, Palo Alto, California.

Elgamal, A., Yang, Z., and Lu, J. (2010). *Cyclic 1D Seismic Ground Response User's Manual Version 1.2*. University of California, San Diego, USA.

Escoffier, S. (2012). Experimental study of the effect of inclined pile on the seismic behavior of pile group. *Soil Dynamics and Earthquake Engineering*. 42: 275-291.

Endres, A., Arnold, J. P., and Roesset, J. M. (1984). Soil-structure response using fixed base structural modes. *Proceedings of 8th World Conference on Earthquake Engineering, California, 1984*. 3: 937-944.

Fenves, G. L., and Serino, G. (1990). Soil-Structure Interaction in Buildings from Earthquake Records. *Earthquake Spectra*. 6(4): 641-655.

Field, E. H., Johnson, P. A., Beresnev, I., and Zeng, Y. (1997) Nonlinear ground-motion amplification by sediments during the 1994 Northridge earthquake. *Nature*. 390: 599-602.

Field, E. H., Kramer, S., Elgamel, A. -W., Bray, J. D., Matasovic, N., Johnson, P. A., Cramer, C., Roblee, C., Wald, D. J., Bonilla, L. F., Dimitriu, P. P, and Anderson, J. G. (1998).

Nonlinear Site Response: Where We're at (A report from a *SCEC/PEER* seminar and workshop). *Seismological Research Letter*. 69(3): 230-234.

Frankel, A. D., Carver, D. L., and Williams, R. A. (2002). Nonlinear and Linear Site Response and Basin Effects in Seattle for the M 6,8 Nisqually, Washington, Earthquake. *Bulletin of the Seismological Society of America.* 92: 2090-2109.

Gajan, S., Kutter, B. L., Phalen, J. D., Hutchinson, T. C., and Martin, G. R. (2005). Centrifuge modeling of load-deformation behavior of rocking shallow foundations. *Soil Dynamics and Earthquake Engineering*. 25: 773-783.

Gariel, J. C., Mohammadioun, B., and Mohammadioun, G. (1993). L'experimentation sismique de Garner Valley: Resultats Preliminaires. *Proc. of the 3eme Colloque National AFPS,* Saint-Remy-les-Chevreuse, France. ES p.18-27.

Gazetas, G. (1991). Formulae and Charts for Impedance Functions of Surface and Embedded Foundations. *Journal of Geotechnical Engineering (ASCE*). 117(9): 1363-1381.

Gazetas, G., and Makris, N. (1991). Dynamic Analysis of Pile-Soil-Pile Interaction. Part I: Analysis of Axial Vibrations. *Earthquake Engineering and Structural Dynamics*. 20(2): 115-132.

Gélis, C., and Bonilla L. F. (2012). 2D P-SV Numerical Study of Soil-Source Interaction in a Nonlinear Basin. *Geophysical Journal International.* 191: 1374-1390.

Georgiannou, V. N., Tsomokos, A., and Stavrou, K. (2008). Monotonic and cyclic behavior of sand under torsional loading. *Géotechnique* 58(2): 113-124.

Ghosh, B., and Madabhushi, S. P. G. (2007). Centrifuge modeling of seismic soil structure interaction effects. *Nuclear Engineering Design*. 237: 887-896.

Gicev, V. (2009). Soil-structure interaction in nonlinear soil. In: Schanz, T., and Iankov, R. eds. *Coupled Site and Soil-Structure Interaction Effects with Application to Seismic Risk Mitigation.* Dordrecht: Springer, pp. 151-177.

Gu, Q. (2008). Finite element response sensitivity and reliability analysis of Soil-Foundation-Structure-Interaction (SFSI) sytems (Doctoral dissertation). University of California, San Diego.

Guéguen, P. (2000). Interaction sismique entre le sol et le bâti: de l'Interaction Sol-Structure à l'Interaction Site-Ville (Doctoral dissertation). Univérsite Joseph Fourier, Grenoble *(in French)*.

Guéguen P., Bard P. -Y., Oliveira, C. S. (2000). Experimental and Numerical Analysis of Soil Motions Caused by Free Vibrations of a Building Model, *Bulletin of the Seismological Society of America.* 90(6): 1464-1479.

Guéguen P., Bard P. -Y., Chavez-Garcia F. J. (2002). Site-City Interaction in Mexico City-Like environments: An Analytical Study, *Bulletin of the Seismological Society of America*. 92(2): 794-811.

Guéguen, P., and Bard, P. -Y. (2005). Soil-structure and soil-structure-soil interaction: Experimental evidence at the Volvi test site. *Journal of Earthquake Engineering.* 9(5): 657-693.

Guéguen, P., Cornou, C., Garambois, S., and Banton, J. (2007). On the Limitation of the H/V Spectral Ratio Using Seismic Noise as an Exploration Tool: Application to the Grenoble Valley (France), a Small Apex Ratio Basin. *Pure and Applied Geophysics.* 164: 115-134.

Guéguen, P. (2009). Sismologie urbaine: aléa local, dynamique des structures, interaction site-ville et vulnérabilité urbaine (HDR Report). Université Joseph Fourier, Grenoble. (*in French*)

Guéguen P., Langlais M., Foray P., Rousseau C., and Maury J. (2011). A natural seismic isolating system: the buried mangrove effects. *Bulletin of the Seismological Society of America.* 101(3): 1073-1080.

Ha, J. G., Lee, S. –H., Kim, D. –S, and Choo, Y. W. (2014). Simulation of soil-foundation-structure interaction of Hualien large-scale seismic test using dynamic centrifuge test. *Soil Dynamics and Earthquake Engineering*. 61-62: 176-187.

Hardin, B. O., and Black, W. L. (1968). Vibration modulus of normally consolidated clay. *Journal of Soil Mechanics and Foundation Division (ASCE)*. 94(2): 353-369.

Hardin, B. O., and Drnevich, V. P. (1970). Shear modulus and dampin in soils –ii: Deisgn equations and curves. *Technical Report UKY 27-70-CE3, Soil Mechanics Series No.2,* University of Kentucky.

Hartzell, S. (1998). Variability in Nonlinear Sediment Response during the 1994 Northridge, California, Earthquake. *Bulletin of the Seismological Society of America.* 88(6): 1426-1437.

Hartzell, S., Bonilla, L. F., and Williams, R. A. (2004) Prediction of Nonlinear Soil Effects. *Bulletin of the Seismological Society of America.* 94(5): 1609-1629.

Haskell, N.A. (1953). The dispersion of surface waves on multilayered media. *Bulletin of the Seismological Society of America.* 43(1): 17-34.

Hill, D. P., Reasenberg, P. A., Michael, A., Arabaz, W. J., Beroza, G., Brumbaugh, D., Brune, J. N., Castro, R., Davis, S., dePolo, D., Ellsworth, W. L., Gomberg, J., Harmsen, S.,

House, L., Jackson, S. M., Johnston, M. J. S., Jones, L., Keller, R., Malone, S., Munguia, L., Nava, S., Pechmann, J. C., Sanford, A., Simpson, R. W., Smith, R. B., Starks, M., Stickney, M., Vidal, A., Walter, S., Wong, V., and Zollweg, J. (1993). Seismicity Remotely Triggered by the Magnitude 7.3 Landers, Caliornia, Earthquake. *Science.* 260:1617-1623.

Holzer, T. L., and Savage, J. C. (2013). Global Earthquake Fatalities and Population. *Earthquake Spectra*. 29(1): 155-175.

Housner, G. W. (1952). Spectrum intensities of strong motion earthquakes. *Proceedings of the Symposium on Earthquake and Blast Effects on Structures*. pp. 21-36.

Housner, G. W. (1957). Interaction of building and ground during an earthquake. *Bulletin of the Seismological Society of America*. 47: 179-186.

Hujeux, J. –C. (1985) . Une loi de comportement pour le chargement cyclique des sols. In : Davidovici, V. ed. *Génie Parasismique*. France : Presses ENPC, pp. 278-302.

ICC-International Code Council. (2000). *2000 International Building Code*.

Idriss, I. M. (1990). Response of Soft Soil Sites During Earthquakes. In J.M. Duncan, ed.,*Proceedings, H. Bolton Seed Memorial Symposium*, BiTech Publishers, Vancouver, British Columbia, Vol. 2, pp. 273-289.

Idriss, I. M. (2011). Use of Vs_{30} to represent Local site Condition. *4th IASPEI/IAEE International Symposium. Effects of Source Geology on Seismic Motion*. August 23-26th, 2011. University of Santa Barbara California.

Ishihara, K. (1996). *Soil Behaviour in Earthquake Geotechnics*. Oxford Engineering Science Series. Oxford University Press.

Jackson, J. (2006). Fatal attraction: living with earthquakes, the growth of villages into megacities, and earthquake vulnerability in the modern world. *Philosophical Transactions of the Royal Society A*. 364:1911-1925.

Jennings, P. C. (1970). Distant Motions from a Building Vibration Test. *Bulletin of the Seismological Society of America.* 60(6): 2037-2043.

Jennings, P. C., and Bielak, J. (1973). Dynamics of building-soil interaction. *Bulletin of the Seismological Society of America*. 63(1): 9-48.

Johnson, P. A., and Jia, X. P. (2005). Nonlinear dynamics, granular media and dynamic earthquake trigerring. *Nature*. 437(6): 871-874.

Kanai, K. (1965). Some new problems of seismic vibrations of a structure. *Proceedings of the Third World Conference on Earthquake Engineering*, Auckland and Wellington, New Zealand, 22 January –1 February 1965, II-260–II-275.

Kanamori, H., Mori, J., Sturtevant, B., Anderson, D. L., and Heaton, T. (1992). Seismic excitation by space shuttles. *Shock Waves.* 2: 89-96.

Karklis, L. (2010) Mega-growth in a seismic world. Retrieved from: http://www.washingtonpost.com/ wp-dyn/content/graphic/2010/02/23/ GR2010022301120.html

Kausel, E., Roesset J. M, and Christian, J. T. (1976). Nonlinear behavior in soil–structure interaction. *Journal of Geotechnical Engineering Division (ASCE)*. 102(GT12): 1159–1178.

Kausel, E. (2010). Early history of soil-structure interaction. *Soil Dynamics and Earthquake Engineering*. 30: 822-832.

Kawakami, H., and Oyunchimeg, M. (2003). Normalized input–output minimization analysis of wave propagation in buildings. *Engineering Structures*, 25(11) : 1429-1442.

Kennett, B.L.N. (1974). Reflections, ray and reverberations, *Bulletin of the Seismological Society of America*, 64: 1685-1696.,

Kham, M. (2004). Propagation d'ondes sismiques dans les bassins sédimentaires: Des effets de site à l'interaction site-ville (Doctoral dissertation). Ecole Nationale des Ponts et Chausées, Paris. *(in French)*

Kham, M., Semblat, J. -F., Bard, P. -Y., and Dangla, P. (2006). Seismic site–city interaction: main governing phenomena through simplified numerical models. *Bulletin of the Seismological Society of America*. 96(5): 1934-1951.

Kim, W. Y., Sykes, L. R., Armitage, J. H., Xie, J. K., Jacob, K. H., Richards, P. G., West, M., Waldhauser, F., Armbruster, J., Seeber, L., Du, X. W., and Lerner-Lam, A. (2001). Seismic waves generated by aircraft impacts and building collapses at World Trade Center, New York City. *EOS, Transactions American Geophysical Union.* 82(47): 565-571.

Kitada, Y., Kinoshita, M., Iguchi, M., and Fukuwa, N. (1998). Soil-Structure Interaction effect on an NPP Reactor Building-Activities of NPEC; Achievements and the Current Status. *Proc. UJNR Workshop on Soil Structure Interaction, Menlo Park, California*. pp. 99-142.

Kittel, C. (2005). *Introduction to solid state physics*. John Wiley and sons

Kohler, M. D., Heaton, T. H., and Bradford, S. C. (2007). Propagating waves in the steel, moment-frame factor building recorded during earthquakes. *Bulletin of the Seismological Society of America*, 97(4): 1334-1345.

Koliopoulos, P. K., Margaris, B. N., and Klimis, N. S. (1998). Duration and energy characteristics of Greek strong motion records. *Journal of Earthquake Engineering*, 2(03) 391-417.

Konno, K., and Ohmachi, T. (1998). Ground-Motion Characteristics Estimated from Spectral Ratio between Horizontal and Vertical Components of Microtremor. *Bulletin of the Seismological Society of America*. 88(1): 228-241.

Kotronis, P, Tamagnini, C., and Grange, S. (Eds.). (2013). *ALERT Doctoral School 2013: Soil-Structure Interaction*. Aussois, France.

Ktenidou, O. -J., Chávez-García, F. J., and Pitilakis, K. D. (2011). Variance Reduction and Signal-to-Noise Ratio: Reducing Uncertainty in Spectral Ratios. *Bulletin of the Seismological Society of America*. 101(2): 619-634.

Kutter, B. L. (1995). Recent Advances in Centrifuge Modeling of Seismic Shaking (State of the Art Paper). *Proceedings of the 3rd International Conference on Recent Advancesin Geotechnical Earthquake Engineering and Soil Dynamics*, April 2-7, 1995, Volume II, St. Louis, Missouri. Paper No. SOA8.

Kramer, S. L. (1996). *Geotechnical Earthquake Engineering*. New Jersey: Prentice Hall.

Lai, C. G., and Martinelli, M. (2013). Soil-structure interaction under earthquake loading: Theoretical framework. In: Kotronis, P, Tamagnini, C., and Grange, S. eds. *ALERT Doctoral School 2013: Soil-Structure Interaction*, pp. 3-43.

Laurendeau, A., Cotton, F., Ktenidou, O. J., Bonilla, L. F., and Hollender, F. (2013). Rock and Stiff-Soil Site Amplification: Dependency on VS30 and Kappa (κ0). *Bulletin of the Seismological Society of America*, 103(6): 3131–3148.

Lawrence, Z., Bodin, P., Langston, C. A., Pearce, F., Gomberg, J., Johnson, P.A., Menq, F.-Y., and Brackman, T. (2008). Induced Dynamic Nonlinear Ground Response at Garner Valley, California. *Bulletin of the Seismological Society of America.*, Vol.98, No. 3, pp. 1412-1428.

Leroueil, S., and Vaughan, P. R. (1990). The general and congruent effects of structure in natural soils and weak rocks. *Géotechnique*. 40(3): 467 –488.

Li, Z., Escoffier, S., and Kotronis, P. (2013). Using centrifuge tests data to identify the dynamic soil properties: Application to Fontainebleau sand. *Soil Dynamics and Earthquake Engineering*. 52: 77-87.

Ljung, L. (1987). *System Identification: Theory for the user*. New Jersey: Prentice Hall.

Lopez-Caballero, F., Modaressi-Farahmand Razavi, A., and Modaressi, H. (2007). Nonlinear numerical method for earthquake site response analysis I – elastoplastic cyclic model and parameter identification strategy. *Bulletin of Earthquake Engineering.* 5: 303-323.

Lou, M., Wang, H., Chen, X., and Zhai, Y. (2011). Structure–soil–structure interaction: Literature review. *Soil Dynamics and Earthquake Engineering*. 31(12): 1724-1731.

Luco, J. E., and Contesse, L. (1973). Dynamic structure-soil-structure interaction. *Bulletin of the Seismological Society of America*. 63(4): 1289-1303.

Luco, J. E. (1980). Linear soil-structure interaction. *Report UCRL-15272, PSA No. 7249808*. Livermore, California: Lawrence Livermore laboratory.

Luco, J. E., Trifunac, M. D., and Wong, H. L. (1987). On the apparent change in the dynamic behavior of a nine-story reinforced concrete building. *Bulletin of the Seismological Society of America*. 77(6): 1961-1983.

Luco, J. E., Trifunac, M. D., and Wong, H. L. (1988). Isolation of soil-structure interaction effects by full-scale forced vibration tests. *Earthquake engineering and structural dynamics*, 16(1): 1-21.

Luco, J. E., and Lanzi, A. (2013). Approximate soil-structure interaction analysis by a perturbation approach: The case of stiff soils. *Soil Dynamics and Earthquake Engineering*. 51: 97-110.

Makris, N., and Gazetas, G. (1992). Dynamic Soil-Pile Interaction. Part II. Lateral and Seismic Response. *Earthquake Engineering & Structural Dynamics.* 21(2): 145-162.

Martinez-Rueda, J. E., Moutsokapas, G., and Tsantali, E. (2008). Predictive Equations to Estimate Arias Intensity and Cumulative Absolute Velocity as a Function of Housner Intensity. *AIP Conference Proceedings*. 1020: 309-316.

Mason, H. B., Trombetta, N. W., Chen, Z., Bray, J. D., Hutchinson, T. C., and Kutter, B. L. (2013). Seismic soil-foundation-structure interaction observed in geotechnical centrifuge experiments. *Soil Dynamics and Earthquake Engineering*. 48: 162-174.

Mehta, K., Snieder, R., and Graizer, V. (2007). Downhole Receiver Gunction: a Case Study. *Bulletin of the Seismological Society of America*. 97: (5): 1396-1403.

Meli, R., Faccioli, E., Muria-Vila, D., Quass, R., and Paolucci, R. (1998). A study of site effects and seismic response of an instrumented building in Mexico City. *Journal of Earthquake Engineering*. 2(1): 89-111.

Michel, C. and Gueguen, P. (2010). Time–Frequency Analysis of Small Frequency Variations in Civil Engineering Structures Under Weak and Strong Motions Using a Reassignment Method. *Structural Health Monitoring*. 9(2): 159-171.

Michel, C., Guéguen P., Choi, Y., and Vidal, M. (2013). Resonance frequencies of shear wall buildingd using deconvolution and Timoshenko beam theory. *submitted to Earthquake Engineering and Structural Dynamics*.

Mikael, A., Guéguen, P., Bard, P. -Y., Roux, P., and Langlais, M. (2013). The Analysis of Long-Term Frequency and Damping Wandering in Buildings Using the Random Decrement Technique. *Bulletin of the Seismological Society of America.*, 103(1): 236-246.

Mucciarelli, M., Gallipoli, M. R., Ponzo, F., and Dolce, M. (2003). Seismic waves generated by oscillating buildings: analysis of a release test. *Soil Dynamics and Earthquake Engineeringi.* 23(4): 255-262.

Mucciarelli, M., Ditommaso, R., Gallipoli, M. R., and Ponzo, F. (2009). Effect of Building-Building Interaction on"Fredd-Field" Ground Motion. *Increasing Seismic Safety by Combining Engineering Technologies and Seismomogical Data. NATO Science for Peace and Security Series C: Environmental Security.* Springer. pp.141-146.

Mucciarelli, M. (2014). The role of site effects at the boundary between seismology and engineering: lessons from recent earthquakes. *ESC Keynote Lecture of the 2nd European Conference on Earthquake Engineering and Seismology.* August 24-29, 2014, Istanbul, Turkey.

Mylonakis, G, Nikolaou, S, and Gazetaz, G. (2006). Footings under seismic loading: Analysis and design issues with emphasis on bridge foundations. *Soil Dynamics and Earthquake Engineering*. 26: 824-853.

Nader, M. N., and Astaneh, A. (1991). Dynamic Behavior of Flexible, Semirigid and Rigid Steel Frames. *Journal of Constructional Steel Research.* 18: 179-192.

Nakata, N., and Snieder, R. (2011). Near Surface Weakening in Japan after the 2011 Tohoku-Oki Earthquake. *Geophysical Research Letters*. 38: L17302.

Nakata, N., and Snieder, R. (2012). Estimating near-surface wave velocities in Japan by applying seismic interferometry to KiK-net data. *Journal of Geophysical Research.*117: B01308.

NEES@BYU. (2003). Final Design Specification for SFSI Test Structure. NEES@UCSB *Internal Report*.

Nigbor, R., Asghari, A., and Nastar, N. (2004). SFSI Test Structure at GVDA: Construction Report. NEES@UCSB *Internal Report*.

Newton, C., and Snieder, R. (2012). Estimating Intrinsic Attenuation of a Building Using Deconvolution Interferometry and Time Reversal. *Bulletin of the Seismological Society of America.* 102(5): 2200-2208.

Ohmachi, T., Inoue, S., Mizuno, K.-I., and Yamada, M. (2011). Estimated cause of extreme acceleration records at the KiK-net IWTH25 station during the 2008 Iwate-Miyage Nairiku earthquake, Japan. *Journal of Japan Association for Earthquake Engineering*. Vol.11. Issue. 1, pp. 1_32-1_47.

Okada, Y., Kasahara, K., Hori, S., Obara, K., Sekiguchi, S., Fujiwara, H., and Yamamoto, A. (2004). Recent progress of seismic observation net- works in Japan-Hi-net, F-net, K-NET and KiK-net. *Earth Planets Space*. 56: xv–xxviii.

Oliveira, C. S., Roca, A., and Goula, X. (Eds.). (2006). *Assessing and managing earthquake risk*. Dordrecht: Springer.

Padrón, L. A., Aznárez, J. J., and Maeso, O. (2009). Dynamic structure–soil–structure interaction between nearby piled buildings under seismic excitation by BEM–FEM model. *Soil dynamics and earthquake engineering*. 29(6): 1084-1096.

Paolucci, R. (1993). Soil-structure interaction effects on an instrumented building in Mexico City. *European Earthquake Engineering.* 3: 33-44.

Pavlenko, O. (2001). Nonlinear Seismic Effects in Soils: Numerical Simulation and Study. *Bulletin of the Seismological Society of America*. 91(2): 381-396.

Pavlenko, O., and Irikura, K. (2002). Changes in Shear Moduli of Liquefied and Nonliquefied Soils during the 1995 Kobe Earthquake and its Aftershocks at Three Vertical-Array Sites. *Bulletin of the Seismological Society of America.*, 92(5): 1952-1969.

Pavlenko, O., and Irikura, K. (2003). Estimation of Nonlinear Time-Dependent Soil Behavior in Strong Ground Motion Based on Vertical Array Data. *Pure and Applied Geophysics*. 160: 2365-2379.

Pech, A., Sánchez-Sesma, F. J., Snieder, R., Ignicio-Caballero, F., Rodríguez-Castellanos, A., and Ortíz-Alemán, J. C. (2012). Estimate of shear wave velocity, and its time-lapse change, from seismic data recorded at the SMNH01 station of KiK-net using seismic interferometry. *Soil Dynamics and Earthquake Engineering.* 39:128-137.

Pecker, A., and Mohammadioun, B. (1991). Downhole instrumentation for the evaluation of non-linear soil response on ground surface motion. *Trans. 11th SMIRT Conf.* K: 1991, Tokyo, Japan, pp.33-38

Pecker, A. (1995). "Validation of small strain properties from recorded weak seismic motions." *Soil Dynamics and Earthquake Engineering*., Vol.14, pp. 399-408.

Pecker, A. (2007). *Dynamique des structures et des ouvrages*. Ecole Nationale des Ponts et Chaussées, France.

Pecker, A., and Chatzigogos, C. T. (2010). Non Linear Soil Structure Interaction: Impact on the Seismic Response of Structures. In: Garevski, M., and Ansal, A. eds. *Earthquake Engineering in Europe*. Dordrecht: Springer, pp. 79-103.

Pecker, A., Paolucci, R., Chatzigogos, C, Correia, A. A., and Figini, R. (2014) The role of non-linear dynamic soil-foundation interaction on the seismic response of structures. *Bulleting of Earthquake Engineering*. 12:1157-1176.

Perrault, M., Guéguen, P., Aldea, A., and Demetriu, S. (2013). Reducing the uncertainties of the fragility curves using experimental testing in existing buildings: the case of the BRD Tower of Bucharest (Romania). *Earthquake Engineering and Engineering Vibration*. 12(4): 643-658.

Péquegnat, C., Guéguen, P., Hatzfeld, D., and Langlais, M. (2008). The French Accelerometric Network (RAP) and National Data Centre (RAP-NDC). *Seismological Research Letters.* 79(1): 79-89.

Phillips, C., and Hashash, Y. M. A. (2009). Damping formulation for nonlinear 1D site response analyses. *Soil Dynamics and Earthquake Engineering.* 29: 1143-1158.

Rahmani, M., and Todorovska, M. I. (2013). 1D system identification of buildings during earthquakes by seismic interferometry with waveform inversion of impulse responses–method and application to Milikan library. *Soil Dynamics and Earthquake Engineering.* 47: 157-174.

Rathje, E. M., Chang, W. –J., Stokoe, K. H., and Cox, B. R. (2004). Evaluation of ground strain from in situ dynamic response. *Proceeding of the 13th World Conference on Earthquake Engineering.*

Reed, J. W., and Kassawara, R. P. (1990). A criterion for determining exceedance of the operating basis earthquake. *Nuclear Engineering and Design*. 123: 387-396.

Régnier, J., Cadet, H., Bonilla, L. F., Bertrand, E., and Semblat, J. -F. (2013). Assessing Nonlinear Behavior of Soils in Seismic Site Response : Statistical Analysis on KiK-net

Strong-Motion Data. *Bulletin of the Seismological Society of America.* 103(3): 1750-1770.

Riedel, I., Guéguen, P., Dunand, F., and Cottaz, S. (2014). Macroscale Vulnerability Assessment of Cities Using Association Rule Learning. *Seismological research letter.* 85(2): 295-305

Roscoe, K. H., and Burland, J. B. (1968). On the generalised stress-strain behaviour of 'wet' clay. In: Heyman, J., and Leckie, F. A. eds. *Engineering plasticity*. London: Cambridge Univ. Press, pp. 535-609.

Roscoe, K. H. (1970). The influence of stains in soil mechanics. Tenth Rankin lecture. *Géotechnique.*20(2): 129-170.

Roullé, A., Foerster, E., Gehl, P., and Bernardie, S. (2007). Comparing nonlinear simulations to the available strong-motion data for site effect analysis in Pointe-à-Pitre (Guadeloupe, French Antilles). *7eme Colloque National AFPS.* Ecole Centrale Paris.

Roumelioti, Z., and Beresnev I.A. (2003). Stochastic Finite-Fault Modeling of Ground Motions from the 1999 Chi-Chi, Taiwan, Earthquake: Application to Rock and Soil Sites with Implications for Nonlinear Site Response. *Bulletin of the Seismological Society of America.*, 93(4): 1691-1702.

Rovithis, E. N., Parashakis, H., and Mylonakis, G. E. (2011). 1D harmonic response of layered inhomogeneous soil: Analytical investigation. *Soil Dynamics and Earthquake Engineering.* 31: 879-890.

Rubinstein, J. L, and Beroza, G. C. (2004). Evidence for Widespread Nonlinear Strong Ground Motion in the Mw 6,9 Loma Prieta Earthquake. *Bulletin of the Seismological Society of America.* 94(5): 1595-1608.

Rubinstein, J. L, and Beroza, G. C. (2005). Depth Constraints on Nonlinear Strong Ground Motion from the 2004 Parkfield Earthquake. *Geophysical Research Letters*. 32: L14313.

Rubenstein, J. L., Uchida, N, and Beroza, G. C. (2007). Seismic velocity reduction caused by the 2003 Tokachi-Oki earthquake. *Journal of Geophysical Research.* 112: B05315.

Rupin, M. (2014). Cavité réverbérante et résonateurs sub-longeur d'onde : approches numériques et expérimentales. *Dissertation*. Université de Grenoble.

Rupin, M., Lemoult, F., Lerosey, G., and Roux, P. (2014). Experimental Demonstration of Ordered and Disordered Multiresonant Metamaterials for Lamb Waves. *Physical review letters*, 112(23), 234301

Şafak, E. (1992). On identification of soil-structure interaction fom recorded motions of buildings. *Earthquake Engineering, Tenth World Conference.* Balkema, Rotterdam. pp. 1885-1890.

Şafak, E. (1995). Detection and identification of soil-structure interaction in buildings from vibration recordings. *Journal of Structural Engineering, ASCE*. 121: 899-906.

Şafak, E. (1998a). New approach to analyzing soil-building systems. *Soil Dynamics and Earthquake Engineering.* 17: 509-517.

Şafak, E. (1998b). Propagation of seismic waves in tall buildings. *The Structural Design of Tall Buildings*. 7: 295-306.

Şafak, E. (1999). Wave-Propagation Formulation of Seismic Response of Multistory Buildings . *Journal of Structural Engineering, ASCE.* April: 426-437.

Şafak, E. (2001). Local site effects and dynamic soil behavior. *Soil Dynamics and Earthquake Engineering.* 21: 453-458.

Saleh, S., Madabhushi, S. P. G. (2010). An investigation into the seismic behavior of dams using dynamic centrifuge modeling. *Bulletin of Earthquake Engineering*. 8: 1479-1495.

Sandikkaya, M. A., Akkar, S., and Bard, P. –Y. (2013). A Nonlinear Site-Amplification Model for the Next Pan-European Ground-Motion Prediction Equations. *Bulletin of the Seismological Society of America*, 103(1): 19-32.

Sato, K, Kokusho, T, Matsumoto, M, and Yamada, E. (1996). Nonlinear seismic response and soil property during strong motion. *Japanese Geotechnical Society/ Special issue of soils and foundations*, pp. 41-52.

Satoh, T, Sato, T, and Kawase, H. (1995). Nonlinear behavior of soil sediments identified by using borehole records observed at the Ashigara Valley, Japan. *Bulletin of the Seismological Society of America*, 85(6): 1821-1834.

Satoh, T, Fushimi, M, and Tatsumi, Y. (2001) Inversion of Strain-Dependent Nonlinear Characteristics of Soils Using Weak and Strong Motions Observed by Borehome Sites in Japan. *Bulletin of the Seismological Society of America*, 91(2): 365-380.

Sawazaki. K, Sato, H., Nakahara, H., and Nishimura, T. (2009). Time-Lapse Changes of Seismic Velocity in The Shallow Ground caused by Strong ground Motion Shock of the 2000 Western-Totori Earthquake, Japan, as revealed from Coda Deconvolution Analysis. *Bulletin of the Seismological Society of America.* 99(1): 352-366.

Schanz, T., and Iankov, R. (Eds.). (2009). *Coupled Site and Soil-Structure Interaction Effects with Application to Seismic Risk Mitigation.* Dordrecht: Springer.

Seed, H. B., and Idriss, I. M. (1969). Soil Moduli and Damping Factors for Dynamic Response Analyses. *Government Funded Technical Reports*. EERC-70/10.

Seed, H. B., and Idriss, I. M. (1970). Seismic response of horizontal soil layers. *Journal of Soil Mechanics (ASCE)*. 94: 1003-1031.

Seed, H. B., Murarka, R., Lysmer, J., and Idriss, I. M. (1976). Relationships of maximum acceleration, maximum velocity, distance from source, and local site conditions for moderately strong earthquakes. *Bulletin of the Seismological Society of America.* 66(4): 1323-1342.

Seed, H. B., Wong, R. T., Idriss, I. M., Tokimatsu, T. (1984). Moduli and Damping Factors for Dynamic Analyses of Cohesionless Soils. *Earthquake Engineering Research Center*. Report No. UCB/EERC-84/14, September, 1984.

Semblat, J. -F., and Luong, M. P. (1998). Wave Propagation through Soils in Centrifuge Testing. *Journal of Earthquake Engineering*. 2(1): 147-171.

Semblat, J. -F., Kham, M., and Bard, P. -Y. (2008). Seismic-wave propagation in alluvial basins and influence of site-city interaction. *Bulletin of the Seismological Society of America*. 98(6): 2665-2678.

Sirles, P. C. (1988). Case Study: Shear Wave Velocity Measurements Before and After Dynamic Compaction of Cohesionless Soil Deposits. *1988 SEG Annual Meeting*. Anaheim, California.

Sleep, N. H. (2010). Nonlinear Behavior of Strong Surface Waves Trapped in Sedimentary Basins. *Bulletin of the Seismological Society of America.*, 100: 826-832.

Snieder, R., and Şafak, E. (2006). Extracting the Building Response Using Seismic Interferometry: Theory and Application to the Milikan Library in Pasadena, California. *Bulletin of the Seismological Society of America.* 96(2): 586-598.

Steidl, J. H., Tumarkin, A. G., and Archuleta, R. J. (1996). What Is a Reference Site? *Bulletin of the Seismological Society of America.* 86(6): 1733-1748.

Steidl, J. H., Archuleta, R.J., Tumarkin, A.G., and Bonilla, L.-F. (1998). Observations and Modeling of Ground Motion and Pore Pressure at the Garner Valley, California, Test Site, in The Effects of Surface Geology on Seismic Motion (K. Irikura, K. Kudo, H. Okada, and T. Sasatani, Eds.), A. A. Balkema, Rotterdam, The Netherlands, Vol. 1, 225–232.

Steidl, J. H., and Seale, S., (2010). Observations and analysis of ground motion and pore pressure at the NEES instrumented geotechnical field sites. *Proceedings of the 5th*

International Conference on Recent Advances in Geotechnical Earthquake Engineering and Soil Dynamics, May 24-29, San Diego, CA, 2010; paper No. 133b, ISBN-887009-15-9.

Steidl, J. H., Gee, R., Seale, S., and Hegarty, P. (2012). Recent Enhancements to the NEES@UCSB Permanently Instrumented Field Sites. *Proceeding of the 15th World Conference on Earthquake Engineering.*

Steidl, J. H., Civilini, F., and Seale, S. (2014). What have we learned after a decade of experiments and monitoring at the NEES@UCSB permanently instrumented field sites. *Proceeding of the 10th U.S. National Conference on Earthquake Engineering,* July 21-25, 2014, Anchorage, Alaska.

Stellar, R. (1996). "New Borehole Geophysical Results at GVDA." NEES@UCSB *Internal Report*.

Stewart, J. P., and Fenves, G. L. (1998). System identification for evaluation soil-structure interaction effects in buildings from strong motion recordings. *Earthquake Engineering and Structural Dynamics.* 27: 869-885.

Stewart, J. P., Seed, R. B., and Fenves, G. L. (1998). Empirical evaluation of nertial soil-structure interaction effects. *Pacific Earthquake Engineering Research Center, University of California, Berkeley.* Report No. PEER-98/07.

Stewart, J. P., Fenves, G. L., and Seed, R. B. (1999a). Seismic soil-structure interaction in buildings. I: Analytical aspects. *Journal of Geotechnical and Geoenvironmental Engineering (ASCE)*. 125(1): 26-37.

Stewart, J. P., Fenves, G. L., and Seed, R. B. (1999b). Seismic soil-structure interaction in buildings. II: Empirical findings. *Journal of Geotechnical and Geoenvironmental Engineering (ASCE)*. 125(1): 38-48.

Stewart, J. P., Whang, D. H., Fox, P. J., and Wallace, J. W. (2002). Applications of UCLA NEES Equipment for Testing of Soil-Foundation-Structure Interaction. *Proceeding of the 7th U.S. National Conference on Earthquake Engineering,* July 21-25, 2002, Boston, Massachusetts. Paper 00018.

Stinson, E. (2013). Characterizing Soil-Foundation-Structure Interaction using Experimental Data from the SFSI Test Structure at the Garner Valley Field Site. *Master Thesis*. Princeton University.

Stokoe, K. H., and Darendeli, M. B. (1998). Laboratory evaluation of the dynamic properties of intact soil specimens: Garner Valley, California. *Internal report.*

Taylor, R. N. (1995). *Geotechnical Centrifuge Technology*. Blackie Academic & Professional, UK.

Theodulidis, N., Bard, P.-Y., Archuleta, R., and Bouchon, M. (1996). Horizontal-to-Vertical Spectral Ratio and Geological Conditions: The Case of Garner Valley Downhole Array in Southern California. *Bulletin of the Seismological Society of America.*, Vol.86, No. 2, pp. 306-319.

Thomson, W. T. (1950). Transmission of elastic waves through a stratified solid medium. *Journal of Applied Physics*. 21(2): 89-93.

Tileylioglu, S. (2008). Evaluation of Soil-Structure Interaction Effects from Field Performance. *Dissertation*. University of California, Los Angeles.

Tileylioglu, S., Nigbor, R. L., and Stewart, J. P. (2008). Determination of soil-structure interaction effects for a model test structure using parametric system identification procedures. *Proceedings of the 4th Geotechnical Earthquake Engineering and Soil Dynamics*, May 18-22, 2008, Sacramento, California.

Todorovska, M. I., and Trifunac, M. D. (2008). Impulse response analysis of the Van Nuys 7-storey hotel during 11 earthquakes and earthquake damage detection. *Structural control and health monitoring*. 15(1): 90-116.

Todorovska, M. I. (2009a). Seismic Interferometry of a Soil-Structure Interaction Model with Coupled Horizontal and Rocking Response. *Bulletin of the Seismological Society of America.* 99(2A): 611-625.

Todorovska, M. I. (2009b). Soil-Structure System Identification of Milikan Library North-South Response during Four Earthquakes (1970-2002): What Caused the Observed Wandering of the System Frequencies?. *Bulletin of the Seismological Society of America.* 99(2A): 626-635.

Todorovska, M. I., and Rahmani, M. T. (2013). System identification of buildings by wave travel time analysis and layered shear beam models – spatial resolution and accuracy. *Structural Control and Health Monitoring*. 20(5): 686-702.

Trifunac, M. D., and Brady, A. G. (1975). A study on the duration of strong earthquake ground motion. *Bulletin of the Seismological Society of America*. 65(3): 581-626.

Trifunac, M. D. (2009). The nature of site response during earthquakes. In: Schanz, T., and Iankov, R. eds. *Coupled Site and Soil-Structure Interaction Effects with Application to Seismic Risk Mitigation.* Dordrecht: Springer, pp. 3-31.

Trifunac, M. D., Todorovska, M. I., Manic M. I., Bulajić B. A (2010). Variability of the fixed-base and soil–structure system frequencies of a building—The case of Borik-2 building. *Structural Control Health Monitoring*. 17: 120–151.

Trombetta, N. W., Mason, H. B., Chen, Z., Hutchinson, T. C., Bray, J. D., and Kutter, B. L. (2013). Nonlinear dynamic foundation and frame structure response observed in geotechnical centrifuge experiments. *Soil Dynamics and Earthquake Engineering*. 50: 117-133.

Trombetta, N. W., Mason, H. B., Chen, Z., Hutchinson, T. C., Zupan, J. D., Bray, J. D., and Kutter, B. L. (2014). Nonlinear Soil-Foundation-Structure and Structure-Soil-Structure Interaction: Centrifuge Test Observations. *Journal of Geotechnical and Geoenvironmental Engineering, ASCE*. 140(5):04013057-(1-11).

Tsuda, K., and Steidl, J. H. (2006). Nonlinear site response from the 2003 and 2005 Miyagi-Oki earthquakes. *Earth, Planets, and Space,* 58, 1593-1597.

Vucetic, M., and Dobry, R. (1991). Effect of Soil Plasticity on Cyclic Response. *Journal of Geotechnical Engineering (ASCE)*. 117:89-107.

Vucetic, M. (1994). Cyclic Threshold Shear Strains in Soils. *Journal of Geotechnical Engineering (ASCE)*. 120:2208-2228.

Wair, B. R., DeJong, J. T., and Shantz, T. (2012). Guidelines for Estimation of Shear Wave Velocity Profiles. *Pacific Earthquake Engineering Research Center, University of California, Berkeley.* Report No. PEER-12/08.

Walling, M., Silva, W., and Abrahamson, N. (2008). Nonlinear Site Amplification Faxtors for Constraining the NGA Models. *Earthquake Spectra*. 24(1): 243-255.

Wapenaar, K., Draganov, D., Snieder, R., Campman, X., and Verdel, A. (2010). Tutorial on seismic interferometry: Part 1 – Basic principles and applications. *Geophysics*. 75(5): 75A195-75A209.

Wirgin, A., and Bard, P. –Y. (1996). Effects of Buildings on the Duration and Amplitude of Ground Motion in Mexico City. *Bulletin of the Seismological Society of America*. 86(3): 914-920.

Wong, H. L., and Trifunac, M. D. (1975) Two-dimensional, antiplane, building-soil-building interaction for two or more buildings and for incident plane SH waves. *Bulletin of the Seismological Society of America*, 65(6): 1862-1885.

Wu, C., Peng, Z., and Assimaki, D. (2009). Temporal Changes in Site Response Associated with the Strong Ground Motion of the 2004 Mw 6.6 Mid-Niigata Earthquake Sequences in Japan. *Bulletin of the Seismological Society of America*. 99(6): 3487-3495.

Yamamuro, A., and Kaliakin, V. N. (Eds.). (2005). Soils Constitutive Models. Evaluation, Selection, and Calibration. *ASCE Geotechnical Special Technical Publication 128, J.* New York: ASCE.

Yang, Z., Elgamal, A., Adalier, K., and Sharp, M. (2004). Container Boundary Effect on Seismic Earth Dam Response in Centrifuge Model Tests. *11th International Conference on Soil Dynamics & Earthquake Engineering and 3rd International Conference on Earthquake Geotechnical Engineering*. University of California, Berkeley, pp. 669-675.

Youd, L. T. (1972). Compaction of sands by repeated shear straining. *Journal of Soil Mechanics and Foundation Division (ASCE)*. 98(7): 709-725.

Youd, T. L., Bartholomew, H. A. J., and Proctor, J. S. (2004) Geotechnical logs and data from permanently instrumented fields sites: Garner Valley Downhole Array (GVDA) and Wildlife Liquefaction Array (WLA). NEES@UCSB *internal report.*

Yu, G., Anderson, J. G., and Siddharthan, R. (1992). On The Characteristics of Nonlinear Soil Response. *Bulletin of the Seismological Society of America*, 83(1): 218-244.

Zeghal, M. and Elgamal, A. W. (1994). Analysis of Site Liquefaction Using Earthquake Records. *Journal of Geotechnical Engineering*. 120 (6): 996-1017.

Zeng, X., and Schofield A. N. (1996). Design and performance of an equivalent-shear-beam container for earthquake centrifuge modeling. *Géotechnique*, 46(1): 83-102.